Modeling of nano-photonic systems using the adaptive Fourier Modal Method and analytical dipole models

Zur Erlangung des akademischen Grades eines

DOKTORS DER NATURWISSENSCHAFTEN

von der Fakultät für Physik des Karlsruher Instituts für Technologie (KIT)

genehmigte

DISSERTATION

von

Jens Küchenmeister

aus Prag

Tag der mündlichen Prüfung: 14.12.2012

Referent: Prof. Dr. Kurt Busch

Korreferent: Prof. Dr. Martin Wegener

To 42,195 meters

Last is just the slowest winner.

Contents

Chapter 1

Introduction

The look at the night sky deeply fascinates me. The idea of perceiving light from stars that may have ceased to exist thousands of years ago is baffling.

Light has always been a source of wonder and a fundamental driving force for mankind's development. Alongside the industrial development of modern times, scientists and engineers have gained a deep understanding of the creation, manipulation and utilization of light. By the end of the 20^{th} century, highly developed light sources such as lasers and light emitting diodes had reached everyday life.

This advancement was helped along by the continued miniaturization in the field of computer technology which offered techniques to fabricate smaller and smaller structures. Eventually, the nano-scale was reached and the interaction of light and matter on the length scale of optical wavelengths could be studied. In this context, the so-called *metamaterials* gained a tremendous amount of interest among scientists [1]. These materials consist of periodically arranged micro- or nanostructured *meta-atoms* whose characteristic structure sizes are smaller than the wavelength of the incident light. Usually, they are composed of dielectric materials and metals. Due to their small size, these meta-atoms are not individually perceived by the incident electro-magnetic waves. They rather act as effective material whose properties can be tailored by a suitable choice of the meta-atom's geometry. By doing so, remarkable physical effects can be observed such as a negative refractive index [2, 3] with the intriguing application of a perfect lens [4].

Parallel to the field of metamaterials the concept of *photonic crystals* emerged. A photonic crystal is composed of periodically arranged, dielectric materials. Again, the structure size is below the wavelength of the incident light. The groundbreaking discovery of this field was the insight of Yablonovitch [5] and John [6] that even though the dielectric materials themselves are transparent for the incident light, the light's propagation within the crystal may be suppressed in all directions for a suitable geometry. In this case, the crystal features a *photonic band gab*. Thus, a suitably constructed crystal can serve as insulator for light which opens the route to the vision of integrated photonic crystal circuitry. Recently, a woodpile photonic crystal structure has been fabricated with a band gap in the visible regime of light [7].

Even though the experimental expertise for fabricating metamaterials and photonic crystals drastically increased during the last decade [8], the manufacturing remains a costly and time-consuming process. Thus, numerical modeling is necessary both for a deeper understanding as well as for finding optimized and/or robust designs. This means that efficient and precise methods to numerically solve Maxwell's equations, which govern the propagation of light, are needed.

In general, we can distinguish between two types of methods for solving these equations—the time-domain simulations, which evolute the light's propagation in a system in time, and the frequency-domain methods, that solve Maxwell's equations for time-harmonic fields. Popular methods in the time-domain are the Finite-Difference Time-Domain Method [9] and the Discontinuous Galerkin Method [10]. In the frequency domain, the Finite Element Method is widely used [11].

One of the methods used to predict the transmission properties of periodic photonic systems (both dielectric and metallic) in the frequency-domain is the Fourier Modal Method (FMM) [12, 13, 14]. Since the investigated systems are periodic, all quantities of the system are expressed as Fourier transforms, i.e., in a plane wave basis. Maxwell's equations are reformulated into an eigenvalue problem the solutions of which are the eigenmodes of the considered system. Particular problems arise at material boundaries which are represented as jumps in the permittivity. Here, two interrelated concepts emerged to substantially improve the method's performance: adaptive coordinates (AC) [15, 16] and adaptive spatial resolution (ASR) [17]. Both change the investigated permittivity and permeability by means of a coordinate transformation. However, there remain questions: a general principle for the construction of the transformations and a proper parameter choice for the transformations are unknown. A large part of this thesis deals with the question of how these problems can be solved. For that, we study the eigenmodes of a fiber and an array of metallic cylinders. Since only two-dimensional AC and ASR transformations have been discussed in literature, we investigate how the advancement of the coordinate transformations towards three dimensions can be accomplished.

Yet even the most advanced numerical methods need modern computational infrastructure and enough time and memory to solve Maxwell's equations with the necessary accuracy. Thus, finding optimized designs, though easier than by experimental means, is still hard due to the large number of geometrical degrees of freedom for a structure. Therefore, it is desirable to have an analytical model at hand which enables fast parameter scans and allows for a deep physical insight. In this thesis, several models describing the transmission of light through slabs of periodic, metallic nanostructures consisting of rods and crosses are presented. They describe the considered nanostructures as superposition of interacting dipoles and, thereby, provide a physical picture how light is transmitted through these structures.

Outline of the thesis

This thesis is structured in the following way: In the second chapter we review the fundamentals of electrodynamics needed for this thesis. This includes Maxwell's equations and the basic description of phenomena occurring in periodic materials.

The third chapter introduces the numerical method of choice, namely the Fourier Modal Method. Besides the solution of Maxwell's equations by means of an eigenvalue problem, it also comprises the use of a scattering matrix algorithm which is particularly helpful for systems with repeating structural patterns in propagation direction. Since one of the two main topics of this thesis is coordinate transformations in the context of the FMM, we use the covariant formulation of Maxwell's equations to change from Cartesian to curvilinear coordinates. In particular, we introduce the concept of the effective permittivity and permeability which contain all information about the coordinate transformations.

In Chapter 4, the FMM is utilized to investigate opal photonic crystals which are dielectric spheres stacked in a face-centered cubic lattice. Here, we analyze certain thickness-dependent

properties of these photonic crystals and compare the numerical solutions of Maxwell's equations to experimental results.

The realization of two-dimensional AC and ASR coordinate transformations for the FMM is discussed in Chapter 5. The chapter contains the analytical construction of several classes of transformations, the visualization of the corresponding transformed permittivities and, most importantly, a study on how the parameters of the transformations have to be chosen in order to obtain accurate results. The chapter is concluded by the formulation of a modularity concept which allows for the construction of transformations for structures with several complex sub-structures.

The subsequent Chapter 6 deals with the generalization of the two-dimensional coordinate transformations to three dimensions. The particular example used is two layers of mutually rotated crosses. For this system, a three-dimensional coordinate transformation is developed and numerically analyzed.

Beyond the numerical solution of Maxwell's equations, Chapter 7 contains several analytical models based on coupled dipoles to describe how light is transmitted through slabs of metallic nanostructures. This is the second main topic of this thesis. Firstly, we review previous work and discuss the investigated physical systems. Secondly, the simple dipole model is presented. It is demonstrated that the model yields good results, particularly for large distances between the slabs. Also, we show that lattice resonances can be incorporated into the model. However, it proves to be insufficient for certain structures, which is why we extend the dipole model to the twin model. At the end of the chapter, several improvements—like near-field coupling and an even further extended model based on a continuous charge distribution—are presented.

The thesis is concluded in Chapter 8, where we summarize the progress in the development of the thesis' two major topics, namely the coordinate transformations for the FMM and the analytical dipole models. Finally, we outline possible future work.

Chapter 2

Fundamentals of Classical Electrodynamics

In this chapter, we discuss the fundamentals of electrodynamics needed in the remainder of this thesis. Naturally, the starting point are the underlying equations, namely Maxwell's equations. Secondly, we introduce two important models which describe dispersive materials. In Section 2.3, the fundamentals of electromagnetic waves are studied. This includes the discussion of plane waves, polarization and polarization-dependent effects in media. In Section 2.5, we examine the continuity conditions that are demanded by Maxwell's equations. Subsequently, we discuss the energy transport of electromagnetic fields. In Section 2.6, the mathematical tools to rewrite Maxwell's equations in curvilinear coordinates are presented. This is followed by the fundamentals of optics in periodic systems in Section 2.7, which comprises the reciprocal lattice, Bloch's theorem and diffraction.

2.1 Maxwell's equations

The equations which describe the phenomena of electrodynamics are *Maxwell's equations*. In materials, their differential form in SI units is [18]

$$\nabla \cdot \mathbf{D} = \rho, \tag{2.1a}$$

$$\nabla \times \mathbf{E} = -\frac{\partial \mathbf{B}}{\partial t}, \tag{2.1b}$$

$$\nabla \cdot \mathbf{B} = 0, \tag{2.1c}$$

$$\nabla \times \mathbf{H} = \mathbf{j} + \frac{\partial \mathbf{D}}{\partial t}, \tag{2.1d}$$

with $\mathbf{E}$ denoting the *electric field* and $\mathbf{B}$ the *magnetic induction*. In general, all fields and sources can be complex and depend on time and space. The source terms ρ and $\mathbf{j}$ are called *free charge density* and *free current density*, respectively. The *magnetic field* $\mathbf{H}$ and the *electric displacement* $\mathbf{D}$ are defined as

$$\mathbf{D} = \varepsilon_0 \mathbf{E} + \mathbf{P}, \tag{2.2a}$$

$$\mathbf{H} = \frac{1}{\mu_0} \mathbf{B} - \mathbf{M}, \tag{2.2b}$$

with $\mathbf{P}$ and $\mathbf{M}$ being the *average electric* and *magnetic dipole moment per unit volume*, respectively. The parameters ε_0 and μ_0 denote the *permittivity* and *permeability in free space*. Included in Eqs. (2.2) is the assumption that higher order moments can be neglected compared to the dipole moment.

In this thesis, we aim at solving Maxwell's equations in the frequency domain. Therefore, we assume a time dependence $e^{-i\omega t}$ for all fields. Furthermore, we restrict ourselves to systems without free charges or currents. With these assumptions, Eqs. (2.1) take the form

$$\begin{aligned} \nabla \cdot \mathbf{D} &= 0, && \text{(2.3a)} \\ \nabla \times \mathbf{E} &= i\omega \mathbf{B}, && \text{(2.3b)} \\ \nabla \cdot \mathbf{B} &= 0, && \text{(2.3c)} \\ \nabla \times \mathbf{H} &= -i\omega \mathbf{D}, && \text{(2.3d)} \end{aligned}$$

where all fields depend on the spatial coordinate $\mathbf{r}$ and the frequency ω. So far, the set of equations is incomplete, since we have not linked the electric and magnetic dipole moments to the fields yet. Here, we consider materials that can be described by

$$\begin{aligned} \mathbf{P}(\mathbf{r},\omega) &= \varepsilon_0 \, \underline{\chi}_{\mathrm{e}}^{(1)}(\mathbf{r},\omega) \; \mathbf{E}(\mathbf{r},\omega), && \text{(2.4a)} \\ \mathbf{M}(\mathbf{r},\omega) &= \mu_0 \, \underline{\chi}_{\mathrm{m}}^{(1)}(\mathbf{r},\omega) \; \mathbf{H}(\mathbf{r},\omega), && \text{(2.4b)} \end{aligned}$$

where we introduced the electric susceptibility $\underline{\chi}_{\mathrm{e}}^{(1)}$ and magnetic susceptibility $\underline{\chi}_{\mathrm{m}}^{(1)}$. Entering those in Eqs. (2.2) yields

$$\begin{aligned} \mathbf{D}(\mathbf{r},\omega) &= \varepsilon_0 \, \underline{\varepsilon}(\mathbf{r},\omega) \; \mathbf{E}(\mathbf{r},\omega), && \text{(2.5a)} \\ \mathbf{B}(\mathbf{r},\omega) &= \mu_0 \, \underline{\mu}(\mathbf{r},\omega) \; \mathbf{H}(\mathbf{r},\omega), && \text{(2.5b)} \end{aligned}$$

which we call the *constitutive relations* in the following. The permittivity $\underline{\varepsilon} = \mathbb{1} + \underline{\chi}_{\mathrm{e}}^{(1)}$ and the permeability $\underline{\mu} = \mathbb{1} + \underline{\chi}_{\mathrm{m}}^{(1)}$ are tensorial quantities. They describe anisotropic materials, which are dispersive, i.e., frequency-dependent. The constitutive relations are linear, which means that the equations above do not describe phenomena of non-linear optics, such as second-harmonic generation. The set of equations formed by Eqs. (2.3) and (2.5) does in fact contain more equations than unknowns. Upon careful inspection, we find that the divergence equations are always fulfilled if $\omega \neq 0$:

$$\mathbf{B} \overset{(2.3b)}{=} \frac{1}{i\omega} \nabla \times \mathbf{E} \quad \Rightarrow \quad \nabla \cdot \mathbf{B} = \frac{1}{i\omega} \nabla \cdot (\nabla \times \mathbf{E}) = 0. \tag{2.6}$$

The other divergence equation follows analogously. Therefore, we only need to solve the curl equations

$$\begin{aligned} \nabla \times \mathbf{E}(\mathbf{r},\omega) &= +i\omega \, \mu_0 \, \underline{\mu}(\mathbf{r},\omega) \; \mathbf{H}(\mathbf{r},\omega), && \text{(2.7a)} \\ \nabla \times \mathbf{H}(\mathbf{r},\omega) &= -i\omega \, \varepsilon_0 \, \underline{\varepsilon}(\mathbf{r},\omega) \; \mathbf{E}(\mathbf{r},\omega). && \text{(2.7b)} \end{aligned}$$

A remarkable property of these equations (and Maxwell's equations in general) is that they do not contain a fundamental length scale. Therefore, we can define all quantities with respect to a length scale a. In particular, we choose the lattice constant of the systems that we investigate in the subsequent chapters. Furthermore, the fields need an additional scaling factor H_0. Thus, we introduce the dimensionless quantities in Tab. 2.1, where we use the speed of light c.

The additional term ω' in the electric field is entered here since we also use this term in our implementation of the Fourier Modal Method introduced in Chapter 3. From a conceptual point of view, it is not needed for transforming to dimensionless units. The wave vector $\mathbf{k}$ is introduced in Section 2.3.1. To improve the readability, we omit the prime in the following. Thereby, we arrive at the dimensionless curl equations:

$$\begin{aligned} \nabla \times \mathbf{E}(\mathbf{r},\omega) &= +i\omega^2 \, \underline{\mu}(\mathbf{r},\omega) \; \mathbf{H}(\mathbf{r},\omega), && \text{(2.8a)} \\ \nabla \times \mathbf{H}(\mathbf{r},\omega) &= -i \quad \underline{\varepsilon}(\mathbf{r},\omega) \; \mathbf{E}(\mathbf{r},\omega). && \text{(2.8b)} \end{aligned}$$

dimensionless quantity	relation to quantitiy in SI units
frequency ω'	$\omega' = \omega \frac{a}{c}$
time t'	$t' = t \frac{c}{a}$
wave vector $\mathbf{k}'$	$\mathbf{k}' = \mathbf{k}\, a$
position $\mathbf{r}'$	$\mathbf{r}' = \frac{\mathbf{r}}{a}$
wavelength λ'	$\lambda' = \frac{\lambda}{a}$
diff. operator ∇'	$\nabla' = \nabla\, a$
magnetic field $\mathbf{H}'$	$\mathbf{H}' = \mathbf{H}\, \frac{1}{H_0}$
electric field $\mathbf{E}'$	$\mathbf{E}' = \mathbf{E}\, \omega'\, c\, \varepsilon_0\, \frac{1}{H_0}$

Table 2.1: Dimensionless quantities used to rewrite Maxwell's equations.

2.2 Material models

In this section, we discuss two models for dispersive materials. Firstly, we examine the Lorentz oscillator model since we design similar models in Chapter 7. Secondly, the Drude model, which describes the permittivity of metals, is reviewed. We use this model in the investigation of metallic test systems.

2.2.1 Lorentz oscillator model

In the early 20th century, H. A. Lorentz developed a classical theory which treats electrons and ions like harmonic oscillators in order to describe optical properties[1] (see Chapter 4 in Ref. [19]). This model gives a good perception of the underlying physics and, moreover, the results are formally identical to results from quantum-mechanical treatment, though some quantities may be interpreted differently (see Ref. [18]). This classical model can be found in various books, e.g., Refs. [20, 21, 22].

First of all, we deduce the equation of motion for a bound electron. This electron shall face a force proportional to the displacement from equilibrium and since we are looking for a realistic model, the electron motion is damped because the electron radiates. In addition, an electromagnetic wave acts on the electron - yet we expect the electron to be non-relativistic ($v \ll c$), so we can focus only on the electric field and neglect the magnetic field. The electric field shall be polarized in x-direction. The result is a linear inhomogeneous differential equation of second order in time

$$m\, \ddot{x}(t) + m\, \Gamma\, \dot{x}(t) + m\, \omega_0^2\, x(t) = -e\, E_{0,\mathrm{local}}\, e^{-i\omega t}, \tag{2.9}$$

where Γ denotes the damping constant and ω_0 the resonance frequency. m and $-e$ denote the electron's mass and charge. Note that, in general, the local field acting on the oscillator can be different from the macroscopic electric field. However, we consider them to be identical since the difference does not affect this simple model of optical properties [18].

As we are interested in the oscillating system, we do not add initial values. Note that the field in Eq. (2.9) is complex - we keep on using complex expressions because it simplifies the analysis. This is possible due to the linearity of Maxwell's equations and the chosen

[1] The optical property we are interested in is how a metallic structure scatters.

constitutive relations. Only the real part of $\mathbf{E}$ corresponds to the physical field. To solve Eq. (2.9), we use a complex and time-harmonic ansatz

$$x(t) = a\, e^{-i\omega t}, \tag{2.10}$$

with $a \in \mathbb{C}$. By entering Eq. (2.10) in Eq. (2.9) we obtain the oscillating solution to the equation of motion

$$x(t) = -\frac{e}{m}\,\frac{1}{\omega_0^2 - \omega^2 - i\omega\Gamma}\, E_0\, e^{-i\omega t}. \tag{2.11}$$

Next, we deduce the permittivity for a system of many bound electrons, i.e., for a medium. Since the dipole moment $\mathbf{p}$ of a single electron at $\mathbf{r}(t)$ is [20]

$$\mathbf{p} = -e\,\mathbf{r}(t), \tag{2.12}$$

we obtain the polarization $\mathbf{P}$ known from Eq. (2.2a) by multiplying with the number of oscillators per unit volume $\mathcal{N}$

$$\mathbf{P} = \frac{e^2}{m}\,\frac{\mathcal{N}}{\omega_0^2 - \omega^2 - i\omega\Gamma}\,\mathbf{E}. \tag{2.13}$$

This is one particular example of a constitutive relation. The isotropic permittivity of this harmonic oscillator system is therefore

$$\varepsilon(\omega) = 1 + \chi(\omega) = 1 + \frac{e^2}{m}\,\frac{\mathcal{N}}{\omega_0^2 - \omega^2 - i\omega\Gamma}, \tag{2.14}$$

which can be split up into real (ε') and imaginary (ε'') parts

$$\varepsilon'(\omega) = 1 + \frac{e^2}{m}\,\frac{\mathcal{N}\,(\omega_0^2 - \omega^2)}{(\omega_0^2 - \omega^2)^2 + \omega^2\Gamma^2}, \tag{2.15a}$$

$$\varepsilon''(\omega) = \frac{e^2}{m}\,\frac{\mathcal{N}\,\omega\Gamma}{(\omega_0^2 - \omega^2)^2 + \omega^2\Gamma^2}. \tag{2.15b}$$

Qualitatively, the permittivity is shown in Fig. 2.1.

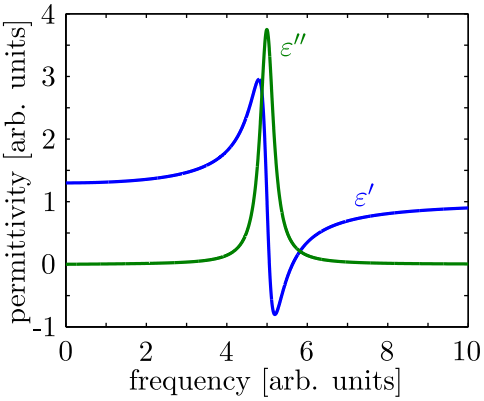

Figure 2.1: Visualization of the Lorentz model's permittivity in Eqs. (2.15) with $\omega_0 = 5$.

As one might expect, both real and imaginary part are connected via a *Kramers-Kronig relation*. Therefore, the following equations hold (see Chapter 2 of Ref. [23]):

$$\varepsilon'(\omega) = 1 + \frac{2}{\pi}\,P\int_0^\infty \frac{\omega'\,\varepsilon''(\omega')}{\omega'^2 - \omega^2}\; d\omega', \tag{2.16}$$

$$\varepsilon''(\omega) = -\frac{2\omega}{\pi}\,P\int_0^\infty \frac{\varepsilon'(\omega') - 1}{\omega'^2 - \omega^2}\; d\omega', \tag{2.17}$$

where $P\int$ denotes the principle value of the integral. Thus, dispersion always leads to absorption since real and imaginary part of the permittivity are connected.

Normal dispersion ($\partial_\omega \varepsilon' > 0$) can be found in all areas except for a narrow interval around the resonance where we find *anomalous dispersion* (see Fig. 2.1). In the area close to the resonance, the imaginary part of the dielectric function has large values and, therefore, we find strong absorption in this frequency range.

2.2.2 Drude model

The essential ingredient of the Drude model is that parts of the electrons are considered to be free in the ion crystal. These electrons are considered a free electron gas. An external field accelerates the charges; however, their mean velocity reaches an equilibrium. This means that the velocity is proportional to the external field strength. The reason why the electrons are not accelerated more and more and that an equilibrium is reached are collisions of the electrons with the crystal's ions.

Mathematically, the equation of motion has the same structure as Eq. (2.9) without a restoring force. The permittivity is found to be

$$\varepsilon_D(\omega) = \varepsilon_\infty - \frac{\omega_p^2}{\omega(\omega + i\gamma_D)}, \tag{2.18}$$

where ω_p is the plasma frequency and γ_D is the damping coefficient. ε_∞ comprises the contribution of the bound electrons [20]. An example for this permittivity is depicted in Fig. 2.2.

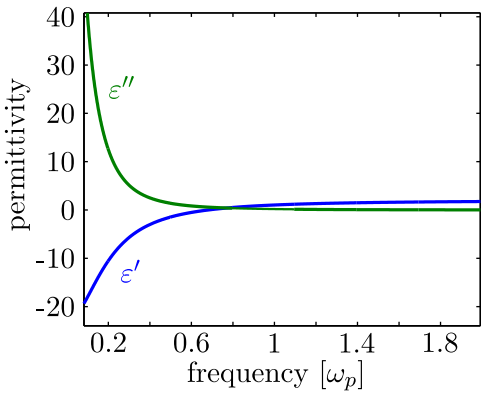

Figure 2.2: Visualization of the real (ε') and imaginary (ε'') part of the Drude model's permittivity in Eq. (2.18). Here, we used $\gamma_D = 0.2\,\omega_p$ and $\varepsilon_\infty = 2$.

For small frequencies, the real part of the permittivity is negative. The imaginary part is large and only little light enters the metal. Thus, metals have a high reflectivity in this frequency range. Above a certain frequency, the real part is positive and the metal becomes transparent. In practice, the free parameters of this model are fit to experimental data [24]. The values we use for the computations in this thesis are found in Ref. [25]. The Drude model yields good results up to the optical regime of light. For small wavelengths in the visible regime of light, however, it has to be extended, e.g., to the Drude-Lorentz model [25].

2.3 Electromagnetic waves

In this section, we first introduce plane waves. Secondly, we visualize the polarization of an electromagnetic wave. Thirdly, we state the Stokes parameters and show how they can be used to visualize a polarization state on the Poincaré sphere. Finally, we discuss polarization-dependent effects.

2.3.1 Plane waves

In this section, we discuss some basics of electromagnetic waves. In particular, we investigate plane waves, which are an elementary solution to Maxwell's equations. More specifically, they solve the wave equation in a linear and homogeneous medium which reads[2]

$$\nabla \times (\nabla \times \mathbf{E}) \overset{(2.3b)}{=} \nabla \times i\omega\mathbf{B} = i\omega\mu \, \nabla \times \mathbf{H} \overset{(2.3d)}{=} \omega^2 \varepsilon\mu \, \mathbf{E}. \tag{2.19}$$

An analogous equation can be formulated for the magnetic field. As stated above, a basic solution is the *plane harmonic wave*. A wave is called plane when it has a spatial dependence in only one direction. The term *harmonic* refers to the time dependence of $e^{-i\omega t}$ with the angular frequency ω. With the *wave vector* $\mathbf{k}$, which may be complex, a plane harmonic wave has the following appearance in a linear and homogeneous medium

$$\mathbf{E} = \mathbf{E}_0 \, e^{-i\omega t + i\mathbf{kr}}, \tag{2.20a}$$

$$\mathbf{H} = \mathbf{H}_0 \, e^{-i\omega t + i\mathbf{kr}}, \tag{2.20b}$$

where $\mathbf{E}_0$ and $\mathbf{H}_0$ are constant. Entering Eqs. (2.20) in Maxwell's equations, we find that $\mathbf{E}_0$ and $\mathbf{H}_0$ are restricted to be transverse, i.e., perpendicular to $\mathbf{k}$. Furthermore, we find the *dispersion relation*

$$\mathbf{k} \cdot \mathbf{k} = \omega^2 \, \varepsilon \, \mu. \tag{2.21}$$

When introducing the refractive index $n(\omega) = \sqrt{\varepsilon(\omega)\mu(\omega)}$, we can write the dispersion relation as

$$\omega = \frac{k}{n}. \tag{2.22}$$

Due to the linearity of Maxwell's equations and of the constitutive relations, we only consider scattering by plane monochromatic waves. Any other incident field can be obtained by superposition [18].

2.3.2 Polarization

A very important property of waves is the *polarization*. The polarization direction of an electromagnetic wave is by definition given by the direction of $\mathbf{E}$. In the following, we use the complex representation of the fields but a real amplitude $\mathbf{E}_0$ because this is easier for visualization. First of all, we point out two special cases and afterwards discuss the most general form of polarization [26].

[2] Here, we use the dimensionless Maxwell equations without the additional scaling factor ω in the $\mathbf{E}$ field in Tab. 2.1.

Linear Polarization. Imagine a plane wave propagating in z-direction. If $\mathbf{E}_0$ in

$$\mathbf{E} = \mathbf{E}_0\, e^{-i\omega t + ikz} \tag{2.23}$$

always points in the same direction perpendicular to $\hat{\mathbf{e}}_z$, i.e., has the form

$$\mathbf{E}_0 = E_{0x}\, \hat{\mathbf{e}}_x + E_{0y}\, \hat{\mathbf{e}}_y, \tag{2.24}$$

we call the wave *linearly polarized*. Both components of the wave

$$E_x = E_{0x}\, e^{-i\omega t + ikz}, \tag{2.25a}$$
$$E_y = E_{0y}\, e^{-i\omega t + ikz}, \tag{2.25b}$$

are in phase. We visualize the real part of the electric field at a fixed time in Fig. 2.3.

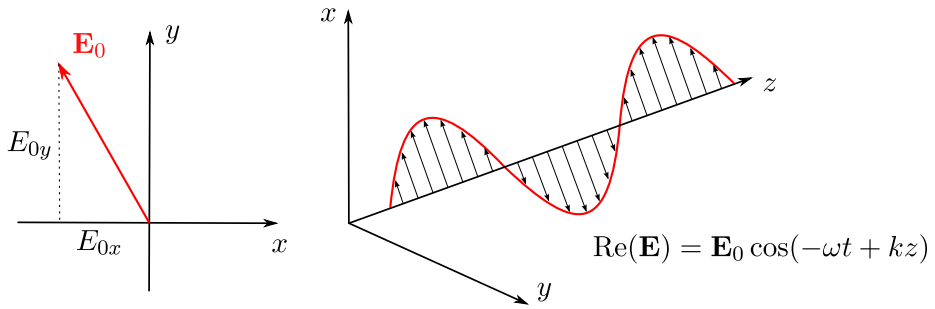

Figure 2.3: A snapshot of the electric field vector of a linearly polarized wave.

Circular Polarization. The next special case is *circularly polarized* light. In this case E_{0x} and E_{0y} are equal (E_0) but the x and y component of the field are dephased by $\pi/2$, i.e.,

$$E_x = E_0\, e^{-i\omega t + ikz}, \tag{2.26a}$$
$$E_y = E_0\, (\pm i)\, e^{-i\omega t + ikz}. \tag{2.26b}$$

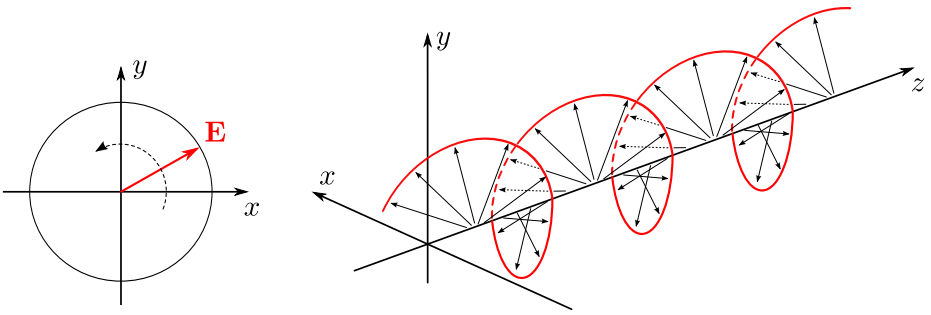

Figure 2.4: A snapshot of the electric field vector of a circularly polarized wave.

The real part of the electric field vector forms a circle in the xy-plane and a circular screw around the z-axis (see Fig. 2.4). If we look alongside the direction of propagation, we see the wave vector screwing clockwise for the case of $+i$ in Eq. (2.26b). This is called σ^+ polarization or *left-handed circular* polarization. Note that we can express a linearly polarized field as a superposition of a right and a left circularly polarized field.

Elliptic Polarization. The most general polarization a wave can exhibit is the *elliptic polarization*. In this case, the electric vector forms an elliptical spiral around the z-axis. This is the case if $E_{0x} \neq E_{0y}$ or the phase difference between the components is not exactly $\pi/2$.

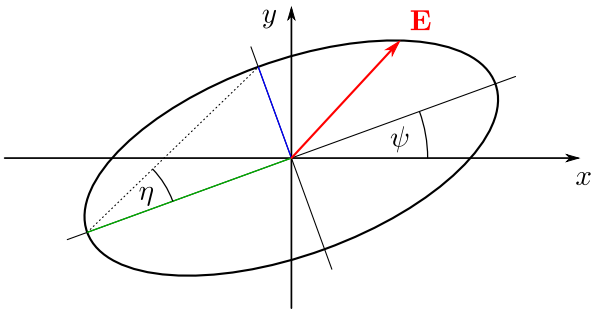

Figure 2.5: Illustration of the azimuthal angle ψ and the ellipticity angle η for elliptic polarization.

The shape of the ellipse in Fig. 2.5 is determined by the two angles ψ and η, the size is dependent on the amplitude of the field. The angle ψ is called *azimuthal angle* and η is called *ellipticity angle*. η is responsible for the sense of rotation. If η is positive, the polarization is right-handed.

2.3.3 Stokes parameters and Poincaré sphere

The Stokes parameters are a tool for easy computation of the polarization state of a given field [20]. Imagine an arbitrary plane wave

$$\mathbf{E}(\mathbf{r},t) = (\hat{\mathbf{e}}_1\, E_1 + \hat{\mathbf{e}}_2\, E_2)\, e^{i\mathbf{kr}-i\omega t}, \tag{2.27}$$

with $\hat{\mathbf{e}}_1$ and $\hat{\mathbf{e}}_2$ being two orthogonal polarization vectors. E_1 and E_2 denote the amplitudes. The Stokes parameters are defined as

$$\begin{aligned} s_0 &= |\hat{\mathbf{e}}_1 \cdot \mathbf{E}|^2 + |\hat{\mathbf{e}}_2 \cdot \mathbf{E}|^2, && \text{(2.28a)}\\ s_1 &= |\hat{\mathbf{e}}_1 \cdot \mathbf{E}|^2 - |\hat{\mathbf{e}}_2 \cdot \mathbf{E}|^2, && \text{(2.28b)}\\ s_2 &= 2\,\mathrm{Re}\left((\hat{\mathbf{e}}_1 \cdot \mathbf{E})^*\,(\hat{\mathbf{e}}_2 \cdot \mathbf{E})\right), && \text{(2.28c)}\\ s_3 &= 2\,\mathrm{Im}\left((\hat{\mathbf{e}}_1 \cdot \mathbf{E})^*\,(\hat{\mathbf{e}}_2 \cdot \mathbf{E})\right), && \text{(2.28d)} \end{aligned}$$

where the asterisk * denotes complex conjugation. The parameter s_0 is proportional to the wave's intensity. We can determine the values of the azimuthal angle and the ellipticity angle by the following representation in spherical coordinates [27]:

$$\begin{aligned} s_1 &= s_0\, \cos 2\eta\, \cos 2\psi, && \text{(2.29a)}\\ s_2 &= s_0\, \cos 2\eta\, \sin 2\psi, && \text{(2.29b)}\\ s_3 &= s_0\, \sin 2\eta, && \text{(2.29c)} \end{aligned}$$

with $-\frac{\pi}{2} \leq \eta < \frac{\pi}{2}$ and $-\frac{\pi}{4} \leq \psi \leq \frac{\pi}{4}$. This can be visualized with the *Poincaré sphere*, see Fig. 2.6.

Every state of polarization of a plane wave of a given intensity (s_0=const.) corresponds to one point on the Poincaré sphere and vice versa. We find linearly polarized waves in the

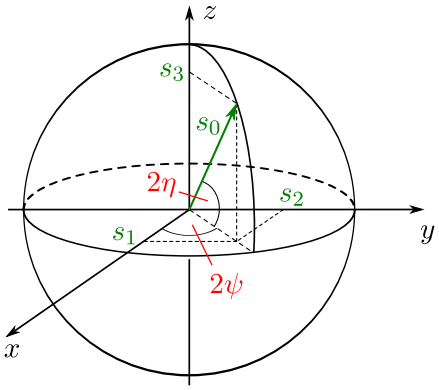

Figure 2.6: Visualization of the Stokes Parameters and of the azimuthal and ellipticity angle on the Poincaré sphere.

equatorial plane where ψ gives the polarization rotation angle towards the x axis. The north-pole of the Poincaré sphere corresponds to right-handed circular polarization. Thus, we only need to know a form similar to Eq. (2.27) to obtain the parameters defining the polarization state.

2.3.4 Polarization-dependent effects

As already pointed out, polarization is a very important concept for electromagnetic waves. There are many effects connected to polarization. We briefly discuss the most important terms. When we talk about linearly polarized waves here, we call the two linearly independent polarization states x and y, which is no restriction, of course.

Linear Birefringence. We call a medium *linear birefringent* when x- and y-polarization are exposed to different refractive indices. This means that the xx- and yy-component of the permittivity tensor in Eq. (2.5a) are not identical.

Circular Birefringence. A material is called *circularly birefringent* when it exhibits two different refractive indices for left- and right-handed circular polarization. In such a material, σ^+ and σ^- travel with different velocities, i.e., they accumulate a phase difference.

This can be an explanation for the so-called *optical activity* when absorption is neglected. A medium is called optically active when the polarization of a linearly polarized wave is rotated while traveling through the medium. A well-known example for a medium showing this effect is crystalline quartz. The effect can be explained in the following way: as stated before, a linearly polarized wave can be decomposed into two circularly polarized waves:

$$\mathbf{E}(0,t) = \begin{pmatrix} E_0 \\ 0 \\ 0 \end{pmatrix} e^{-i\omega t} = \underbrace{\frac{1}{2}\begin{pmatrix} E_0 \\ iE_0 \\ 0 \end{pmatrix} e^{-i\omega t}}_{\sigma^+-\text{polarization}} + \underbrace{\frac{1}{2}\begin{pmatrix} E_0 \\ -iE_0 \\ 0 \end{pmatrix} e^{-i\omega t}}_{\sigma^--\text{polarization}}. \tag{2.30}$$

If the two refractive indices n_r and n_l for the circular polarizations are different then the field

looks the following way after traveling a length of l into the medium:

$$\begin{aligned}\mathbf{E}(l,t) &= \frac{1}{2}E_0\begin{pmatrix}1\\ i\\ 0\end{pmatrix}e^{-i\omega t+ikn_l l}+\frac{1}{2}E_0\begin{pmatrix}1\\ -i\\ 0\end{pmatrix}e^{-i\omega t+ikn_r l}\\ &= \frac{1}{2}E_0\left[\begin{pmatrix}1\\ i\\ 0\end{pmatrix}e^{-ikl(n_r-n_l)/2}+\begin{pmatrix}1\\ -i\\ 0\end{pmatrix}e^{ikl(n_r-n_l)/2}\right]e^{-i\omega t+iknl}\\ &= E_0\begin{pmatrix}\cos\varphi\\ \sin\varphi\\ 0\end{pmatrix}e^{-i\omega t+iknl},\end{aligned} \tag{2.31}$$

with $n = (n_l + n_r)/2$ and $\varphi = kl(n_r - n_l)/2$. Thus, the polarization is rotated due to the different refractive indices.

Linear Dichroism. The term *linear dichroism* stands for a different degree of absorption of x and y polarized light by a medium. This can be used to polarize light: polyvinyl alcohol films appropriately impregnated with iodine transmit up to 80 per cent of light polarized in one plane and less than one per cent of light polarized perpendicularly [27].

Circular Dichroism. In analogy to birefringence, the term *circular dichroism* refers to an absorption behaviour that is different for σ^+ and σ^- light. As we have stated, circular birefringence rotates incident linearly polarized light. If the medium additionally shows circular dichroism, the transmitted light is no longer linearly polarized but rotated and elliptically polarized since the amplitudes of the left- and right-handed parts are no longer equal due to the different absorption.

2.4 Continuity conditions

In this section, we examine certain restrictions at an interface between two materials which follow directly from Maxwell's equations. The discussion follows Ref. [20]. First, let us assume two adjacent media 1 and 2. At the surface, there may be a surface charge density σ and a surface current density $\mathbf{K}$. This is depicted in Fig. 2.7.

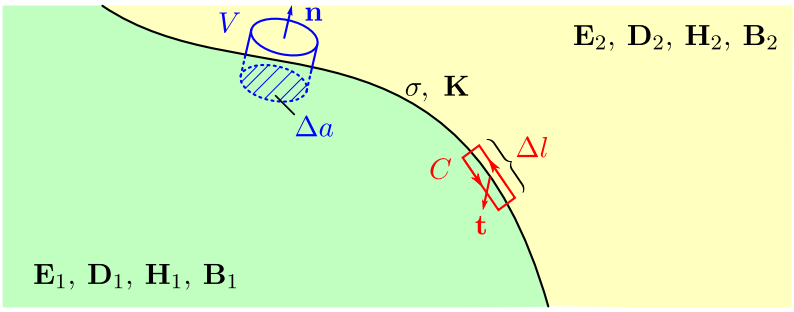

Figure 2.7: Sketch of two materials with a common interface. Along this interface, we allow a surface charge density σ and a surface current density $\mathbf{K}$.

The sketch in Fig. 2.7 also contains a volume V which is a cylinder with face area Δa and infinitesimal height. In each medium, there is one face of the cylinder. Analogously, we define a rectangle with infinitesimal height and length Δl which is arranged so that its surface normal $\mathbf{t}$ is a tangential vector of the interface. We start by investigating the cylinder volume. For that, we use Eq. (2.1a) and integrate it over the volume V, see Eq. (2.32), step (a):

$$(\mathbf{D}_2 - \mathbf{D}_1) \cdot \mathbf{n}\ \Delta a \overset{\text{(d)}}{=} \oint_{\partial V} \mathbf{D} \cdot\ d\mathbf{A} \overset{\text{(c)}}{=} \int_V \nabla \cdot \mathbf{D}\ d^3r \overset{\text{(a)}}{=} \int_V \rho\ d^3r \overset{\text{(b)}}{=} \sigma\ \Delta a. \quad (2.32)$$

In step (b) we used the assumption that the free charge density ρ forms a surface charge density σ which is homogeneous in the small face area Δa. In step (c), we applied Gauss' law which transforms the volume integral over the divergence into a surface integral. This surface integral is evaluated in step (d), where we only find contributions of the cylinder's faces since the height is negligibly small. Here, $\mathbf{n}$ denotes the surface normal of the cylinder's face which corresponds to the normal of the interface. If the surface charge density vanishes, we find

$$(\mathbf{D}_2 - \mathbf{D}_1) \cdot \mathbf{n} = 0, \quad (2.33a)$$
$$(\mathbf{B}_2 - \mathbf{B}_1) \cdot \mathbf{n} = 0, \quad (2.33b)$$

where we already entered that we can use the same argumentation for the magnetic induction $\mathbf{B}$ using Eq. (2.1c). Therefore, the normal components of $\mathbf{D}$ and $\mathbf{B}$ have to be continuous along an uncharged interface.

Similarly, we investigate the rectangular area C in Fig. 2.7. Here, we use the surface integral over Eq. (2.1d) and obtain step (a) of

$$(\mathbf{t} \times \mathbf{n}) \cdot (\mathbf{H}_2 - \mathbf{H}_1)\ \Delta l \overset{\text{(d)}}{=} \oint_{\partial C} \mathbf{H} \cdot d\mathbf{s} \overset{\text{(c)}}{=} \int_C (\nabla \times \mathbf{H}) \cdot d\mathbf{A} \overset{\text{(a)}}{=} \int_C \left(\mathbf{j} + \frac{\partial \mathbf{D}}{\partial t}\right) \cdot d\mathbf{A} \overset{\text{(b)}}{=} \mathbf{K} \cdot \mathbf{t}\ \Delta l \quad (2.34)$$

In step (b), we used that the temporal derivative of $\mathbf{D}$ has only a finite value and the height of the rectangle C was assumed to be infinitesimal. Also, analogously to the surface charge density in Eq. (2.32), we obtain the surface current density $\mathbf{K}$ on the right hand side of step (b). In step (c), we use Stokes' theorem, which converts the surface integral over the rectangle C into a line integral along the boundary of C. Again, only the terms for the height vanish and we obtain the relation in step (d). The result for the electric field is deduced analogously. In the absence of a surface current density, we obtain

$$\mathbf{n} \times (\mathbf{H}_2 - \mathbf{H}_1) = 0, \quad (2.35a)$$
$$\mathbf{n} \times (\mathbf{E}_2 - \mathbf{E}_1) = 0. \quad (2.35b)$$

Thus, the parallel components of $\mathbf{H}$ and $\mathbf{E}$ are continuous along the interface.

2.5 Energy transport

Naturally, electromagnetic fields carry energy. The energy density u in a field is given by [20]

$$u = \frac{1}{2}\ (\mathbf{E} \cdot \mathbf{D} + \mathbf{B} \cdot \mathbf{H}), \quad (2.36)$$

where the fields are the physical (real) parts of the complex fields. By defining the *Poynting vector* $\mathbf{S} = \mathbf{E} \times \mathbf{H}$, we can formulate a continuity equation, which is also known as Poynting's theorem:

$$\frac{\partial u}{\partial t} + \nabla \cdot \mathbf{S} = -\mathbf{j} \cdot \mathbf{E}. \tag{2.37}$$

It can be derived from Maxwell's equations [27]. Without electric currents, the energy density can only change by an energy flux density which one identifies as the Poynting vector $\mathbf{S}$. If there are currents in the system, the energy density may also change due to the work the fields do on charged particles.

The Poynting vector can be used to deduce the electromagnetic energy that crosses the boundary of a closed surface ∂V which encloses the volume V [18]. Then,

$$W = \int_{\partial V} \mathbf{S} \cdot d\mathbf{A} \tag{2.38}$$

is the net rate of the energy flux, i.e., the amount of energy that flows through the surface per unit time.

Since we consider time-harmonic fields throughout this thesis, we use the quantity

$$\langle \mathbf{S} \rangle = \frac{1}{2} \mathrm{Re} \left(\mathbf{E} \times \mathbf{H}^* \right), \tag{2.39}$$

which is the *time-averaged Poynting vector*, consisting of the complex-valued fields used in the actual calculation.

2.6 Curvilinear coordinates

In the next chapter, we introduce the Fourier Modal Method in curvilinear coordinates. Here, we discuss the fundamentals that are needed, in particular co- and contravariance. In general, these terms describe how quantities change under coordinate transformations. In principle, these transformations can be of arbitrary dimension, e.g., four-dimensional in special relativity [20]. In this thesis, we only transform in space, i.e., in three dimensions.

In this introduction to curvilinear coordinates, we first examine how the basis vectors change since this can easily be illustrated. Secondly, we transform the components of the vectors. Thirdly, we introduce the metric tensor which relates the co- and contravariant components.

Assume a Cartesian coordinate system $O\bar{x}^1\bar{x}^2\bar{x}^3$. The basis vectors of this system are denoted by $\bar{\mathbf{d}}_i$, $i = 1, 2, 3$. Any point in space is then given in the form

$$\mathbf{r} \;=\; \bar{x}^1\bar{\mathbf{d}}_1 + \bar{x}^2\bar{\mathbf{d}}_2 + \bar{x}^3\bar{\mathbf{d}}_3 \;\overset{(*)}{=}\; \bar{x}^i\bar{\mathbf{d}}_i, \tag{2.40}$$

where the Einstein sum convention was applied in $(*)$, meaning that repeated indices are implicitly summed over. Next, we want to switch to a three-dimensional curvilinear coordinate system which is called $Ox^1x^2x^3$ in the following. Every point has a unique representation in both coordinate systems. They are linked by the mappings

$$\bar{x}^1 \;=\; \bar{x}^1\left(x^1, x^2, x^3\right), \tag{2.41a}$$

$$\bar{x}^2 \;=\; \bar{x}^2\left(x^1, x^2, x^3\right), \tag{2.41b}$$

$$\bar{x}^3 \;=\; \bar{x}^3\left(x^1, x^2, x^3\right). \tag{2.41c}$$

Since we want to be able to switch back and forth between Cartesian and curvilinear space, we demand that the mappings are invertible. In essence, the task we deal with in the subsequent two chapters is how to obtain the transformations in Eq. (2.41). Although we restrict ourselves to certain special cases of Eq. (2.41) later, we continue here with this most general form.

As stated above, we want to derive two sets of basis vectors: the covariant basis vectors $\mathbf{d}_i$ and the contravariant basis vectors $\mathbf{d}^i$, $i = 1, 2, 3$. They are depicted in two dimensions in Fig. 2.8.

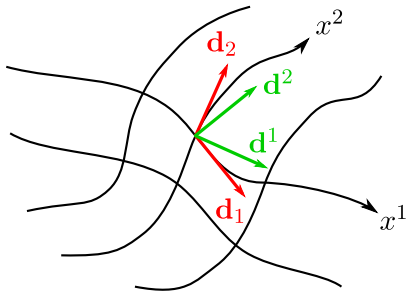

Figure 2.8: Sketch of the covariant (red, $\mathbf{d}_i$) and contravariant (green, $\mathbf{d}^i$) basis vectors of the curvilinear coordinate lines in Cartesian space.

As sketched, the covariant basis vectors are defined such that they are tangential to the curvilinear coordinate lines in Cartesian space. In contrast, the contravariant basis vectors are perpendicular to the coordinate lines. The two bases are dual. The direction of the tangents to the coordinate lines is obtained via [28]

$$\mathbf{d}_i = \frac{\partial \bar{x}^k}{\partial x^i} \bar{\mathbf{d}}_k, \tag{2.42}$$

which is the covariant transformation. The contravariant (dual) basis vectors can then be constructed from the covariant basis vectors in Eq. (2.42) by

$$\mathbf{d}^i = \frac{1}{2} \frac{\xi^{ijk}}{\det(J)} \mathbf{d}_j \times \mathbf{d}_k. \tag{2.43}$$

Here, ξ^{ijk} denotes the Levi-Civita symbol which is 1 for $(ijk) = (123)$ and even permutations thereof, -1 for odd permutations and 0 otherwise. The symbol ξ is used instead of the usual ε to avoid confusion with the permittivity tensor. J denotes the Jacobian of the transformation in Eq. (2.41). With the abbreviation $\partial_i = \partial/\partial x^i$ it reads

$$J = \begin{pmatrix} \partial_1 \bar{x}^1 & \partial_2 \bar{x}^1 & \partial_3 \bar{x}^1 \\ \partial_1 \bar{x}^2 & \partial_2 \bar{x}^2 & \partial_3 \bar{x}^2 \\ \partial_1 \bar{x}^3 & \partial_2 \bar{x}^3 & \partial_3 \bar{x}^3 \end{pmatrix}. \tag{2.44}$$

Naturally, the contravariant basis vectors can also be deduced directly from the transformation and the Cartesian basis $\bar{\mathbf{d}}_i = \bar{\mathbf{d}}^i$. They are given by

$$\mathbf{d}^i = \frac{\partial x^i}{\partial \bar{x}^k} \bar{\mathbf{d}}^k, \tag{2.45}$$

which is the contravariant transformation. After discussing the transformation of the basis vectors, we next deal with the components. The components of any vector $\mathbf{s}$ with Cartesian components $\bar{s}_i = \bar{s}^i$ transform like

$$s_i = \frac{\partial \bar{x}^k}{\partial x^i} \bar{s}_k, \qquad s^i = \frac{\partial x^i}{\partial \bar{x}^k} \bar{s}^k. \tag{2.46}$$

Thus, the vector can be written in both bases, i.e.,

$$\mathbf{s} \;=\; s^i \mathbf{d}_i \;=\; s_i \mathbf{d}^i. \tag{2.47}$$

The link between the covariant and contravariant basis is the metric tensor g^{ij}. It relates the co- and contravariant components by

$$s^i = g^{ij} s_j. \tag{2.48}$$

Practically, this metric can be calculated from the coordinate transformation in Eqs. (2.41) by

$$g_{ij} \;=\; \frac{\partial \bar{x}^k}{\partial x^i} \frac{\partial \bar{x}^l}{\partial x^j} \bar{g}_{kl}, \tag{2.49a}$$

$$g^{ij} \;=\; \frac{\partial x^i}{\partial \bar{x}^k} \frac{\partial x^j}{\partial \bar{x}^l} \bar{g}^{kl}. \tag{2.49b}$$

Here, $\bar{g}_{kl} = \bar{g}^{kl}$ refers to the Cartesian metric which is the three-dimensional unit matrix. For further use we define the determinant of the metric which can be written in terms of the Jacobian determinant and reads

$$g \;=\; \det(g_{ij}) \;=\; \det(J)^2. \tag{2.50}$$

With these preparations at hand, we can formulate Maxwell's equations in an arbitrary coordinate system. They are stated and discussed in Chapter 3.

2.7 Fundamentals of periodic systems

Since we deal with periodic systems and, in particular, photonic crystals throughout this thesis, some properties of such systems are discussed in this section. The physical quantity that is periodic in our considered systems is the permittivity. Periodicity means that we can move by some lattice vector

$$\mathbf{R} = l_1 a_1 \mathbf{d}_1 + l_2 a_2 \mathbf{d}_2 + l_3 a_3 \mathbf{d}_3, \qquad l_i \in \mathbb{Z}, \qquad i = 1, 2, 3, \tag{2.51}$$

in space and still find the same permittivity, i.e.,

$$\varepsilon(\mathbf{r}) = \varepsilon(\mathbf{r} + \mathbf{R}). \tag{2.52}$$

The basis vectors $\mathbf{d}_i$ in Eq. (2.51) were introduced in the preceding section. The quantities a_i are the lattice constants in each direction i.

In this section, we first define the reciprocal lattice. Second, we state Bloch's theorem which has an important impact on the choice of our basis functions in the FMM. Finally, we discuss diffraction.

2.7.1 Reciprocal lattice

The reciprocal lattice is defined by the reciprocal lattice vectors

$$\mathbf{G} = m_1 \frac{2\pi}{a_1} \mathbf{d}^1 + m_2 \frac{2\pi}{a_2} \mathbf{d}^2 + m_3 \frac{2\pi}{a_3} \mathbf{d}^3, \qquad m_i \in \mathbb{Z}, \qquad i = 1, 2, 3, \tag{2.53}$$

where we used the contravariant basis vectors $\mathbf{d}^i$. An example is depicted in Fig. 2.9.

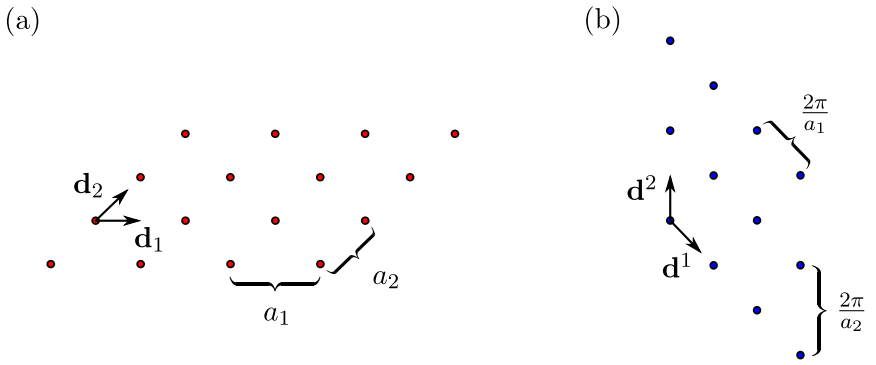

Figure 2.9: The real space lattice in panel (a) is defined by the covariant basis vectors. The reciprocal lattice, as shown in panel (b), is spanned by the contravariant basis vectors $\mathbf{d}^i$.

The real space and the reciprocal space are connected by a Fourier transformation. Thus, we can expand the permittivity in a sum over reciprocal lattice points, i.e.,

$$\varepsilon(x^1, x^2, x^3) = \sum_{m=\{m_1,m_2,m_3\}} \varepsilon_m \; e^{im_1 \frac{2\pi}{a_1} x^1 + im_2 \frac{2\pi}{a_2} x^2 + im_3 \frac{2\pi}{a_3} x^3}, \tag{2.54}$$

where we introduced the multi-index $m = \{m_1, m_2, m_3\}$. The coefficients of this expansion can be deduced by

$$\varepsilon_m = \frac{1}{a_1 a_2 a_3} \int_0^{a_1} \int_0^{a_2} \int_0^{a_3} \varepsilon(x^1, x^2, x^3) e^{-im_1 \frac{2\pi}{a_1} x^1 - im_2 \frac{2\pi}{a_2} x^2 - im_3 \frac{2\pi}{a_3} x^3} dx^1 \; dx^2 \; dx^3. \tag{2.55}$$

2.7.2 Bloch's theorem

Bloch's theorem was originally a solution to the Schrödinger equation for electrons in periodic potentials [29]. In mathematics, it is also known as *Floquet theorem*, a theorem for partial differential equations with periodic coefficients. It states that the energy eigenfunctions of the periodic system have to have the form

$$\Psi_{\mathbf{k}}(\mathbf{r}) = u_{\mathbf{k}}(\mathbf{r}) e^{i\mathbf{k}\cdot\mathbf{r}}, \tag{2.56}$$

where the function $u_{\mathbf{k}}(\mathbf{r})$ obeys the same periodicity as the underlying crystal, i.e., $u_{\mathbf{k}}(\mathbf{r}) = u_{\mathbf{k}}(\mathbf{r} + \mathbf{R})$. However, this wave description in periodic media also applies to other fields such as electromagnetic waves in photonic crystals [30]. A reformulation of Eq. (2.56) gives

$$\Psi_{\mathbf{k}}(\mathbf{r} + \mathbf{R}) = u_{\mathbf{k}}(\mathbf{r} + \mathbf{R}) e^{i\mathbf{k}\cdot\mathbf{r}} e^{i\mathbf{k}\cdot\mathbf{R}} = \Psi_{\mathbf{k}}(\mathbf{r}) \; e^{i\mathbf{k}\cdot\mathbf{R}} \tag{2.57}$$

which states that the fields at two points, which are a lattice vector $\mathbf{R}$ apart, only differ by a phase factor $e^{i\mathbf{k}\cdot\mathbf{R}}$. When Maxwell's equations are solved numerically, it is important to choose basis functions which obey Bloch's theorem. We keep this in mind when we discuss the Fourier Modal Method in Chapter 3.

Furthermore, it is sufficient to consider waves with $\mathbf{k}$ vectors in the first Brillouin zone, since

$$\Psi_{\mathbf{k}+\mathbf{G}}(\mathbf{r}) = \Psi_{\mathbf{k}}(\mathbf{r}) \tag{2.58}$$

holds true for any reciprocal lattice vector $\mathbf{G}$ because $e^{i\mathbf{G}\cdot\mathbf{R}}$ is unity for all vectors $\mathbf{G}$ and $\mathbf{R}$. Therefore, all possible $\mathbf{k}$ values can be constructed from the first Brillouin zone.

2.7.3 Diffraction

The behavior of plane waves for systems as depicted in Fig. 2.10 is of particular importance in this thesis. The system consists of an input layer, a structured layer with in-plane periodicity and an output layer. If the periodicity in the structured layer is one-dimensional, i.e., invariant in one in-plane direction, we call the layer a *lamellar grating*. If it is two-dimensional, it is called a *crossed grating*.

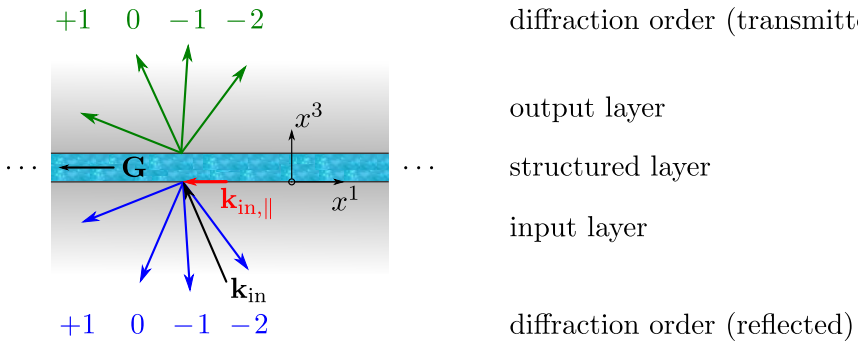

Figure 2.10: We distinguish between the input, structured and output layer. The parallel components of the plane waves has to be conserved across each interface. In the transmitted and reflected fields we find several plane waves. Their wave vector's parallel components are the sum of $\mathbf{k}_{\mathrm{in},\parallel}$ and a reciprocal lattice vector $\mathbf{G}$. The transmitted and reflected orders all feature the same frequency as the incident plane wave.

Without a structured layer, a plane wave propagating from the input into the output layer obeys Snell's law [27]. The component of the wave vector that is parallel to the interface in the input layer has to be the same in the output layer. Together with the dispersion relation of the two media, this yields a certain angular relation for the wave vectors of the incident and the transmitted plane wave. In particular, the transmitted light consists only of one plane wave. The same applies to the reflected light.

A fundamentally different behavior is found for the system containing the structured layer, where we find several transmitted (and reflected) plane waves. In order to understand why, we start out with an incident plane wave with wave vector

$$\mathbf{k}_{\mathrm{in}} = \alpha_0\, \mathbf{d}^1 + \beta_0\, \mathbf{d}^2 + \gamma_0\, \mathbf{d}^3. \tag{2.59}$$

As in the case of Snell's law, the parallel component of the wave vector has to be conserved across the interface from input to structured layer. However, we have shown in Eq. (2.58) that a reciprocal lattice vector added to the plane wave does not yield a different frequency of the Bloch wave in the structured layer. At the second interface, from structured to output region, the parallel components of the waves' $\mathbf{k}$ vectors have to be conserved again. Thus, we find transmitted plane waves with $\mathbf{k}$ vectors having the parallel components

$$\mathbf{k}_{\parallel} = \mathbf{k}_{\mathrm{in},\parallel} + \mathbf{G}, \qquad \mathbf{G} = m_1 \frac{2\pi}{a_1}\, \mathbf{d}^1 + m_2 \frac{2\pi}{a_2}\, \mathbf{d}^2, \qquad m_i \in \mathbb{Z}, \qquad i = 1, 2, \tag{2.60}$$

where $m = \{m_1, m_2\}$ is a multi-index like in Section 2.7.1 which defines the *diffraction order*. The same argument applies to the reflected fields. The total reflected and transmitted field

are then given by the so-called *Rayleigh expansion* [31]:

$$\mathbf{E}_{\text{trans}} = \sum_m \mathbf{E}_{\text{trans},m}\, e^{i\alpha_{m_1}x^1 + i\beta_{m_2}x^2 + i\gamma_m x^3}, \tag{2.61a}$$

$$\mathbf{E}_{\text{refl}} = \sum_m \mathbf{E}_{\text{refl},m}\, e^{i\alpha_{m_1}x^1 + i\beta_{m_2}x^2 - i\gamma_m x^3}. \tag{2.61b}$$

The sign of the x^3-coordinate is already chosen in such a way that $\gamma_m > 0$ describes upwards propagating, transmitted waves in Eq. (2.61a) and downward propagating, reflected waves in Eq. (2.61b). The total field in the input layer is the sum of the incident plane wave and the reflected fields. The components of transmitted plane waves' $\mathbf{k}$ vectors have to obey both Eq. (2.60) and the dispersion relations in the media. Thus, the components read

$$\alpha_{m_1} = \alpha_0 + m_1\frac{2\pi}{a_1}, \tag{2.62}$$

$$\beta_{m_2} = \beta_0 + m_2\frac{2\pi}{a_2}, \tag{2.63}$$

where the γ_m-component is derived by

$$\mathbf{k}\cdot\mathbf{k} = n^2\omega^2. \tag{2.64}$$

Here, we also use that the frequency ω of the diffracted wave does not change. In Eq. (2.64), n is the refractive index of either the input or the output region.

Although we can find many solutions of Eq. (2.64), only a finite number of them yield a propagation constant γ_m that is real. The other solutions are imaginary and are called *evanescent*. They decay exponentially and, thus, only contribute to the near-field. Furthermore, they do not transport energy.

How many different real solutions of Eq. (2.64) exist strongly depends on the system's parameters—the refractive indices of the input and output region, the frequency and angle of the incident plane waves, and the lattice constants a_i. For wavelengths that are larger than $n \cdot a_i$, only one transmitted and reflected wave exists (*zeroth order*). When the wavelength is increased, there appear new solutions of Eq. (2.64) at certain wavelengths. Then, an additional diffraction order appears. This results in a redistribution of energy between the orders which is observable as features in the transmittance and reflectance spectra. They are known as *Rayleigh* or *Wood anomalies* [32].

Chapter 3

The Fourier Modal Method

In this chapter, we introduce the Fourier Modal Method for anisotropic materials in curvilinear coordinates [12, 33, 34]. For that, we first state Maxwell's equations in arbitrary coordinate systems in Section 3.1 and discuss how the transformation from Cartesian to curvilinear coordinates changes the form of the permittivity and permeability. Secondly, we introduce the considered systems and the slicing of the system into layers. Also, we discuss the basic idea that the electromagnetic fields are expressed in terms of the structure's eigenmodes. In Section 3.3, we reformulate Maxwell's equation into an eigenvalue problem which yields the eigenmodes in each slice. The slices are then connected to ensure the continuity conditions for the electromagnetic fields by a scattering matrix algorithm which is the content of Section 3.4. The chapter is concluded with some practical remarks in Section 3.5.

3.1 Maxwell's equations in curvilinear coordinates

3.1.1 Motivation

The Fourier Modal Method solves Maxwell's equations by transforming them to Fourier space and solving the resulting eigenvalue problem which yields the eigenmodes of the system. The Fourier transformation is performed on a Cartesian grid. Naturally, this Cartesian grid does not always fit to the investigated structures. Particular problems occur when the structures are not grid-aligned, i.e., when their surface is not parallel to the coordinate lines of the grid. Then, the Fourier transformation effectively perceives a stair-cased structure, see Fig. 3.1.

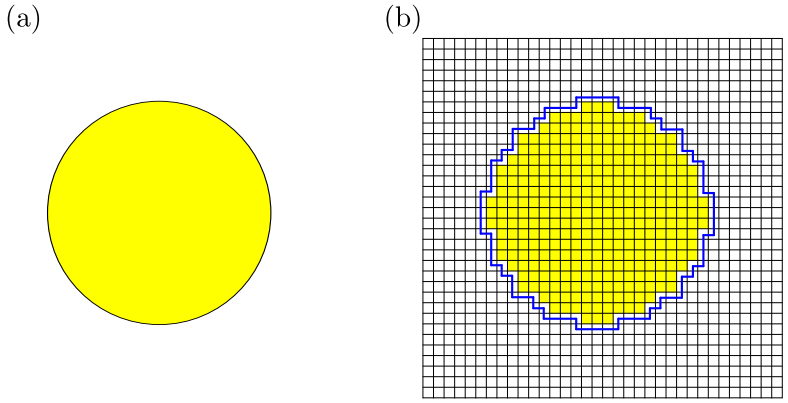

Figure 3.1: Due to the discretization on a Cartesian grid, the FMM perceives the stair-cased structure in panel (b) instead of the round structure in panel (a).

This problem is not exclusively found in the FMM since several other numerical methods rely on a structured or even Cartesian grid. To tackle this problem, Ward and Pendry had an important insight [35]: a coordinate transformation can be used in such a way that Maxwell's equations keep their form and the shapes of the structures of interest change beneficially. The change in the structure is accounted for purely by changing the permittivity and permeability. This procedure is of great help since "we need only write one computer code in a Cartesian system" [35]. In the following years, their work was developed further [36, 37].

Only few years after the publication of Ref. [35], coordinate transformations were used in the context of the Fourier Modal Method. Granet used them to increase the spatial resolution near material boundaries [17] to tackle another specific problem of the FMM besides the stair-casing, namely the Gibbs phenomenon which is described in App. A. Several other publications followed—they are discussed in Chapter 5. There, we deal which the question how suitable coordinate transformations can be obtained. However, before we deal with the concrete transformations, we introduce the covariant Maxwell equations which allow the use of an arbitrary coordinate system. We then present the Fourier Modal Method for this set of equations.

3.1.2 Reformulation of Maxwell's equations

In Section 2.6, we discussed how we can transform the coordinate system from Cartesian to curvilinear by means of Eqs. (2.41). Here, we examine how this change transfers to Maxwell's equations. When changing from a Cartesian grid with coordinates $\bar{x}^i$ to a curvilinear grid with coordinates x^i, the curl equations read [35, 36, 12]

$$\xi^{ijk}\partial_j E_k = i\omega\,\mu_0\,\sqrt{g}\frac{\partial x^i}{\partial \bar{x}^k}\frac{\partial x^j}{\partial \bar{x}^l}\bar{\mu}^{kl}\;H_j, \tag{3.1a}$$

$$\xi^{ijk}\partial_j H_k = -i\omega\,\varepsilon_0\,\sqrt{g}\frac{\partial x^i}{\partial \bar{x}^k}\frac{\partial x^j}{\partial \bar{x}^l}\bar{\varepsilon}^{kl}\;E_j. \tag{3.1b}$$

ξ^{ijk} is the Levi-Cevita symbol. Also, we assume linear constitutive relations like before. The term g is the metric determinant as introduced in Eq. (2.50). $\bar{\varepsilon}^{kl}$ and $\bar{\mu}^{kl}$ are the permittivity and permeability in the Cartesian space, respectively. The covariant Maxwell equations, which are valid in any coordinate system, can be obtained by defining

$$\varepsilon^{ij} = \sqrt{g}\frac{\partial x^i}{\partial \bar{x}^k}\frac{\partial x^j}{\partial \bar{x}^l}\;\bar{\varepsilon}^{kl}, \tag{3.2a}$$

$$\mu^{ij} = \sqrt{g}\frac{\partial x^i}{\partial \bar{x}^k}\frac{\partial x^j}{\partial \bar{x}^l}\;\bar{\mu}^{kl}, \tag{3.2b}$$

which we call the *effective permittivity*[1] and *effective permeability*. Having defined these quantities, we rewrite Maxwell's equations in the covariant, dimensionless form we use later in the FMM.[2] They read

$$\xi^{\rho\sigma\tau}\frac{\partial_\sigma}{i}E_\tau = \omega^2\mu^{\rho\sigma}H_\sigma, \tag{3.3a}$$

$$\xi^{\rho\sigma\tau}\frac{\partial_\sigma}{i}H_\tau = -\varepsilon^{\rho\sigma}E_\sigma. \tag{3.3b}$$

[1] In the remainder of this thesis, we also use the synonymous term "transformed permittivity".
[2] See Tab. 2.1 for the definition of the dimensionless and renormalized quantities.

It is important to realize that the coordinate transformation from Cartesian to curvilinear grid solely enters the effective permittivity and permeability. This is the overall result of the discussed publication of Ward and Pendry [35]. Two things should be mentioned regarding the effective permittivity[3]: Firstly, the structure's shape changes in general, i.e., the effective permittivity looks different compared to the permittivity in the Cartesian space. This is a desired effect since we use this to obtain a grid-aligned structure surface. Secondly, the effective permittivity features drastically different material properties than the permittivity in the Cartesian space. Upon inspecting Eq. (3.2a), we find that an isotropic permittivity in the untransformed space is transformed into an anisotropic effective permittivity.

The formulation of the effective permittivity, which absorbs all details of the coordinate transformation, is also of great help for introducing coordinate transformations into classical FMM codes. The reason is that any FMM code that is able to handle anisotropic material tensors can easily be changed such that it supports coordinate transformations: the only modification that has to be done (once the coordinate transformation is known) is the derivation of the effective permittivity. This is of particular interest since open source FMM codes are published (see Refs. [38, 39]) that do not yet include coordinate transformations.

3.2 Considered systems and field expansion

Using the Fourier Modal Method, we analyze systems which are periodic in the one or two directions and finite in the third direction. The plane featuring the periodicity defines the x^1- and x^2-direction. The x^3-direction is perpendicular to this plane. An example of such a system is depicted in Fig. 3.2(a), together with the $\mathbf{k}$-vector of the plane wave that we assume to be incident on the structure. We distinguish between three different regions: The input half space, the structured region containing the periodic structures, possible sub- and superstrates, and the output half space. The regions are sketched in Fig. 3.2(b).

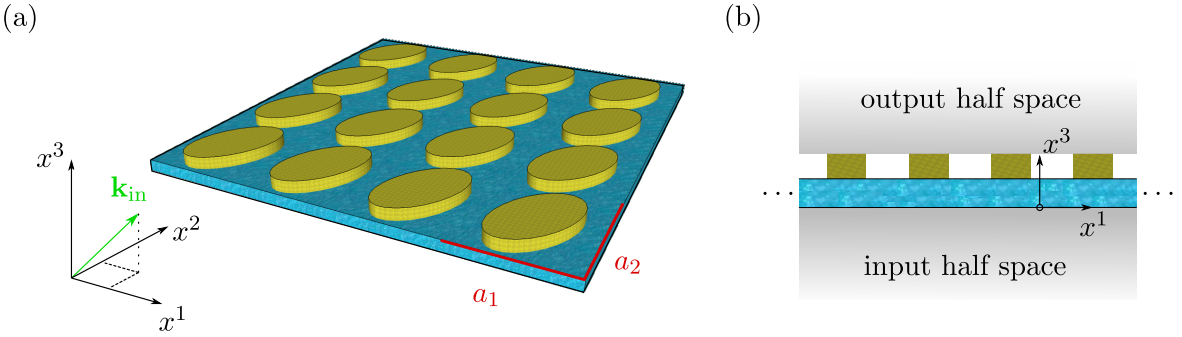

Figure 3.2: The Fourier Modal Method is suited for structures featuring a periodicity in one or two directions. Panel (a) displays such a periodic arrangement. This plane of periodicity defines the x^1- and x^2-direction. The x^3 axis is perpendicular to this plane. Panel (b) shows that we categorize the system into three regions: the input half space, the structured region with an arbitrary number of structured layers, possibly sub- and superstrate layers, and an output half space. The light incident on the structure is a plane wave with wavevector $\mathbf{k}_{\text{in}}$.

[3] Whenever we transform the permittivity in the Cartesian space to the effective permittivity, we always proceed analogously with the permeability. To increase the readability, we do not always explicitly mention the permeability.

In practice, we often deal with structures that are not piecewise homogeneous in x^3 direction. These structures are decomposed into several slices each of which is homogeneous in x^3 direction. How many slices are needed to obtain convergence has to be tested for each new structure. A sketch of the slicing procedure is depicted in Fig. 3.3.

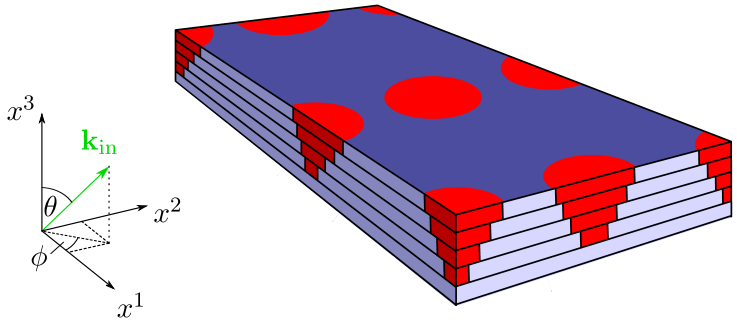

Figure 3.3: A structure that is not piecewise homogeneous in x^3-direction, e.g., a layer of spheres, has to be approximated by slicing it such that each slice is homogeneous is x^3-direction.

The incident plane wave with wave vector $\mathbf{k}_{\text{in}} = (\alpha_0, \beta_0, \gamma_0)$ is given by [40]

$$E_\sigma\left(x^1, x^2, x^3\right) = E_{0,\sigma}\, e^{i\alpha_0 x^1 + i\beta_0 x^2 + i\gamma_0 x^3}, \tag{3.4a}$$

$$H_\sigma\left(x^1, x^2, x^3\right) = H_{0,\sigma}\, e^{i\alpha_0 x^1 + i\beta_0 x^2 + i\gamma_0 x^3}, \tag{3.4b}$$

where $\sigma = 1, 2, 3$. Using the angles θ and ϕ as defined in Fig. 3.3, we find the components of the wave vector to be

$$\alpha_0 = k_{\text{in}} \sin\theta \cos\phi, \qquad \beta_0 = k_{\text{in}} \sin\theta \sin\phi, \qquad \gamma_0 = k_{\text{in}} \cos\phi, \tag{3.5}$$

where k_{in} is related to the wave vector in vacuum k_0 by $k_{\text{in}} = \sqrt{\varepsilon_{\text{in}}} k_0$. $\sqrt{\varepsilon_{\text{in}}}$ is the permittivity of the input half space and μ_{in} is assumed to be unity. Choosing a plane wave as incident light is not a restriction since we can obtain other incident fields as superpositions of plane waves. Also, the polarization of the wave can be arbitrary. For simplicity, we always calculate two distinct polarizations: s-polarization (also referred to as TE) and p-polarization (TM). s-polarization denotes the case where the electric field is perpendicular to the scattering plane defined by the x^3 axis and $\mathbf{k}_{\text{in}}$. In contrast, p polarization means that the electric field is parallel to this plane. For both cases, the coefficients in Eqs. (3.4) read

$$\text{s pol.}: \qquad \mathbf{E}_0 = \begin{pmatrix} E_0 \sin\phi \\ -E_0 \cos\phi \\ 0 \end{pmatrix}, \quad \mathbf{H}_0 = \begin{pmatrix} E_0 \sqrt{\varepsilon_{\text{in}}} \cos\theta \cos\phi \\ E_0 \sqrt{\varepsilon_{\text{in}}} \cos\theta \sin\phi \\ -E_0 \sqrt{\varepsilon_{\text{in}}} \sin\theta \end{pmatrix} \tag{3.6}$$

and

$$\text{p pol.}: \qquad \mathbf{E}_0 = \begin{pmatrix} E_0 \cos\theta \cos\phi \\ E_0 \cos\theta \sin\phi \\ -E_0 \sin\theta \end{pmatrix}, \quad \mathbf{H}_0 = \begin{pmatrix} -E_0 \sqrt{\varepsilon_{\text{in}}} \sin\phi \\ E_0 \sqrt{\varepsilon_{\text{in}}} \cos\phi \\ 0 \end{pmatrix}. \tag{3.7}$$

In the Fourier Modal Method, Maxwell's equations are solved in each of the slices depicted in Fig. 3.3 separately. Thereafter, the slices are combined by the scattering matrix algorithm we discuss in Section 3.4. The next step is to describe how we solve Maxwell's equations in

the slices. The basic idea is that we express the electric and magnetic field as a superposition of the slice's eigenmodes. For that, we realize that the fields in the structured slices have to obey Bloch's theorem (see Section 2.7.2) due to the periodicity. Since this is the case, it is a sensible approach to choose basis functions for the eigenmode expansion of the electric and magnetic field that obey this periodicity and Bloch's theorem automatically. Thus, we expand the fields in plane waves obeying Bloch's theorem, i.e., we make the ansatz of a Fourier expansion. The electric field then reads

$$E_\sigma\left(x^1, x^2, x^3\right) = \sum_{m=\{m_1,m_2\}} \tilde{E}_{\sigma m}\left(x^3\right)\ e^{i\alpha_{m_1}x^1 + i\beta_{m_2}x^2}, \qquad \sigma = 1,2,3. \tag{3.8}$$

Here, α_{m_1} and β_{m_2} are given by

$$\alpha_{m_1} = \alpha_0 + m_1\frac{2\pi}{a_1}, \qquad \beta_{m_2} = \beta_0 + m_2\frac{2\pi}{a_2}, \qquad m_1, m_2 = 0,\ \pm1,\ \pm2,\ \ldots \tag{3.9}$$

The magnetic field is expanded analogously. In practice, the summation over m_1 and m_2 has to be truncated. This raises the question which area in reciprocal space should be covered. The two most general choices are a rectangular and a circular truncation. Both possibilities are displayed in Fig. 3.4 and are used in the computations presented in this thesis.

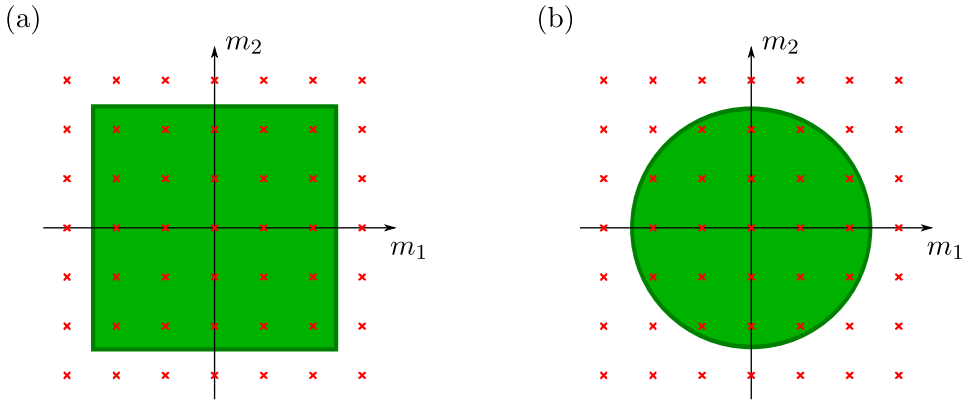

Figure 3.4: Different truncation schemes in reciprocal space for the field expansion in Eq. (3.8). Panels (a) and (b) display a rectangular and a circular truncation, respectively.

Since we demanded that each slice is homogeneous in x^3-direction, we can further specify the form of the field in Eq. (3.8). Due to the homogeneity, we can assume that the dependence in x^3-direction is a plane wave $e^{i\gamma x^3}$. Thus, an eigenmode E'_σ of the electric field has the general form

$$E'_\sigma\left(x^1, x^2, x^3\right) = \sum_{m=\{m_1,m_2\}} \tilde{E}_{\sigma m}\ e^{i\gamma x^3}\ e^{i\alpha_{m_1}x^1 + i\beta_{m_2}x^2}, \qquad \sigma = 1,2,3. \tag{3.10}$$

The total field is then given by a superposition of these eigenmodes. After having defined the form of the electromagnetic fields, we can proceed to the reformulation of Maxwell's equations into the eigenvalue problem of the Fourier Modal Method.

3.3 Derivation of the eigenvalue problem

We want to solve the set of equations (3.3). In these equations, derivatives of the fields occur. As an example, we have a look at the derivative of an $\mathbf{E}$ field component E_σ with respect to x^1. For clarity, we use only the five Fourier coefficients closest to the origin. With the fields in Eq. (3.10), the derivative becomes

$$\begin{aligned}\frac{\partial_1}{i}E_\sigma &= \sum_{m=\{m_1,m_2\}} \tilde{E}_{\sigma m}\; e^{i\gamma x^3}\; \alpha_{m_1}\; e^{i\alpha_{m_1}x^1+i\beta_{m_2}x^2} \\ &= \underbrace{\begin{pmatrix} \alpha_{-1} & 0 & 0 & 0 & 0 \\ 0 & \alpha_0 & 0 & 0 & 0 \\ 0 & 0 & \alpha_0 & 0 & 0 \\ 0 & 0 & 0 & \alpha_0 & 0 \\ 0 & 0 & 0 & 0 & \alpha_1 \end{pmatrix}}_{=:\,\underline{\alpha}} \cdot \underbrace{\begin{pmatrix} \tilde{E}_{\sigma,\{-1,0\}} \\ \tilde{E}_{\sigma,\{0,-1\}} \\ \tilde{E}_{\sigma,\{0,0\}} \\ \tilde{E}_{\sigma,\{0,1\}} \\ \tilde{E}_{\sigma,\{1,0\}} \end{pmatrix}}_{=:\,\tilde{\mathbf{E}}_\sigma} \cdot \begin{pmatrix} e^{i\alpha_{-1}x^1+i\beta_0x^2} \\ e^{i\alpha_0x^1+i\beta_{-1}x^2} \\ e^{i\alpha_0x^1+i\beta_0x^2} \\ e^{i\alpha_0x^1+i\beta_1x^2} \\ e^{i\alpha_1x^1+i\beta_0x^2} \end{pmatrix} e^{i\gamma x^3}. \end{aligned} \tag{3.11}$$

Here, we first have a matrix-vector multiplication, followed by a scalar product. The vector $\tilde{\mathbf{E}}_\sigma$ contains the Fourier coefficients of the electric field's σ-component. Analogously, the matrix $\underline{\beta}$ for the derivative with respect to x^2 is defined. For that, it is important to retain the order of the Fourier coefficients. Thus, we find

$$\begin{aligned}\frac{\partial_2}{i}E_\sigma &= \sum_{m=\{m_1,m_2\}} \tilde{E}_{\sigma m}\; e^{i\gamma x^3}\; \beta_{m_1}\; e^{i\alpha_{m_1}x^1+i\beta_{m_2}x^2} \\ &= \underbrace{\begin{pmatrix} \beta_{0} & 0 & 0 & 0 & 0 \\ 0 & \beta_{-1} & 0 & 0 & 0 \\ 0 & 0 & \beta_0 & 0 & 0 \\ 0 & 0 & 0 & \beta_1 & 0 \\ 0 & 0 & 0 & 0 & \beta_0 \end{pmatrix}}_{=:\,\underline{\beta}} \cdot \underbrace{\begin{pmatrix} \tilde{E}_{\sigma,\{-1,0\}} \\ \tilde{E}_{\sigma,\{0,-1\}} \\ \tilde{E}_{\sigma,\{0,0\}} \\ \tilde{E}_{\sigma,\{0,1\}} \\ \tilde{E}_{\sigma,\{1,0\}} \end{pmatrix}}_{=\,\tilde{\mathbf{E}}_\sigma} \cdot \begin{pmatrix} e^{i\alpha_{-1}x^1+i\beta_0x^2} \\ e^{i\alpha_0x^1+i\beta_{-1}x^2} \\ e^{i\alpha_0x^1+i\beta_0x^2} \\ e^{i\alpha_0x^1+i\beta_1x^2} \\ e^{i\alpha_1x^1+i\beta_0x^2} \end{pmatrix} e^{i\gamma x^3}. \end{aligned} \tag{3.12}$$

Thereby, we know how to handle the derivatives in Eqs. (3.3)—they become matrix multiplications of $\underline{\alpha}$ and $\underline{\beta}$ with the fields' coefficient vectors. In order to solve Maxwell's equations in Fourier space, the next step is Fourier transforming the right hand sides of Eqs. (3.3). This is a complicated endeavor since particular care has to be taken due to the jumps in the permittivity and the fields. The derivation of the Fourier transformed constitutive relations can be found in App. A.

After dealing with the derivatives and the Fourier transformation of the constitutive relations, we can present the covariant Maxwell equations in Fourier space. They read

$$\underline{\beta}\tilde{\mathbf{E}}_3 - \gamma\tilde{\mathbf{E}}_2 = \omega^2\left(\left[\!\left[\mu^{11}\right]\!\right]\tilde{\mathbf{H}}_1 + \left[\!\left[\mu^{12}\right]\!\right]\tilde{\mathbf{H}}_2 + \left[\!\left[\mu^{13}\right]\!\right]\tilde{\mathbf{H}}_3\right), \tag{3.13a}$$

$$\gamma\tilde{\mathbf{E}}_1 - \underline{\alpha}\tilde{\mathbf{E}}_3 = \omega^2\left(\left[\!\left[\mu^{21}\right]\!\right]\tilde{\mathbf{H}}_1 + \left[\!\left[\mu^{22}\right]\!\right]\tilde{\mathbf{H}}_2 + \left[\!\left[\mu^{23}\right]\!\right]\tilde{\mathbf{H}}_3\right), \tag{3.13b}$$

$$\underline{\alpha}\tilde{\mathbf{E}}_2 - \underline{\beta}\tilde{\mathbf{E}}_1 = \omega^2\left(\left[\!\left[\mu^{31}\right]\!\right]\tilde{\mathbf{H}}_1 + \left[\!\left[\mu^{32}\right]\!\right]\tilde{\mathbf{H}}_2 + \left[\!\left[\mu^{33}\right]\!\right]\tilde{\mathbf{H}}_3\right), \tag{3.13c}$$

$$\underline{\beta}\tilde{\mathbf{H}}_3 - \gamma\tilde{\mathbf{H}}_2 = -\left(\left[\!\left[\varepsilon^{11}\right]\!\right]\tilde{\mathbf{E}}_1 + \left[\!\left[\varepsilon^{12}\right]\!\right]\tilde{\mathbf{E}}_2 + \left[\!\left[\varepsilon^{13}\right]\!\right]\tilde{\mathbf{E}}_3\right), \tag{3.13d}$$

$$\gamma\tilde{\mathbf{H}}_1 - \underline{\alpha}\tilde{\mathbf{H}}_3 = -\left(\left[\!\left[\varepsilon^{21}\right]\!\right]\tilde{\mathbf{E}}_1 + \left[\!\left[\varepsilon^{22}\right]\!\right]\tilde{\mathbf{E}}_2 + \left[\!\left[\varepsilon^{23}\right]\!\right]\tilde{\mathbf{E}}_3\right), \tag{3.13e}$$

$$\underline{\alpha}\tilde{\mathbf{H}}_2 - \underline{\beta}\tilde{\mathbf{H}}_1 = -\left(\left[\!\left[\varepsilon^{31}\right]\!\right]\tilde{\mathbf{E}}_1 + \left[\!\left[\varepsilon^{32}\right]\!\right]\tilde{\mathbf{E}}_2 + \left[\!\left[\varepsilon^{33}\right]\!\right]\tilde{\mathbf{E}}_3\right). \tag{3.13f}$$

The matrices $[\![\varepsilon^{ij}]\!]$ and $[\![\mu^{ij}]\!]$ are defined in App. A. They contain Fourier coefficients of the effective permittivity and permeability in a complex arrangement. When examining Eqs. (3.13) one finds that we replaced the six Maxwell equations with $6\,N$ equations, with N being the number of Fourier coefficients. The reason is that we omitted the vector from Eq. (3.11) that contains the plane wave basis functions. This is due to the fact that the basis functions are linearly independent and, thus, we can directly equate the coefficients. Consequently, the entire system of equations (3.13) only contains the coefficients.

To reformulate these equations into an eigenvalue problem, we first solve for the coefficients of the electric and magnetic field's x^3 component. Eqs. (3.13c) and (3.13f) yield

$$\tilde{\mathbf{H}}_3 = \left[\!\left[\mu^{33}\right]\!\right]^{-1}\left(\frac{1}{\omega^2}\underline{\alpha}\tilde{\mathbf{E}}_2 - \frac{1}{\omega^2}\underline{\beta}\tilde{\mathbf{E}}_1 - \left[\!\left[\mu^{31}\right]\!\right]\tilde{\mathbf{H}}_1 - \left[\!\left[\mu^{32}\right]\!\right]\tilde{\mathbf{H}}_2\right), \tag{3.14a}$$

$$\tilde{\mathbf{E}}_3 = \left[\!\left[\varepsilon^{33}\right]\!\right]^{-1}\left(-\underline{\alpha}\tilde{\mathbf{H}}_2 + \underline{\beta}\tilde{\mathbf{H}}_1 - \left[\!\left[\varepsilon^{31}\right]\!\right]\tilde{\mathbf{E}}_1 - \left[\!\left[\varepsilon^{32}\right]\!\right]\tilde{\mathbf{E}}_2\right). \tag{3.14b}$$

Next, we enter

$$\text{Eqs. (3.14}a\text{) and (3.14}b\text{) in } \begin{matrix}\text{Eq. (3.13}a\text{)}\\ \text{Eq. (3.13}b\text{)}\\ \text{Eq. (3.13}e\text{)}\\ \text{Eq. (3.13}d\text{)}\end{matrix} \text{ and solve for } \begin{matrix}\gamma\left(-\tilde{\mathbf{E}}_2\right)\\ \gamma\tilde{\mathbf{E}}_1\\ \gamma\tilde{\mathbf{H}}_1\\ \gamma\tilde{\mathbf{H}}_2\end{matrix}.$$

The electric and magnetic field are ordered like this due to historic reasons—this is the way the eigenvalue problem is implemented in our code. Finally, the equations assume the form of an eigenvalue problem to which we refer to as the *large eigenproblem* in the following. It reads

$$\gamma\begin{pmatrix}-\tilde{\mathbf{E}}_2\\ \tilde{\mathbf{E}}_1\\ \tilde{\mathbf{H}}_1\\ \tilde{\mathbf{H}}_2\end{pmatrix} = \begin{pmatrix}\mathbf{A_{11}} & \mathcal{F}\\ \mathcal{G} & \mathbf{A_{22}}\end{pmatrix}\begin{pmatrix}-\tilde{\mathbf{E}}_2\\ \tilde{\mathbf{E}}_1\\ \tilde{\mathbf{H}}_1\\ \tilde{\mathbf{H}}_2\end{pmatrix} \tag{3.15}$$

with the matrices

$$\mathbf{A_{11}} := \begin{pmatrix}-\left[\!\left[\breve{\mu}^{13}\right]\!\right]\underline{\alpha} - \underline{\beta}\left[\!\left[\breve{\varepsilon}^{32}\right]\!\right] & \underline{\beta}\left[\!\left[\breve{\varepsilon}^{31}\right]\!\right] - \left[\!\left[\breve{\mu}^{13}\right]\!\right]\underline{\beta}\\ \underline{\alpha}\left[\!\left[\breve{\varepsilon}^{32}\right]\!\right] - \left[\!\left[\breve{\mu}^{23}\right]\!\right]\underline{\alpha} & -\underline{\alpha}\left[\!\left[\breve{\varepsilon}^{31}\right]\!\right] - \left[\!\left[\breve{\mu}^{23}\right]\!\right]\underline{\beta}\end{pmatrix}, \tag{3.16}$$

$$\mathcal{F} := \begin{pmatrix}\omega^2\left[\!\left[\breve{\mu}^{11}\right]\!\right] - \underline{\beta}\left[\!\left[\breve{\varepsilon}^{23}\right]\!\right]\underline{\beta} & \omega^2\left[\!\left[\breve{\mu}^{12}\right]\!\right] + \underline{\beta}\left[\!\left[\breve{\varepsilon}^{33}\right]\!\right]\underline{\alpha}\\ \underline{\alpha}\left[\!\left[\breve{\varepsilon}^{33}\right]\!\right]\underline{\beta} + \omega^2\left[\!\left[\breve{\mu}^{21}\right]\!\right] & -\underline{\alpha}\left[\!\left[\breve{\varepsilon}^{33}\right]\!\right]\underline{\alpha} + \omega^2\left[\!\left[\breve{\mu}^{22}\right]\!\right]\end{pmatrix}, \tag{3.17}$$

$$\mathcal{G} := \begin{pmatrix}-\frac{1}{\omega^2}\underline{\alpha}\left[\!\left[\breve{\mu}^{33}\right]\!\right]\underline{\alpha} + \left[\!\left[\breve{\varepsilon}^{22}\right]\!\right] & -\frac{1}{\omega^2}\underline{\alpha}\left[\!\left[\breve{\mu}^{33}\right]\!\right]\underline{\beta} - \left[\!\left[\breve{\varepsilon}^{21}\right]\!\right]\\ -\frac{1}{\omega^2}\underline{\beta}\left[\!\left[\breve{\mu}^{33}\right]\!\right]\underline{\alpha} - \left[\!\left[\breve{\varepsilon}^{12}\right]\!\right] & -\frac{1}{\omega^2}\underline{\beta}\left[\!\left[\breve{\mu}^{33}\right]\!\right]\underline{\beta} + \left[\!\left[\breve{\varepsilon}^{11}\right]\!\right]\end{pmatrix}, \tag{3.18}$$

$$\mathbf{A_{22}} := \begin{pmatrix}-\underline{\alpha}\left[\!\left[\breve{\mu}^{31}\right]\!\right] - \left[\!\left[\breve{\varepsilon}^{23}\right]\!\right]\underline{\beta} & -\underline{\alpha}\left[\!\left[\breve{\mu}^{32}\right]\!\right] + \left[\!\left[\breve{\varepsilon}^{23}\right]\!\right]\underline{\alpha}\\ -\underline{\beta}\left[\!\left[\breve{\mu}^{31}\right]\!\right] + \left[\!\left[\breve{\varepsilon}^{13}\right]\!\right]\underline{\beta} & -\underline{\beta}\left[\!\left[\breve{\mu}^{32}\right]\!\right] - \left[\!\left[\breve{\varepsilon}^{13}\right]\!\right]\underline{\alpha}\end{pmatrix}. \tag{3.19}$$

In these definitions we introduced the matrices $[\![\breve{\varepsilon}^{ij}]\!]$ and $[\![\breve{\mu}^{ij}]\!]$ which read

$$[\![\breve{\varepsilon}^{11}]\!] = [\![\varepsilon^{11}]\!] - [\![\varepsilon^{13}]\!] [\![\varepsilon^{33}]\!]^{-1} [\![\varepsilon^{31}]\!], \tag{3.20a}$$
$$[\![\breve{\varepsilon}^{12}]\!] = [\![\varepsilon^{12}]\!] - [\![\varepsilon^{13}]\!] [\![\varepsilon^{33}]\!]^{-1} [\![\varepsilon^{32}]\!], \tag{3.20b}$$
$$[\![\breve{\varepsilon}^{13}]\!] = [\![\varepsilon^{13}]\!] [\![\varepsilon^{33}]\!]^{-1}, \tag{3.20c}$$
$$[\![\breve{\varepsilon}^{21}]\!] = [\![\varepsilon^{21}]\!] - [\![\varepsilon^{23}]\!] [\![\varepsilon^{33}]\!]^{-1} [\![\varepsilon^{31}]\!], \tag{3.20d}$$
$$[\![\breve{\varepsilon}^{22}]\!] = [\![\varepsilon^{22}]\!] - [\![\varepsilon^{23}]\!] [\![\varepsilon^{33}]\!]^{-1} [\![\varepsilon^{32}]\!], \tag{3.20e}$$
$$[\![\breve{\varepsilon}^{23}]\!] = [\![\varepsilon^{23}]\!] [\![\varepsilon^{33}]\!]^{-1}, \tag{3.20f}$$
$$[\![\breve{\varepsilon}^{31}]\!] = [\![\varepsilon^{33}]\!]^{-1} [\![\varepsilon^{31}]\!], \tag{3.20g}$$
$$[\![\breve{\varepsilon}^{32}]\!] = [\![\varepsilon^{33}]\!]^{-1} [\![\varepsilon^{32}]\!], \tag{3.20h}$$
$$[\![\breve{\varepsilon}^{33}]\!] = [\![\varepsilon^{33}]\!]^{-1}. \tag{3.20i}$$

For the definition of $[\![\breve{\mu}^{ij}]\!]$, ε is exchanged with μ. A short notation for these matrices can be obtained with the operator l_3^- defined in Eq. (A.20). With this operator, we can write Eqs. (3.20) as $[\![\breve{\varepsilon}^{ij}]\!] = l_3^- [\![\varepsilon^{ij}]\!]$.

A case that occurs often is an effective permittivity with only in-plane anisotropy, i.e.,

$$\varepsilon = \begin{pmatrix} \varepsilon^{11} & \varepsilon^{12} & 0 \\ \varepsilon^{21} & \varepsilon^{22} & 0 \\ 0 & 0 & \varepsilon^{33} \end{pmatrix}, \qquad \mu = \begin{pmatrix} \mu^{11} & \mu^{12} & 0 \\ \mu^{21} & \mu^{22} & 0 \\ 0 & 0 & \mu^{33} \end{pmatrix}. \tag{3.21}$$

We find such an effective permittivity for example when we apply a two-dimensional coordinate transformation in the x^1x^2-plane to an isotropic permittivity in the Cartesian space. When the effective permittivity and permeability assume this form, the matrices $\mathbf{A_{11}}$ and $\mathbf{A_{22}}$ are zero and the eigenproblem decomposes into the two equations

$$\gamma \begin{pmatrix} -\tilde{\mathbf{E}}_2 \\ \tilde{\mathbf{E}}_1 \end{pmatrix} = \mathcal{F} \begin{pmatrix} \tilde{\mathbf{H}}_1 \\ \tilde{\mathbf{H}}_2 \end{pmatrix}, \qquad \gamma \begin{pmatrix} \tilde{\mathbf{H}}_1 \\ \tilde{\mathbf{H}}_2 \end{pmatrix} = \mathcal{G} \begin{pmatrix} -\tilde{\mathbf{E}}_2 \\ \tilde{\mathbf{E}}_1 \end{pmatrix}, \tag{3.22}$$

which we can insert into each other to gain the *small eigenproblem*, which reads

$$\gamma^2 \begin{pmatrix} -\tilde{\mathbf{E}}_2 \\ \tilde{\mathbf{E}}_1 \end{pmatrix} = \mathcal{F}\mathcal{G} \begin{pmatrix} -\tilde{\mathbf{E}}_2 \\ \tilde{\mathbf{E}}_1 \end{pmatrix}. \tag{3.23}$$

Alternatively, we could solve an equivalent equation for the magnetic field. When the effective permittivity has a form as in Eq. (3.21) or when it is even simpler, we use the small rather than the large eigenproblem. The reason is simple: it is only half the size and, thus, the time and memory needed for the solution reduce drastically. In our numerical framework, the eigenproblems are solved using the LAPACK library [41] or the MKL library [42] on Intel machines. Once the numerical eigenmodes, i.e., the propagation constants γ_j and the field's Fourier coefficients, are obtained, we can expand the electric and magnetic field in each slice into the slice's eigenmodes. For the small eigenproblem this is rather easy: for every eigenmode with eigenvalue γ_j we find the corresponding eigenmode with propagation constant -γ_j. We always choose the complex square root of $\sqrt{\gamma^2}$ such that $\mathrm{Im}\,(\gamma_j) > 0$.

In principle, the large eigenvalue problem should also yield the same modes propagating in positive and in negative x^3 direction. However, this is numerically not always the case and, thus, requires a distinction of the eigenmodes into two different sets of forward and backward propagating eigenmodes. For further details we refer to [33].

Finally, the fields expanded in eigenmodes read

$$E_\sigma\left(x^1, x^2, x^3\right) = \sum_{m,j} \underbrace{\tilde{E}_{\sigma m,j} \cdot \left(u_j \; e^{i\gamma_j x^3} + d_j e^{-i\gamma_j x^3}\right)}_{=:\, \tilde{E}_{\sigma m,j}(x^3)} \cdot e^{i\alpha_{m_1} x^1 + i\beta_{m_2} x^2}, \tag{3.24a}$$

$$H_\sigma\left(x^1, x^2, x^3\right) = \sum_{m,j} \underbrace{\tilde{H}_{\sigma m,j} \cdot \left(u_j \; e^{i\gamma_j x^3} - d_j e^{-i\gamma_j x^3}\right)}_{=:\, \tilde{H}_{\sigma m,j}(x^3)} \cdot e^{i\alpha_{m_1} x^1 + i\beta_{m_2} x^2}, \tag{3.24b}$$

for $\sigma = 1, 2$. The field components in x^3-direction can be derived using Eqs. (3.14). In Eqs. (3.24), the scalar u_j is the amplitude of the j^{th} upward propagating mode and, correspondingly, d_j denotes the j^{th} downward propagating mode's amplitude.[4] These quantities are unknown so far—they depend on the light that is incident on the structure. Their values are determined with the help of the scattering matrix algorithm, which we present in the subsequent section.

3.4 Scattering matrix algorithm

So far, we sliced the system into several layers, including the incoming and output half space. We obtained the field solutions in each layer in an eigenmode basis by solving the eigenproblem of the system. The quantities that still have to be determined are the amplitudes that describe how strongly each eigenmode is excited in each slice. The amplitude of the j^{th} upward propagating mode (positive x^3 direction) was denoted by u_j. Next, we combine these amplitudes to a vector $\mathbf{u}^l = (\; \ldots \;, u_j^l, \; \ldots \;)$ where we added the superscript l to mark that these are the amplitudes in the l^{th} layer.

The link between two layers is their common interface. Here, the continuity conditions for Maxwell's equations have to be fulfilled. By demanding that the parallel fields are continuous, we obtain relations for the amplitudes. The general procedure is relating the amplitudes of waves that are incident onto the interface with outgoing waves. Therefore, we define the scattering matrix that connects the amplitudes of the eigenmodes in layers l and $l+1$ (see Fig. 3.5) like

$$\begin{pmatrix} \mathbf{u}^{l+1} \\ \mathbf{d}^{l} \end{pmatrix} = \underline{\mathbf{S}}(l, l+1) \cdot \begin{pmatrix} \mathbf{u}^{l} \\ \mathbf{d}^{l+1} \end{pmatrix}. \tag{3.25}$$

The whole derivation follows Refs. [13, 40]. Note that the amplitudes both on the left and on the right hand side of Eq. (3.25) are defined in different layers. An alternative formulation for scattering problems is the T matrix. In this approach, the amplitudes on the bottom side of the interface are linked with the amplitudes on the top side. However, this can lead to numerical instabilities where evanescent modes show exponential growth. The S matrix in the formulation we present here avoids these issues.

[4] The terms *upward* and *downward propagating* refer to the positive and negative x^3-direction, respectively.

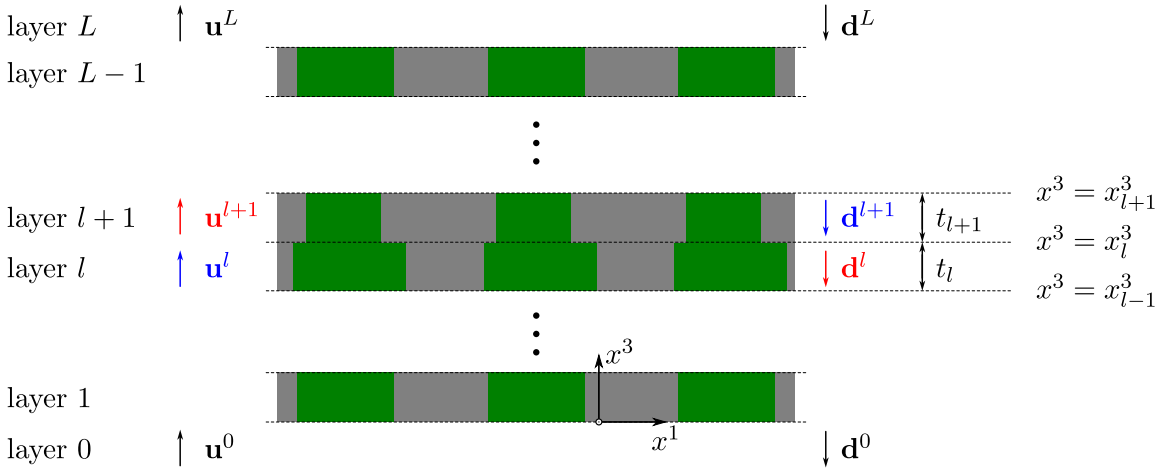

Figure 3.5: Sketch of the sliced system and of the amplitude vectors. The S matrix links the amplitudes of the waves that are incident on the layers' interface with the amplitudes of the outgoing fields. The l^{th} layer has the thickness t_l.

As a first step, we rewrite parts of the fields in Eqs. (3.24) in a convenient form[5] in each layer l:

$$\begin{pmatrix} \tilde{\mathbf{E}}_1(\hat{x}^3) \\ \tilde{\mathbf{E}}_2(\hat{x}^3) \\ \tilde{\mathbf{H}}_1(\hat{x}^3) \\ \tilde{\mathbf{H}}_2(\hat{x}^3) \end{pmatrix}_l = \underbrace{\begin{pmatrix} \tilde{\mathbf{E}}_{1,j} & \tilde{\mathbf{E}}_{1,j} \\ \tilde{\mathbf{E}}_{2,j} & \tilde{\mathbf{E}}_{2,j} \\ \tilde{\mathbf{H}}_{1,j} & -\tilde{\mathbf{H}}_{1,j} \\ \tilde{\mathbf{H}}_{2,j} & -\tilde{\mathbf{H}}_{2,j} \end{pmatrix}_l}_{=:\,\underline{\mathbf{M}}_l} \cdot \begin{pmatrix} \underline{\mathbf{\Phi}}_l(\hat{x}^3) & 0 \\ 0 & \underline{\mathbf{\Phi}}_l(t_l - \hat{x}^3) \end{pmatrix} \cdot \begin{pmatrix} \mathbf{u}^l \\ \mathbf{d}^l \end{pmatrix}, \qquad \hat{x}^3 \in [0, t_l]. \quad (3.26)$$

Here, we introduced the propagation matrix $\underline{\mathbf{\Phi}}_l(\hat{x}^3)$ which is diagonal and contains the elements $e^{i\gamma_j^l \hat{x}^3}$. The variable $\hat{x}^3$ is defined such that it is zero at the lower boundary of the slice, i.e., at $x^3 = x^3_{l-1}$, and t_l at the upper boundary, i.e., at $x^3 = x^3_l$. In this sense, $\hat{x}^3$ is the x^3 coordinate in the local coordinate system of the slice. The matrix $\underline{\mathbf{M}}_l$ contains the Fourier coefficients of all eigenmodes in slice l. The coefficient vectors of the eigenmodes j are arranged column by column in $\underline{\mathbf{M}}_l$. With these preparations at hand, we can demand the continuity for the electric and magnetic field's in-plane components. Thus, we demand that

$$E^l_\sigma(x^3_l - 0) \stackrel{!}{=} E^{l+1}_\sigma(x^3_l + 0), \qquad H^l_\sigma(x^3_l - 0) \stackrel{!}{=} H^{l+1}_\sigma(x^3_l + 0), \qquad \sigma = 1, 2. \quad (3.27)$$

It is important to note that these conditions directly translate to the coefficients since we use the same plane wave basis in every layer. Therefore, we can utilize the definitions in Eq. (3.26) and reformulate the continuity conditions like

$$\underline{\mathbf{M}}_l \cdot \begin{pmatrix} \underline{\mathbf{\Phi}}_l(t_l)\ \mathbf{u}_l \\ \underline{\mathbf{\Phi}}_l(0)\ \mathbf{d}_l \end{pmatrix} = \underline{\mathbf{M}}_{l+1} \cdot \begin{pmatrix} \underline{\mathbf{\Phi}}_{l+1}(0)\ \mathbf{u}_{l+1} \\ \underline{\mathbf{\Phi}}_{l+1}(t_{l+1})\ \mathbf{d}_{l+1} \end{pmatrix}. \quad (3.28)$$

Here, all phases are defined such that the modes are evaluated at the correct position, i.e., at the interface between layers l and $l+1$. Next, we invert $\underline{\mathbf{M}}_l$ in Eq. (3.28) and obtain

$$\begin{pmatrix} \underline{\mathbf{\Phi}}_l(t_l)\ \mathbf{u}_l \\ \mathbf{d}_l \end{pmatrix} = \underbrace{\underline{\mathbf{M}}_l^{-1}\ \underline{\mathbf{M}}_{l+1}}_{=:\,\underline{\mathbf{I}}(l,l+1)} \cdot \begin{pmatrix} \mathbf{u}_{l+1} \\ \underline{\mathbf{\Phi}}_{l+1}(t_{l+1})\ \mathbf{d}_{l+1} \end{pmatrix}, \quad (3.29)$$

[5] This particular form refers to the small eigenvalue problem. The equivalent form for the large eigenproblem differs only little and can be found in Ref. [33].

where we introduced the interface matrix $\underline{\mathbf{I}}(l, l+1)$. So far, we related the amplitudes of different layers with each other. The next step is deriving the form of the scattering matrix. In particular, we assume an existing S matrix $\underline{\mathbf{S}}(l, m)$ and want to derive how the next slice is added, i.e., how $\underline{\mathbf{S}}(l, m+1)$ can be obtained. The $\underline{\mathbf{S}}(l, m)$ matrix relates the amplitudes like[6]

$$\begin{pmatrix} \mathbf{u}_m \\ \mathbf{d}_l \end{pmatrix} = \underline{\mathbf{S}}(l, m) \cdot \begin{pmatrix} \mathbf{u}_l \\ \mathbf{d}_m \end{pmatrix} =: \begin{pmatrix} \underline{\mathbf{S}}_{11} & \underline{\mathbf{S}}_{12} \\ \underline{\mathbf{S}}_{21} & \underline{\mathbf{S}}_{22} \end{pmatrix} \begin{pmatrix} \mathbf{u}_l \\ \mathbf{d}_m \end{pmatrix}. \tag{3.30}$$

The interface matrix between the layers l and $l+1$ is obtained like in Eq. (3.29).

$$\begin{pmatrix} \underline{\mathbf{\Phi}}'_m \mathbf{u}_m \\ \mathbf{d}_m \end{pmatrix} = \underline{\mathbf{I}}(m, m+1) \cdot \begin{pmatrix} \mathbf{u}_{m+1} \\ \underline{\mathbf{\Phi}}'_{m+1} \mathbf{d}_{m+1} \end{pmatrix} = \begin{pmatrix} \underline{\mathbf{I}}_{11} & \underline{\mathbf{I}}_{12} \\ \underline{\mathbf{I}}_{21} & \underline{\mathbf{I}}_{22} \end{pmatrix} \begin{pmatrix} \mathbf{u}_{m+1} \\ \underline{\mathbf{\Phi}}'_{m+1} \mathbf{d}_{m+1} \end{pmatrix}, \tag{3.31}$$

where we defined $\underline{\mathbf{\Phi}}'_m := \underline{\mathbf{\Phi}}_m(t_m)$. With the known matrices $\underline{\mathbf{S}}(l, m)$ and $\underline{\mathbf{I}}(m, m+1)$ we find the system of equations:

$$\begin{aligned}
\mathbf{u}_m &= \underline{\mathbf{S}}_{11}\ \mathbf{u}_l + \underline{\mathbf{S}}_{12}\ \mathbf{d}_m, && (3.32a)\\
\mathbf{d}_l &= \underline{\mathbf{S}}_{21}\ \mathbf{u}_l + \underline{\mathbf{S}}_{22}\ \mathbf{d}_m, && (3.32b)\\
\mathbf{u}_m &= \left(\underline{\mathbf{\Phi}}'_m\right)^{-1} \left(\underline{\mathbf{I}}_{11}\ \mathbf{u}_{m+1} + \underline{\mathbf{I}}_{12}\ \underline{\mathbf{\Phi}}'_{m+1}\ \mathbf{d}_{m+1}\right), && (3.32c)\\
\mathbf{d}_m &= \underline{\mathbf{I}}_{21}\ \mathbf{u}_{m+1} + \underline{\mathbf{I}}_{22}\ \underline{\mathbf{\Phi}}'_{m+1}\ \mathbf{d}_{m+1}. && (3.32d)
\end{aligned}$$

The scattering matrix $\underline{\mathbf{S}}(l, m+1)$ is supposed to have the form

$$\begin{pmatrix} \mathbf{u}_{m+1} \\ \mathbf{d}_l \end{pmatrix} = \underline{\mathbf{S}}(l, m+1) \cdot \begin{pmatrix} \mathbf{u}_l \\ \mathbf{d}_{m+1} \end{pmatrix} =: \begin{pmatrix} \hat{\underline{\mathbf{S}}}_{11} & \hat{\underline{\mathbf{S}}}_{12} \\ \hat{\underline{\mathbf{S}}}_{21} & \hat{\underline{\mathbf{S}}}_{22} \end{pmatrix} \begin{pmatrix} \mathbf{u}_l \\ \mathbf{d}_{m+1} \end{pmatrix}. \tag{3.33}$$

By first entering Eqs. (3.32c) and (3.32d) in Eq. (3.32a) and second entering Eq. (3.32d) in Eq. (3.32b), we obtain the recursion formula by which we connect the scattering matrices. It reads

$$\begin{aligned}
\hat{\underline{\mathbf{S}}}_{11} &= \left(\underline{\mathbf{I}}_{11} - \underline{\mathbf{\Phi}}'_m\ \underline{\mathbf{S}}_{12}\ \underline{\mathbf{I}}_{21}\right)^{-1} \underline{\mathbf{\Phi}}'_m\ \underline{\mathbf{S}}_{11} && (3.34a)\\
\hat{\underline{\mathbf{S}}}_{12} &= \left(\underline{\mathbf{I}}_{11} - \underline{\mathbf{\Phi}}'_m\ \underline{\mathbf{S}}_{12}\ \underline{\mathbf{I}}_{21}\right)^{-1} \left(\underline{\mathbf{\Phi}}'_m\ \underline{\mathbf{S}}_{12}\ \underline{\mathbf{I}}_{22}\ \underline{\mathbf{\Phi}}'_{m+1} - \underline{\mathbf{I}}_{12}\ \underline{\mathbf{\Phi}}'_{m+1}\right) && (3.34b)\\
\hat{\underline{\mathbf{S}}}_{21} &= \underline{\mathbf{S}}_{21} + \underline{\mathbf{S}}_{22}\ \underline{\mathbf{I}}_{21}\ \hat{\underline{\mathbf{S}}}_{11} && (3.34c)\\
\hat{\underline{\mathbf{S}}}_{22} &= \underline{\mathbf{S}}_{22}\ \hat{\underline{\mathbf{S}}}_{12} + \underline{\mathbf{S}}_{22}\ \underline{\mathbf{I}}_{22}\ \underline{\mathbf{\Phi}}'_{m+1} && (3.34d)
\end{aligned}$$

The derived recursion formula allows to build a scattering matrix for the entire structure. The most important feature is that repeated structures have the same scattering matrices and, thus, these matrices need only be calculated once and can be multiplied several times with themselves [13]. This is highly efficient since this allows to numerically access very long systems with very little computational effort. The final scattering matrix is $\underline{\mathbf{S}}(0, L)$ which connects the fields that are incident on the structure with the reflected and transmitted fields. Since we normally illuminate the structure with a plane wave in positive x^3 direction and no light from above, we can write the transmitted amplitudes $\mathbf{u}^L$ and the reflected amplitudes $\mathbf{d}^0$ as

$$\begin{aligned}
\mathbf{u}^L &= \underline{\mathbf{S}}_{11}(0, L)\ \mathbf{u}^0, && (3.35)\\
\mathbf{d}^0 &= \underline{\mathbf{S}}_{21}(0, L)\ \mathbf{u}^0. && (3.36)
\end{aligned}$$

Sometimes the calculation of field distributions somewhere in the crystal in a layer l is desired. For that, two scattering matrices have to be derived, namely $\underline{\mathbf{S}}(0, l)$ and $\underline{\mathbf{S}}(l, L+1)$. Since they follow the same principles as the ones discussed above, we refer to Refs. [13, 40, 34, 33] for more details.

[6] To avoid an overcrowded notation, we omit the nomenclature (l, m) of the scattering matrix in the following.

3.5 Practical remarks

Important quantities in the investigation of structures are the transmittance and reflectance which are given by the normalized time-averaged energy flux in x^3 direction. Thus, we have to calculate the x^3 component of the Poynting vector, which reads

$$S_3 = \frac{1}{2}\mathrm{Re}\left(E_1 \cdot H_2^* - E_2 \cdot H_1^*\right). \tag{3.37}$$

Once this quantity is obtained, the transmittance and reflectance can be calculated with the incident Poynting flux S_3^{inc} via

$$T = \frac{\left|S_3^{\mathrm{trans}}\right|}{\left|S_3^{\mathrm{inc}}\right|}, \qquad R = \frac{\left|S_3^{\mathrm{refl}}\right|}{\left|S_3^{\mathrm{inc}}\right|}. \tag{3.38}$$

Due to the change to curvilinear coordinates we face peculiarities that should be discussed. In general, it is important to distinguish between quantities in the transformed and in the physical space. If one is given and the other is desired, they have to be properly translated into each other. Mostly, this statement refers to the electric and magnetic fields. The question is how the coefficients of the fields' Fourier expansion alter upon coordinate system change. For practical purposes, we have two choices [34]:

✧ **Fields on the curvilinear grid.**

In this case, the coefficients of any of the magnetic and electric field's components (represented by the coefficient vector $\boldsymbol{\Psi}_i$) is transformed like

$$\bar{\boldsymbol{\Psi}}_i = \left[\!\left[\frac{\partial x^k}{\partial \bar{x}^i}\right]\!\right] \cdot \boldsymbol{\Psi}_k. \tag{3.39}$$

Here, we entered the Toeplitz matrix of the coordinate transformation's derivative. Thus, we obtain the fields on the curvilinear mesh. This can be desired when we increase the density of coordinate lines along a structure interface. Then, we can plot the fields on this mesh, i.e., with an increased number of discretization points near the surface. Such an approach can be of particular interest when the jump in the fields due to the continuity conditions of Maxwell's equations at material boundaries is supposed to be studied.

✧ **Fields on Cartesian grid.**

Sometimes, we do not want the field values on the curvilinear grid, but instead on a Cartesian grid. Naturally, this means that we need an additional change of the coefficients since the basis changes from curvilinear to Cartesian. Thus, we enter an additional transformation matrix to Eq. (3.39). The coefficients of the magnetic and electric field are then obtained via

$$\bar{\boldsymbol{\Psi}}_i = L \cdot \left[\!\left[\frac{\partial x^k}{\partial \bar{x}^i}\right]\!\right] \cdot \boldsymbol{\Psi}_k, \tag{3.40}$$

with the transformation matrix [34]

$$\begin{aligned} L_{mn} &= \int_0^1 d\bar{x}^1 d\bar{x}^2 \; e^{-i\alpha_{m_1}\bar{x}^1 + i\alpha_{n_1}x^1 - i\beta_{m_2}\bar{x}^2 + i\beta_{n_2}x^2} \\ &= \int_0^1 dx^1 dx^2 \; \det(J) e^{-i\alpha_{m_1}\bar{x}^1 + i\alpha_{n_1}x^1 - i\beta_{m_2}\bar{x}^2 + i\beta_{n_2}x^2}, \end{aligned} \tag{3.41}$$

which describes the change from the plane wave basis in the transformed space to the plane wave basis of the Cartesian space. The definitions for α_i and β_i are found in Section 3.2. J is the Jacobian from Eq. (2.44).

A last important remark has to be made on the determination of the Poynting flux. One possible solution is the classical way of calculating the magnetic and electric field in the Cartesian coordinate system (see Eq. (3.40)) and determining the Poynting vector as their cross product like in Eq. (3.38). An alternative formulation, that we use in Chapter 6 for three-dimensional coordinate transformations, is given in Section 6.6 of Ref. [33]. Since the derivation is lengthy we do not present it here. The essence is that the transmitted power is determined by calculating the sum over the transmitted power of each normalized eigenmode which is given by the square root of the eigenmode's amplitude u. For this procedure, the modes have to be orthonormal [33].

Chapter 4

Opal Photonic Crystals

In this chapter, the classical Fourier Modal Method without coordinate transformations and with an isotropic permittivity is used for the simulation of opal photonic crystals. By computing the optical response of this periodic arrangement of dielectric spheres, the numerical method demonstrates its great advantages.

In Section 4.1, we discuss the basics of opals, especially their composition and fabrication. In Section 4.2, a study on the polarization behavior of the transmitted light in opal photonic crystals is presented. We analyze polarization effects for different crystal thicknesses. Effectively, this is the topic of our submitted manuscript Ref. [43]. The chapter is concluded with Section 4.3, where axial anisotropy is examined. The results shown here are also found in our manuscript Ref. [44].

The projects described in this chapter were conducted in collaboration with Prof. Sergei G. Romanov from the University of Erlangen-Nuremberg, who performed the experimental parts of the analysis. Furthermore, Christian Wolff from our group contributed valuable insights with band-structure calculations (using MPB [45]) and Bloch mode studies. I performed the computations with the Fourier Modal Method using a code that was mainly written by Sabine Essig and participated in the theoretical analysis.

4.1 Introduction

Opals consist of small dielectric spheres stacked in an either hexagonal close packed (hcp) or face centered cubic (fcc) arrangement [46, 1]. The hcp arrangement corresponds to sphere layers that are stacked in ABABAB order. The fcc ordered crystal describes an ABCABC stacking, cf. Figs. 4.1(b) and (c). Which form is assumed depends on the conditions during the self-organized fabrication. The samples that we discuss here take the ABCABC form. For this, a hydrophilic glass slide with a meniscus is dipped into a suspension containing the dielectric spheres. By applying an acoustic-noise-agitation technique and by pulling the glass slide up and off the suspension, samples of size 25×75 mm^2 can easily be fabricated [47]. A scanning electron micrograph (SEM) of an actual experimental realization is depicted in Fig. 4.1(a). Naturally, the crystal does not possess a perfect fcc structure. In the course of this chapter we will comment on imperfections in the crystal and their role in the transmission behavior.

Opals exhibit rich physical features - especially their transmittance and reflectance spectra are interesting due to photonic stop bands, see Refs. [48, 49]. Also, these spectra feature interesting effects when the incident light is polarized, see Ref. [47]. This is the field that we

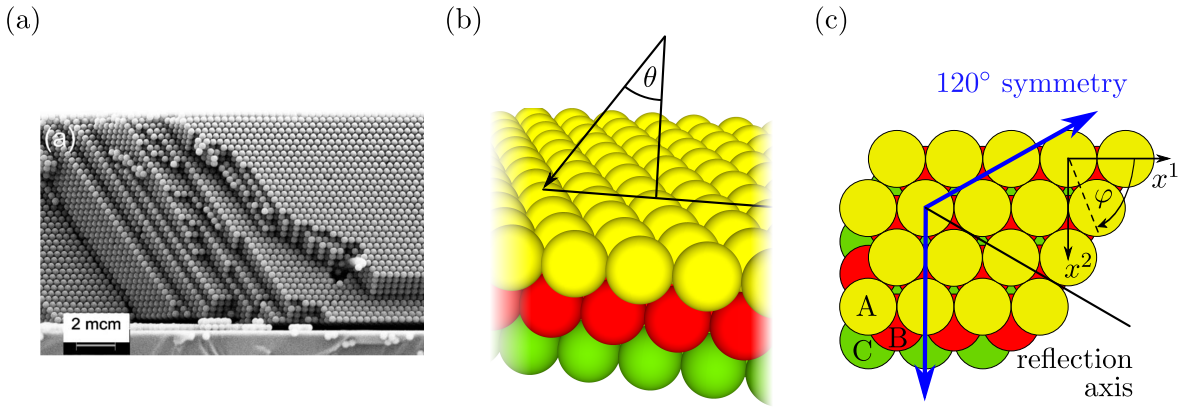

Figure 4.1: Opal photonic crystals in fcc arrangement. An experimental realization is imaged in panel (a). The picture is taken from Ref. [47]. The fcc lattice with its stacking order ABCABC is depicted in panels (b) and (c).

perform our investigations in—we impinge polarized light onto the crystal and analyze the angle- and polarization-resolved spectra.

In our investigations, we consider PMMA (poly-methyl methacrylate) spheres. The material's permittivity is $\varepsilon_{\text{PMMA}} = 1.489^2 \approx 2.217$. The spheres in our first investigation have a diameter of $D = 558$ nm. Due to the fcc arrangement displayed in Fig. 4.1(c), the lattice constant is $a = 2D = 1116$ nm. The space between the spheres is filled with air, i.e., $\varepsilon_{\text{bg}} = 1$ is used as background material. The layers of spheres are deposited on a glass substrate with $\varepsilon_{\text{glass}} = 2.25$, which is included in the numerical computations.

The geometry of the lattice is incorporated in the FMM computations by using a hexagonal unit cell with lattice vectors $(a, 0)$ and $a \cdot (1/2, \sqrt{3}/2)$. Since the structure is repeated in x^3 direction after 3 layers (ABCABC), the unit cell in x^3 direction consists of three layers of spheres.

4.2 Thickness-dependent polarization dynamics

In a first study, we investigate a sample of 23 layers arranged in ABCABC stacking, cf. Fig. 4.1(b) and (c). Thus, the sample has a total height of about 13 μm. The angle of incidence θ is defined as sketched in Fig. 4.1(b). θ and the wavelength of the incident light were varied and the obtained transmittance in zeroth order is color-coded in Fig. 4.2. The angle φ is zero for all calculations in this section. The incident light is s-polarized, i.e., the electric field vector is perpendicular to the plane of incidence. In Fig. 4.2, the zeroth order transmittance into s-polarization (from now on called T_{ss}) is depicted in the left column, i.e., panels (a) and (c), and the zeroth order transmittance in p-polarization (from now on called T_{sp}) is depicted in the right column, i.e., panels (b) and (c). The numerical results obtained with the FMM are depicted in panels (c) and (d) and the measured spectra are shown in panels (a) and (b). The FMM computations were performed with 97 plane waves in the lateral direction. Since the jump in the permittivity between air and PMMA is rather small, this number is sufficient [34]. Also, we used 20 slices in x^3 direction to resolve one layer of spheres.

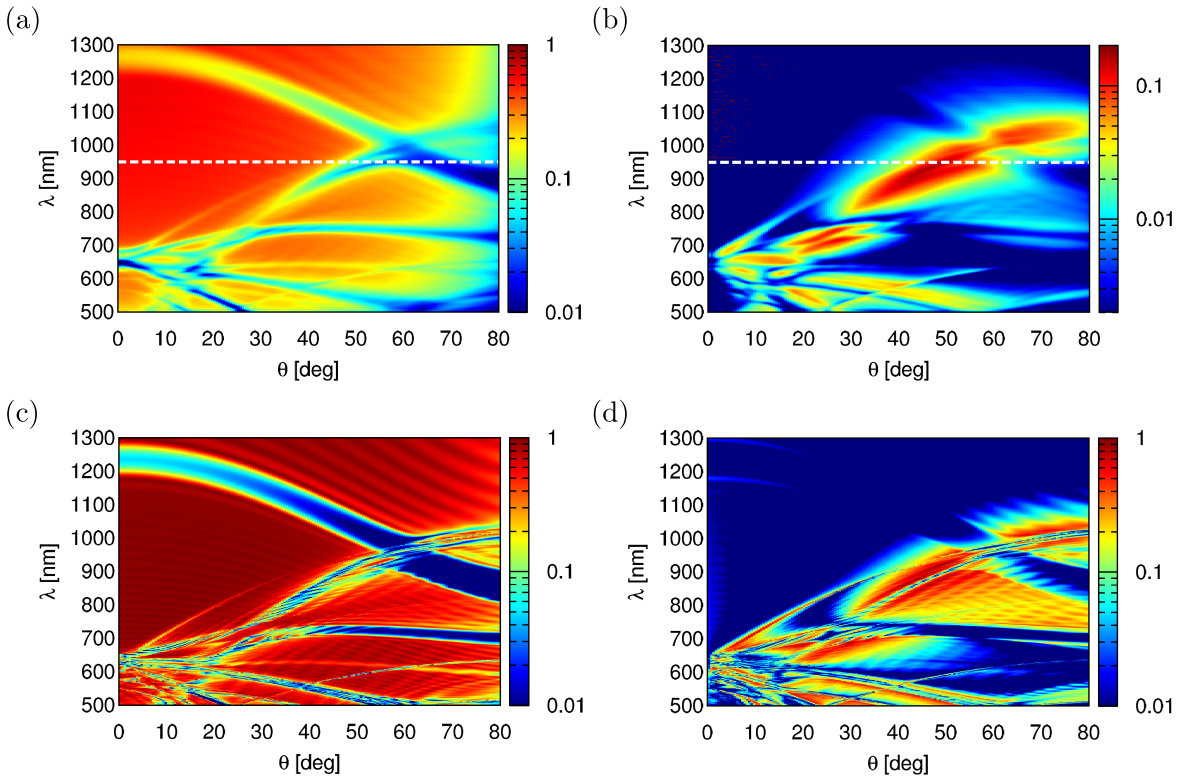

Figure 4.2: Experimental and numerical transmittance spectra. The incident plane wave is s-polarized. The zeroth order transmittance in s-polarization (left column) and p-polarization (right column) is color-coded. Panels (a) and (b) depict the experimental results, while panels (c) and (d) show the results of the FMM computations. We sampled the wavelength in steps of 1 nm and θ in steps of 0.5°. The white, dashed line in panels (a) and (b) indicates a change in the used spectrometer. The plots are taken from our manuscript Ref. [43].

The comparison between numerical and physical data is very interesting: The first, striking observation is the very good qualitative agreement. Especially the measured transmittance minima in T_{ss} are very well reproduced by the numerical simulations. In fact, it is stunning that the various fine features measured for small values of theta (0° to 20°) and for high frequencies (500 nm to 700 nm) are reproduced this well. After all, the numerical transmittance is the result of an ab-initio computation—no fit parameter of any sort has been incorporated in the simulation.

The second striking behavior is that T_{ss} has stop bands where values of effectively zero are reached. Also, there are parameter regions where almost all the transmitted light has changed its polarization from s- to p-polarization. The corresponding transmittance T_{sp} from s- into p-polarization is depicted in Fig. 4.2(d).

The third property of the results in Fig. 4.2 that stands out is the difference in magnitude of the experimental and the numerical cross transmittance T_{sp} (compare the color bars in panels (b) and (d)). Although the features match well, the values of the measurements are about a factor of three lower than their numerical counterpart. The reason was found to be a different stacking orientation in distinct regions of the opal photonic crystal. Since a rotation by 60° corresponds to a reversal of the stacking order (cf. Fig. 4.1(c)), two areas with different crystal

orientation next to each other lead to a cancellation of the cross polarized transmittance in the far field. Therefore, an imperfectly stacked opal photonic crystal does not exhibit the same high T_{sp} values which are predicted by ab-initio numerics of the perfectly periodic crystal. To show that this really is the source of the problem, Christian Wolff suggested an analysis of the used opal sample with a polarized microscope. The results are shown in Fig. 4.3. Here, photos of the sample are shown where the incident light is both unpolarized (panel (a)) and polarized (panel (b)). In the unpolarized case, the sample has the same color in all regions. This means that the opal is stacked in an fcc arrangement everywhere and does not show areas with, e.g., hcp arrangement. In the polarized case, the picture displays different colors—therefore, the polarized light is transmitted differently in particular parts of the sample. Thus, Fig. 4.3 strongly suggests that the stacking order is the reason for the discrepancy between the results in Figs. 4.2(b) and (d). In fact, the measured values of T_{sp} depend on the concrete area of the sample that is illuminated. A different area would yield a different ratio of ABC and ACB stacked layers and, thus, the values of T_{sp} would change.

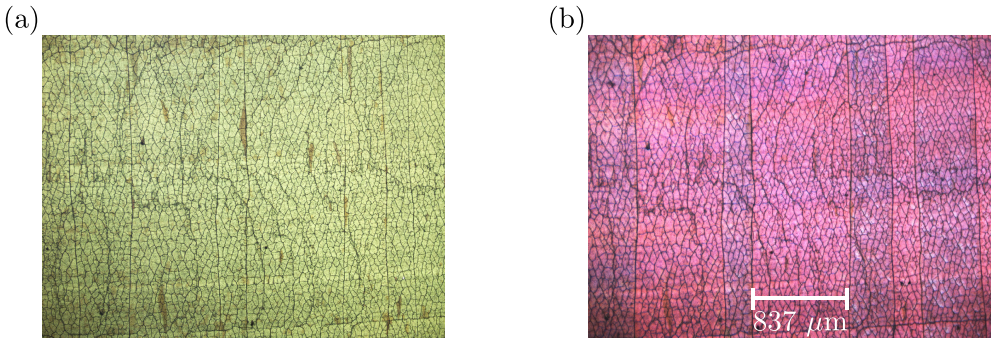

Figure 4.3: Unpolarized (panel (a)) and polarized (panel (b)) micrograph of the opal photonic crystal. Different stacking orders manifest themselves in different transmission of polarized light. Since the sample shows different colors in panel (b), the sample cannot be an ideal and perfectly periodic photonic crystal. This explains the difference in the strength of the T_{sp} measurement to the numerical data (cf. Figs. 4.2(b) and (d)). The vertical stripes occur since the sample 'grows' in vertical direction. Images are courtesy of Prof. Sergei G. Romanov.

As stated above, both numerical and experimental spectra reach high values for the cross transmittance. This is a remarkable property and the apparent question is whether this is a bulk or a surface effect. A surface effect would change if the surface was terminated differently. On the other hand, a bulk effect would leave a clear finger print upon changing the thickness of the sample. Here, we apply one of the great strengths of the FMM and the scattering matrix algorithm. Above we discussed that we set up a scattering matrix for a unit cell in x^3 direction consisting of three layers of spheres. Since the arrangement is repeated several times, we can just multiply the matrices an appropriate number of times and obtain the corresponding scattering matrix for the entire system. Naturally, such a matrix multiplication is not very costly. Hence, we can easily obtain the transmittance for very thick samples by just multiplying the corresponding scattering matrix with itself often enough.

In order to test whether the high cross transmittance values are dominated by surface or bulk effects, we performed computations for an incident wavelength of 900 nm and angles around $\theta = 45°$. These parameters correspond to a region where T_{sp} is very high in Figs. 4.2(b) and (d). The investigated systems contain up to 140 crystal planes. Since we multiply the scattering matrices several times, it is important to make sure that the error for one layer of

spheres is as small as possible in order to avoid an exponentiation of the error. Therefore, we use 349 plane waves in the lateral plane for the field expansion and dissect each layer of spheres into 40 slices.

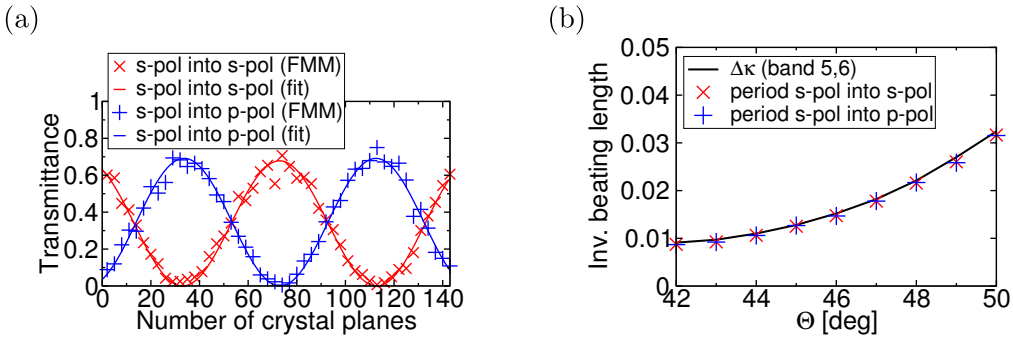

Figure 4.4: Panel (a) displays T_{ss} (red) and T_{sp} (blue) for a varying number of crystal planes. The data is computed with the FMM for $\theta = 45°$ and a wavelength of 900 nm. The solid lines are sinusoidal fits to the numerical data. We performed several studies like in panel (a) for different values of θ. For each θ a sinusoidal curve is fitted to the data and the period is extracted. Panel (b) displays these results together with their prediction from a band structure analysis, see Refs. [43, 50] for details. The plots are taken from Ref. [43]

In Fig. 4.4(a), the transmittance from s-polarization into s-polarization (red crosses) and into p-polarization (blue crosses) for an incidence angle of $\theta = 45°$ at 900 nm is depicted as a function of the number of opal layers. Besides minor deviations, the data shows a sinusoidal behavior, both for T_{ss} and T_{sp}. Also, both functions reach effectively zero. This shows that the polarization conversion has to be a bulk effect—not only does it vary periodically with the number of opal layers but also vanishes for certain thicknesses. This implies that it cannot be a surface effect since a surface effect would be present for all sample thicknesses.

The next step is that we can perform a calculation like in 4.4(a) for several angles of incidence. So for $\theta = 42°$ to $\theta = 50°$ we performed FMM computations for a varying number of opal planes and fitted sinusoidal curves to the data. As a result, Fig. 4.4(b) displays the period length of the sinusoidal fits as a function of θ. They are all on one curve and, excitingly, this curve can be predicted. Christian Wolff showed in a very elaborate study that the period lengths can directly be related to certain features in the band structure and the corresponding Bloch modes. The interested reader can find this analysis in Refs. [43, 50].

Finally, it is instructive to have a look at the polarization state of the transmitted light in terms of Stokes parameters. Figure 4.5 depicts the Stokes parameters for 4 to 76 opal planes for an incident plane wave of wavelength 900 nm and $\theta = 45°$. The numbers in the central plot are the numbers of layers. The red circle sketches the projection of the Poincaré sphere, see Section 2.3.3. Its north pole is marked with a red diamond. Upon transmission through the opal layers, the polarization state changes from linearly s-polarized to circular polarization after about 20 layers. Thereafter, it changes to linearly p-polarized after about 40 layers and changes back to s-polarized via the opposite circular polarization. A stacking of the sphere layers in ACB order would result in the opposite path around the Poincaré sphere.

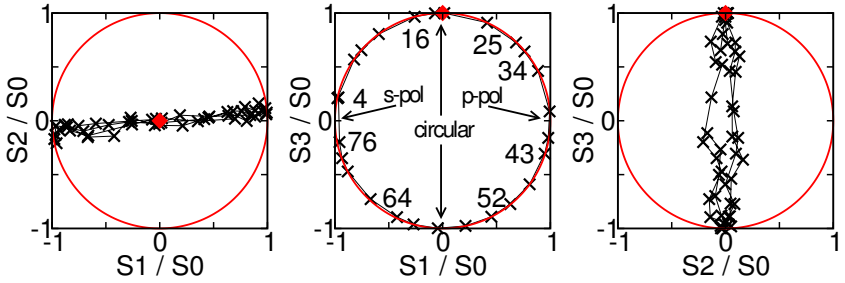

Figure 4.5: The Stokes parameters depict how the polarization state of the transmitted light changes with increasing number of opal layers. It changes from linearly s-polarized to circular polarization, then to p-polarization and then back to s-polarization via the counter-rotating circular polarization. The red diamond indicates the north pole of the Poincaré sphere. The plots are taken from Ref. [43]

4.3 Axial anisotropy in opal photonic crystals

So far, we varied the angle of incidence θ. Naturally, we can also choose a specific value of θ and vary the angle φ as sketched in Fig. 4.1(c). The investigated experimental sample is different than in the previous section. It consists of 25 layers of spheres with a diameter of $D = 368$ nm. In the following, we choose two different angles θ and vary φ.

A sketch of the symmetry properties of the opal photonic crystal slab is depicted in Fig. 4.1(c), where the 120° symmetry and the reflection axis of the system are depicted. Due to this symmetry we only investigate the angular range of $[0°, 120°]$. To show that this suffices, Fig. 4.6(a) depicts the total transmittance for $\theta = 65°$, all angles φ and incoming p-polarization. The minima for small wavelengths show a three-fold, i.e., 120°, symmetry. Figure 4.6(b) shows a close-up of panel (a) where the effect of the reflection axis sketched in Fig. 4.1(c) is observable. For large wavelengths an effective six-fold symmetry shows. A possible explanation is that the wavelength is so large that the wave perceives the crystal as an effective medium. Then, the surface termination, which is one layer of spheres with a six-fold symmetry, would explain the six-fold symmetry in the transmittance spectra.

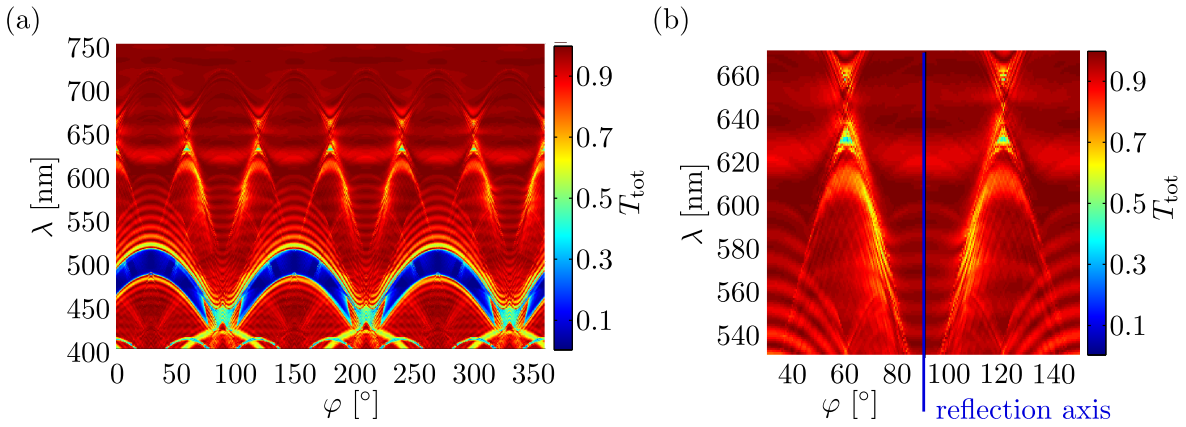

Figure 4.6: Total transmittance (all orders and polarizations) for $\theta = 65°$ and incoming p-polarized light. The spectra show the symmetries sketched in Fig. 4.1(c), namely the 120° symmetry with a reflection axis.

In the following, transmittance plots for the zeroth Bragg order are shown which were obtained with 97 plane waves. For instance, T_{sp} denotes the zeroth order transmittance in p-polarization for incoming light with s-polarization. The transmittance data is plotted in a logarithmic gray-scale plot. For pseudo-color plots on a linear scale, see App. B. There, the transmittances in all orders and for all polarizations are shown.

In the case of $\theta = 30°$, we find light transmitted into the 0^{th} and the 1^{st} order. The experimental transmittance is shown in Fig. 4.7, whereas the numerically calculated spectra are depicted in Fig. 4.8.

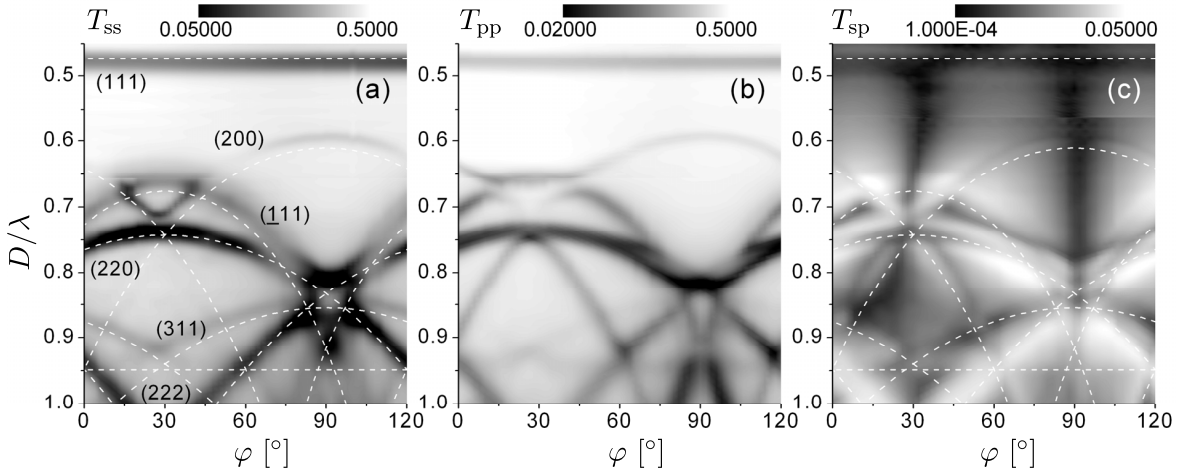

Figure 4.7: Experimental data for the transmittances T_{ss} (incoming s-polarization, zeroth order transmittance in s-polarization), T_{pp} (incoming p-polarization, zeroth order transmittance in p-polarization) and T_{sp} (incoming s-polarization, zeroth order transmittance in p-polarization) with an angle of incidence $\theta = 30°$. The white, dashed lines indicate the resonances of scattering at lattice planes (hkl) described by a Bragg model. The plots are taken from Ref. [44].

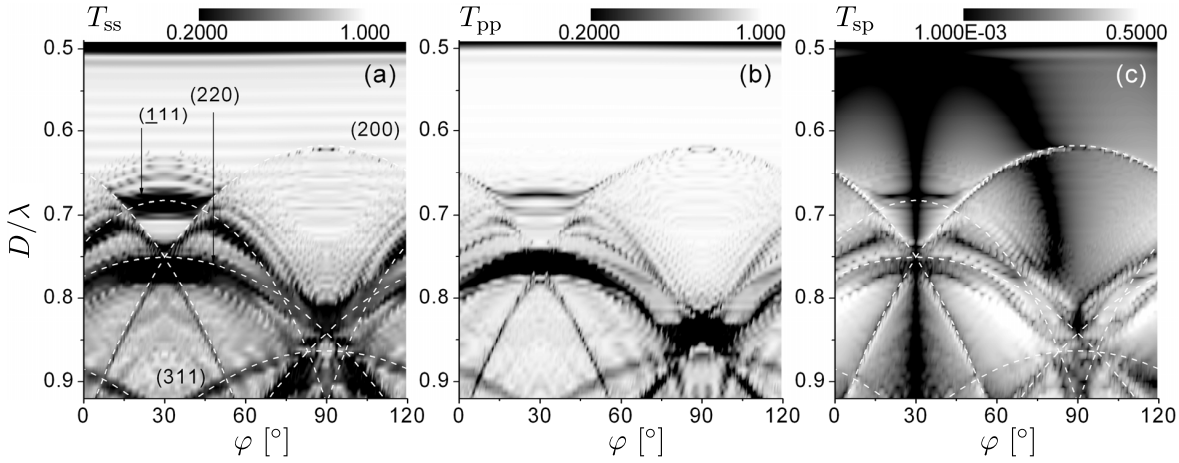

Figure 4.8: Numerical data obtained with the FMM corresponding to Fig. 4.7. The plots are taken from Ref. [44].

As in the previous section, the magnitudes of the transmitted light in numerics and experiment differ. However, the overall agreement of experiment and simulation is qualitatively good. In both plots, dashed white lines indicate the position of diffraction resonances. They

are retrieved by superimposing Bragg resonances obtained by applying a one-dimensional Bragg model to the opal lattice. Then, the resonance condition is given by [44]

$$\lambda = 2d_{hkl}n_{\text{eff}}\sqrt{1-\sin^2\left(\sphericalangle\mathbf{r}_\varphi, \hat{\mathbf{n}}_{hkl}\right)} \tag{4.1}$$

where d_{hkl} is the inter-plane spacing between (hkl)-planes, (hkl) being the Miller indices of the crystal planes. Further, $\mathbf{r}_\varphi$ is given by

$$\mathbf{r}_\varphi = \mathbf{r}_\theta\cos\varphi + \hat{\mathbf{n}}_{111}(\hat{\mathbf{n}}_{111}\mathbf{r}_\theta)(1-\cos\varphi) + \hat{\mathbf{n}}_{111}\times\mathbf{r}_\theta\sin\varphi \tag{4.2}$$

where $\mathbf{r}_\theta$ is the unit vector along the propagation direction of the incident light field. $\hat{\mathbf{n}}_{111}$ is the normal vector of the (111) plane which is the layer of close-packed spheres as shown in Figs. 4.1(b) and (c). A sketch is also provided in Fig. 4.9. The effective index of refraction n_{eff} is obtained by fitting to the angle dispersion of the (111) resonances, with a result of $n_{\text{eff}} = 1.387$ which effectively corresponds to the filling fraction of the unit cell.[1]

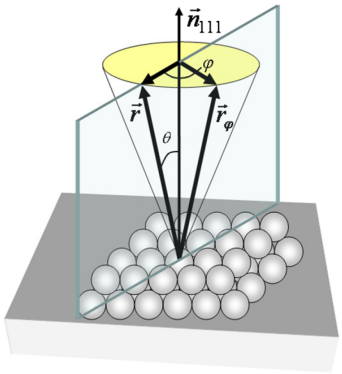

Figure 4.9: Sketch for the quantities used to calculate the lattice resonances via the Bragg model, taken from Ref. [44].

Similar to $\theta = 30°$, spectra for $\theta = 65°$ were measured and calculated. The results are depicted in Figs. 4.10 and 4.11 for experiment and numerics, respectively.

[1] Since the filling fraction of the opal fcc structure is about 74%, the theoretical effective refractive index would be $n_{\text{eff}} = \sqrt{0.74n_{\text{PMMA}}^2 + 0.26n_{\text{air}}^2} = 1.379$.

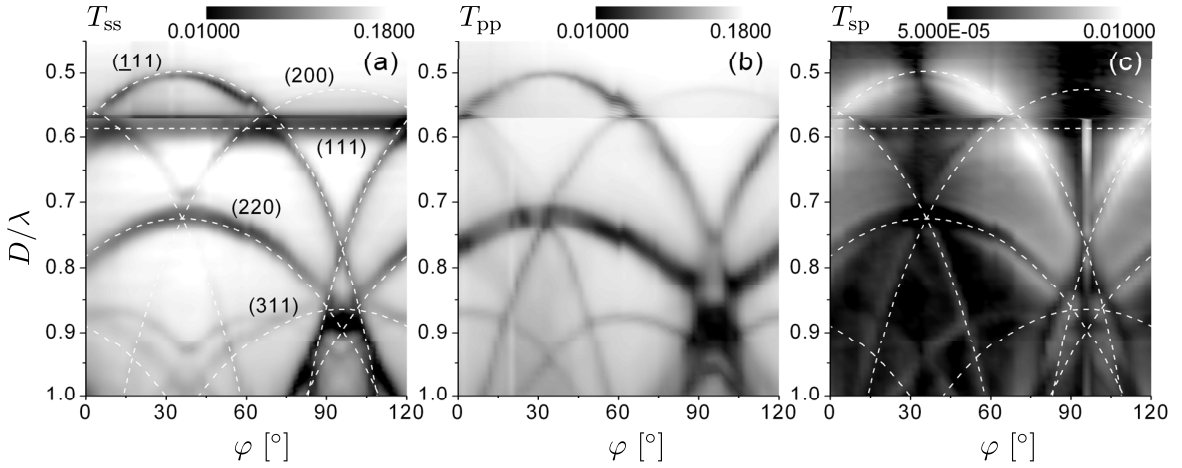

Figure 4.10: Experimental data for T_{ss}, T_{pp} and T_{sp} with an angle of incidence $\theta = 65°$. The plots are taken from Ref. [44].

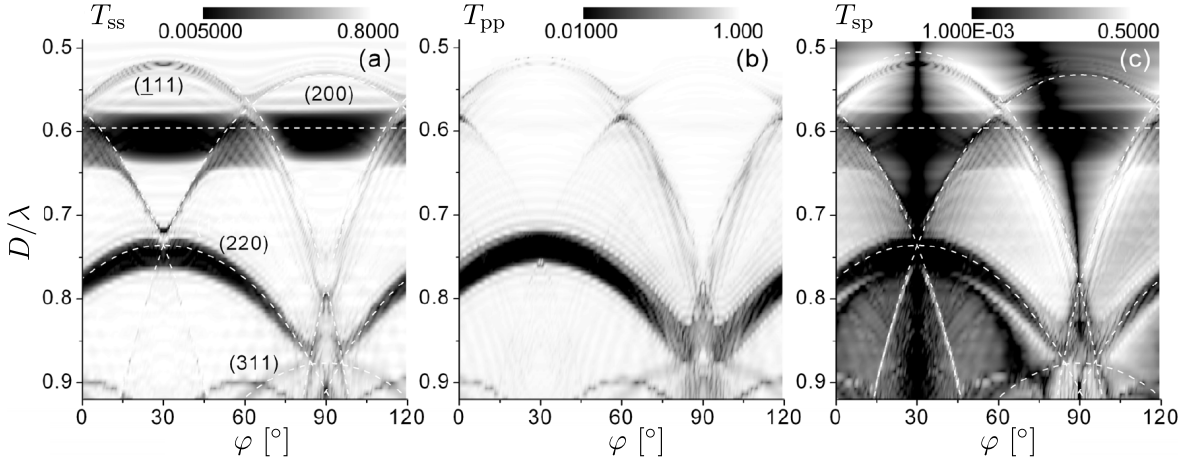

Figure 4.11: Numerical data corresponding to Fig. 4.10. The plots are taken from Ref. [44].

In general, the Bragg model describes the resonances very well. This is not a priori clear since the Bragg model assumes an infinite crystal while the investigated sample is finite in x^3 direction. For $\theta = 65°$, light is transmitted into orders higher than the first, while $\theta = 30°$ yields only scattering into zeroth and first order, cf. Appendix B. Certain further symmetry considerations and the effects of stacking faults regarding symmetries in the transmittance are discussed in Ref. [44].

Chapter 5

Two-Dimensional Coordinate Transformations

In the previous chapter, we discussed the fundamentals of coordinate transformations and argued that such transformations change the shape of the permittivity and permeability. In this chapter, we investigate how suitable coordinate transformations are obtained for a given problem or structure. The transformations constructed and analyzed in this chapter are of the form

$$\bar{x}^1 = \bar{x}^1\Big(x^1, x^2\Big), \tag{5.1a}$$

$$\bar{x}^2 = \bar{x}^2\Big(x^1, x^2\Big), \tag{5.1b}$$

$$\bar{x}^3 = x^3. \tag{5.1c}$$

This means we transform the permittivity and the permeability only in the lateral plane which is perpendicular to the slicing direction of the FMM.

The chapter is structured in the following way: Firstly, we discuss how the restriction to the lateral plane affects the transformed permittivity. Secondly, we review work that has been published on the topic of the construction of one- and two-dimensional meshes[1]. In Section 5.3 we discuss analytical mesh generation in great detail: Three different types of analytical meshes are introduced, namely nondifferentiable, smoothed and differentiable meshes. We also examine important technical aspects like transformations for coordinate line compression, the enforcement of periodic boundary conditions, and treatment of nonrectangular unit cells. In Section 5.4, we have a close look at how the different types of meshes and different sets of mesh parameters influence the performance of the method. This is done by studying a waveguide and a metallic cylinder array as test systems. The chapter is concluded by the formulation of a modularity concept for analytical mesh construction.

[1]The terms “coordinate transformation” and “mesh” are used synonymously in the remainder of this thesis.

5.1 Transformed permittivity

Since the coordinate transformations we examine in this chapter are not fully three-dimensional, the tensors of the effective permittivity and permeability are not fully anisotropic. Assuming an isotropic permittivity $\bar{\varepsilon}$ in the Cartesian space, see Eq. (3.2a), the form of the effective permittivity is

$$\varepsilon^{11} = \sqrt{g}\,\bar{\varepsilon}\left(\frac{\partial x^1}{\partial \bar{x}^1}\frac{\partial x^1}{\partial \bar{x}^1} + \frac{\partial x^1}{\partial \bar{x}^2}\frac{\partial x^1}{\partial \bar{x}^2}\right), \tag{5.2a}$$

$$\varepsilon^{12} = \sqrt{g}\,\bar{\varepsilon}\left(\frac{\partial x^1}{\partial \bar{x}^1}\frac{\partial x^2}{\partial \bar{x}^1} + \frac{\partial x^1}{\partial \bar{x}^2}\frac{\partial x^2}{\partial \bar{x}^2}\right), \tag{5.2b}$$

$$\varepsilon^{21} = \sqrt{g}\,\bar{\varepsilon}\left(\frac{\partial x^2}{\partial \bar{x}^1}\frac{\partial x^1}{\partial \bar{x}^1} + \frac{\partial x^2}{\partial \bar{x}^2}\frac{\partial x^1}{\partial \bar{x}^2}\right) = \varepsilon^{12}, \tag{5.2c}$$

$$\varepsilon^{22} = \sqrt{g}\,\bar{\varepsilon}\left(\frac{\partial x^2}{\partial \bar{x}^1}\frac{\partial x^2}{\partial \bar{x}^1} + \frac{\partial x^2}{\partial \bar{x}^2}\frac{\partial x^2}{\partial \bar{x}^2}\right), \tag{5.2d}$$

$$\varepsilon^{33} = \sqrt{g}\,\bar{\varepsilon}. \tag{5.2e}$$

The other entries of the effective permittivity tensor are zero. The effective permeability looks analogously. Since the effective permittivity tensor is anisotropic in the transverse plane but not fully anisotropic, we can still use the small eigenvalue problem of the FMM.

Upon inspecting Eq. (5.2) one finds that the derivatives $\partial x^i/\partial \bar{x}^j$ are needed. This means that we need the transformations $x^i(\bar{x}^j, \bar{x}^k)$ instead of the ones in Eq. (5.1). We obtain them using the relation

$$\begin{pmatrix} \frac{\partial x^1}{\partial \bar{x}^1} & \frac{\partial x^1}{\partial \bar{x}^2} & 0 \\ \frac{\partial x^2}{\partial \bar{x}^1} & \frac{\partial x^2}{\partial \bar{x}^2} & 0 \\ 0 & 0 & 1 \end{pmatrix} = \bar{J} \overset{(i)}{=} J^{-1} = \begin{pmatrix} \frac{\partial \bar{x}^1}{\partial x^1} & \frac{\partial \bar{x}^1}{\partial x^2} & 0 \\ \frac{\partial \bar{x}^2}{\partial x^1} & \frac{\partial \bar{x}^2}{\partial x^2} & 0 \\ 0 & 0 & 1 \end{pmatrix}^{-1} \overset{(ii)}{=} \frac{1}{\det(J)} \begin{pmatrix} \frac{\partial \bar{x}^2}{\partial x^2} & -\frac{\partial \bar{x}^1}{\partial x^2} & 0 \\ -\frac{\partial \bar{x}^2}{\partial x^1} & \frac{\partial \bar{x}^1}{\partial x^1} & 0 \\ 0 & 0 & 1 \end{pmatrix} \tag{5.3}$$

This statement for the Jacobian J uses (i) the inverse function theorem and (ii) Cramer's rule. Thereby, the general procedure to obtain the transformed permittivity is to first set up the transformations like in Eq. (5.1). Then, we retrieve the derivatives necessary for Eq. (5.2) by means of Eq. (5.3).

Although it may seem like a technicality at this point, it is worth to have a closer look at the numerical differentiation rule we use in our numerical framework. It reads

$$\frac{\partial \bar{x}^1}{\partial x^1}\Big(x_i^1, x_j^2\Big) \approx \frac{-\bar{x}^1\Big(x_{i+2}^1, x_j^2\Big) + 8\bar{x}^1\Big(x_{i+1}^1, x_j^2\Big) - 8\bar{x}^1\Big(x_{i-1}^1, x_j^2\Big) + \bar{x}^1\Big(x_{i-2}^1, x_j^2\Big)}{12\Delta x^1}. \tag{5.4}$$

Here, Δx^1 is the step size of the discretization in x^1 direction. At the edges of the computational domain, i.e., the unit cell, the derivatives are calculated using periodic boundaries. It is important to realize that the rule used for numerical differentiation directly influences the structures we investigate: using a different rule results in different derivatives in Eq. (5.2). Thereby, the numerical differentiation rule changes the appearance of the permittivity and permeability in the transformed space.

The question answered in the following is how the transformations in Eq. (5.1) can be constructed. Before constructing them, we briefly review other works on this topic.

5.2 Review of related work

In recent years, different approaches emerged to construct two-dimensional meshes for the Fourier Modal Method. Conceptually, we can distinguish two avenues: analytical and numerical mesh generation. While the former tries to implement general rules to construct a mesh by setting up functions by hand, the latter tries to implement a general procedure that is able to cope with arbitrary permittivity profiles. Both methods feature specific advantages. The strength of the automated, numerical mesh generation is that it offers a highly versatile tool since any given permittivity can be treated. Analytical coordinate transformations, on the other hand, offer a lot of freedom in terms of selective and systematic change in the mesh properties. They can also be very time efficient: when a large parameter scan is required in which the geometrical parameters of the structure are varied, analytical transformations are easily adjusted. The work presented in this thesis concentrates on analytical mesh generation.

The first coordinate transformations were published for lamellar grating structures [17, 51], i.e., structures where each slice in z direction is effectively one-dimensional. An adaptive mesh is then constructed by a suitable function $\bar{x}^1 = \bar{x}^1(x^1)$. The aim is to increase the density of discretization points at certain specific points, namely at the jumps in the permittivity between different materials. We refer to this concept of manipulating the density of coordinate lines as *adaptive spatial resolution (ASR)*. The ASR transformation we use in our computations is based on the one presented in Ref. [51]. It is described in detail in Section 5.3.7.

An important step towards two-dimensional, analytic mesh generation in the context of the FMM was published by Granet et al. [52]. They extended the method to crossed gratings. However, the mesh consisted of two superimposed one-dimensional transformations, each in one direction. Therefore, the applicability was limited to rectangular structures. The first true two-dimensional mesh was published by Weiss et al. [15]. The authors obtain a mesh for a cylindrical structure, see Fig. 5.1(a). The coordinate lines follow the surface of the structure under investigation—we refer to this principle from now on as *adaptive coordinates (AC)*. In addition, the authors apply an ASR function which is observable by the high coordinate line density along the surface in Fig. 5.1(a). The effect of applying this two-dimensional transformation is investigated for a dielectric and a metallic test system. While it was an excellent first attempt to use analytical ASR and AC in the FMM, it still lacked both a general construction principle and a motivation or guide on how to obtain proper parameters for the transformations.

Automated, numerical mesh generation in the context of the FMM has recently been proposed by Essig et al. [16]. Here, the underlying idea is to set up an energy functional which is minimized to obtain a suitable mesh. An example is depicted in Fig. 5.1(b). The energy functional contains different terms for various purposes. First, it contains the so-called gradient energy the effect of which is to increase the density of coordinate lines along the structure's surface. It is called gradient energy since it is constructed such that the gradient of the given permittivity distribution enters the calculation—a large gradient represents a sudden change in the permittivity, e.g., a material boundary. The second term is called tangential energy and is designed in a way that the coordinate lines are aligned parallel to the structure's surface. Again, the gradient of the permittivity is used. The third and final term is called compression energy. Its purpose is to restore the Cartesian mesh such that the mesh is distorted only as much as necessary. The authors of Ref. [16] demonstrate the strength of the automated, numerical mesh generator by applying it to several different structures.

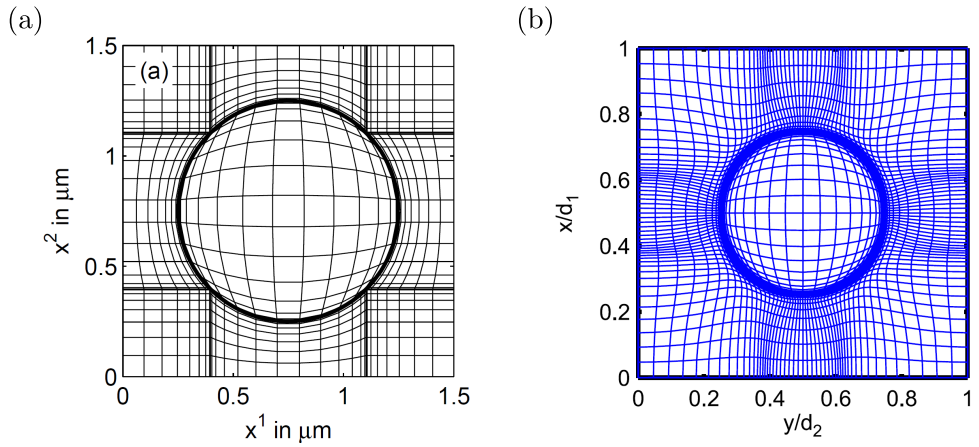

Figure 5.1: Published work on analytical and numerical mesh generation in the context of the FMM. Panel (a) displays an analytical mesh for a cylindrical structure. The figure is taken from Ref. [15]. Panel (b) shows a mesh obtained by applying an automated mesh generator to a cylinder. The figure is taken from Ref. [16].

Unfortunately, like in the case of Ref. [15], no guidelines are formulated how an optimal mesh can be obtained. Moreover, the transformed permittivity is not necessarily grid-aligned, see Ref. [33].

5.3 Mesh construction

In the previous section, we briefly reviewed work that has been published on the topic of two-dimensional mesh generation for the Fourier Modal Method. Both analytical and numerical approaches show improved performance compared to the classic FMM formulation. On the other hand, no guidelines or general principles were formulated on how a mesh has to be constructed and which parameters are optimal. In fact, up to this point it remained unclear whether there existed an optimal choice or sweet spots for the mesh parameters. This changed by the publication of Ref. [53]. In this work, Thomas Zebrowski, Kurt Busch and I first showed the peculiarities occurring when using the mesh by Weiss et al. in Fig. 5.1(a). Then, we presented different types of meshes and investigated their influence on the convergence behavior. This Section 5.3 and Section 5.4 are effectively taken from Ref. [53], with some supplemental information added. This work arose from close cooperation with Thomas Zebrowski and Kurt Busch who participated in the conceptional development. I designed the coordinate transformations, constructed the mappings and performed the convergence and performance studies. The FMM code used was written mainly by Thomas Zebrowski and Sabine Essig, minor parts were contributed by myself.

5.3.1 Motivation

Before we present different approaches to the actual construction of coordinate transformations in the subsequent sections, we describe the general idea of adaptive coordinates in more detail by way of an example. Without coordinate transformation, the permittivity distribution within a unit cell of a cylindrical fiber array may look like the one depicted in Fig. 5.2(a). Here, we display the material matrix of a fiber with $\varepsilon_{\text{fib}} = 2$ in a background material with $\varepsilon_{bg} = 1$ on a grid with 1024×1024 points. This is the same discretization we

use in our computations in Section 5.4. We discussed above that an analytical coordinate transformation for a cylinder is given in Ref. [15], see Fig. 5.1(a). An enlarged sector of the mesh is shown in Fig. 5.2(b). The mesh has two important properties. Firstly, there are many points where the mesh is not differentiable—some of them are marked with green, dashed circles. Secondly, there is one point (marked with a red circle) where the coordinate lines in $\bar{x}^1$- and in $\bar{x}^2$-direction are parallel. In the following, we show how this transformation affects the eigenvalue problem of the FMM. As we have argued in Chapter 3, the matrix that is Fourier transformed when using FMM with AC and/or ASR is not the permittivity itself but rather the effective permittivity defined in Eq. (3.2a). For our present example, we depict the ε^{11}-component of the tensor in Fig. 5.2(c). Several features are worth pointing out: Firstly, the structure is now grid-aligned, i.e., the coordinate transformation maps the circular fiber cross section onto a squarish geometry for which the Fourier factorization rules are much more effective. Secondly, depending on the tensor component under investigation the nondifferentiable points in the mesh lead to discontinuities in the effective permittivity. The third feature is actually not visible here since the color scale is saturated at 4: In the corners of the material square, values in excess of 5000 are reached. In order to understand why, we investigate the derivative $\partial x^1/\partial \bar{x}^1$. We have shown in Eq. (5.3) that it is given by

$$\frac{\partial x^1}{\partial \bar{x}^1} = \underbrace{\left(\frac{\partial \bar{x}^1}{\partial x^1}\frac{\partial \bar{x}^2}{\partial x^2} - \frac{\partial \bar{x}^1}{\partial x^2}\frac{\partial \bar{x}^2}{\partial x^1}\right)^{-1}}_{=|J|^{-1}} \frac{\partial \bar{x}^2}{\partial x^2}. \tag{5.5}$$

If the coordinate lines of the mesh are parallel in $\bar{x}^1$- and $\bar{x}^2$-direction at one point, the determinant of the Jacobian J of the coordinate transformation will become zero at this point. This leads to a diverging derivative $\partial x^1/\partial \bar{x}^1$ and, thereby, to a diverging effective permittivity, see Eq. (3.2a).

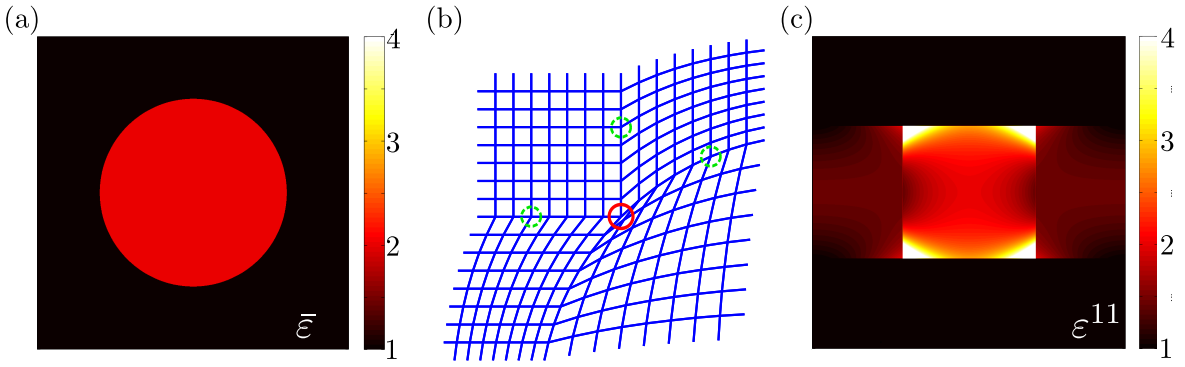

Figure 5.2: Illustration of the effect of adaptive coordinates. Panel (a) depicts the permittivity distribution for a fiber with radius 0.3 centered in a square unit cell within a Cartesian coordinate system. Panel (b) displays a section of the nondifferentiable fiber mesh from Ref. [15]. Some points where the mesh is nondifferentiable are marked with green, dashed circles. The point where the coordinate lines of the mesh are parallel in $\bar{x}^1$- and $\bar{x}^2$-direction is marked with a red circle. Panel (c) displays the ε^{11}-component of the effective permittivity tensor that is obtained when the adaptive coordinates from (b) are applied to (a). In the transformed space, the effective permittivity tensor is fully grid-aligned but the numerical values at the rectangle edges are several orders of magnitude larger than 4. The color scale has been saturated at 4 in order to show more features.

In the following sections, we show how to construct various classes of meshes. The first class is very similar to the one just discussed—in the transformed space, the material distribution assumes a rectangular form. As hinted to above, this means that the material surface is enclosed by four specific coordinate lines and no specific attention to smoothness is paid. We delineate how to construct such *nondifferentiable meshes* even for complex structures in section 5.3.2. The second class of meshes, called *smoothed meshes*, is built in such a way that the four specific coordinate lines are smooth. In section 5.3.3, we discuss that this does not yet lead to fully differentiable meshes. However, smoothed meshes deform the shape of the structure in the transformed space away from the advantageous rectangular forms. Finally, we construct a third class of meshes for which all coordinate lines are differentiable everywhere in the unit cell. This *differentiable meshing* is discussed in Section 5.3.4.

At the end of this section, I would like to point out the two distinct interpretations that may be associated with the coordinate transformations discussed here. The first interpretation is that we map a given permittivity distribution onto a new distribution according to a given mesh. This means that we go from bent coordinate lines to straight coordinate lines (or material surfaces) as shown in Fig. 5.2. This interpretation is particularly useful when we discuss the shape of the effective permittivity in the FMM. The second interpretation is used for constructing the meshes. Then we talk about how to map straight coordinate lines onto bent lines that match the surface given by the material distribution. Both these interpretations are valid—which one to use depends on whether the construction or the application of the meshes is emphasized.

5.3.2 Construction of nondifferentiable meshes

In this section, we show how to construct nondifferentiable meshes associated with complex structures by way of a particular example, the crescent-shaped structure depicted in Fig. 5.3(a). Its tips are rounded so that it is defined by six quantities: the radius r_1 and the center (M_1, N_1) of the large (outer) circle, the radius r_2 and the center (M_2, N_2) of the small (inner) circle, and the radii r_3 and r_4 of the tiny circles that form the tips (see Fig. 5.3(b)). We assume that these quantities are given and, furthermore, that the crescent is symmetric (i.e., $r_4 = r_3$) and not rotated in the unit cell, i.e., $M_1 = M_2$. While this makes the following example simpler, it does in no way restrict the method. Henceforth, all geometric quantities such as radii, side lengths, etc., are given in units of the lattice constant.

The crescent is composed of four circle arcs described by

$$\left(x^1 - M_i\right)^2 + \left(x^2 - N_i\right)^2 = r_i^2, \qquad i = 1, ..., 4, \tag{5.6}$$

where the circles are labeled by their numbers 1 to 4. After some geometric considerations (see Fig. 5.3(b)), we find the center of circle 3 at

$$N_3 = \frac{(r_2 + r_3)^2 - (r_1 - r_3)^2 + N_1^2 - N_2^2}{2N_1 - 2N_2}, \quad M_3 = M_1 - \sqrt{(r_1 - r_3)^2 - (N_3 - N_1)^2}. \tag{5.7}$$

The point $P = (x_P^1, x_P^2)$ where the tip circle 3 meets the outer circle 1 is given by

$$x_P^1 = M_3 - r_3 \cos\left(\arctan\left(\frac{N_3 - N_1}{M_1 - M_3}\right)\right), \quad x_P^2 = N_3 + \sqrt{r_3^2 - (x_P^1 - M_3)^2}, \tag{5.8}$$

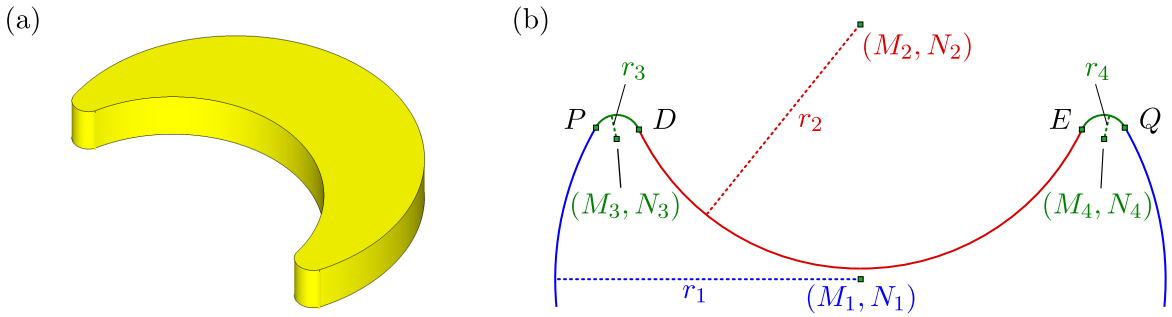

Figure 5.3: Layout of a complex unit cell for the illustration of mesh construction. A crescent with rounded tips is described by four circles—a large, outer circle (blue, radius r_1), a small, inner circle (red, radius r_2), and two tiny circles at the crescent tips (radii r_3 and r_4). To define the orientation of the crescent within the unit cell, the centers (M_1, N_1) and (M_2, N_2) of the inner and outer circles need to be specified. The centers (M_3, N_3) and (M_4, N_4) of the tiny circles are uniquely determined once the centers of the inner and outer circles and the radii of all four circles are specified.

while the intersection point $D = (x_D^1, x_D^2)$ of circle 3 and 2 is

$$x_D^1 = M_3 + r_3 \cos\left(\arctan\left(\frac{N_2 - N_3}{M_2 - M_3}\right)\right), \qquad x_D^2 = N_3 + \sqrt{r_3^2 - (x_D^1 - M_3)^2}. \tag{5.9}$$

We now proceed with the actual meshing procedure. Firstly, as many coordinate lines as necessary are selected so that their mapping to the structure's surface leads to its complete coverage. Secondly, the surface is parametrized so as to obtain an analytical expression for the mapping of the coordinate lines from step one. Thirdly, the mappings for the remaining coordinate lines are obtained by linear interpolation between the selected coordinate lines.

For the linear transition we define the useful function

$$LT(c, \bar{c}, d, \bar{d}, x) = \frac{\bar{d} - \bar{c}}{d - c}\, x + \bar{c} - c\, \frac{\bar{d} - \bar{c}}{d - c} \tag{5.10}$$

which, as a function of $x \in [c, d]$, defines a straight line through the points $(c, \bar{c})$ and $(d, \bar{d})$. Moreover, we can enter entire coordinate lines in LT (i.e., $c = c(y)$, etc.) such that LT describes the linear transition between these coordinate lines. Therefore, when a coordinate line $c(y)$ is mapped on a new coordinate line $\bar{c}(y)$ and a coordinate line $d(y)$ is mapped on a new coordinate line $\bar{d}(y)$ then the mapping of the coordinate line x is given by LT. In Fig. 5.4, we provide an illustration of such a mapping where the left and right vertical coordinate lines are mapped onto curved lines (green and blue). The coordinate lines in between (marked with crosses) are given by a linear transition from the left to the right curved line, i.e., the distances on the horizontal axis are equal between the coordinate lines. As in any linear function, it does not matter in which sequence the points (or coordinate lines) are arranged—i.e., $LT(c, \bar{c}, d, \bar{d}, e) \equiv LT(d, \bar{d}, c, \bar{c}, e)$.

Based on this, we illustrate in Figs. 5.5(a) and 5.5(b) the meshing of the crescent-shaped structure introduced in Fig. 5.3. First, the four characteristic points P, Q, R and S are found. Point P is given by Eq. (5.8) and point $R = (x_R^1, x_R^2)$ is given by the intersection of the

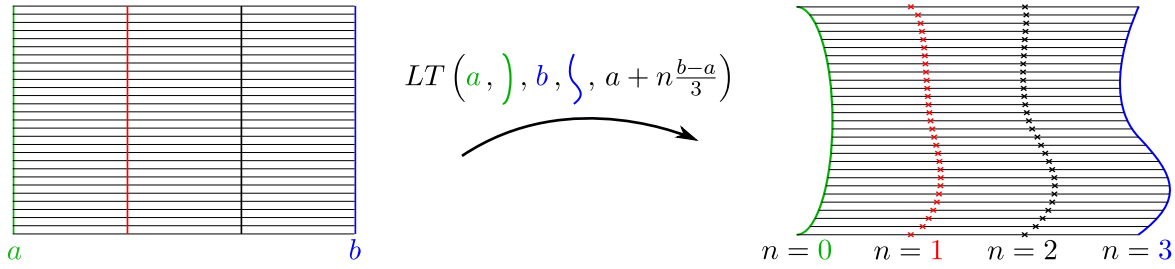

Figure 5.4: Illustration of a linear transition from Cartesian coordinate lines to curved coordinate lines via the linear transition function LT. The straight coordinate lines a and b are, respectively, mapped to the green and blue bent coordinate lines. The mapped lines in between (marked with crosses) are given by the linear transition between the bent outer lines.

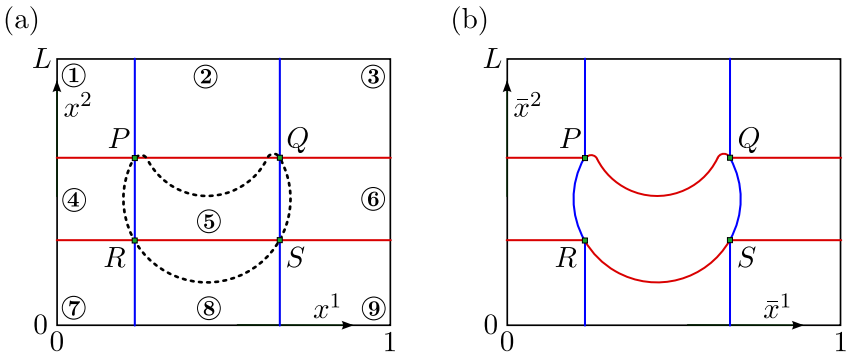

Figure 5.5: Illustration of how to mesh complex structures. Specific coordinate lines that pass through the structure's characteristic points are selected (panel (a)) and subsequently mapped to the structure's surface.

(Cartesian) coordinate line x_P^1 with the structure surface. Then, points Q and R follow from the structure's symmetry.

$$R=\left(x_P^1,N_1-\sqrt{r_1^2-(x_R^1-M_1)^2}\right),\qquad Q=(2M_1-x_P^1,x_P^2),\qquad S=(x_Q^1,x_R^2).\quad(5.11)$$

The (Cartesian) coordinate lines passing through any two of these characteristic points divide the unit cell into the zones ① to ⑨. Secondly, the so selected (Cartesian) coordinate lines have to be deformed in order to follow the crescent's surface and this surface has to be parametrized (see Eq. (5.6)). Third and final, we have to find the two-dimensional transformation function $\left(\bar{x}^1\left(x^1,x^2\right),\bar{x}^2\left(x^1,x^2\right)\right)$ that maps the unit cell to itself by a linear transition between these deformed coordinate lines. This is done separately for all nine zones in the unit cell and we will discuss only zone ④ (see Figs. 5.5(a) and 5.5(b)). The red (horizontal) coordinate lines in zone ④ in Fig. 5.5(a) are not affected by the mapping (i.e. they are in the same position in Figs. 5.5(a) and 5.5(b)). This means that the mapping for $\bar{x}^2$ (corresponding to the horizontal red lines) is the identity mapping

$$\bar{x}^2\Big(x^1,x^2\Big)=x^2,\qquad\qquad\Big(x^1,x^2\Big)\in④.\qquad(5.12)$$

The same applies to the leftmost coordinate line. The rightmost coordinate line experiences

a deformation from a straight line to the arc given in Eq. (5.6). Explicitly, this reads

$$\begin{aligned}\bar{x}^1\Big(x^1,x^2\Big) &= LT\Big(\underbrace{0}_{\text{map left edge onto itself}},\underbrace{0}_{\text{map left edge onto itself}},\underbrace{x_P^1}_{\text{map } PR \text{ coordinate line on circle arc}},\underbrace{M_1-\sqrt{r_1^2-\left(x^2-N_1\right)^2}}_{\text{map } PR \text{ coordinate line on circle arc}},x^1\Big)\\ &\overset{\text{Eq. (5.10)}}{=} \left(M_1-\sqrt{r_1^2-\left(x^2-N_1\right)^2}\right)\frac{x^1}{x_P^1}, \qquad \Big(x^1,x^2\Big)\in ④. \end{aligned} \tag{5.13}$$

The interior coordinate lines have thus been mapped with the help of the linear transition LT as described above. Analogous mappings can be constructed for all other zones in the unit cell $[0,1]\times[0,L]$.

A compact representation of the complete coordinate transformation is facilitated by defining circle arc (CA) functions for either the left, right, top, or bottom side of the crescent. Their form is derived from Eq. (5.6) by choosing the correct sign of the square root

$$\begin{aligned} CA_{L/R}\left(i,x^2\right) &= M_i \mp \sqrt{r_i^2-\left(x^2-N_i\right)^2},\\ CA_{T/B}\left(i,x^1\right) &= N_i \pm \sqrt{r_i^2-\left(x^1-M_i\right)^2}, \end{aligned} \qquad i=1,...,4. \tag{5.14}$$

Here, the subscripts L,R,T, and B refer to left, right, top, and bottom, respectively.

Finally, upon introducing the point $E=(x_E^1,x_E^2)=(2M_1-x_D^1,x_D^2)$, we arrive at the complete coordinate transformation as

$$\bar{x}^1\Big(x^1,x^2\Big)=\begin{cases} x^1 & \left(x^1,x^2\right)\in ①,②,\\ & \quad ③,⑦,⑧,⑨\\ LT\left(0,0,x_P^1,CA_L\left(1,x^2\right),x^1\right) & \left(x^1,x^2\right)\in ④\\ LT\left(x_P^1,CA_L\left(1,x^2\right),x_Q^1,CA_R\left(1,x^2\right),x^1\right) & \left(x^1,x^2\right)\in ⑤\\ LT\left(x_Q^1,CA_R\left(1,x^2\right),1,1,x^1\right) & \left(x^1,x^2\right)\in ⑥. \end{cases} \tag{5.15}$$

The $\bar{x}^2$ mapping is more complex but the construction follows the same principles. It reads

$$\bar{x}^2\big(x^1,x^2\big)=$$

$$\begin{cases} x^2 & \left(x^1,x^2\right)\in ①,\\ & \quad ③,④,⑥,⑦,⑨\\ LT\left(L,L,x_P^2,CA_T\left(3,x^1\right),x^2\right) & x^1\le x_D^1\\ LT\left(L,L,x_P^2,CA_B\left(2,x^1\right),x^2\right) & x^1\in\left(x_D^1,x_E^1\right) \quad \Big\} \quad \left(x^1,x^2\right)\in ②\\ LT\left(L,L,x_P^2,CA_T\left(4,x^1\right),x^2\right) & x_E^1\le x^1\\ LT\left(x_P^2,CA_T\left(3,x^1\right),x_R^2,CA_B\left(1,x^1\right),x^2\right) & x^1\le x_D^1\\ LT\left(x_P^2,CA_B\left(2,x^1\right),x_R^2,CA_B\left(1,x^1\right),x^2\right) & x^1\in\left(x_D^1,x_E^1\right) \quad \Big\} \quad \left(x^1,x^2\right)\in ⑤\\ LT\left(x_P^2,CA_T\left(4,x^1\right),x_R^2,CA_B\left(1,x^1\right),x^2\right) & x_E^1\le x^1\\ LT\left(x_R^2,CA_B\left(1,x^1\right),0,0,x^2\right) & \left(x^1,x^2\right)\in ⑧. \end{cases} \tag{5.16}$$

We shortly discuss the $\bar{x}^2$ mapping in zone ②. The upper edge of zone ② is mapped to itself (L). The upper red (horizontal) line in Fig. 5.5(a) is mapped on the line between P and Q consisting of the three circles $3,2$ and 4. The parts in between are again given by the linear transition function LT.

In Fig. 5.6(a), we display the resulting mesh. In addition, we may compress the coordinate lines towards the crescent's surface as depicted in Fig. 5.6(b). However, we postpone a discussion of coordinate line compression to Section 5.3.7.

The construction principle described above represents a very general procedure and can be applied to a great variety of structures. For instance, Fig. 5.7 displays characteristic points, selected coordinate lines and the resulting mesh for a step-index fiber.

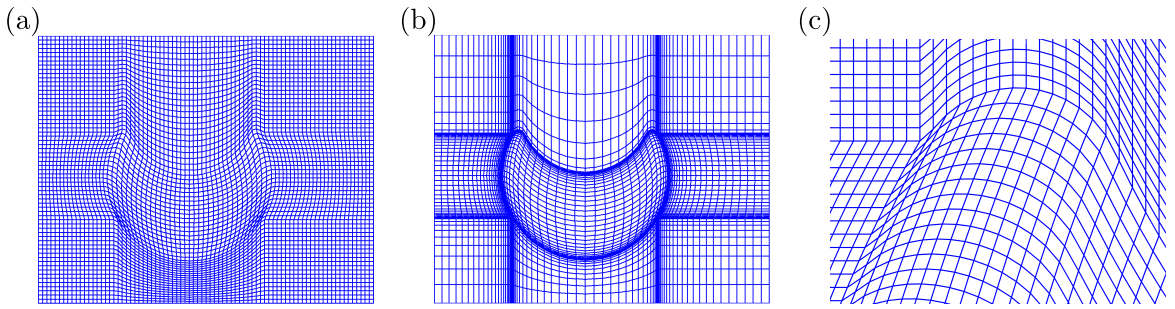

Figure 5.6: Nondifferentiable meshes for a crescent with parameters $r_1 = 0.25$, $r_2 = 0.2$, $r_3 = r_4 = 0.02$, $M_1 = 0.45$, $N_1 = 0.38$, $M_2 = M_1$, $N_2 = 0.5884$, $L = 0.8$. Panel (a) displays the basic analytical mesh. Panel (b) depicts a mesh where an additional coordinate line compression using the parameters $G = 0.05$, $\Delta x^1 = 0.4$, $\bar{x}_1^1 = x_P^1$, $\bar{x}_2^1 = x_Q^1$, $\Delta x^2 = 0.4$, $\bar{x}_1^2 = x_R^2$, $\bar{x}_2^2 = x_P^2$ has been applied (see Section 5.3.7 for details). Panel (c) features a close-up of (a) of the left crescent tip.

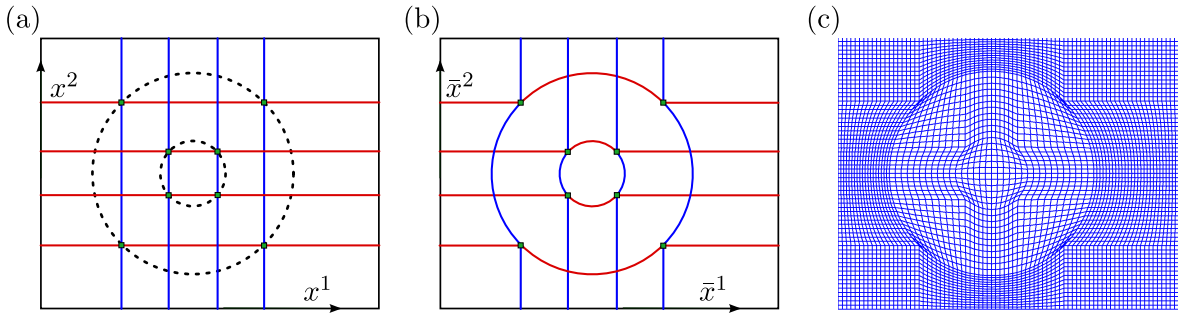

Figure 5.7: Characteristic points, selected coordinate lines, and nondifferentiable mesh for a step-index fiber. The outer radius is 0.3 and the inner radius is 0.1. The circles are centered in (0.45,0.4) and the unit cell is $[0, 1] \times [0, 0.8]$.

It is worth pointing out that the general construction principle described here reproduces the cylinder mesh by Weiss et al. [15] (see also Figs. 5.1(a) and 5.2(b)). In the subsequent sections, we will use this simple structure in order to illustrate the construction of smoothed and fully differentiable meshes and to compare their performance in actual FMM computations.

5.3.3 Construction of smoothed meshes

The construction principle for the above meshes has two key properties. Firstly, at the characteristic points the meshes are typically nondifferentiable. Secondly, at some points the coordinate lines are parallel in $\bar{x}^1$- and in $\bar{x}^2$-direction (see Fig. 5.2(b)). The latter causes a divergent effective permittivity (see Eq. (3.2a)). Therefore, we describe a way to design smoothed meshes that avoid these singularities in the following. In this context, *smoothed* means that the characteristic coordinate lines are mapped to smooth curves. This results in meshes the partial derivatives of which are still discontinuous at several points. In this sense, the present section represents an intermediate step from nondifferentiable to fully differentiable meshes which are discussed in the subsequent section.

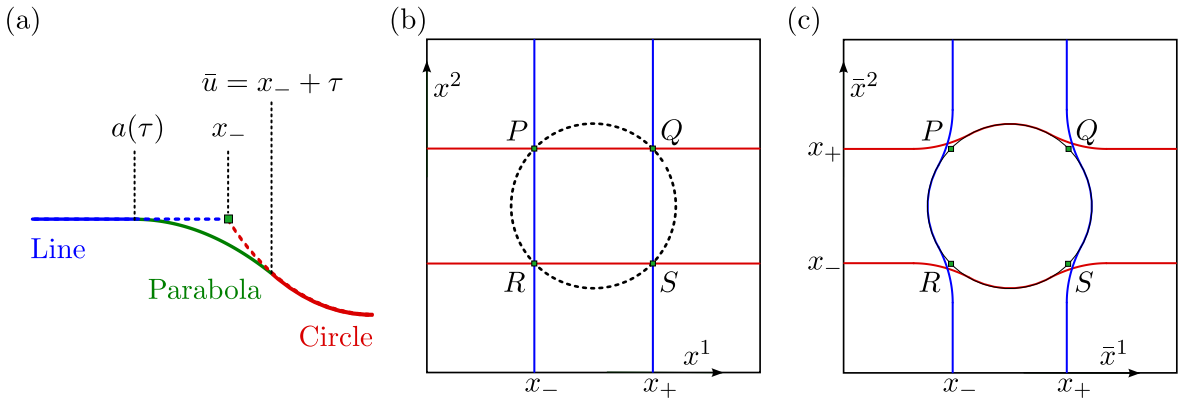

Figure 5.8: Illustration of the construction principle for smoothed meshes. Panel (a) depicts how the nondifferentiable transition from (Cartesian) characteristic line to a circle arc (as described in Section 5.3.2) is smoothed by a (differentiable) parabola. The parabola and the circle arc meet at the point $\bar{u} = x_- + \tau$ with smoothing parameter τ. Straight line and parabola meet at a which also depends on τ. Panels (b) and (c) show how the characteristic coordinate lines passing through P, Q, R and S are mapped.

For illustrative purposes, we consider a square unit cell $[0,1] \times [0,1]$ with a circle of radius r located in the center. Just as in the previous section, we choose characteristic points, namely the four points $R = (x_-, x_-)$, $S = (x_+, x_-)$, $P = (x_-, x_+)$ and $Q = (x_+, x_+)$, where we have introduced the abbreviations $x_\pm = 0.5 \pm \frac{r}{\sqrt{2}}$.

In order to obtain partial differentiability for the characteristic coordinate lines, we smooth the transition from straight line to circle arc with a parabola (see Fig. 5.8(a)). The parabola is adjusted such that it is differentiable both at point a and at point $\bar{u}$. We determine $\bar{u}$ by *choosing* a smoothing parameter τ, i.e., $\bar{u} = x_- + \tau$. Apparently, this adjustment of the transition function is not unique and one could use functions other than parabolas. By assuming a general form of

$$g(x^1, a, b, x_-) = b(x^1 - a)^2 + x_- \tag{5.17}$$

for the parabola g we assure continuity and differentiability at a. Demanding continuity and differentiability at $\bar{u}$ determines the parameters a and b.

$$a = -\frac{2}{\bar{u} - 0.5}\left(-\sqrt{r^2 - (\bar{u} - 0.5)^2} + 0.5 - x_-\right)\sqrt{r^2 - (\bar{u} - 0.5)^2} + \bar{u}, \tag{5.18a}$$

$$b = \frac{1}{4}(\bar{u} - 0.5)^2\left[\left(-\sqrt{r^2 - (\bar{u} - 0.5)^2} + 0.5 - x_-\right)\left(r^2 - (\bar{u} - 0.5)^2\right)\right]^{-1}. \tag{5.18b}$$

The mapping itself is performed with the same methods as described in the preceding section. The coordinate lines that pass through any pair of characteristic points P, Q, R, S are mapped onto the smoothed curves as depicted in Fig. 5.8. The other coordinate lines follow by a linear transition. The functions needed are given in Eq. (5.10), Eq. (5.17) and by $CA_{\pm}(x^1) = \pm\sqrt{r^2 - (x^1 - 0.5)^2} + 0.5$.

The mapping for the horizontal lines, i.e., the component $\bar{x}^2$ then reads

$$\bar{x}^2\Big(x^1, x^2\Big) =$$

$$\begin{cases} x^2, & x^1 \in [0,a) \cup (1-a,1], \quad x^2 \in [0,1] \\ \left.\begin{array}{ll} LT\left(0,0,x_-, g(x^1,a,b,x_-), x^2\right), & x^1 \in [a,\bar{u}] \\ LT\left(0,0,x_-, CA_-\left(x^1\right), x^2\right), & x^1 \in (\bar{u},1-\bar{u}) \\ LT\left(0,0,x_-, g(x^1,1-a,b,x_-), x^2\right), & x^1 \in [1-\bar{u},1-a] \end{array}\right\} & x^2 \in [0,x_-] \\ \left.\begin{array}{ll} LT\left(x_-, g(x^1,a,b,x_-), x_+, g(x^1,a,-b,x_+), x^2\right), & x^1 \in [a,\bar{u}] \\ LT\left(x_-, CA_-\left(x^1\right), x_+, CA_+\left(x^1\right), x^2\right), & x^1 \in (\bar{u},1-\bar{u}) \\ LT\left(x_-, g(x^1,1-a,b,x_-), x_+, g(x^1,1-a,-b,x_+), x^2\right), & x^1 \in [1-\bar{u},1-a] \end{array}\right\} & x^2 \in (x_-,x_+) \\ \left.\begin{array}{ll} LT\left(x_+, g(x^1,a,-b,x_+), 1, 1, x^2\right), & x^1 \in [a,\bar{u}] \\ LT\left(x_+, CA_+\left(x^1\right), 1, 1, x^2\right), & x^1 \in (\bar{u},1-\bar{u}) \\ LT\left(x_+, g(x^1,1-a,-b,x_+), 1, 1, x^2\right), & x^1 \in [1-\bar{u},1-a] \end{array}\right\} & x^2 \in [x_+,1] \end{cases} \tag{5.19}$$

The mapping for the vertical lines, i.e., the component $\bar{x}^1$ can be found in an analogous manner. For our simple system, symmetry mandates that the coordinate $\bar{x}^1$ is constructed from the horizontal line mapping, Eq. (5.19), by interchanging x^1 and x^2. In Fig. 5.9, we depict the final results of this mapping (cf. Fig. 5.2(b) for a corresponding 'unsmoothed' mesh). An important effect of this smoothing procedure is that the structure's surface is no longer grid-aligned in the undistorted, Cartesian space described by Eq. (3.2a). This is visualized in the subsequent section.

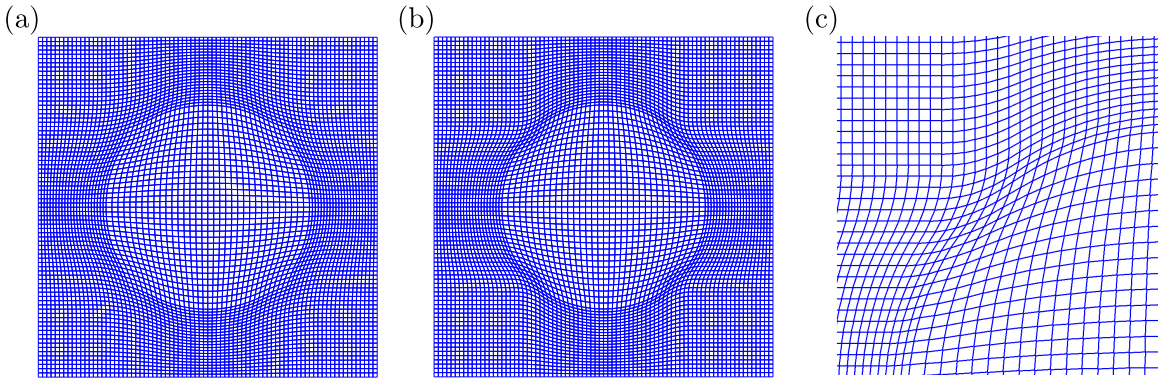

Figure 5.9: Smoothed meshes for a circular structure (radius $r = 0.3$) centered in a square unit cell. Panels (a) and (b) depict meshes with smoothing parameters $\tau = 0.07$ and $\tau = 0.035$, respectively. Panel (c) shows a close-up of the mesh in (b).

Nevertheless, upon inspecting the above expressions we find that the mesh is nondifferentiable at points $x^1 \in (a, 1-a)$, $x^2 = x_{\pm}$ and $x^1 = x_{\pm}$, $x^2 \in (a, 1-a)$. The effect of this

nondifferentiability manifests itself in a sudden change of the density of coordinate lines between outside and within the circular structure (see Fig. 5.9). As mentioned above, without any smoothing (i.e., Eq. (5.19) with $\tau = 0$) we obtain the expressions for the circle mesh as described in Ref. [15]. In the remainder, we refer to this mesh as the *nondifferentiable circle mesh*.

Before we design differentiable meshes, we demonstrate that we can construct a different smoothed mesh with different properties: Instead of making the specific coordinate lines of the nondifferentiable mesh smooth, we construct new specific coordinate lines which are also smooth but enclose the entire surface of the cylinder. However, this procedure again leads to a diverging effective permittivity.

In Fig. 5.10 we depict the construction principle for this alternative smoothed mesh.

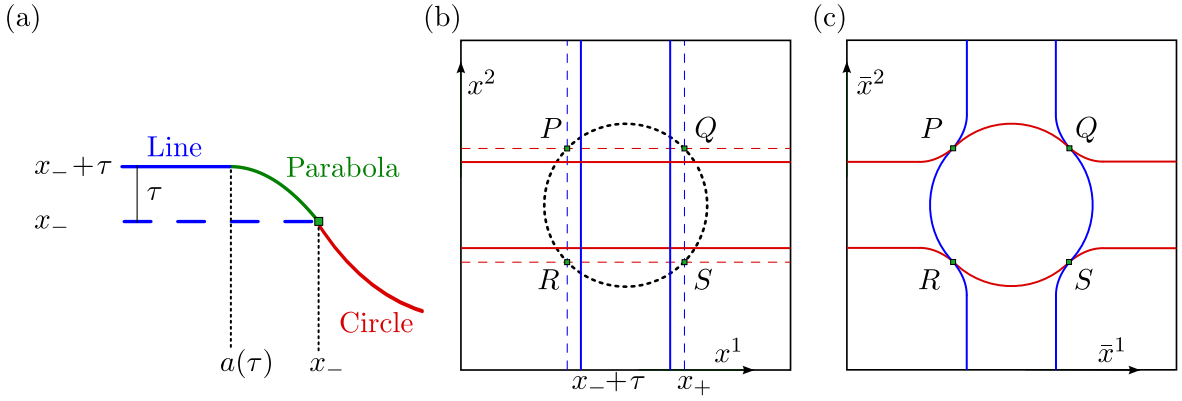

Figure 5.10: Illustration of the construction principle for the alternative smoothed mesh. Panel (a) depicts how the nondifferentiable transition from (Cartesian) characteristic line to the circle arc is smoothed by a (differentiable) parabola. In contrast to the smoothed mesh described above, the parabola and the circle arc meet at the point x_-. Thus, the entire surface of the cylinder is enclosed by characteristic lines. Straight line and parabola meet at a which also depends on τ. Panels (b) and (c) show how the characteristic coordinate lines (solid) passing through P, Q, R and S are mapped. The dashed lines in panel (b) are the characteristic lines of the smoothed mesh in Fig. 5.8.

The basic idea is that the parabola transition has its starting point at a point on the circle, compare Figs. 5.8(a) and 5.10(a). The free parameter used is again called τ—only this time it has a different meaning: it directly defines the new characteristic lines. In each direction, they are given by $x_- + \tau$ and $x_+ - \tau$, with $x_\pm = 0.5 \pm r/\sqrt{2}$. The points P, Q, R, S are identical to the ones in Fig. 5.8. As before, we have to obey continuity and differentiability conditions. The result is a parabola of the form

$$g\left(x^1, a, b, \tau\right) = b\,\left(x^1 - a\right)^2 + x_- + \tau, \tag{5.20}$$

with parameters

$$a(\tau) = \frac{2\tau\sqrt{r^2 - (x_- - 0.5)^2}}{x_- - 0.5} + x_-, \qquad b = -\frac{1}{4}\frac{(x_- - 0.5)^2}{\tau\,(r^2 - (x_- - 0.5)^2)}. \tag{5.21}$$

Thereby, we essentially constructed the characteristic lines—the entire mapping is obtained using the LT-function and the methodology described in Section 5.3.2. However, the effective

permittivity diverges due to the way we constructed the mesh: In P, Q, R, S the vertical and horizontal coordinate lines are parallel, see Fig. 5.10(c). As we argued in Section 5.3.1, this immediately leads to a diverging transformed permittivity.

The idea of discussing this alternative mesh is to show that a smoothed mesh is still able to enclose the entire surface. This means that smoothness (or differentiability) and an entirely enclosed surface do not form an irreconcilable conflict. On the other hand, we argued that this is not a way to get rid of the dilemma of the diverging effective permittivity. Therefore, we do not include performance calculations of this mesh in Section 5.4.

Next, we improve the smoothed meshes and illustrate how to construct fully two-dimensional differentiable meshes, i.e., meshes for which all partial derivatives exist and are continuous at all points throughout the unit cell.

5.3.4 Construction of differentiable meshes

In the case of smoothed meshes we performed the "parabola construction" only for the coordinate lines passing through the characteristic points. The coordinate lines in between were obtained by linear interpolation and it is this linear interpolation that eventually leads to discontinuous partial derivatives. Therefore, we can obtain fully differentiable meshes by applying the "parabola-construction" to *all* coordinate lines. We reuse the illustrative example of the previous section: a circle with radius r which is centered in a square unit cell $[0,1] \times [0,1]$. The intersection of parabola and straight line is given by a just like in Eq. (5.18a). Also, we use the same definition of $x_\pm$ and of $\bar{u} = x_- + \tau$. Again, τ is the only free parameter and determines to what extent the mesh is smoothed. In Fig. 5.11(a), we display how the unit cell is divided for the construction of the mapping. We restrict our discussion to the mapping in the zones ① to ⑥—the other regions may be treated in an analogous fashion or follow directly from symmetry considerations.

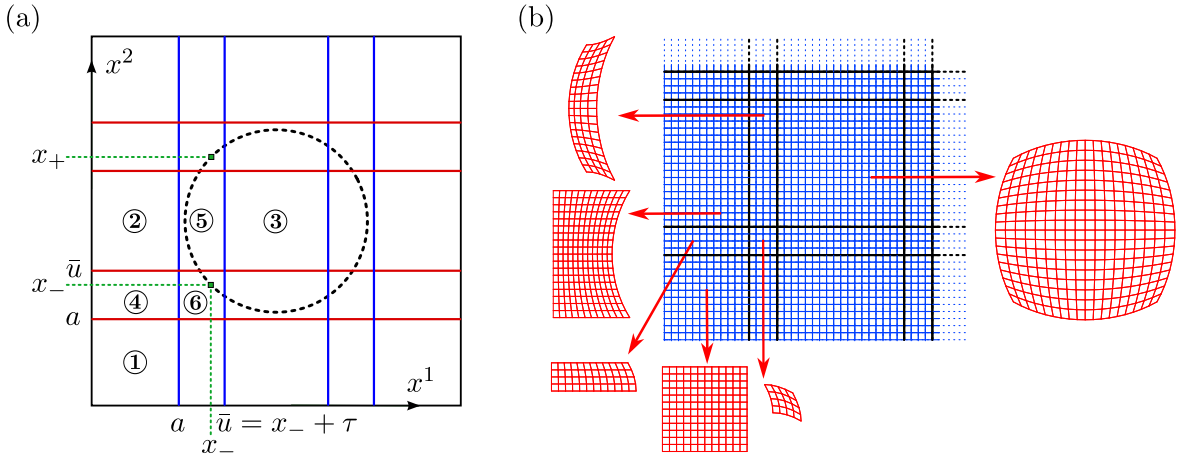

Figure 5.11: Illustration of the construction principle for differentiable meshes. Panel (a) shows the partitioning of the unit cell and panel (b) depicts the resulting differentiable mapping.

Zones ①, ②, ③: In these regions, we choose the mappings exactly as in the case of the nondifferentiable circle mesh (see Ref. [15] or Section 5.3.3); the mappings read

$$\bar{x}^1\Big(x^1,x^2\Big) = x^1, \qquad \bar{x}^2\Big(x^1,x^2\Big) = x^2, \qquad \Big(x^1,x^2\Big) \in ①, \tag{5.22}$$

$$\bar{x}^1\Big(x^1,x^2\Big) = \frac{x^1}{x_-}\left(0.5 - \sqrt{r^2-\left(x^2-0.5\right)^2}\right), \quad \bar{x}^2\Big(x^1,x^2\Big) = x^2, \qquad \Big(x^1,x^2\Big) \in ②, \tag{5.23}$$

$$\bar{x}^1\Big(x^1,x^2\Big) = \frac{2x^1-1}{x_+-x_-}\sqrt{r^2-\left(x^2-0.5\right)^2} + \frac{1}{2}, \; \bar{x}^2\Big(x^1,x^2\Big) = \bar{x}^1(x^2,x^1), \; \Big(x^1,x^2\Big) \in ③. \tag{5.24}$$

Zone ④: To construct the mapping in this zone we have to deal with transitions from straight lines (zone ①) to ellipse arcs (zone ②). The general form of the ellipse arcs is given by

$$r^2 = \Big(\bar{x}^1 - x_0^1\Big)^2\,\delta + \Big(\bar{x}^2 - x_0^2\Big)^2\,\gamma \tag{5.25}$$

with the parameters x_0^1, x_0^2, δ and γ. From this, we can infer the ellipse parameters in zone ② by comparing with the mapping in Eq. (5.23): $x_0^1 = \frac{1}{2}\,\frac{x^1}{x_-},\; x_0^2 = 0.5,\; \delta = \left(\frac{x_-}{x^1}\right)^2,\; \gamma = 1.$ We aim to connect the straight lines (i.e., the identity mapping) in zone ① with the ellipse arcs by a family of parabolas of the form

$$\bar{x}^1\Big(x^1,x^2\Big) = b\Big(x^1\Big)\Big(x^2-a\Big)^2 + x^1, \qquad \bar{x}^2\Big(x^1,x^2\Big) = x^2, \qquad \Big(x^1,x^2\Big) \in ④. \tag{5.26}$$

Note that even though a is still given by Eq. (5.18a), b is not a constant anymore as it has been in Eq. (5.18b)—thus $b(x^1)$ parametrizes the family of parabolas. Continuity and differentiability at $\bar{x}^2 = \bar{u}$ require that

$$b\Big(x^1\Big) = \frac{\frac{1}{4}\left(\bar{u}-x_0^2\right)^2}{\frac{\delta}{\gamma^2}\left(r^2-\gamma\left(\bar{u}-x_0^2\right)^2\right)\left(-\sqrt{\frac{1}{\delta}\left(r^2-\gamma\left(\bar{u}-x_0^2\right)^2\right)}+x_0^1-x^1\right)}. \tag{5.27}$$

Zone ⑤: To find suitable differentiable mappings in the zones ⑤ and ⑥ we will utilize an alternative approach: We formulate the requirements in terms of continuity and differentiability and then make an ansatz to find appropriate functions. We start by considering the boundary conditions for the $\bar{x}^1(x^1,x^2)$ component in zone ⑤ which follow directly from the transformations in the neighboring zones ② and ③. Continuity requires

$$\begin{aligned}
\bar{x}^1(a,x^2) &\overset{(5.23)}{=} \tfrac{a}{x_-}\left(0.5-\sqrt{r^2-\left(x^2-0.5\right)^2}\right),\\
\bar{x}^1(\bar{u},x^2) &\overset{(5.24)}{=} \tfrac{2\bar{u}-1}{x_+-x_-}\sqrt{r^2-\left(x^2-0.5\right)^2}+0.5,
\end{aligned} \tag{5.28}$$

whereas differentiability requires

$$\begin{aligned}
\left.\tfrac{\partial\bar{x}^1}{\partial x^1}\right|_{(a,x^2)} &\overset{(5.23)}{=} \tfrac{1}{x_-}\left(0.5-\sqrt{r^2-\left(x^2-0.5\right)^2}\right), \quad & \left.\tfrac{\partial\bar{x}^1}{\partial x^1}\right|_{(\bar{u},x^2)} &\overset{(5.24)}{=} \tfrac{2\sqrt{r^2-\left(x^2-0.5\right)^2}}{x_+-x_-},\\
\left.\tfrac{\partial\bar{x}^1}{\partial x^2}\right|_{(a,x^2)} &\overset{(5.23)}{=} \tfrac{a}{x_-}\tfrac{x^2-0.5}{\sqrt{r^2-\left(x^2-0.5\right)^2}}, & \left.\tfrac{\partial\bar{x}^1}{\partial x^2}\right|_{(\bar{u},x^2)} &\overset{(5.24)}{=} -\tfrac{2\bar{u}-1}{x_+-x_-}\tfrac{x^2-0.5}{\sqrt{r^2-\left(x^2-0.5\right)^2}}.
\end{aligned} \tag{5.29}$$

Next, we make an ansatz for the mapping inside zone ⑤ using a function f which is assumed to be differentiable but otherwise still unknown. The ansatz reads

$$\bar{x}^1\Big(x^1,x^2\Big) = \bar{x}^1\Big(a,x^2\Big)\,\frac{x^1-\bar{u}}{a-\bar{u}} + \bar{x}^1\Big(\bar{u},x^2\Big)\,\frac{x^1-a}{\bar{u}-a} + f\Big(x^1,x^2\Big)\Big(x^1-\bar{u}\Big)\Big(x^1-a\Big). \tag{5.30}$$

This ansatz fulfills the continuity requirements of Eq. (5.28) provided f does not exhibit a pole at $x^1 = a$ or $x^1 = \bar{u}$. Furthermore, the ansatz ensures that the derivative with respect to x^2 fulfills Eq. (5.29) provided $(\partial f/\partial x^2)$ does not exhibit poles at $x^1 = a$ or $x^1 = \bar{u}$. The remaining requirements refer to the derivative of Eq. (5.30) with respect to x^1 which reads

$$\begin{aligned}\frac{\partial \bar{x}^1}{\partial x^1}\Big(x^1, x^2\Big) &= \frac{\bar{x}^1(a, x^2)}{a - \bar{u}} + \frac{\bar{x}^1(\bar{u}, x^2)}{\bar{u} - a} + \frac{\partial f}{\partial x^1}\Big(x^1, x^2\Big)\Big(x^1 - \bar{u}\Big)\Big(x^1 - a\Big) \\ &\quad + f\Big(x^1, x^2\Big)\Big(x^1 - a\Big) + f\Big(x^1, x^2\Big)\Big(x^1 - \bar{u}\Big). \end{aligned} \tag{5.31}$$

Evaluating Eq. (5.31) at $\bar{u}$ and a and comparing with Eq. (5.29) results in

$$\begin{aligned} f(\bar{u}, x^2) &= \tfrac{1}{\bar{u}-a}\left(-\tfrac{\bar{x}^1(a,x^2)}{a-\bar{u}} - \tfrac{\bar{x}^1(\bar{u},x^2)}{\bar{u}-a} + \tfrac{\partial \bar{x}^1}{\partial x^1}\Big|_{(\bar{u},x^2)}\right), \\ f(a, x^2) &= \tfrac{1}{a-\bar{u}}\left(-\tfrac{\bar{x}^1(a,x^2)}{a-\bar{u}} - \tfrac{\bar{x}^1(\bar{u},x^2)}{\bar{u}-a} + \tfrac{\partial \bar{x}^1}{\partial x^1}\Big|_{(a,x^2)}\right). \end{aligned} \tag{5.32}$$

We would like to emphasize that every function f that fulfills Eq. (5.32) and does not have poles at $x^1 = a$ or $x^1 = \bar{u}$ is a suitable function so that the ansatz made in Eq. (5.30) fulfills all requirements in Eqs. (5.28) and (5.29). We choose a linear function which is given by

$$f\Big(x^1, x^2\Big) = \frac{f(\bar{u}, x^2) - f(a, x^2)}{\bar{u} - a}\, x^1 + f\Big(\bar{u}, x^2\Big) - \frac{f(\bar{u}, x^2) - f(a, x^2)}{\bar{u} - a}\bar{u}. \tag{5.33}$$

Thereby, we acquired a differentiable mapping $\bar{x}^1(x^1, x^2)$ in zone ⑤—namely Eq. (5.30) with f given by Eq. (5.33).

We obtain the remaining differentiable mapping $\bar{x}^2(x^1, x^2)$ in this zone by a "parabola-construction" as in the case of zone ④, this time, however, in the x^2-direction

$$\bar{x}^2\Big(x^1, x^2\Big) = b\Big(x^2\Big)\Big(x^1 - a\Big)^2 + x^2. \tag{5.34}$$

Then, $b(x^2)$ is identical to Eq. (5.27) except that δ is interchanged with γ and x_0^1 with x_0^2. The ellipse parameters taken from the $\bar{x}^2$ transformation in zone ③ (see Eq. (5.24)) are

$$x_0^1 = 0.5, \quad x_0^2 = 0.5, \quad \gamma = \left(\frac{x_+ - x_-}{2x^2 - 1}\right)^2, \quad \delta = 1. \tag{5.35}$$

Zone ⑥: In this zone we only need to find the mapping of one component because any point in this area obeys the symmetry relation

$$\Big(\bar{x}^1\Big(x^1, x^2\Big), \bar{x}^2\Big(x^1, x^2\Big)\Big) = \Big(\bar{x}^2\Big(x^2, x^1\Big), \bar{x}^1\Big(x^2, x^1\Big)\Big). \tag{5.36}$$

The boundary conditions for this zone are derived from the mappings in zones ④ and ⑤. In particular, we use symmetry to connect the $\bar{x}^2$ mapping in zone ⑤ (Eq. (5.34)) to the $\bar{x}^1$ mapping in the area $[\bar{u}, 1 - \bar{u}] \times [a, \bar{u}]$. With the abbreviations $\Delta := x_+ - x_-$, $\bar{v} := \bar{u} - 0.5$ and $s := \sqrt{r^2 - \bar{v}^2}$ the boundary conditions read

$$\begin{aligned} \bar{x}^1(a, x^2) &\overset{(5.26)}{=} b'(a)\left(x^2 - a\right)^2 + a, && \text{with} && b'(a) \overset{(5.27)}{=} \tfrac{1}{4}\tfrac{a}{x_-}\tfrac{\bar{v}^2}{(-s+0.5-x_-)\, s^2}, \\ \bar{x}^1(\bar{u}, x^2) &\overset{(5.34)}{=} b''(\bar{u})\left(x^2 - a\right)^2 + \bar{u}, && \text{with} && b''(\bar{u}) \overset{(5.35)}{=} \tfrac{1}{2}\tfrac{\bar{v}^3}{(s-0.5\Delta)\,\Delta\, s^2}, \end{aligned} \tag{5.37}$$

$$\begin{aligned} \tfrac{\partial \bar{x}^1}{\partial x^2}\Big|_{(a,x^2)} &\overset{(5.26)}{=} 2b'(a)\left(x^2 - a\right), & \tfrac{\partial \bar{x}^1}{\partial x^1}\Big|_{(a,x^2)} &\overset{(5.26)}{=} \tfrac{1}{4}\tfrac{\bar{v}^2\left(x^2-a\right)^2}{(-s+0.5-x_-)\; x_-\; s^2} + 1, \\ \tfrac{\partial \bar{x}^1}{\partial x^2}\Big|_{(\bar{u},x^2)} &\overset{(5.34)}{=} 2b''(\bar{u})\left(x^2 - a\right), & \tfrac{\partial \bar{x}^1}{\partial x^1}\Big|_{(\bar{u},x^2)} &\overset{(5.34)}{=} \tfrac{1}{2}\tfrac{\bar{v}^2\left(x^2-a\right)^2}{(s-0.5\Delta)\,\Delta\, s^2} + 1. \end{aligned} \tag{5.38}$$

In order to find the desired mapping, we take advantage of the generality of our formalism developed above—Eqs. (5.30) to (5.33) are all perfectly valid for the present considerations. Upon inserting Eqs. (5.37) and (5.38) in Eqs. (5.30) to (5.33), we finish the construction of a mesh that is differentiable everywhere in the unit cell. The mappings in the zones are depicted separately in Fig. 5.11(b). The parabola transitions are recognizable very well at the edges of the mapped zones ⑤ and ⑥. The only free parameter used for the construction of the differentiable mesh of the circle is the smoothing parameter τ. In Fig. 5.12 we depict the resulting meshes for two different values of τ.

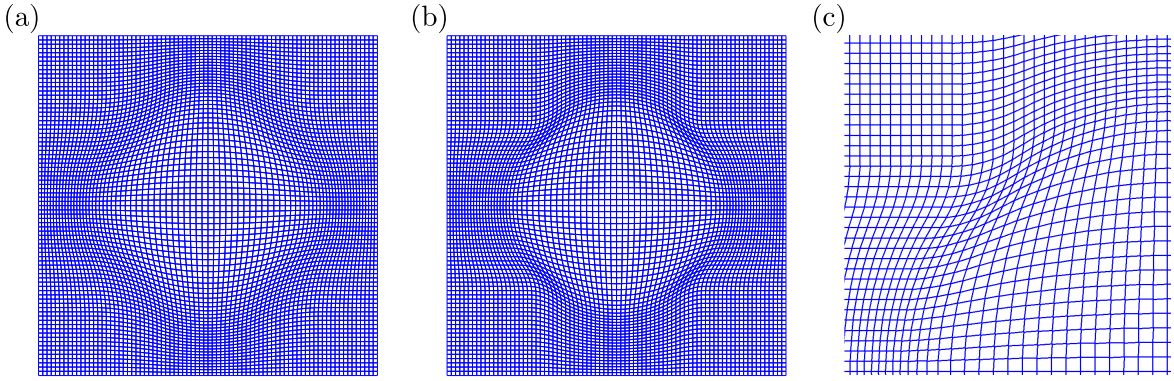

Figure 5.12: Differentiable meshes for a circular structure (radius $r = 0.3$) centered in a square unit cell. Panels (a) and (b) depict meshes with smoothing parameters $\tau = 0.07$ and $\tau = 0.035$, respectively. Panel (c) shows a close-up of the mesh in (b).

Finally, it is very instructive to compare the transformed permittivities for the different mesh types. In Fig. 5.13, we display the ε^{11}-component of the effective permittivity for the nondifferentiable (panel (a)), a smoothed (panel (b)), and a differentiable mesh (panel (c)) for a circular structure of radius 0.3 that is centered within a square $[0, 1] \times [0, 1]$ unit cell. The corresponding meshes are displayed in Figs. 5.2(b), 5.9(b), and 5.12(b), respectively. In all cases, only the area $[0.2, 0.8] \times [0.2, 0.8]$ is shown and the effective permittivity has been sampled with 1024×1024 points (the same sampling is used for the numerical simulations which we present in section 5.4). The circular structure is assumed to have a permittivity of $\varepsilon_{\text{circ}} = 2$ and $\varepsilon_{\text{bg}} = 1$ is used for the background. Figure 5.13(a) depicts the distribution we have already shown in Fig. 5.2(c).

First, we observe that the different mappings indeed transform the circular structure into a square-shaped object. For the above sampling, the effective permittivity values for the nondifferentiable mesh exceed 5000 in the corners of the square, a clear sign of the unavoidable singularities associated with applying a nondifferentiable mesh to a circular structure (see Section 5.3.1). In addition, the circle is exactly mapped to the square. For the smoothed as well as for the differentiable mesh the circle is mapped on a square with rounded corners and is, thus, not fully grid-aligned. However, the values of the effective permittivity are considerably lower in both cases. The difference between them is the slightly different behavior at the structure's boundaries. The effective permittivity of the differentiable mesh shows jumps only at the surface of the transformed structure. In contrast, the effective permittivity of the smoothed mesh features additional discontinuities since it is not differentiable everywhere (see Section 5.3.3). We find qualitatively similar behavior for all non-zero components of the effective permittivity tensor.

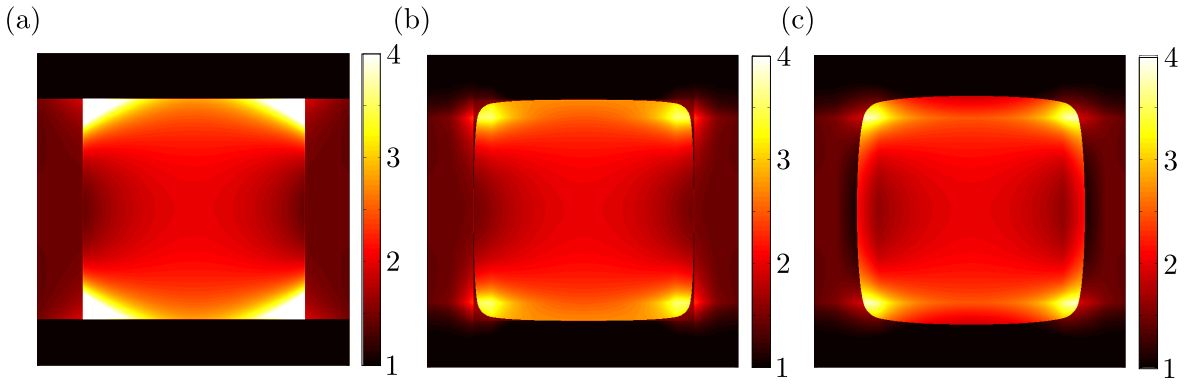

Figure 5.13: ε^{11}-component of the effective permittivity for different meshes for a circular structure (radius $r = 0.3$) that is centered in a square unit cell. Panels (a), (b), and (c) show the transformed permittivity for the nondifferentiable, the smoothed, and the differentiable meshes of Figs. 5.2(b), 5.9(b), and 5.12(b), respectively. For a sampling with 1024×1024 points, the values at the corners of the rectangle for the nondifferentiable mesh exceed 5000. However, we have saturated the color scale at 4 in order to be able to display more features. The smoothed and differentiable meshes have been constructed with a smoothing parameter $\tau = 0.035$. All plots show the sector $[0.2, 0.8] \times [0.2, 0.8]$ of the $[0, 1] \times [0, 1]$ unit cell.

Based on the above observations, it is an interesting question to ask which of the meshes will exhibit the best convergence characteristics for FMM-computations. The strictly grid-aligned effective permittivity for the nondifferentiable meshes is ideally suited for the Fourier factorization rules but its rather high values are clearly detrimental. The situation is reversed for the smoothed and the differentiable mesh.

However, before we address this question, we first complete the discussion of the mesh construction in the following sections, where we provide guidelines for the realization of periodic meshes for low-symmetry motifs in the unit cell (Section 5.3.5), the construction of meshes for nonrectangular lattices (Section 5.3.6), and the implementation of adaptive spatial resolution via coordinate line compression (Section 5.3.7).

In order to prepare for the latter, we note in the case of the nondifferentiable and the smoothed mesh that the coordinate line which is mapped to the circle's surface is given by x_- (see Fig. 5.8). In order to find the corresponding coordinate line α for the differentiable mesh, we numerically compute the point that fulfills

$$0.5 - r = \bar{x}^1(\alpha, 0.5), \qquad (\alpha, 0.5) \in ⑤. \tag{5.39}$$

5.3.5 Enforcing Periodicity

The meshes that we have constructed in the previous sections exhibit a mandatory requirement for being used with FMM computations: They are periodic, i.e., every coordinate line enters and leaves the unit cell at opposing unit cell edges. Apparently, certain meshes that are generated by our formalism described above do not exhibit this property (see, e.g., Fig. 5.14). For instance, in order to construct a mesh for a square array of ellipses, the natural choice

of characteristic points are those where the major and minor axes pierce the ellipse's surface. However, if the ellipse is rotated relative to the square lattice, our formalism leads to nonperiodic meshes.

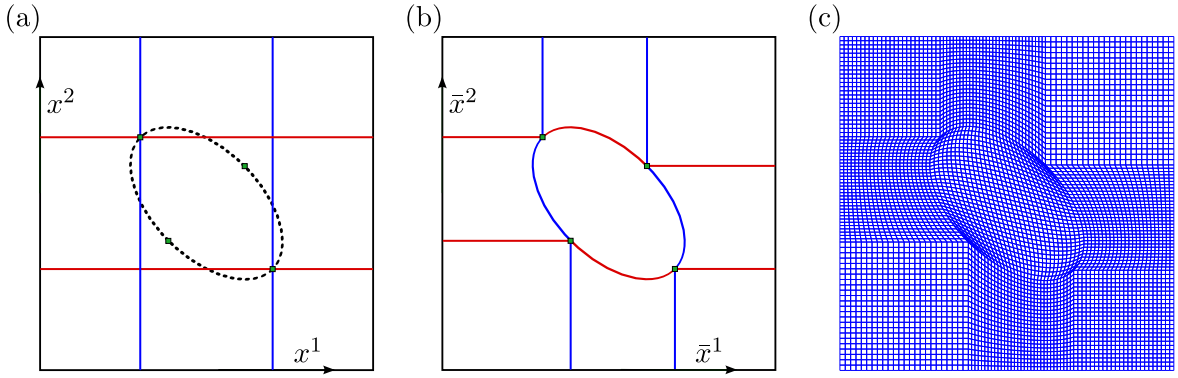

Figure 5.14: Construction points and mesh for an elliptical structure that is not aligned with the axes of the square array associated with the unit cell. This example further illustrates how our construction principle may lead to aperiodic meshes.

There are three ways to restore periodicity. Firstly, one could choose a different set of characteristic points that does lead to periodic meshes. Secondly, one can change the way the characteristic coordinate lines are mapped. We depict this approach in Figs. 5.15(a) and 5.15(b). Here, the characteristic coordinate lines were modified by additional straight line segments (dashed) so that the coordinate lines leave the unit cell at the same point at which they entered at the opposite face of the unit cell. The dashed part does not have to be composed of straight lines—other functions such as higher order polynomials are conceivable as well. Thirdly, one can use a *mirror structure*. We illustrate this approach in Fig. 5.15(c). Here, a mesh for the cross section of a trapezoidal rib waveguide has been created. The periodicity is assured by an additional structure in the unit cell which features similar geometrical properties as the structure under investigation and, thus, periodicity is restored. As this mirror structure has the same permittivity as the background medium it is physically nonexistent and the numerical artifacts created by the distorted mesh are negligible.

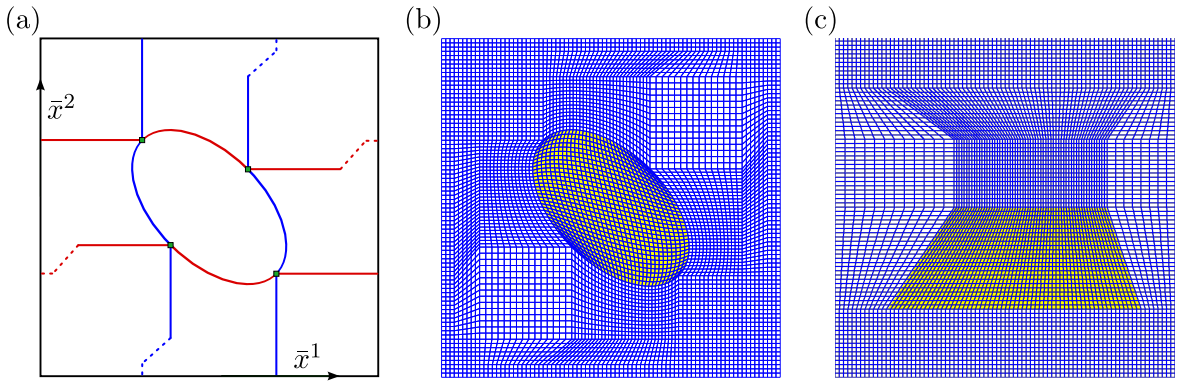

Figure 5.15: Illustration of different approaches for enforcing periodicity of meshes. Panels (a) and (b) depict the method of adding linear transitions to the outer edge of the unit cell. Panel (c) illustrates the method of the mirror structure. Color has been added to mark the actual structure.

In order to demonstrate that neither the mirror-structure approach nor the linear transitions

to the unit cell edges lead to discernible errors, we investigate the rib waveguide sketched in Fig. 5.16(a). To obtain a converged result we used 2601 Fourier coefficients with a real space discretization of 1024×1024 points. The unit cell is $4\,\mu$m $\times 4\,\mu$m and the symmetric trapezoid has a top length of 240 nm and a bottom length of 960 nm. Its height is 360 nm. This trapezoid consists of silicon with a dielectric constant $\varepsilon_s = 12.1$ while the background medium is air with $\varepsilon_{\mathrm{bg}} = 1$. The incoming wavelength was chosen to be the telecom wavelength at 1550 nm.

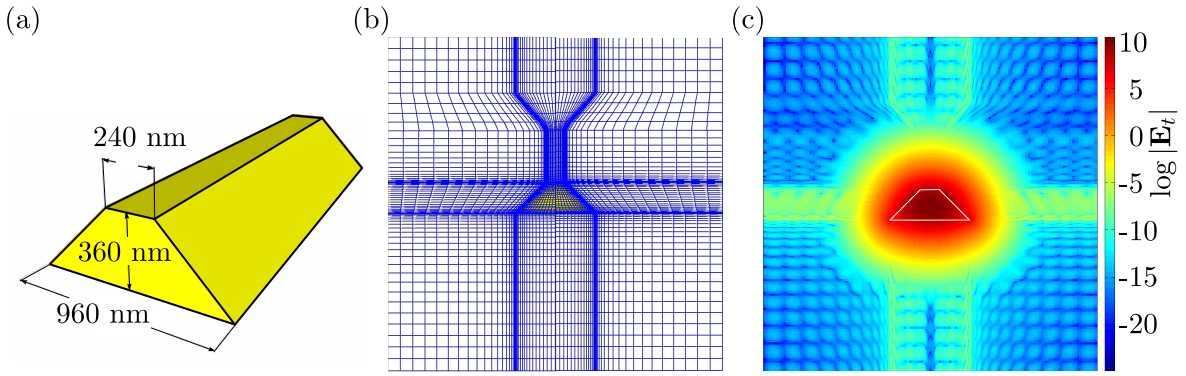

Figure 5.16: Analysis of a square array of silicon waveguides with trapezoidal cross section using the mirror-structure approach for periodic mesh construction. Panel (a) depicts a schematic of the system. Panels (b) and (c) show the periodic mesh for the trapezoidal structure and the absolute value of the transverse electric field distribution of the fundamental mode on a logarithmic scale, respectively. There are no discernible detrimental effects due to the mirror structure that is used to ensure periodicity of the mesh. The yellow color in panel (b) and the white trapezoid in panel (c) have been added to guide the eye.

Figure 5.16(c) shows the absolute value of the transverse electric field of the rib waveguide's fundamental mode[2]. Since the permittivity is transformed according to Eq. (3.2a), any coordinate line other than the identity will result in a distortion of the effective permittivity. Yet, Fig. 5.16(c) shows that the values of the numerical artifacts in the region of the mirror structure are several orders of magnitude lower than the values of the physical fields at the trapezoid.

5.3.6 Nonrectangular unit cells

So far, we have focused on rectangular unit cells. Apparently, for many systems more freedom in the unit cell choice is highly desirable. In fact, treating nonrectangular unit cells in the framework of FMM without adaptive meshing is well known [54]. In this section, we briefly discuss how adaptive meshing for a nonrectangular unit cell can be realized and present an array of circular rods in a hexagonal lattice as an example.

The basic idea is to map the hexagonal unit cell to a rectangular one (including the structure!), perform the mesh generation as discussed in the previous sections and map the rectangular unit cell (including the mesh) back to the hexagonal unit cell. A mapping between

[2] At this point I thank Benjamin Lutz for applying the trapezoidal mesh to this system and for providing the field plot of this waveguide's fundamental mode.

a nonrectangular unit cell with lattice angle α and a rectangular unit cell is given by [54]

$$\begin{aligned} x_\alpha &= x_{\text{rec}} + y_{\text{rec}} \sin\alpha \quad &\longleftrightarrow \quad x_{\text{rec}} &= x_\alpha - y_\alpha \tfrac{\sin\alpha}{\cos\alpha}, \\ y_\alpha &= y_{\text{rec}} \cos\alpha \quad &\longleftrightarrow \quad y_{\text{rec}} &= y_\alpha \tfrac{1}{\cos\alpha}. \end{aligned} \tag{5.40}$$

Here, the coordinates x_α, y_α, and x_{rec}, y_{rec} refer to the coordinates in ordinary (Cartesian) and transformed space, respectively. We illustrate this in Figs. 5.17(a) and 5.17(b), where, in addition, we also depict a circle which we would like to mesh. Upon mapping the nonrectangular unit cell to a rectangular one, the circle that is centered in the unit cell turns into an ellipse. We can mesh this ellipse by means of any of the methods discussed in Sections 5.3.2-5.3.4 (where applicable together with the methods to recover periodic meshes introduced in Section 5.3.5). Mapping back to ordinary (Cartesian) space then delivers the final mesh as displayed in Fig. 5.17(c). Actually, we have obtained this mesh by first compressing the coordinate lines (see Section 5.3.7) of the ellipse mesh displayed in Fig. 5.15(b) and mapping back this mesh to ordinary (Cartesian) space.

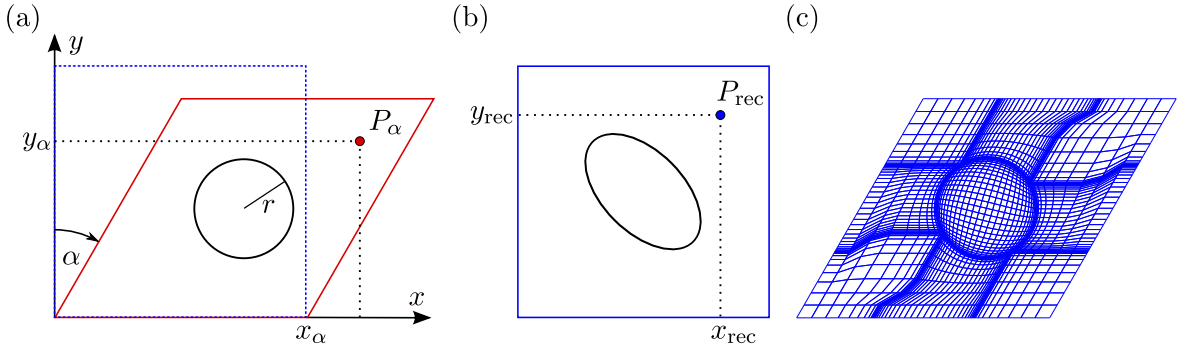

Figure 5.17: Illustration of the meshing in nonrectangular unit cells. Panel (a) depicts the structure in ordinary (Cartesian) space—a circular rod in a hexagonal lattice. Panel (b) shows the transformed structure when the nonrectangular unit cell is mapped to the rectangular unit cell—the circle turns into an ellipse. Panel (c) shows the mesh in the original unit cell that is obtained by meshing the ellipse and mapping this mesh back into ordinary (Cartesian) space. The parameters are $r = 0.2$, $\alpha = 30°$ and a $[0,1] \times [0,1]$ unit cell.

It is important to realize that the nonrectangular unit cell given by Eq. (5.40) is still described in a Cartesian coordinate system, i.e., we do not switch to an oblique-angled coordinate system. Hence, the equation of a circle remains valid and we can perform the mapping to the rectangular unit cell according to

$$\text{Circle}_\alpha = \left\{ (x,y) : \left(x - \frac{1}{2}(1+\sin\alpha)\right)^2 + \left(y - \frac{1}{2}\cos\alpha\right)^2 = r^2 \right\}, \tag{5.41}$$

$$\begin{aligned} \text{Circle}_{\text{rec}} &\overset{(5.40)}{=} \left\{ \left(x - y\frac{\sin\alpha}{\cos\alpha}, y\frac{1}{\cos\alpha}\right) : \left(x - \frac{1}{2}(1+\sin\alpha)\right)^2 + \left(y - \frac{1}{2}\cos\alpha\right)^2 = r^2 \right\}, \\ &= \left\{ (x,y) : \left(x + y\sin\alpha - \frac{1}{2}(1+\sin\alpha)\right)^2 + \left(y\cos\alpha - \frac{1}{2}\cos\alpha\right)^2 = r^2 \right\}. \end{aligned} \tag{5.42}$$

In order to perform the mesh generation analytically, we have to extract the ellipse parameters from Eq. (5.42). An ellipse with center (x_0, y_0) that is rotated by an angle ϕ with semi-axes c and d is described by

$$\begin{pmatrix} x - x_0 & y - y_0 \end{pmatrix} \begin{pmatrix} \cos\phi & -\sin\phi \\ \sin\phi & \cos\phi \end{pmatrix} \begin{pmatrix} c^{-2} & 0 \\ 0 & d^{-2} \end{pmatrix} \begin{pmatrix} \cos\phi & \sin\phi \\ -\sin\phi & \cos\phi \end{pmatrix} \begin{pmatrix} x - x_0 \\ y - y_0 \end{pmatrix} = 1. \tag{5.43}$$

Comparing Eq. (5.42) with Eq. (5.43) yields

$$c = r\ (1-\sin\alpha)^{-1/2}, \quad d = r\ (1+\sin\alpha)^{-1/2}, \quad \phi = -45^\circ, \quad (x_0, y_0) = (0.5, 0.5). \tag{5.44}$$

By symmetry, another solution which yields the same ellipse is $\phi = 45^\circ$ and c and d interchanged. The resulting ellipse is shown in Fig. 5.17(b). We have obtained the resulting mesh displayed in Fig. 5.17(c) using the mapping in Eq. (5.40) with $\alpha = 30^\circ$ (hexagonal lattice).

This procedure is not limited to unit cells with straight edges. In fact, unit cells of almost arbitrary shape can be handled this way—as long as the unit cell can be described by a mapping of the form of Eq. (5.40) . If such a mapping is known, we proceed as explained above: the curvilinear unit cell and the structure inside are mapped to a Cartesian unit cell. Then, we construct a mesh for the mapped structure. By mapping this mesh back we obtain an adaptive mesh for the structure in the curvilinear unit cell.

5.3.7 Compression of coordinate lines - adaptive spatial resolution

As stated several times above, it is often very desirable to increase the density of coordinate lines within a structure or at its surface in order to realize adaptive spatial resolution (ASR). We have used such coordinate compressions for constructing the meshes depicted in Fig. 5.6(b), Fig. 5.16(b), and Fig. 5.17(c). In this section, we provide the required details. In essence, ASR and adaptive coordinates (AC) are performed sequentially—first, the coordinate lines are compressed and then the mapping for the AC is applied. Technically, ASR is just another coordinate transformation. A good proposal for a one-dimensional compression function can be found in Ref. [51]. In general, we have to apply two-dimensional compressions which we construct by two successive one-dimensional compressions after slightly modifying the compression functions of Ref. [51]. In Fig. 5.18(a), we display an illustrative example of such a one-dimensional compression.

The transformation function of Ref. [51] is

$$\bar{x}(x) = \alpha + \beta x + \frac{\gamma}{2\pi}\ \sin\!\left(2\pi\ \frac{x - x_{l-1}}{x_l - x_{l-1}}\right), \qquad x \in [x_{l-1}, x_l], \quad l = 2, ..., n \tag{5.45}$$

with

$$\alpha = \frac{x_l \bar{x}_{l-1} - x_{l-1}\bar{x}_l}{x_l - x_{l-1}}, \quad \beta = \frac{\bar{x}_l - \bar{x}_{l-1}}{x_l - x_{l-1}}, \quad \gamma = (x_l - x_{l-1})\,G - (\bar{x}_l - \bar{x}_{l-1}), \tag{5.46}$$

where $\{x_l : \ \ l = 1, ..., n\}$ and $\{\bar{x}_l : \ \ l = 1, ..., n\}$ denote two sets of points. By design, this means that $\bar{x}(x_l) = \bar{x}_l$ for $l = 1, ..., n$. Furthermore, G denotes the slope of the function at all positions x_l. The compressed coordinates are described by $\bar{x}(x)$—the transformation is a linear function superimposed with a sine. In the vicinity of the points $\bar{x}_l$ the coordinate line density is increased—for instance, these points could represent material interfaces along the x-coordinate line. The interval $[x_{l-1}, x_l]$ is mapped onto the interval $[\bar{x}_{l-1}, \bar{x}_l]$. In order to maintain periodicity with period L, one chooses $\bar{x}_1 = 0$ and $\bar{x}_n = L$. This means that the coordinate lines are compressed at the unit cell edges. For the structures considered in Ref. [51] this is intended. We, on the other hand, would like to place the structures in the center of the unit cell. This amounts to shifting the compression function and we show how to accomplish this with two material interfaces. This is generalized straightforward to more interfaces.

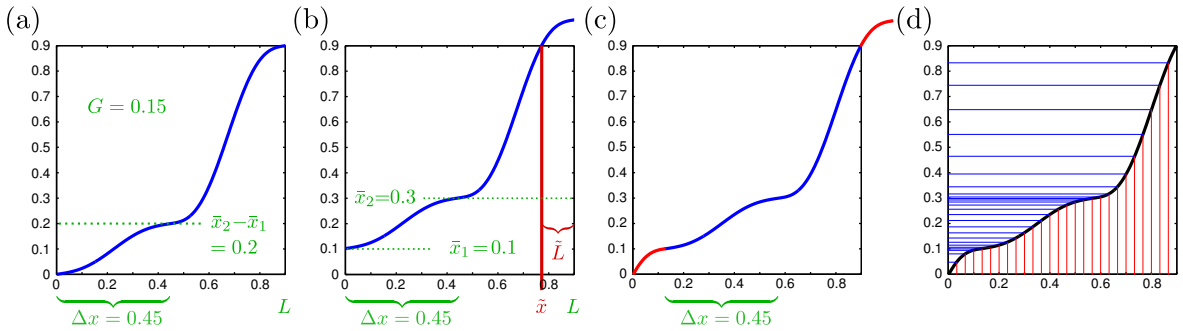

Figure 5.18: Illustration of how to shift the compression function from Ref. [51]. In all panels x is plotted on the horizontal axis and $\bar{x}$ on the vertical axis. Panel (a) depicts the original compression function. Panel (b) shows how the function is shifted to larger values. The point of intersection where the transformed coordinate leaves the unit cell is denoted by $\tilde{x}$. In panel (c) the compression function is shifted by exactly this amount to the right. The piece that is outside the unit cell in panel (c) is attached to the left side due to periodicity. Panel (d) shows how the equidistant coordinate lines (vertical) are mapped onto compressed coordinate lines (horizontal).

We start with two parallel material interfaces in the unit cell located at two given coordinates $\bar{x}_1$ and $\bar{x}_2$. Furthermore, we assume that the length of the interval that is mapped to $[\bar{x}_1, \bar{x}_2]$ is given—it is referred to as Δx. Then, we perform the mapping Eq. (5.45) as if the first material interface lied at 0.

$$x \in [0, \Delta x]: \qquad \bar{x}(x) = \frac{\bar{x}_2 - \bar{x}_1}{\Delta x}\, x + \frac{G\,\Delta x - (\bar{x}_2 - \bar{x}_1)}{2\pi}\, \sin\!\left(2\pi \frac{x}{\Delta x}\right), \tag{5.47a}$$

$$x \in [\Delta x, L]: \qquad \bar{x}(x) = \tilde{\alpha} + \tilde{\beta} x + \tilde{\gamma}\, \sin\!\left(2\pi \frac{x - \Delta x}{L - \Delta x}\right). \tag{5.47b}$$

Here, we introduced the abbreviations

$$\tilde{\alpha} = \frac{L\,(\bar{x}_2 - \bar{x}_1) - \Delta x\, L}{L - \Delta x}, \quad \tilde{\beta} = \frac{L - (\bar{x}_2 - \bar{x}_1)}{L - \Delta x}, \quad \tilde{\gamma} = \frac{G\,(L - \Delta x) - (L - (\bar{x}_2 - \bar{x}_1))}{2\pi}. \tag{5.48}$$

The result is depicted in Fig. 5.18(a)—we now have a compression at two interfaces with the correct spacing between them, albeit at the wrong locations. In order to achieve the compression in the interior in the unit cell, we first shift the function by $\bar{x}_1$ upwards, see Fig. 5.18(b). The point where the compression function intersects with the unit cell edge, denoted $\tilde{x}$, is

$$L = \tilde{\alpha} + \tilde{\beta}\tilde{x} + \tilde{\gamma}\, \sin\!\left(2\pi \frac{\tilde{x} - \Delta x}{L - \Delta x}\right) + \bar{x}_1 \tag{5.49}$$

Unfortunately, Eq. (5.49) is a transcendental equation and, therefore, we have to find the point $\tilde{x}$ numerically. Next, we shift the function to the right by $\tilde{L} = L - \tilde{x}$, see Fig. 5.18(c). The part that is still outside the unit cell (marked in red) is attached to the left side of the unit cell—this makes sense due to periodic boundaries in the FMM. Finally, in Fig. 5.18(d) we depict how the equidistant, vertical coordinate lines are now mapped to the compressed horizontal lines. The compression function for two material interface points $\bar{x}_1$ and $\bar{x}_2$ in the

interior of the unit cell then reads

$$x \in [0, \tilde{L}]: \quad \bar{x}(x) = \tilde{\alpha} + \tilde{\beta}\,(x + \tilde{x}) + \tilde{\gamma}\ \sin\left(2\pi \frac{x + \tilde{x} - \Delta x}{L - \Delta x}\right) + \bar{x}_1 - L\,, \tag{5.50}$$

$$x \in (\tilde{L}, \tilde{L} + \Delta x): \quad \bar{x}(x) = \frac{\bar{x}_2 - \bar{x}_1}{\Delta x}\left(x - \tilde{L}\right) + \frac{G\,\Delta x - (\bar{x}_2 - \bar{x}_1)}{2\pi}\ \sin\left(2\pi \frac{x - \tilde{L}}{\Delta x}\right) + \bar{x}_1, \tag{5.51}$$

$$x \in [\tilde{L} + \Delta x, L]: \quad \bar{x}(x) = \tilde{\alpha} + \tilde{\beta}\left(x - \tilde{L}\right) + \tilde{\gamma}\ \sin\left(2\pi \frac{x - \tilde{L} - \Delta x}{L - \Delta x}\right) + \bar{x}_1. \tag{5.52}$$

It needs to be stressed that one needs to start with the separation Δx of the interfaces instead of starting with their exact locations x_1 and x_2 (as has been the case in Eq. (5.45)). This is due to the fact that these locations are determined by the shift of the entire function and cannot be specified beforehand.

In Figs. 5.19(a) and 5.19(b), we display two examples of compression functions. They are plotted together as a two dimensional mesh in Fig. 5.19(c) where the compression in Fig. 5.19(a) was applied in the horizontal direction and the compression in Fig. 5.19(b) in the vertical direction. When choosing the compression parameters it is important to make sure that $\bar{x}$ is monotonically increasing. If a constant coordinate line density is desired, the transformations above offer a simple way to do so. For two compression points, G is chosen to be $(\bar{x}_2 - \bar{x}_1)/\Delta x$ which leads to a vanishing prefactor of the sine in Eq. (5.45). This is how we have obtained the compression in Fig. 5.19(b).

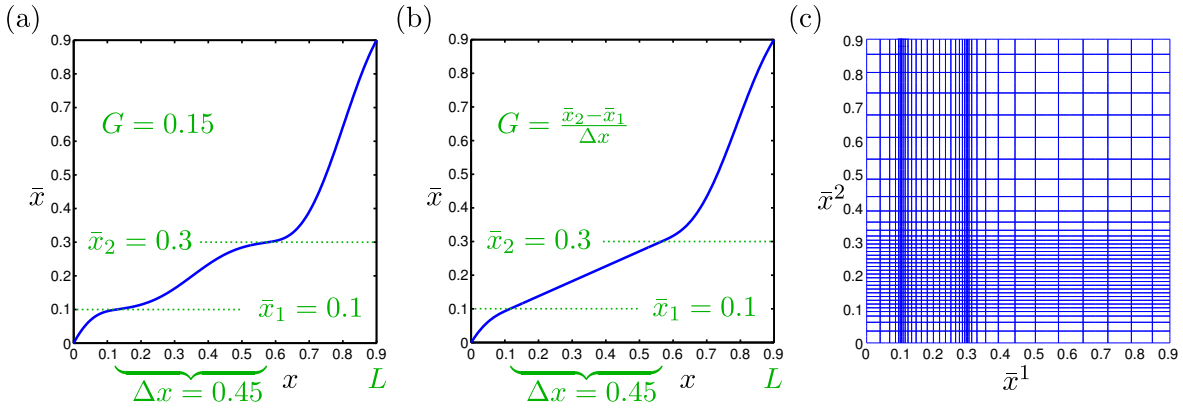

Figure 5.19: Illustration how two one-dimensional compression functions are combined to a two-dimensional compressed mesh. The compression in (a) is applied in horizontal direction and the compression depicted in (b) (with a constant density between $\bar{x}_1$ and $\bar{x}_2$) is applied in the vertical direction. Panel (c) depicts the resulting mesh.

It is an interesting aspect how ASR alone transforms the permittivity. To illustrate this, Fig. 5.20 displays components of the transformed permittivity when the mesh in Fig. 5.19 is applied to empty space, i.e., the permittivity in the untransformed space is $\varepsilon_{bg} = 1$ in the entire unit cell. The off-diagonal elements of the effective permittivity are zero. The shape of the effective permittivity is rather counter-intuitive. The basic property is: the more the mesh is varied away from a Cartesian mesh, i.e., the more it is compressed or the more the coordinate lines are bent, the more the effective permittivity is going to be changed.

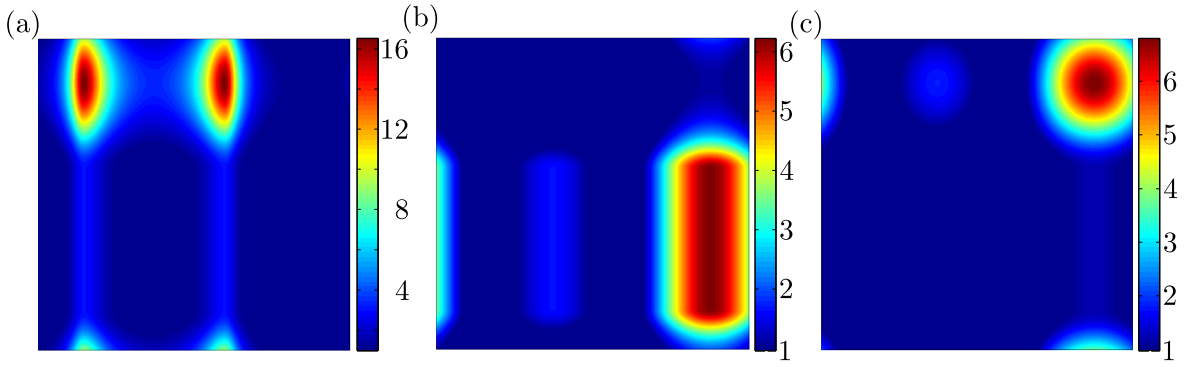

Figure 5.20: Transformed permittivity for the mesh in Fig. 5.19(c) in empty space with $\varepsilon_{bg} = 1$ and 1024×1024 points. Panels (a), (b) and (c) depict ε^{11}, ε^{22} and ε^{33}, respectively. The more the mesh is distorted from the Cartesian mesh, the more the transformed permittivity changes, cf. Fig. 5.19(c).

This completes our illustration of adaptive coordinates with adaptive spatial resolution: In order to obtain meshes as those depicted in Fig. 5.6(b), we first map a Cartesian grid to a grid that is compressed in certain regions by way of Eqs. (5.50) - (5.52). We then use this locally compressed grid as input for the adaptive coordinate mapping which deforms the grid in the desired way (nondifferentiable, smoothed, or differentiable), e.g., as in Eqs. (5.15) and (5.16).

The smoothed meshes remove the singularities in the effective permittivity, Eq. (3.2a), of the nondifferentiable meshes and only certain discontinuities in the partial derivatives remain. These discontinuities, too, can be removed by using differentiable meshes. Obviously, this removal of singularities and discontinuities will be conductive for the convergence of FMM. However, another important aspect of the smoothed and the differentiable meshes is that—in contrast to the nondifferentiable meshes—the structure's surface is no longer grid-aligned in the transformed space described by Eq. (3.2a) (see Fig. 5.13). Yet, the correct representation of the structure and the success of the Fourier factorization rules critically depends on grid-alignment.

The answer to the question which aspect is more important under which circumstances is the subject of the subsequent section.

5.4 Suitable parameter choice and convergence characteristics

More generally, in this section we deal with the important question which type of mesh and which mesh parameters are suitable for a given structure. The number of parameters for the mesh generation is very large—for each given frequency and structure, we can vary the compression of the mesh (parameters G and Δx), we can use different types of meshes (Cartesian, nondifferentiable, smoothed, and differentiable) some of which have a smoothing parameter τ, and we have to choose how many points are used for the real space discretization. As it is impossible to display every combination of those parameters, we aim at presenting the overall tendencies along with corresponding rules-of-thumb that we found in our extensive parameter scans.

Firstly, we examine dielectric structures. We start with a study on how and why different parameters change the convergence results of the propagation constants of low-lying eigenmodes. This will result in guidelines how to find suitable parameters. Secondly, we repeat this exercise for metallic structures and their convergence characteristics.

5.4.1 Dielectric structures

In order to investigate the convergence behavior of the FMM with different meshes for dielectric structures, we choose a fiber with a cylindrical cross section as a test system. This choice is motivated by the availability of analytical solutions for the guided eigenmodes of a single cylindrical waveguide[3], see Ref. [55]. For such modes, the inherent periodicity of the FMM computations is of no relevance once the unit cell is sufficiently large, i.e., we are then performing a supercell computation. Clearly, this also means that we should exercise care for modes that are close to the cut-off as they might be fairly extended. In our subsequent computations this has been carefully checked.

Specifically, we consider a fiber of radius of $r = 800$ nm that is centered within a square unit cell and the index of which will be varied. The lattice constant is $d = 4000$ nm with a background material of $\varepsilon_{bg} = 1$. The number of plane waves will be varied, but they will always come from within a circle in reciprocal space centered around the origin. We analyze this system for a wavelength of $\lambda = 800$ nm.

As a measure for the mesh quality, we compute the maximum relative error of the effective refractive index of the first ten guided eigenmodes for a given number of plane waves, i.e.,

$$\text{error} = \max\left\{ \frac{\left|n_{\text{eff,analyt,1st mode}} - n_{\text{eff,num,1st mode}}\right|}{n_{\text{eff,analyt,1st mode}}}, \quad \ldots \quad , \frac{\left|n_{\text{eff,analyt,10th mode}} - n_{\text{eff,num,10th mode}}\right|}{n_{\text{eff,analyt,10th mode}}} \right\},$$

where the effective refractive index of an eigenmode with propagation constant γ is given by $n_{\text{eff}} = \lambda\gamma/(2\pi)$. First, we compare the different types of meshes for a small dielectric contrast. We initially refrain from compressing the coordinate lines in order to separate ASR and AC effects. In Fig. 5.21(a), we depict the convergence characteristics for a fiber with dielectric constant $\varepsilon_{\text{fib}} = 2$. The smoothed and especially the differentiable mesh performs better than the Cartesian or the nondifferentiable mesh. From now on, we will concentrate on the comparison of nondifferentiable and differentiable meshes since the smoothed meshes show a worse quality than the differentiable meshes when a compression is used.

[3] I thank Thomas Zebrowski for kindly providing his implementation of the analytical eigenmode solutions.

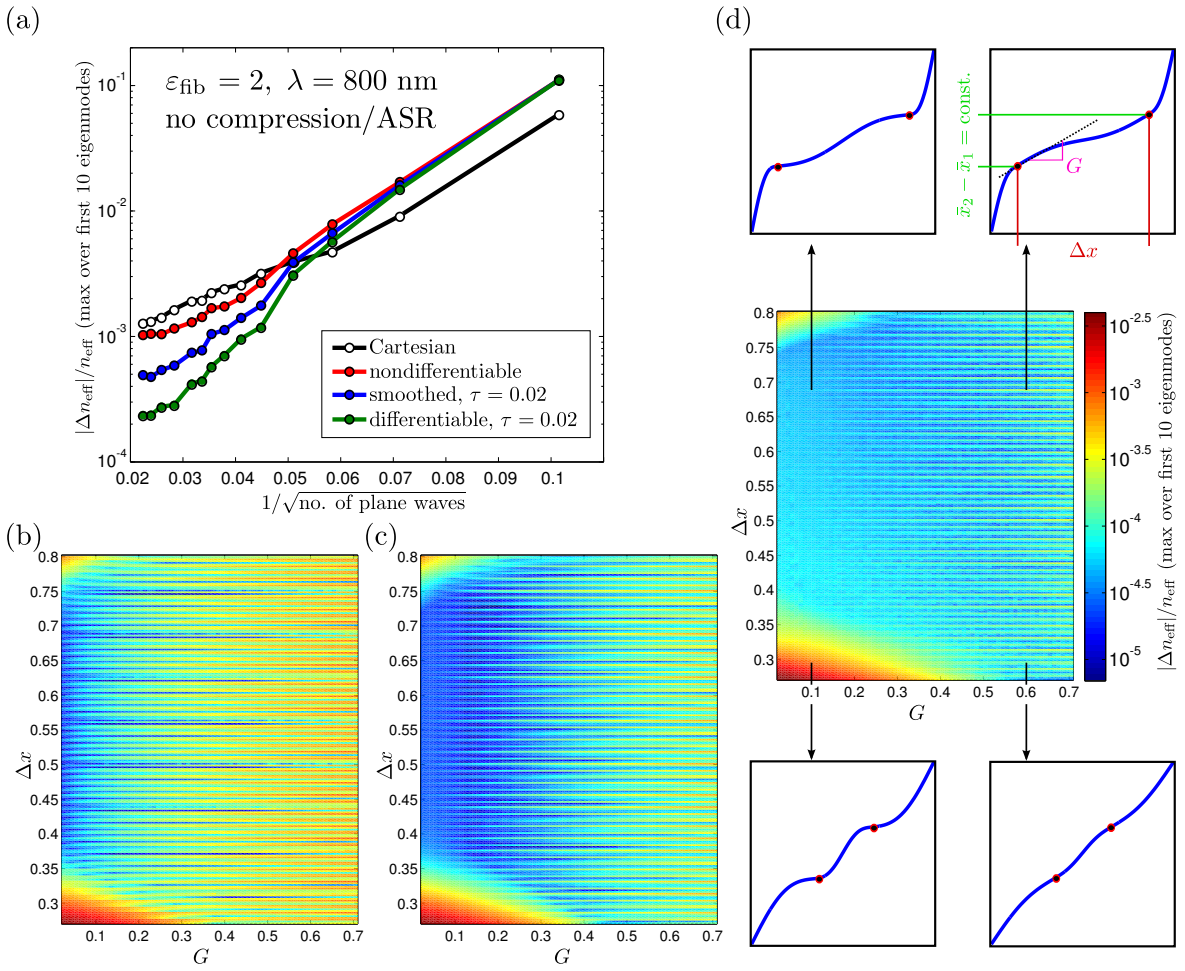

Figure 5.21: Convergence characteristics of different meshes for computing the effective index of refraction of guided modes in a low-index fiber. Panel (a) displays the convergence characteristics of Cartesian, nondifferentiable, smoothed, and differentiable meshes without coordinate line compression. Panels (b) to (d) depict the corresponding dependence of the relative error (color-coded) on the compression parameters G and Δx for a fixed number of 997 plane waves. The same compression function is applied in $\bar{x}^1$- and $\bar{x}^2$-direction. All computations have been performed on a grid with 1024×1024 sampling points in transformed space. Panel (b) displays the results for the nondifferentiable mesh. Panels (c) and (d) depict results for the differentiable mesh with $\tau = 0.002$ and $\tau = 0.015$, respectively. The sketches in panel (d) depict compression functions for four specific pairs of G and Δx. The color bar of panel (d) also applies to panels (b) and (c).

As the cylindrical fiber is centered in the square unit cell we can apply the same compression function in $\bar{x}^1$- and $\bar{x}^2$-direction. The material surface, i.e., the compression points are $\bar{x}_1 = x_-$ and $\bar{x}_2 = x_+$ for the nondifferentiable mesh and $\bar{x}^1 = \alpha$ and $\bar{x}^2 = 1-\alpha$ for the differentiable mesh (see section 5.3.3 and 5.3.4, respectively). In Figs. 5.21(b) to 5.21(d) we display the dependence of the error on the compression parameters G and Δx for the nondifferentiable mesh ($\tau = 0$, panel (b)) and the differentiable mesh with parameters $\tau = 0.002$ (panel (c)) and $\tau = 0.015$ (panel (d)). Each computation has been performed with 997 plane waves in

conjunction with a discretization in transformed space of 1024×1024 points. In these graphs the parameter G has been stepped in 0.01 intervals and Δx in 0.0025 intervals. We have used the same parameter stepping for G and Δx in Figs. 5.21 to 5.24. For illustrative purposes, we display in Fig. 5.21(d) selected compression functions for vastly different parameter values G and Δx.

From Fig. 5.21(b), we infer that the nondifferentiable mesh performs well for small values of G. This is intuitive since a small value of G means that the coordinate line density at the surface of the structure is increased. However, we obtain the best results for this mesh for larger values of G at specific values of Δx. For most values of these optimal combinations G and Δx, a small change in Δx quickly compromises this optimal performance and results in significantly larger errors. This is in contrast to the characteristics of the differentiable mesh. For this mesh with $\tau = 0.002$, we infer from Fig. 5.21(c) very good performance for nearly all combinations of G and Δx. The differentiable mesh with $\tau = 0.015$ exhibits a slightly worse performance but the qualitative behavior that very good results can be found for a wide parameter range is retained (see Fig. 5.21(d)). Another feature which we extract from Figs. 5.21(b) to 5.21(d) is that, for a fixed value of G, the error exhibits an apparent oscillatory dependence on Δx. We will return to this issue once we have addressed the role of certain parameters.

To sum up our (partial) findings up to this point (see Fig. 5.21), nondifferentiable meshes yield the overall best results but their performance sensitively depends on the correct choice of mesh parameters. On the other hand, the differentiable meshes perform nearly as well as the optimal nondifferentiable meshes but offer the advantage of being much less sensitive to parameter change.

As alluded to above, an interesting aspect is how the meshes perform for different numbers of plane waves. Therefore, we have carried out similar computations as those depicted in Fig. 5.21 but this time with 293 plane waves. We display the results in Fig. 5.22 for the nondifferentiable mesh (panel (a)), the differentiable mesh with $\tau = 0.002$ (panel (b)) and with $\tau = 0.015$ (panel (c)). We do find our above (partial) summary confirmed: While the nondifferentiable mesh performs best it does so only for very specific combinations of G and Δx, the differentiable meshes yield slightly worse results though for a much wider range of mesh parameters.

Moreover, these findings remain valid when the dielectric contrast is increased. In Fig. 5.23 we display the results for computations using again 997 plane waves (as in Fig. 5.21) but this time for a fiber with larger permittivity $\varepsilon_{\text{fib}} = 10$. The background material is again $\varepsilon_{bg} = 1$. We have further checked that the above (partial) conclusion holds true for other values of the permittivity by performing calculations with varying ε_{fib} where the compression parameters have been kept the same (not shown) as well as for varying wavelengths where all other parameters have been kept the same (not shown).

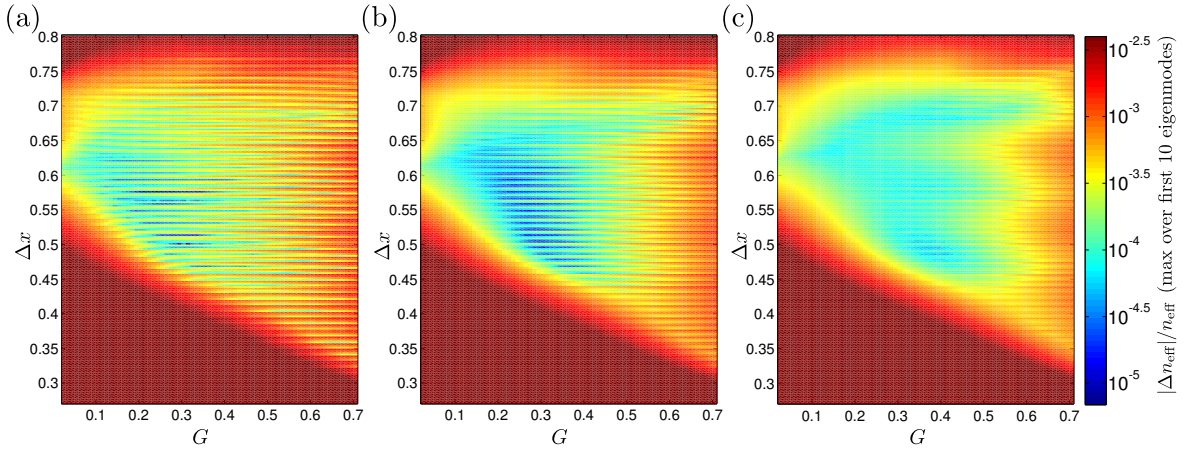

Figure 5.22: Dependence of the relative error (color-coded) for a low-index fiber on the compression parameters G and Δx for 293 planes waves and 1024×1024 discretization points in transformed space (cf. Fig. 5.21 for the results of the same system with 997 plane waves). Panel (a) depicts the results for the nondifferentiable mesh and panels (b) and (c) depict the results for the differentiable mesh with $\tau = 0.002$ and $\tau = 0.015$, respectively. The color bar of panel (c) also applies to panels (b) and (c).

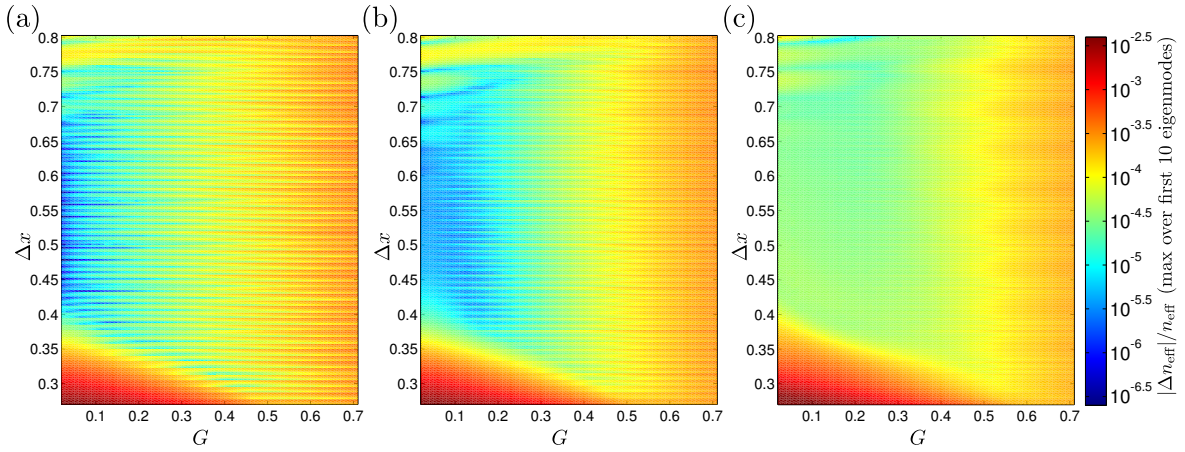

Figure 5.23: Dependence of the relative error (color-coded) for a high-index fiber on the compression parameters G and Δx for 997 planes waves and 1024×1024 discretization points (cf. Fig. 5.21 for the results of a low-index fiber with the same number of plane waves). Panel (a) depicts the results for the nondifferentiable mesh and panels (b) and (c) depict the results for the differentiable mesh with $\tau = 0.002$ and $\tau = 0.015$, respectively. The color bar of panel (c) also applies to panels (b) and (c).

An important issue which we have yet to address is the influence of the real space discretization. We have performed all the previous computations with 1024×1024 discretization points in order to take full advantage of the capabilities of the Fast Fourier Transform. However, we have to be aware that such a discretization must not necessarily be optimal for a given problem, including our fiber system. This may become apparent by the following argument: As described in Section 5.3.1, the nondifferentiable mesh leads to a diverging permittivity at

specific points in space. Depending on the number of real space points we use in the computations, the coordinate lines are either close to these points or not. Hence, the maximum permittivity values 'seen' by the numerical framework changes drastically when changing the number of real space points. Another important issue is the size of the structure 'seen' by the numerics—placing a coordinate line right on the surface of the structure or next to the surface changes its effective size. In our fiber system, for instance, the effective refractive indices of the modes change according to how far away the coordinate lines are from the structure's surface. A potential way of dealing with this problem could be increasing the number of sampling points or to find ways of appropriately distributing a given number of points. As the former option might require considerable computational resources, we will, in the following, pursue the latter option.

In order to start the quantitative analysis, we perform computations for the same low-index fiber for which we have obtained the results of Fig. 5.21—this time only with 1000 instead of 1024 discretization points per dimension. We depict our results in Fig. 5.24. As expected, the largest changes occur for the nondifferentiable mesh (cf. Fig. 5.21(b) and Fig. 5.24(a)).

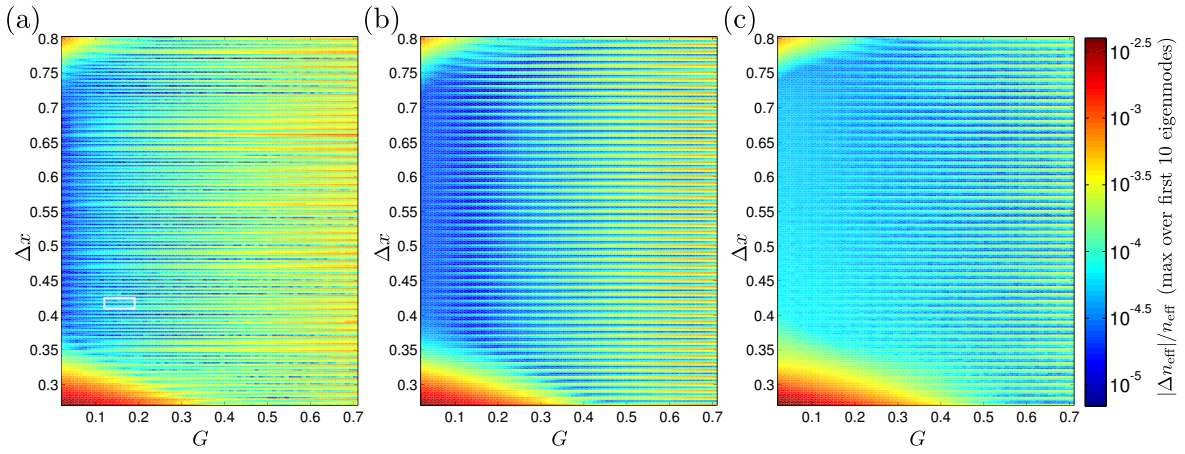

Figure 5.24: Dependence of the relative error (color-coded) for a low-index fiber on the compression parameters G and Δx for 997 planes waves and 1000×1000 discretization points (cf. Fig. 5.21 for the results of the same system with 1024×1024 discretization points). Panel (a) depicts the results for the nondifferentiable mesh and panels (b) and (c) depict the results for the differentiable mesh with $\tau = 0.002$ and $\tau = 0.015$, respectively. The color bar of panel (c) also applies to panels (b) and (c). The area within the white box in panel (a) is selected for further detailed investigation in Fig. 5.25.

Upon this (rather minimal) change of the real space discretization, the results for the differentiable meshes with $\tau = 0.002$ and $\tau = 0.015$ in Figs. 5.24(b) and 5.24(c), respectively, do not change much relative to Figs. 5.21(c) and 5.21(d). Of course, this has been expected as otherwise FMM computations would be rather useless to begin with. Nevertheless, throughout Fig. 5.24 we observe the same interesting feature which we have already pointed out in the context of Fig. 5.21: For a fixed value of G, the error apparently oscillates as a function of Δx. Therefore, we now turn to the analysis of this issue and investigate the parameter region delineated by the white box in Fig. 5.24(a) in more detail, i.e., with a much higher resolution in G and Δx.

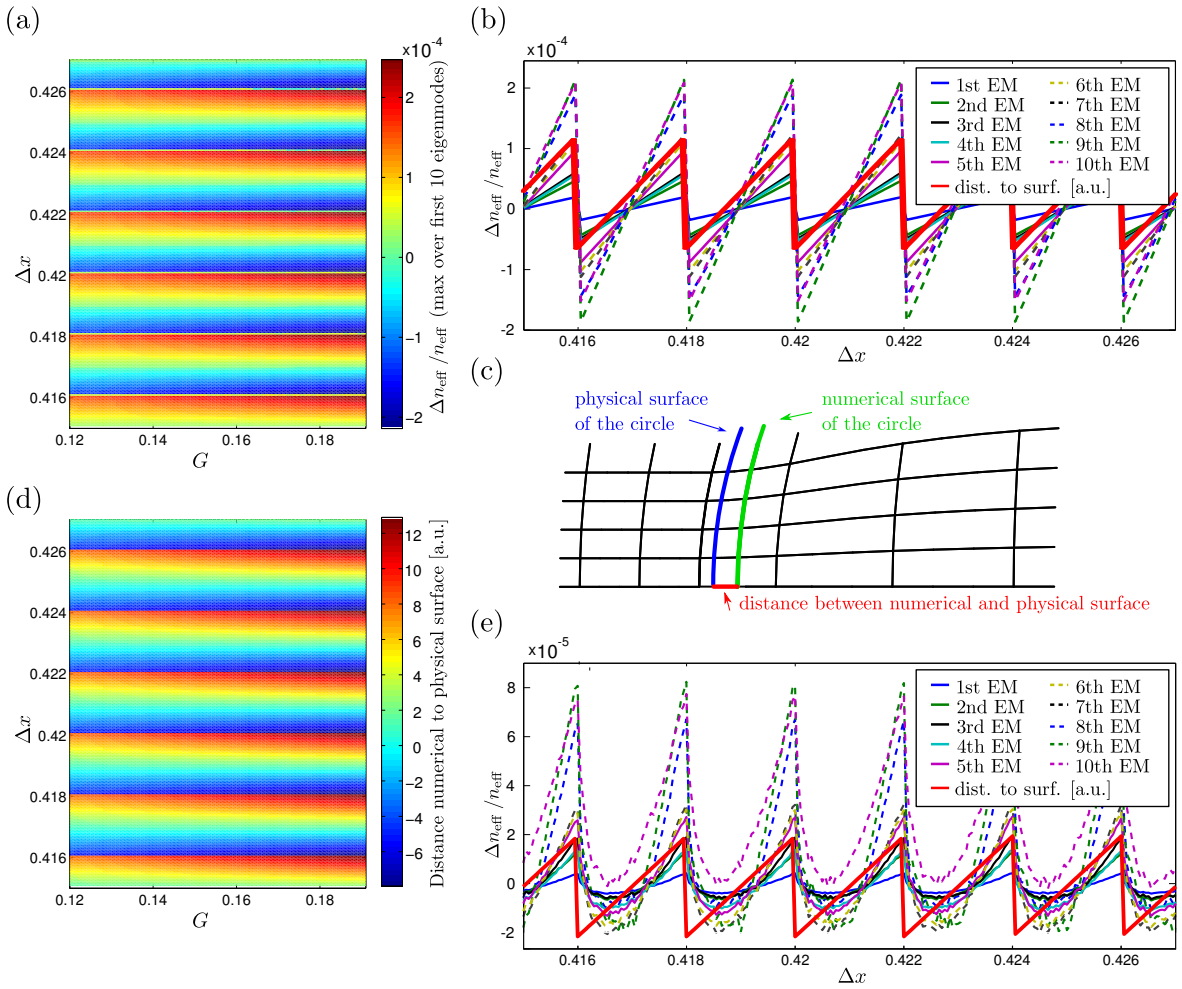

Figure 5.25: Detailed investigation of the error associated with nondifferentiable and differentiable meshes. Panel (a) represents a blow-up of the results highlighted in the white box of Fig. 5.24(a). The maximum relative error of the first ten guided eigenmodes of a low-index fiber have been obtained with 997 plane waves and 1000×1000 real-space points in steps of 0.001 for G and 0.00005 for Δx. Panel (b) depicts a line-cut through (a) at $G = 0.165$ and the relative error of each of the first ten guided eigenmodes together with the distance of the structure's physical surface to the numerical surface. Panel (c) illustrates the definition of the numerical surface as the center between the two coordinate lines closest to the physical surface. Panel (d) displays the computed distance between numerical and physical surface for the same parameter range that is used in (a). Panel (e) displays the results of a similar computation as shown in (b), this time using the differentiable mesh with $\tau = 0.002$ and $G = 0.165$.

Indeed, while the error changes continuously with G, it exhibits oscillations and even jumps as a function of Δx. This indicates that the error can be linked to the number of coordinate lines within the structure—recall, that Δx determines how many coordinate lines are inside the structure, while G controls the density at the surface. In order to investigate this, we show in Fig. 5.25(b) the dependence on Δx of the relative error of the effective refractive index for each of the first ten eigenmodes for a fixed value $G = 0.165$. In addition, we depict the distance between the physical surface and the numerical surface. The latter is given by

the center of the two coordinate lines closest to the physical surface (for an illustration, see Fig. 5.25(c)). The dependence of this distance on the compression parameters G and Δx is also shown in Fig. 5.25(d). There exists a strong correlation between the accuracy of the FMM computations and the distance between physical and numerical surface. As a matter of fact, the results of the FMM computations for the nondifferentiable mesh are optimal when the physical and the numerical surface coincide and deteriorate rapidly, when we move away from these sweet spots. The reason the color scale in Fig. 5.25(d) is asymmetric around zero is that the coordinate line density within the fiber is (by construction) marginally smaller than outside for the AC mesh, see Fig. 5.7.

In Fig. 5.25(e) we display corresponding results of the relative error of each of the first ten guided eigenmodes using a differentiable mesh with $\tau = 0.002$. As expected, the above effect is visible, too, i.e., the error oscillates as a function of Δx for a fixed value of G. However, the amplitude of the oscillations is significantly reduced relative to the amplitude of the nondifferentiable mesh (cf. Fig. 5.25(b)), in particular for the low-lying modes; for our low-index fiber system about one order of magnitude.

We have conducted extensive studies for values of G larger and smaller than those shown in Fig. 5.25, for a larger and smaller number of plane waves, and for larger values of the dielectric permittivity contrast. In all cases, the behavior as depicted in Fig. 5.25 is qualitatively reproduced.

An interesting aspect is how the method reacts to a deliberate disturbance. For that, we consider the same system as in Fig. 5.25(e), i.e., the differentiable mesh for the fiber. As we have discussed at the end of Section 5.3.4, the coordinate line where we compress the mesh is not given by x_- like in Sections 5.3.2 and 5.3.3 but by α in Eq. (5.39). This is only a slight variation since α and x_- are very close together. On the other hand, we have observed that the performance of the method crucially depends on the correct numerical representation of the physical surface. Figure 5.26 shows the result of deliberately compressing the differentiable mesh at x_- instead of α. The error of the effective refractive index over the first 10 guided eigenmodes is color-coded.

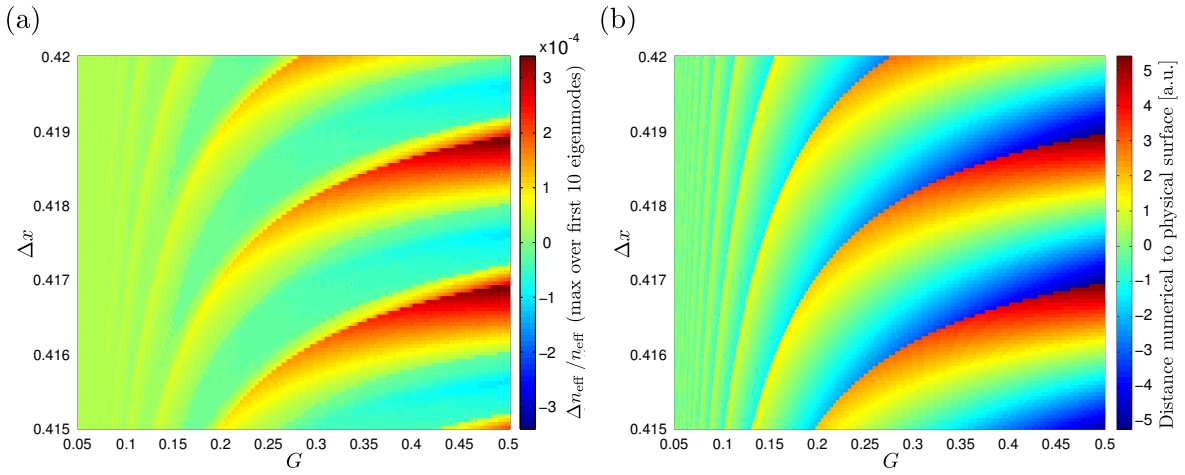

Figure 5.26: Error for a differentiable mesh with a wrong compression point. Panel (a) displays the numerical calculation of the eigenmode error and panel (b) displays the distance from numerical to physical surface for the mesh. Both agree qualitatively. 997 plane waves and 1000×1000 real space points were used. G was sampled in steps of 0.001 and Δx in steps of 0.00005.

In Fig. 5.26(a) the numerical computations are shown. In contrast to Fig. 5.25(a), the error does not show jumps at certain fixed positions in Δx. In Fig. 5.26(b) the distance between numerical and physical surface of the mesh is depicted. The general behavior is identical to Fig. 5.26(a).[4] This means that the correct surface representation is still the dominant parameter even when the mesh is compressed at the wrong position. The reason for the arcs occurring in Fig. 5.26 is that by compressing at a position other than at the surface of the structure, the percentage of the coordinate lines within the structure does not only depend on Δx any more but also on G. This insight might be of help when a mesh for a more complex structure is employed—as long as the jumps occur like in Fig. 5.25, the compression is performed at the correct coordinate line(s). In case the error behaves like in Fig. 5.26, the compression was inadvertently carried out at an incorrect position.

This leads us to our final conclusion regarding ASR and AC within FMM for dielectric structures. The nondifferentiable mesh performs well for small values of G as this corresponds to a good representation of the singularities in the effective permittivity due to an increased density of coordinate lines at the surface. However, special care has to be exercised when choosing the real space discretization and the parameters for the compression function(s). More precisely, the number of real space points and the parameters G and Δx have to be chosen such as to best represent the surface of the physical system. Here, an inconsistent choice of the mesh parameters easily leads to a rather significant loss of accuracy and/or erratic behavior with regard to convergence. The differentiable mesh exhibits the same qualitative behavior but is considerably less sensitive to the actual parameter choice, especially in terms of accuracy— good performance is achieved over a wide range of compression parameters G and Δx. Overall, the nondifferentiable mesh with optimal parameters does deliver somewhat better results than the differentiable mesh. This is the manifestation of the grid-aligned effective permittivity of the nondifferentiable mesh which is more compliant with the Fourier factorization rules than the differentiable mesh (see Section 5.3.4).

5.4.2 Metallic structures

We now turn to an investigation of metallic systems. Whereas much of the above discussion qualitatively also applies in this case, the relative weighting of the above issues is rather different. This may be seen as follows. Metals are characterized by permittivities with negative real part. In turn, this leads to a finite penetration of the electromagnetic field into the metal as well as to large field enhancements near the surfaces. As a result, we expect that surfaces and their adequate representation is even more important for metallic structures than for dielectric structures.

To be specific, we consider the same system that has been discussed in Ref. [15]. This means that we investigate a square array (lattice constant $d = 700$ nm) of metallic cylinders (height 50 nm, radius 150 nm) in air. The cylinders are centered in the unit cell and their axes are oriented in propagation direction. For the metal we use the permittivity given by a Drude model with the parameters $\epsilon_\infty = 9.0685$, a plasma frequency $\omega_D = 1.3544 \cdot 10^{16}$ Hz and a damping coefficient $\gamma = 1.1536 \cdot 10^{14}$ Hz, corresponding to gold [25]. In the absence of analytic solutions for this problem, we have computed transmittance, reflectance and absorbance spectra for normal incidence using several different compression functions and

[4] The position of the zeros should be compared (color-code green). They correspond to parameter pairs where the error is minimal (Fig. 5.26(a)) and the numerical and physical surface coincide (Fig. 5.26(b)).

found qualitatively the same results. In Fig. 5.27(a) we display the corresponding spectra using the nondifferentiable mesh, 1750 plane waves and a compression with parameters $G = 0.02$ and $\Delta x = 0.5$. We find the resonance frequency at 829 nm which is the subject of our further investigation. Specifically, in Fig. 5.27(b) we compare the convergence behavior of the reflectance for the nondifferentiable mesh, two smoothed, and two differentiable meshes using the same compression function as in Fig. 5.27(a).

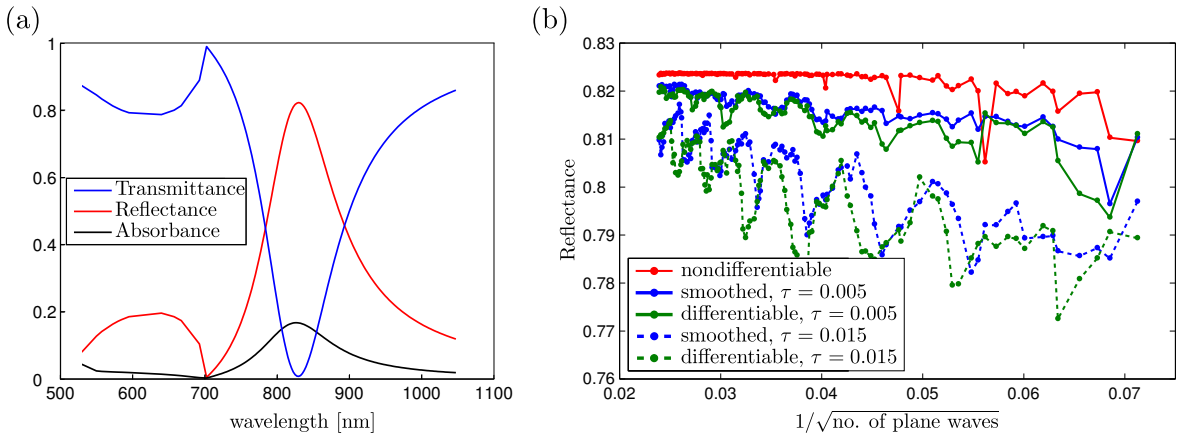

Figure 5.27: Convergence characteristics of different meshes for a square array of metallic cylinders of finite height. Panel (a) shows the transmittance, reflectance, and absorbance spectra that have been computed using 1750 plane waves and the nondifferentiable mesh. Our data agree well with those of Ref. [15] for this system. Panel (b) depicts the convergence characteristics (in terms of plane waves) of the reflectance for different meshes at the resonance frequency of 829 nm. The data in panels (a) and (b) have been obtained by using the same compression function with parameters $G = 0.02$ and $\Delta x = 0.5$ and a real space discretization of 1024×1024 points.

From Fig. 5.27(b), we infer that the nondifferentiable mesh exhibits a considerably faster and less erratic convergence behavior than the smoothed and differentiable meshes. Along the lines of our analysis for dielectric systems, we have traced this to the fact that the transformed effective permittivity fails to be grid-aligned for the smoothed and differentiable meshes. Therefore, it is less compliant with the Fourier factorization rules.

In contrast to dielectric structures, Fig. 5.27(b) strongly suggests that resolving the entire surface and creating a grid-aligned structure for the transformed permittivity is crucial for the performance when investigating metals with the FMM. Here, the nondifferentiable mesh has a distinct advantage over the smoothed and the differentiable meshes.

Just as in the dielectric case, it is interesting to have a closer look at the compression parameters G and Δx. Consequently, we display in Fig. 5.28 the dependence of the reflectance at the resonance on G and Δx for a fixed number of 997 plane waves and a real space discretization of 1024×1024 points when using different meshes.

For the nondifferentiable mesh, we observe the same characteristics as in the dielectric case (smooth dependence on G with a preference for low values, oscillatory behavior as a function of Δx). In contrast, the differentiable mesh exhibits a rather erratic behavior over much of the parameter space. Consequently, for metallic structures we obtain (not unexpectedly)

that an accurate representation of the surface is of paramount importance and that this can be facilitated best via the nondifferentiable mesh.

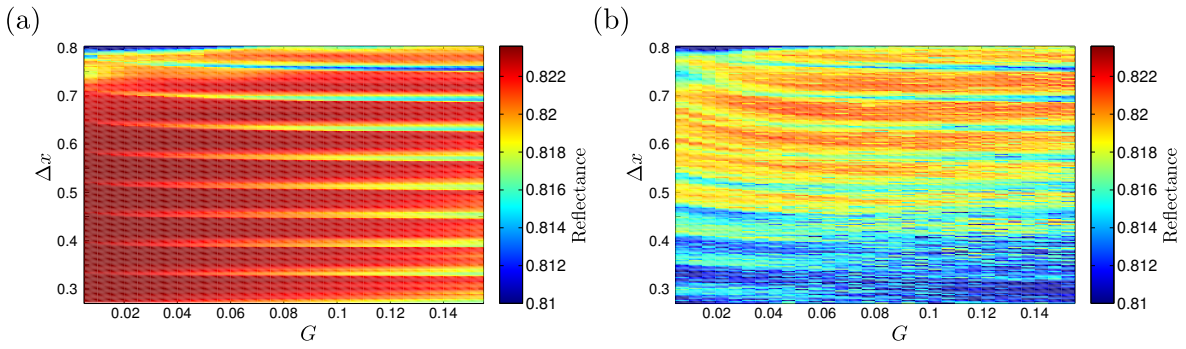

Figure 5.28: Dependence of the on-resonance reflectance from a square array of finite-height metallic cylinders on the compression parameters G and Δx for different meshes. Panel (a) shows the results when using the nondifferentiable mesh and panel (b) shows the results when using the differentiable mesh with $\tau = 0.005$. All computations have been performed with 997 plane waves with a real space grid of 1024×1024 sampling points. The parameter G has been stepped in 0.005 intervals and Δx in 0.0025 intervals. The color scale was saturated at 0.81.

5.4.3 Summary

In the last two sections we have dealt with several important aspects of the FMM when using adaptive coordinates (AC) and adaptive spatial resolution (ASR). Firstly, we have demonstrated how different issues in analytical mesh generation such as maintaining periodicity, non-rectangular unit cells and compression of coordinate lines at material interfaces can be mastered even for rather complex structures. Secondly, we have provided construction guidelines for different types of meshes such as nondifferentiable, smoothed and differentiable meshes. Through a careful convergence study, we have discovered 'sweet spots' for the nondifferentiable mesh where a judicious choice of real space discretization and compression parameters leads to an optimal surface representation that efficiently treats the (for this mesh unavoidable) singularities in the effective permittivity. As the nondifferentiable meshes naturally lead to the best grid-alignment, i.e., to optimal compliance with regard to the Fourier factorization rules, the nondifferentiable mesh turns out to be the best choice—provided one knows what one is doing and one can realize the correct surface representation.

The differentiable meshes exhibit a comparable performance for dielectric structures and are considerably less sensitive to the correct choice of compression parameters. This is welcome news for black-box approaches. For metals, however, obtaining grid-aligned structures is of paramount importance and the optimized nondifferentiable mesh still performs rather well (necessarily less efficient than in the dielectric case) whereas the smoothed and the differentiable mesh clearly fall behind (but are, of course, still much better than a simple Cartesian grid).

5.5 Modularity concept

In this section, I present an additional idea on the topic of mesh construction. As discussed throughout this chapter, there are two different strategies regarding mesh generation—analytical and numerical. The downside of analytical mesh generation is that every new structure has to be studied carefully to decide which specific coordinate lines should be used, even when it consists of an arrangement of previously meshed structures. Therefore, it could be an interesting thought to set up certain modules that can be reused several times in one mesh. The basic modularity concept is illustrated in Figs. 5.29 and 5.30.

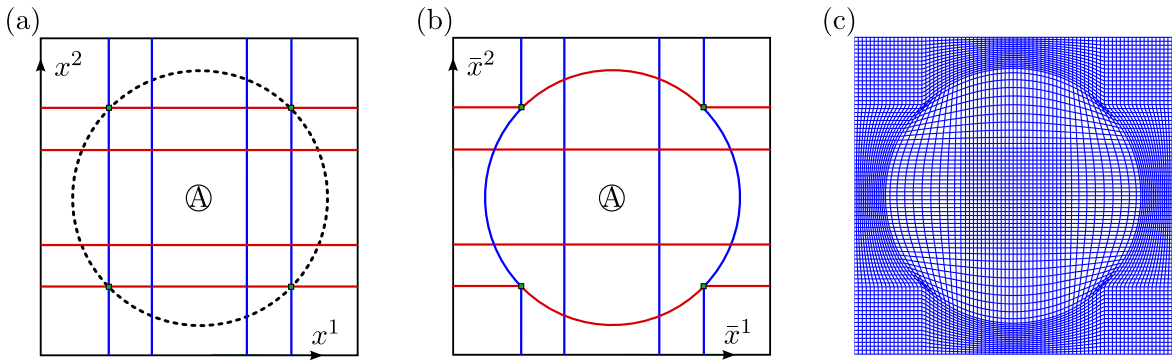

Figure 5.29: First step in the construction of a mesh with the modularity concept. The inner region is mapped onto itself and is, thus, still Cartesian, see panels (a) and (b). The corresponding mesh is depicted in panel (c). The second step is to replace the Cartesian mapping with any other (properly scaled) mapping in order to obtain sub-structures, see Fig. 5.30.

Here, we define characteristic lines that are quite similar to the ones in Fig. 5.7, i.e., a mesh for a large circular structure with a sub-structure in the middle. The difference to the mesh in Fig. 5.7 is an altered behavior in the center: instead of meshing a specific sub-structure like another circle, we intentionally map the area Ⓐ onto itself. Thereby, we have a Cartesian area in the middle of our mesh. This is where the idea of modularity comes into play—in a second step we can replace the Cartesian mapping with any of the mappings that we have acquired already (properly scaled, of course). An example is shown in Fig. 5.30(a), where the Cartesian mapping in the center of the large circle is replaced with a small circle. Alternatively, we could have put in the crescent or any other meshed structure. Moreover, we can assemble even more complex structures—this is depicted in Fig. 5.30(b), where we entered several more circles. A test system that could be studied with such a mesh is a structured fiber with several cores. This may be of help for the investigation of new FMM applications such as the simulation of photonic crystal fibers [56] or liquid crystal infiltrated fibers [57].

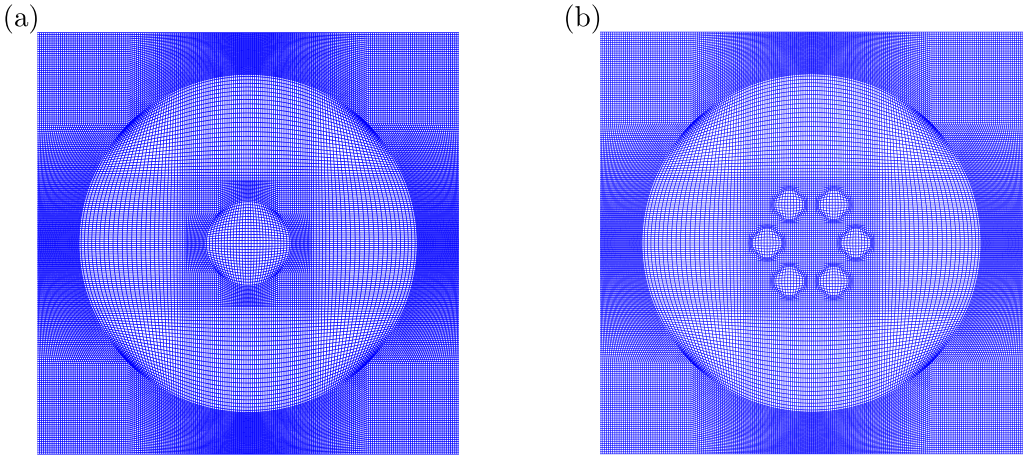

Figure 5.30: Complex meshes obtained using the modularity concept. The Cartesian region of the mapping (see Fig. 5.29) is replaced by a scaled mapping of a circle (panel (a)) and even a complex arrangement of circles (panel(b)).

Chapter 6

Three-Dimensional Coordinate Transformations

In Chapter 5, we have shown that adaptive spatial resolution (ASR) and adaptive coordinates (AC) are of great help for the Fourier Modal Method when it comes to solving Maxwell's equations, especially in systems containing metals. A basic problem in this context is that structures in different slices might need different ASR and AC meshes. In recent years, several interesting structures were fabricated that fall into this category. For example, twisted-cross photonic metamaterials, see Fig. 6.1(a), can lead to strong optical activity. Gold helix photonic metamaterials, as shown in Figs. 6.1(b) and (c) can be used as broadband circular polarizers. Such structures have in common that the shape of the metallic parts of the material distribution changes upon changing the x^3 coordinate. First studies with different two-dimensional AC and ASR meshes in adjacent layers, performed in our group by Sabine Essig [34], were ambivalent since problems such as energy loss and artificial reflections appeared.

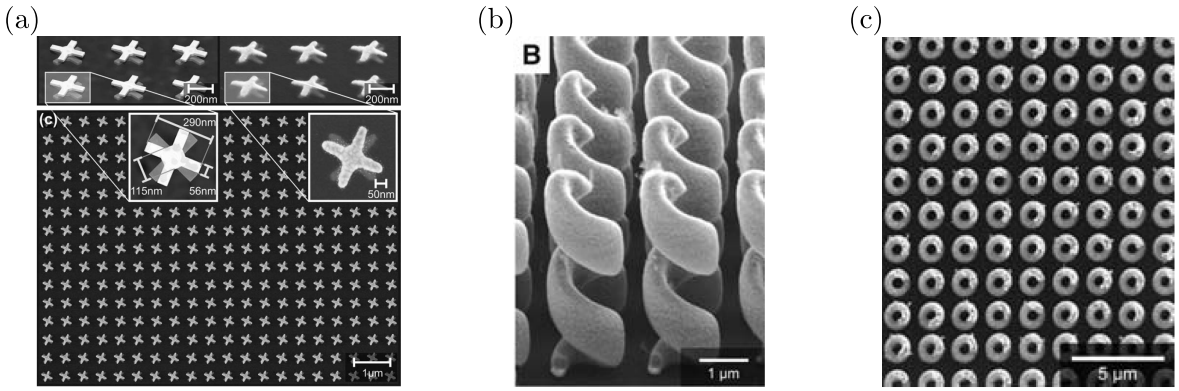

Figure 6.1: Experimental realizations of metallic systems which are difficult to investigate with the FMM. Panel (a) shows a system of twisted-cross metamaterials. The picture is taken from Ref. [58]. Panels (b) and (c) depict gold helix metamaterials (side and top view, respectively) which can be used as circular polarizer. The pictures are taken from Ref. [59].

In this chapter, we tackle these particular problems by means of a three-dimensional coordinate transformation. The structure investigated for this purpose are two layers of mutually rotated crosses with a layer of air between them[1], see Fig. 6.2. A physical discussion of this structure is found in Chapter 7 where we develop models to describe the transmission

[1]Naturally, crosses floating in air are not a very realistic test system. However, we could easily replace the air's permittivity by any other dielectric permittivity. This setup is chosen for the sake of simplicity.

properties of light through such an arrangement of crosses. In order to handle this type of structures in the FMM, we set up a suitably designed three-dimensional coordinate transformation to enhance the density of coordinate lines along each surface in each layer. The coordinate transformations we design in the following have the form

$$\bar{x}^1 = \bar{x}^1\Big(x^1, x^2, x^3\Big), \tag{6.1a}$$

$$\bar{x}^2 = \bar{x}^2\Big(x^1, x^2, x^3\Big), \tag{6.1b}$$

$$\bar{x}^3 = x^3. \tag{6.1c}$$

As we show in Section 6.1, this leads to a fully anisotropic transformed permittivity and permeability. Thereby, we cannot use the small eigenproblem of the FMM since Maxwell's equations do not decouple into separate eigenproblems for the in-plane **H**- and **E**-fields. Hence, the large eigenproblem of the FMM has to be utilized, see Section 3.3. In Section 6.2, we briefly discuss efforts of coordinate transformations in x^3 direction which can be found in literature. This is followed by the description of the three-dimensional mesh construction in Section 6.3. Since it is very instructive, we plot the transformed permittivity in Section 6.4. Subsequently, we deal with the actual numerical investigation of the problem. In these preliminary numerical results in Section 6.5, we encounter several problems, for some of which we discuss possible solutions in Section 6.6. The terminology of Chapter 5 is retained throughout this chapter. In particular, we use the methodology of nondifferentiable meshes.

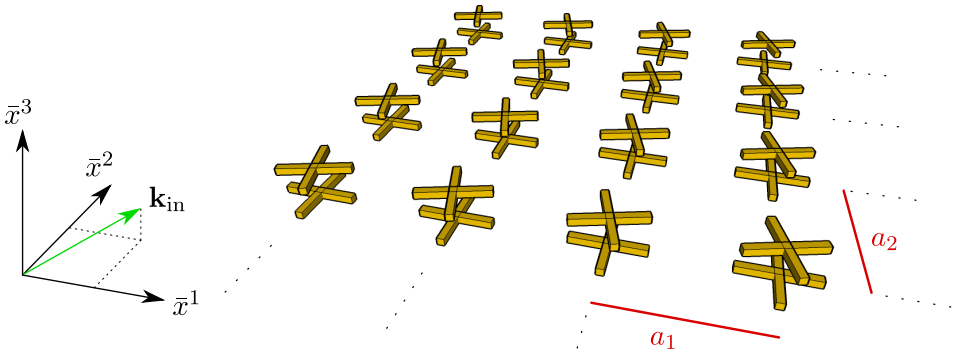

Figure 6.2: Sketch of the structure under investigation in this chapter. For this structure we create a three-dimensional mesh and study its impact on FMM computations.

The results in this chapter were obtained in close cooperation with Thomas Zebrowski. I designed the three-dimensional mesh and provided the transformed permittivity and permeability tensors. Thomas Zebrowski implemented the full anisotropic FMM, I contributed minor parts to the implementation.

6.1 Transformed permittivity

In this section, we briefly investigate the transformed permittivity tensor for transformations of the form given in Eqs. (6.1). Assuming an isotropic permittivity distribution $\bar{\varepsilon}$ in the Cartesian space, see Eq. (3.2a), the effective permittivity ε^{ij} reads

$$\varepsilon^{11} = \sqrt{g}\,\bar{\varepsilon}\left(\frac{\partial x^1}{\partial \bar{x}^1}\frac{\partial x^1}{\partial \bar{x}^1}+\frac{\partial x^1}{\partial \bar{x}^2}\frac{\partial x^1}{\partial \bar{x}^2}+\frac{\partial x^1}{\partial \bar{x}^3}\frac{\partial x^1}{\partial \bar{x}^3}\right), \tag{6.2a}$$

$$\varepsilon^{12} = \sqrt{g}\,\bar{\varepsilon}\left(\frac{\partial x^1}{\partial \bar{x}^1}\frac{\partial x^2}{\partial \bar{x}^1}+\frac{\partial x^1}{\partial \bar{x}^2}\frac{\partial x^2}{\partial \bar{x}^2}+\frac{\partial x^1}{\partial \bar{x}^3}\frac{\partial x^2}{\partial \bar{x}^3}\right), \tag{6.2b}$$

$$\varepsilon^{13} = \sqrt{g}\,\bar{\varepsilon}\,\frac{\partial x^1}{\partial \bar{x}^3}, \tag{6.2c}$$

$$\varepsilon^{21} = \sqrt{g}\,\bar{\varepsilon}\left(\frac{\partial x^2}{\partial \bar{x}^1}\frac{\partial x^1}{\partial \bar{x}^1}+\frac{\partial x^2}{\partial \bar{x}^2}\frac{\partial x^1}{\partial \bar{x}^2}+\frac{\partial x^2}{\partial \bar{x}^3}\frac{\partial x^1}{\partial \bar{x}^3}\right) = \varepsilon^{12}, \tag{6.2d}$$

$$\varepsilon^{22} = \sqrt{g}\,\bar{\varepsilon}\left(\frac{\partial x^2}{\partial \bar{x}^1}\frac{\partial x^2}{\partial \bar{x}^1}+\frac{\partial x^2}{\partial \bar{x}^2}\frac{\partial x^2}{\partial \bar{x}^2}+\frac{\partial x^2}{\partial \bar{x}^3}\frac{\partial x^2}{\partial \bar{x}^3}\right), \tag{6.2e}$$

$$\varepsilon^{23} = \sqrt{g}\,\bar{\varepsilon}\,\frac{\partial x^2}{\partial \bar{x}^3}, \tag{6.2f}$$

$$\varepsilon^{31} = \sqrt{g}\,\bar{\varepsilon}\,\frac{\partial x^1}{\partial \bar{x}^3} = \varepsilon^{13}, \tag{6.2g}$$

$$\varepsilon^{32} = \sqrt{g}\,\bar{\varepsilon}\,\frac{\partial x^2}{\partial \bar{x}^3} = \varepsilon^{23}, \tag{6.2h}$$

$$\varepsilon^{33} = \sqrt{g}\,\bar{\varepsilon}. \tag{6.2i}$$

ε^{13} assumes such a simple form because $\partial x^3/\partial \bar{x}^i = \delta_{3i}$. Eqs. (6.2) mean that even though the transformations in Eqs. (6.1) are not the most complex transformations possible, they already lead to a fully anisotropic permittivity tensor since x^1 and x^2 now depend on $\bar{x}^3$, i.e., $\partial x^1/\partial \bar{x}^3 \neq 0$ and $\partial x^2/\partial \bar{x}^3 \neq 0$. The permeability has a similar form. Like in two-dimensional meshing, we construct the mappings $\bar{x}^i(x^j)$ and not $x^i(\bar{x}^j)$—therefore, we have to derive the corresponding derivatives used in Eqs. (6.2) from $\bar{x}^i(x^j)$. They are calculated using the Jacobian $\bar{J}$ and its inverse, i.e.,

$$\begin{pmatrix} \frac{\partial x^1}{\partial \bar{x}^1} & \frac{\partial x^1}{\partial \bar{x}^2} & \frac{\partial x^1}{\partial \bar{x}^3} \\ \frac{\partial x^2}{\partial \bar{x}^1} & \frac{\partial x^2}{\partial \bar{x}^2} & \frac{\partial x^2}{\partial \bar{x}^3} \\ \frac{\partial x^3}{\partial \bar{x}^1} & \frac{\partial x^3}{\partial \bar{x}^2} & \frac{\partial x^3}{\partial \bar{x}^3} \end{pmatrix} \overset{(6.1)}{=} \begin{pmatrix} \frac{\partial x^1}{\partial \bar{x}^1} & \frac{\partial x^1}{\partial \bar{x}^2} & \frac{\partial x^1}{\partial \bar{x}^3} \\ \frac{\partial x^2}{\partial \bar{x}^1} & \frac{\partial x^2}{\partial \bar{x}^2} & \frac{\partial x^2}{\partial \bar{x}^3} \\ 0 & 0 & 1 \end{pmatrix} = \bar{J} \overset{(*)}{=} J^{-1} = \begin{pmatrix} \frac{\partial \bar{x}^1}{\partial x^1} & \frac{\partial \bar{x}^1}{\partial x^2} & \frac{\partial \bar{x}^1}{\partial x^3} \\ \frac{\partial \bar{x}^2}{\partial x^1} & \frac{\partial \bar{x}^2}{\partial x^2} & \frac{\partial \bar{x}^2}{\partial x^3} \\ 0 & 0 & 1 \end{pmatrix}^{-1}$$

$$= \frac{1}{\frac{\partial \bar{x}^1}{\partial x^1}\frac{\partial \bar{x}^2}{\partial x^2}-\frac{\partial \bar{x}^1}{\partial x^2}\frac{\partial \bar{x}^2}{\partial x^1}} \begin{pmatrix} \frac{\partial \bar{x}^2}{\partial x^2} & -\frac{\partial \bar{x}^1}{\partial x^2} & \frac{\partial \bar{x}^1}{\partial x^2}\frac{\partial \bar{x}^2}{\partial x^3}-\frac{\partial \bar{x}^1}{\partial x^3}\frac{\partial \bar{x}^2}{\partial x^2} \\ -\frac{\partial \bar{x}^2}{\partial x^1} & \frac{\partial \bar{x}^1}{\partial x^1} & \frac{\partial \bar{x}^1}{\partial x^3}\frac{\partial \bar{x}^2}{\partial x^1}-\frac{\partial \bar{x}^1}{\partial x^1}\frac{\partial \bar{x}^2}{\partial x^3} \\ 0 & 0 & \frac{\partial \bar{x}^1}{\partial x^1}\frac{\partial \bar{x}^2}{\partial x^2}-\frac{\partial \bar{x}^1}{\partial x^2}\frac{\partial \bar{x}^2}{\partial x^1} \end{pmatrix}, \tag{6.3}$$

where we again used the inverse function theorem in $(*)$. The derivatives of x^3 with respect to $\bar{x}^1$ and $\bar{x}^2$ are zero because of Eq. (6.1c).

6.2 Review of related work

A method related to three-dimensional transformations is the Chandezon method [60]. There, grating problems can be made easier by transforming the surface between adjacent layers from curvy to flat. However, our problem in the context of the structures depicted in Fig. 6.1 is not a curvy surface. Therefore, the Chandezon method, although transforming in x^3 direction, cannot be of help.

In the Fourier Modal Method, there have also been attempts to incorporate transformations in the slicing direction. Vallius and Honkanen applied their ASR function to multilevel profiles [51]. However, the in-plane coordinate transformations include only ASR in one direction, i.e., they are one-dimensional. Also, the numerical results are not too convincing and questions about the effects of artificial reflections and energy loss due to the mesh are not addressed.

A different approach was presented by Gushchin and Tishchenko [61]. They investigated a periodically modulated surface, i.e., a lamellar, corrugated grating. Instead of stair-casing in x^3-direction, they attempt to introduce slanted walls in order to achieve an improved approximation of the modulated surface. Even though their numerical results are positive, they do not perform the investigation for metallic systems. Also, the slices are only one-dimensional, i.e., invariant in one transverse direction. Unfortunately, even though the method is interesting, we cannot utilize it since our problem is different: while Gushchin and Tishchenko work on the improvement of bent slices, we face slices ideal for the FMM, i.e., straight in x^3-direction, see Fig. 6.2. Our problem at hand is to rotate the cross in the second layer. For that, we need AC in three dimensions. To the best of my knowledge, there are no published attempts to apply three-dimensional AC and ASR coordinate transformations in the context of the FMM.

6.3 Mesh construction

The overall aim of this section is to obtain a three-dimensional coordinate transformation of the form in Eqs. (6.1) for the system depicted in Fig. 6.2. It consists of two layers of mutually rotated crosses—the first cross[2] is grid-aligned and the second cross is rotated by the angle φ_0.

The general idea is to create a mesh for a rotated cross with a rotation angle that depends on the x^3 coordinate. This means that we start with an unrotated mesh since the cross in the lower layer is grid-aligned. Then, the mesh is rotated[3] with increasing x^3 up to the second layer where it is rotated by φ_0. Behind the structure, the mesh can be rotated back to the original shape.

Since three-dimensional meshing is a complex endeavor, this section is structured the following way: Firstly, the general train of thought is outlined. Secondly, we discuss the construction of the underlying two-dimensional mesh for a cross. Thirdly, the planar mapping for the rotated cross is utilized to create a three-dimensional coordinate transformation. Fourth and final, the use of adaptive spatial resolution (ASR) is addressed.

[2] "The first cross" means in this context the cross with the smaller x^3 value. The x^3-axis is defined along the propagation direction of the incident light.

[3] The detailed meaning of the term "the mesh is rotated" is explained in the subsequent section.

6.3.1 General train of thought

We pointed out that metallic systems with different structures in each layer are difficult for the FMM. We tackle this problem the following way: assume the second cross of our test structure in Fig. 6.2 would be grid-aligned above the first cross. Then, we could apply the same ASR transformation in every layer. Thus, no matching problems between the layers would arise. The key point is now that we can accomplish this using adaptive coordinates. In the previous chapter, we transformed the shape of the structure—a circle was transformed into a square and the optical properties were changed accordingly. However, we do not have to change the structure's shape, we can also 'just' rotate it.

A delicate point is that we have to make sure during the construction of the mesh that the second cross is exactly above the first cross. This means that we cannot choose arbitrary characteristic coordinate lines and points[4]. An example with a bad choice is depicted in Fig. 6.3.

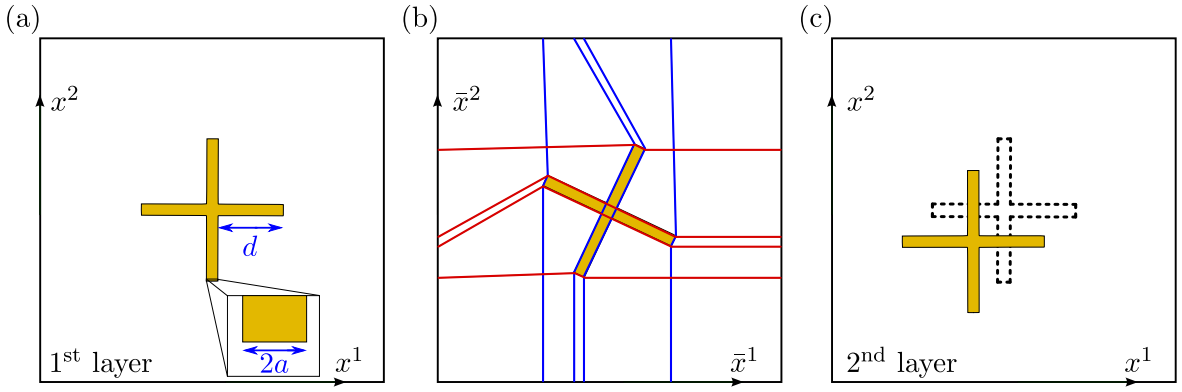

Figure 6.3: Bad choice for characteristic lines for three-dimensional meshing. The cross in the first layer is grid-aligned, see panel (a). In order to use the same ASR function in every layer, the second cross needs to be rotated via AC such that it is right above the first cross. Although the characteristic coordinate lines (blue and red) as chosen in panel (b) result in a transformed permittivity for the cross that is grid-aligned, they fail to map the cross in the second layer directly over the first cross, see panel (c).

Here, the characteristic lines (see Fig. 6.3(b)) were chosen in such a way that the transformed permittivity features a grid-aligned cross (see Fig. 6.3(c)) which is at the wrong position, i.e., not above the first cross depicted in Fig. 6.3(a).

The conclusion is that we have to stop choosing points that are 2D-characteristic for the structure. Instead, three-dimensional meshing requires that we choose points and coordinate lines that are *3D-characteristic*. In the next section, we show how this is accomplished for the system of crosses.

[4] In Chapter 5, the characteristic lines were used to define and construct the mapping, see for example Fig. 5.5. The points where the characteristic lines intersect are called characteristic points.

6.3.2 Two-dimensional mesh for a rotated cross

In this section, we deal with the construction of the underlying planar mesh that we utilize in the subsequent section to build a three-dimensional mapping. We have argued that characteristic three-dimensional coordinate lines have to be chosen. A possible choice is depicted in Fig. 6.4.

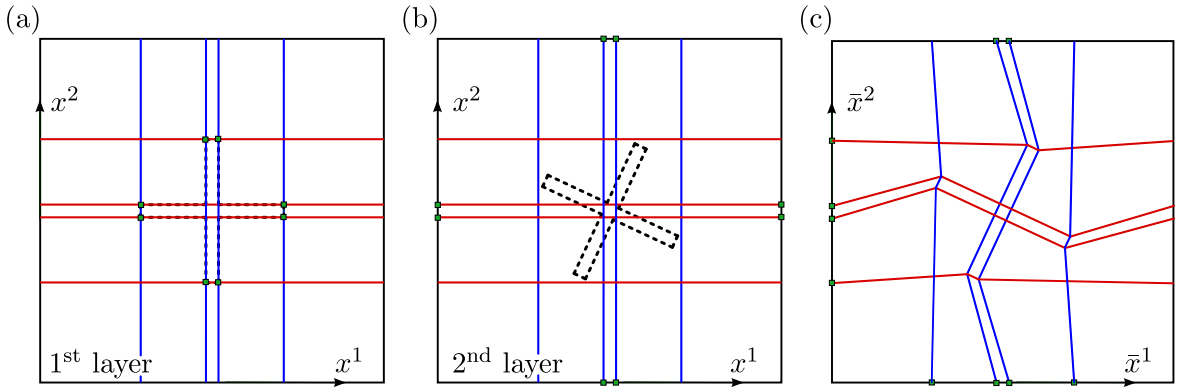

Figure 6.4: Possible choice for 3D-characteristic coordinate lines/points. The points marked in green in panel (a) define the characteristic coordinate lines. They would also have to be used for the mesh construction in the second layer, see panel (b). A construction sketch for a possible mesh is depicted in panel (c).

This choice is realizable but the mesh would be distorted at several points. As we have seen in Chapter 5, this directly leads to a strongly varying transformed permittivity. Also, the construction would be rather lengthy due to the large number of different zones for the mapping. A rather simple and elegant choice of 3D-characteristic lines for this problem is depicted in Fig. 6.5. Here, the lines and the mesh that we use in the following are shown.

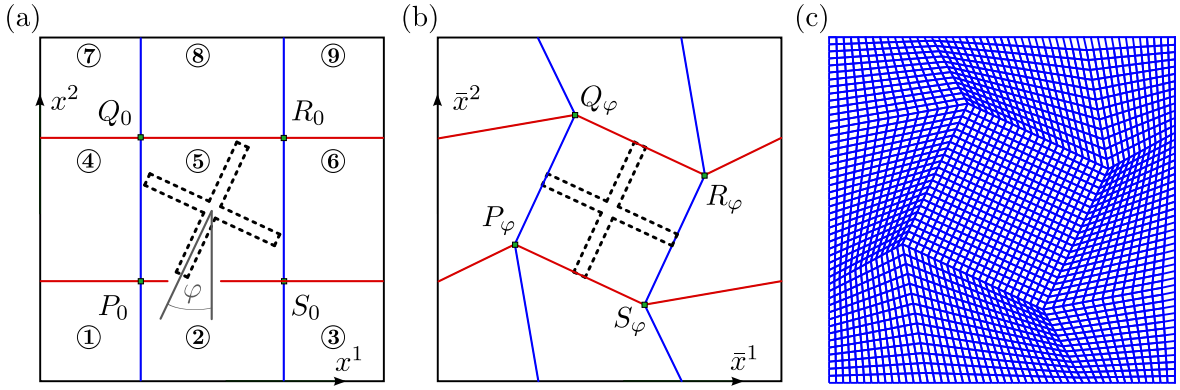

Figure 6.5: Characteristic points for a rotated cross' mesh. Panel (a) displays the partitioning of the $[0,1]\times[0,1]$ unit cell—the points are 3D-characteristic and stem from the unrotated cross, cf. Fig. 6.4(a). Panel (b) sketches how these coordinate lines are mapped to form the mesh (panel (c)).

The motivation of this choice is that the mapping for zone ⑤ is just a Cartesian grid that is rotated. As we show in Section 6.4, this causes the transformed permittivity in this region to be the same as the untransformed permittivity, only rotated by φ.

The points P_0, Q_0, R_0, S_0 are defined by the intersection points of the outer blue and red lines in Fig. 6.4(a), i.e., $Q_0 = (Q_{0,x^1}, Q_{0,x^2}) = (d_-, d_+),\ P_0 = (d_-, d_-),\ R_0 = (d_+, d_+),\ S_0 = (d_+, d_-)$ with $d_\pm = 0.5 \pm a \pm d$ and a and d like sketched in Fig. 6.3(a). The corresponding points in Fig. 6.5(b) are given by

$$P_{\varphi,x^1} = 0.5 - m\cos\left(\varphi - \arccos\left(\frac{a+d}{m}\right)\right) - d\sin\varphi, \tag{6.4a}$$

$$P_{\varphi,x^2} = 0.5 + m\sin\left(\varphi - \arccos\left(\frac{a+d}{m}\right)\right) - d\cos\varphi, \tag{6.4b}$$

$$\left(S_{\varphi,x^1}, S_{\varphi,x^2}\right) = \left(P_{\varphi,x^1} + 2(d+a)\cos\varphi,\ P_{\varphi,x^2} - 2(d+a)\sin\varphi\right), \tag{6.4c}$$

$$\left(Q_{\varphi,x^1}, Q_{\varphi,x^2}\right) = \left(P_{\varphi,x^1} + 2(d+a)\sin\varphi,\ P_{\varphi,x^2} + 2(d+a)\cos\varphi\right), \tag{6.4d}$$

$$\left(R_{\varphi,x^1}, R_{\varphi,x^2}\right) = \left(S_{\varphi,x^1} + 2(d+a)\sin\varphi,\ S_{\varphi,x^2} + 2(d+a)\cos\varphi\right), \tag{6.4e}$$

with the abbreviation $m = \sqrt{a^2 + (a+d)^2}$. The points P_0, Q_0, R_0, S_0 partition the unit cell in every layer.

Before constructing the mesh we have to recognize a systematical difference to our previous two-dimensional, nondifferentiable mesh generation. In Chapter 5, we also defined points that divided the unit cells, see for example Fig. 5.5. These points were mapped onto themselves since they were always on the structure's surface. In contrast to this, the 3D-characteristic points P_0, Q_0, R_0, S_0 are not on the surface of the rotated cross. Therefore, they are not mapped onto themselves. Instead, they are mapped onto $P_\varphi, Q_\varphi, R_\varphi, S_\varphi$.

On first sight, this might be a technical detail. However, it changes the way we construct the mapping. In Chapter 5, we could easily construct the mapping like in Eq. (5.13). This procedure gets more complicated when we choose the mesh construction points to be 3D-characteristic, i.e., not structure-specific. We start by constructing the mapping in zone $① = \{(x^1, x^2) :\ x^1 \in [0, P_{0,x^1}],\ x^2 \in [0, P_{0,x^2}]\}$, where we utilize the $LT(c, \bar{c}, d, \bar{d}, x)$-function introduced in Eq. (5.10) which, as a reminder, defines a straight line through the points $(c, \bar{c})$ and $(d, \bar{d})$ as a function of $x \in [c, d]$. The mapping reads

$$\begin{aligned} \bar{x}^1\left(x^1, x^2\right) &= LT\left(0, 0, P_{0,x^1}, H_1(x^2), x^1\right), \qquad (x^1, x^2) \in ① \\ &\quad \text{with} \quad H_1\left(x^2\right) = LT\left(0, P_{0,x^1}, P_{0,x^2}, P_{\varphi,x^1}, x^2\right), \end{aligned} \tag{6.5a}$$

$$\begin{aligned} \bar{x}^2\left(x^1, x^2\right) &= LT\left(0, 0, P_{0,x^2}, H_2(x^1), x^2\right), \qquad (x^1, x^2) \in ① \\ &\quad \text{with} \quad H_2\left(x^1\right) = LT\left(0, P_{0,x^2}, P_{0,x^1}, P_{\varphi,x^2}, x^1\right). \end{aligned} \tag{6.5b}$$

The help functions H_1 and H_2 are visualized in Fig. 6.6(b). The essential change in the mapping procedure compared to Section 5.3.2 is that we cannot map each coordinate independently from the other coordinate any more. This means, that the $\bar{x}^1$- and $\bar{x}^2$-mappings need to be designed such that they yield the desired results when they are combined.

Upon carefully inspecting Eqs. (6.5) we observe that the mesh construction conceptually differs in the help functions H_i. Instead of directly parameterizing the function between the points $(P_{0,x^1}, 0)$ and P_φ we have to make sure that P_0 is mapped onto P_φ. This is accomplished by the form of Eq. (6.5a). In the scheme from Chapter 5, the help function for $\bar{x}^1$ would have read $LT(0, P_{0,x^1}, P_{\varphi,x^2}, P_{\varphi,x^1}, x^2)$. Again, this scheme cannot be used since P_0 is not mapped onto itself, i.e., $P_0 \neq P_\varphi$.

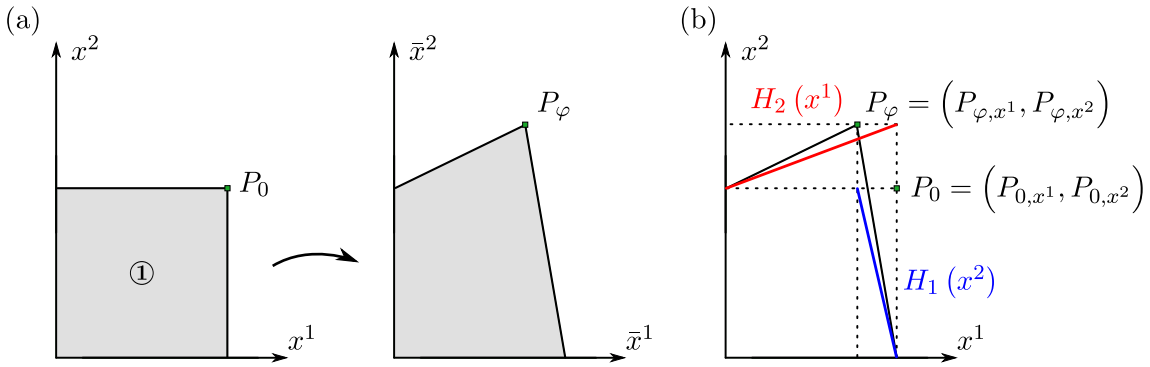

Figure 6.6: Panel (a) displays the mapping of the first zone. Since P_0 is not mapped onto itself, we have to alter the nondifferentiable mapping formalism established in Section 5.3.2. Panel (b) displays the help functions H_1 and H_2 we employ to construct the mapping in Eqs. (6.5).

The $\bar{x}^1$ mapping in the other zones is constructed analogously and reads

$$\bar{x}^1\left(x^1,x^2\right) = \begin{cases} LT\left(P_{0,x^1}, H_1(x^2), S_{0,x^1}, H_3(x^2), x^1\right), & (x^1,x^2) \in ② \\ LT\left(S_{0,x^1}, H_3(x^2), 1, 1, x^1\right), & (x^1,x^2) \in ③ \\ LT\left(0, 0, P_{0,x^1}, H_5(x^2), x^1\right), & (x^1,x^2) \in ④ \\ LT\left(P_{0,x^1}, H_5(x^2), S_{0,x^1}, H_7(x^2), x^1\right), & (x^1,x^2) \in ⑤ \\ LT\left(S_{0,x^1}, H_7(x^2), 1, 1, x^1\right), & (x^1,x^2) \in ⑥ \\ LT\left(0, 0, P_{0,x^1}, H_9(x^2), x^1\right), & (x^1,x^2) \in ⑦ \\ LT\left(Q_{0,x^1}, H_9(x^2), R_{0,x^1}, H_{11}(x^2), x^1\right), & (x^1,x^2) \in ⑧ \\ LT\left(R_{0,x^1}, H_{11}(x^2), 1, 1, x^1\right), & (x^1,x^2) \in ⑨ \end{cases} \tag{6.6}$$

with the help functions

$$\begin{aligned} H_3(x^2) &= LT\left(0, S_{0,x^1}, S_{0,x^2}, S_{\varphi,x^1}, x^2\right), \quad H_5(x^2) = LT\left(P_{0,x^2}, P_{\varphi,x^1}, Q_{0,x^2}, Q_{\varphi,x^1}, x^2\right), \\ H_7(x^2) &= LT\left(S_{0,x^2}, S_{\varphi,x^1}, R_{0,x^2}, R_{\varphi,x^1}, x^2\right), \quad H_9(x^2) = LT\left(Q_{0,x^2}, Q_{\varphi,x^1}, 1, Q_{0,x^1}, x^2\right), \\ H_{11}(x^2) &= LT\left(R_{0,x^2}, R_{\varphi,x^1}, 1, R_{0,x^1}, x^2\right). \end{aligned} \tag{6.7}$$

The $\bar{x}^2$ mapping is given by

$$\bar{x}^2\left(x^1,x^2\right) = \begin{cases} LT\left(0, 0, P_{0,x^2}, H_4(x^1), x^2\right), & (x^1,x^2) \in ② \\ LT\left(0, 0, P_{0,x^2}, H_6(x^1), x^2\right), & (x^1,x^2) \in ③ \\ LT\left(P_{0,x^2}, H_2(x^1), Q_{0,x^2}, H_8(x^1), x^2\right), & (x^1,x^2) \in ④ \\ LT\left(P_{0,x^2}, H_4(x^1), Q_{0,x^2}, H_{10}(x^1), x^2\right), & (x^1,x^2) \in ⑤ \\ LT\left(S_{0,x^2}, H_6(x^1), R_{0,x^2}, H_{12}(x^2), x^2\right), & (x^1,x^2) \in ⑥ \\ LT\left(Q_{0,x^2}, H_8(x^1), 1, 1, x^2\right), & (x^1,x^2) \in ⑦ \\ LT\left(Q_{0,x^2}, H_{10}(x^2), 1, 1, x^2\right), & (x^1,x^2) \in ⑧ \\ LT\left(R_{0,x^2}, H_{14}(x^2), 1, 1, x^2\right), & (x^1,x^2) \in ⑨ \end{cases} \tag{6.8}$$

with the help functions

$$\begin{aligned} H_4(x^1) &= LT\left(P_{0,x^1}, P_{\varphi,x^2}, S_{0,x^1}, S_{\varphi,x^2}, x^1\right), \qquad H_6(x^1) = LT\left(S_{0,x^1}, S_{\varphi,x^2}, 1, S_{0,x^2}, x^1\right), \\ H_8(x^1) &= LT\left(0, Q_{0,x^2}, Q_{0,x^1}, Q_{\varphi,x^2}, x^1\right), \quad H_{10}(x^1) = LT\left(Q_{0,x^1}, Q_{\varphi,x^2}, R_{0,x^1}, R_{\varphi,x^2}, x^1\right), \\ H_{12}(x^1) &= LT\left(R_{0,x^1}, R_{\varphi,x^2}, 1, R_{0,x^2}, x^1\right). \end{aligned} \tag{6.9}$$

Here, the LT functions in Eqs. (6.6) and (6.8) describe the linear transition between the characteristic coordinates lines. This means that these LT functions define the coordinate line density in each zone. The help functions H_i, on the other hand, are linear since the characteristic coordinate lines are mapped on piecewise linear functions, see Fig. 6.5(b). They would have to be replaced by other functions if the red and blue lines in Fig. 6.5(b) were bent instead of linear.

The resulting planar mesh is depicted in Fig. 6.5(c). In the subsequent section, we show how this mesh is enhanced to form a three-dimensional coordinate transformation.

6.3.3 Construction of the three-dimensional transformation

In the previous section, we obtained a mesh for a cross with arbitrary rotation angle φ. We discussed that this transformation can be applied in the layer of the rotated cross to align it to the grid in transformed space. However, the idea is to change the coordinate system *in between the crosses continuously*. This means that we obtain a different planar mesh for every value of x^3. This value of x^3 directly translates into a rotation angle. Explicitly, we perform coordinate transformations in the space between the crosses, too. At his point it becomes clear why we built the planar mesh in the subsequent section the way we did—for a given value of x^3 we only compute the rotation angle $\varphi(x^3)$ and easily obtain the planar mesh using Eqs. (6.6) and (6.8). Thus, we can write Eqs. (6.1) in a more precise way, i.e.,

$$\bar{x}^1 = \bar{x}^1\Big(x^1\Big(\bar{x}^3\Big),\ x^2\Big(\bar{x}^3\Big)\ \Big), \tag{6.10a}$$

$$\bar{x}^2 = \bar{x}^2\Big(x^1\Big(\bar{x}^3\Big),\ x^2\Big(\bar{x}^3\Big)\ \Big), \tag{6.10b}$$

$$\bar{x}^3 = x^3. \tag{6.10c}$$

The next step is to formulate the dependence of the rotation angle φ on the x^3 coordinate. The lower surface of the lower cross defines the $x^3 = 0$ plane. The height of one cross is denoted h and the distance between the crosses is denoted b. The upper cross is rotated by φ_0. The lower cross is not rotated. In between, we choose a linear function to make the transition from $\varphi = 0$ to $\varphi = \varphi_0$ since it seems the most reasonable approach. Thereby, we obtain the dependence of the mesh parameter φ on the x^3 coordinate:

$$\varphi\left(x^3\right) = \frac{\varphi_0}{b}\ \left(x^3 - h\right), \qquad x^3 \in [h, h+b]. \tag{6.11}$$

When numerically investigating this system, we rotate the mesh to φ_0 in the second layer and then rotate it back to the Cartesian mesh behind the second cross. The rotation back to the Cartesian mesh is performed on the distance b, such that the rotation to φ_0 and back is symmetric. This means that the rotation angle for the mesh construction behind the second cross is given by

$$\varphi\left(x^3\right) = -\frac{\varphi_0}{b}\ \left(x^3 - 2h - 2b\right), \qquad x^3 \in [2h+b, 2h+2b]. \tag{6.12}$$

Hereby, we complete the construction of the three-dimensional AC mapping.[5] In the following section, we briefly comment on ASR before we visualize the transformed permittivity in Section 6.4.

6.3.4 Adaptive spatial resolution

Up to this point we created an AC mesh leading to a fully anisotropic effective permittivity where the gold crosses are grid-aligned in both layers. Since we designed the three-dimensional adaptive coordinates such that the crosses are right above each other, it suffices to apply a two-dimensional, planar adaptive spatial resolution transformation function. The same ASR function is applied in every layer. We discussed the form of such functions with two material surfaces in great detail in Section 5.3.7. Since we need four compression points for the crosses, this transformation has to be adjusted. The expressions and the construction principle in Section 5.3.7 are very general though and can easily be extended for four compression points. We compress the mesh at the points $0.5-a-d, 0.5-a, 0.5+a, 0.5+a+d$ in each direction of the $[0,1]\times[0,1]$ unit cell since these are the coordinate lines enclosing the structure's surface, see Figs. 6.3(a), 6.4(a) and 6.5(a).

6.4 Visualization of the effective permittivity

Constructing a mesh is a rather complex and technical procedure. Visualizing its effect by plotting the transformed permittivity is, therefore, important to gain a deeper understanding of coordinate transformations in the FMM in general. For that, we choose a specific test system and plot the effective permittivity tensor elements together with the corresponding mesh. As stated above, the same ASR function is applied in all layers. Here, we only visualize the effect the adaptive coordinates have on the transformed permittivity.

The test system is a square lattice of crosses, mutually rotated by $\varphi_0 = 15°$. The lattice constant is 600 nm. The half-width of one cross' arm is $a = 25$ nm, the arm length is $d = 100$ nm. The cross height is $h = 25$ nm and the distance between the crosses is $b = 50$ nm. We assume the crosses to consist of gold, described by a Drude model with the parameters $\epsilon_\infty = 9.0685$, a plasma frequency $\omega_D = 1.3544\cdot 10^{16}$ Hz and a damping coefficient $\gamma = 1.1536\cdot 10^{14}$ Hz, see Ref. [25]. The wavelength we used for Fig. 6.7 is 1000 nm. The color scale in Figs. 6.7(a) and 6.7(c) has been saturated at 0 for ε^{11} and ε^{33} in order to see more features, even though the real part of the dielectric function of the gold crosses is about -42. We depict the ε^{11}, ε^{12}, ε^{13} and ε^{33} components of the effective permittivity. This suffices since the permittivity tensor is symmetric, e.g., $\varepsilon^{12} = \varepsilon^{21}$, and the mapping in Fig. 6.5 is C_4 symmetric. This results in ε^{22} and ε^{23} being ε^{11} and ε^{13} rotated counter clockwise by 90°, respectively. In all plots, we discretize the effective permittivity with 1024×1024 points.

In Fig. 6.7(a), the permittivity for the first layer is depicted. Since the cross is already grid-aligned, the rotation angle φ is zero and we have a Cartesian mesh. Therefore, the background ($\bar{\varepsilon}_{\mathrm{bg}} = 1$) and the cross permittivity ($\mathrm{Re}\,(\bar{\varepsilon}_{\mathrm{cross}}) \approx -42$) stay like they are in the untransformed space. In Fig. 6.7(b) the permittivity between the crosses is plotted. All tensor

[5] In the subsequent sections, the phrase "the mesh is rotated" is used. This is a bit colloquial but a lot shorter than "the parameter φ, which we used for the construction of the mesh, is increased". Naturally, this does not mean that the mesh itself is rotated; we always deal with a square, unrotated unit cell. However, the grid in zone ⑤, see Fig. 6.5, is rotated.

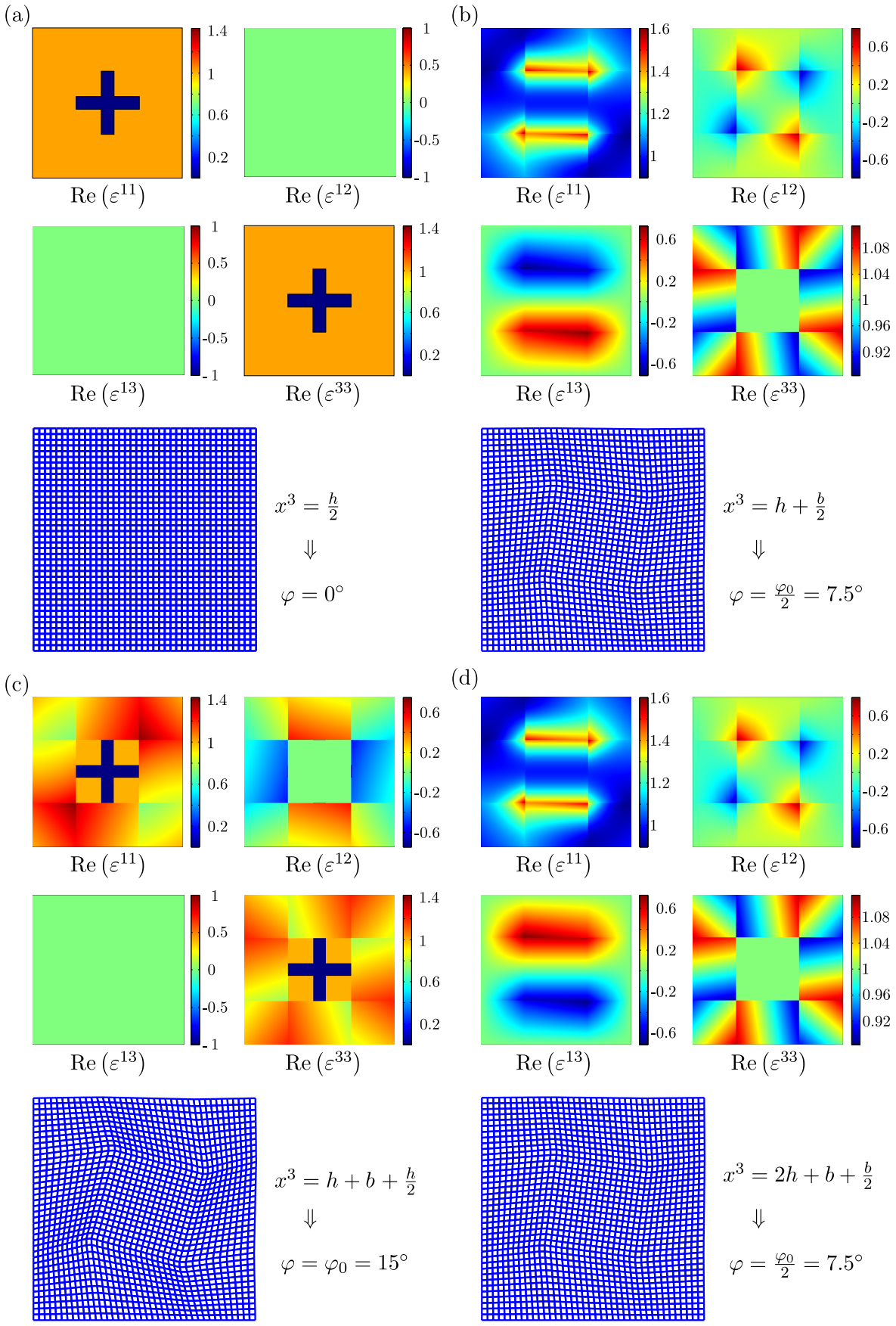

Figure 6.7: Real part of the effective permittivity for two layers of mutually rotated crosses transformed with the three-dimensional AC transformation. See text for further details.

components are non-zero and exhibit a strong spatial variation. Note that the permittivity in the untransformed, physical space has the value 1 everywhere in the unit cell since the volume in between the crosses is assumed to consist of air only.

The transformed permittivity inside the second layer of crosses is shown in Fig. 6.7(c). Here, the effective permittivity tensor is not fully anisotropic because the mesh does not change along x^3 within the second layer. A further observation is that our aim of a grid-aligned gold cross is achieved. In the vicinity of the gold-cross the permittivity has the value 1—this is due to the fact that the mesh was designed to be a rotated Cartesian mesh in zone ⑤ in Section 6.3.2. Finally, behind the second layer of crosses, the mesh is rotated back to $\varphi = 0°$. Behind the first cross the rotation angle φ (which is the x^3-dependent mesh parameter) increased. Behind the second cross it decreases. This sense of rotation is observable well in the ε^{13} components, compare Figs. 6.7(b) and 6.7(d). In this component, the sign changes due to the different sense of rotation with respect to the x^3 coordinate.

Having obtained the coordinate transformations and the effective permittivities, we investigate their performance in the subsequent section.

6.5 Preliminary numerical results

Before presenting actual computations, it is worth pointing out numerical advantages and disadvantages of the presented approach. The classical FMM faces a problem when it is applied to the test structure since the structure is not grid-aligned. This means that in-plane stair-casing and the Gibbs phenomenon massively reduce the method's accuracy. In fact, even if 10,000 plane waves could be used we would still face the problem of the in-plane stair-casing. So even when the classical FMM would lead to converged results for such a system it would only provide the converged result for the stair-cased, i.e., unphysical, structure. This could, in principle, be tackled by increasing both the number of the real space points for the Fourier transformation as well as the number of plane waves for the field expansion. However, especially memory is limited and, therefore, convergence for a system such as our test system can hardly be reached with classical FMM. This is the case even though only the small eigenproblem of the FMM needs to be solved which is 2^3 times faster than the large eigenproblem and consumes $(1/2)^2$ of the memory.

In contrast to this, our approach creates fully anisotropic tensors. Thus, the large FMM eigenproblem has to be solved, with much higher effort needed. The underlying aim is to obtain much more accurate results. Apparently, we have to slice the system into several more layers because each value of x^3 features a different effective permittivity. On the other hand, the metallic structures are fully grid-aligned and we can increase the density everywhere along the surface. So the trade would be to endure the computation of more layers but on the other hand gain better results with a much smaller number of plane waves.

In the following, we present first numerical investigations for such a three-dimensional transformation. The first test in Section 6.5.1 is an empty lattice calculation which means that the permittivity is unity everywhere in the physical, untransformed system. Thereafter, in Section 6.5.2, we investigate the numerical results of our test system of periodically arranged, mutually rotated crosses.

6.5.1 Empty lattice calculation

An important step in the method's validation is performing consistency checks such as an empty lattice calculation. We have performed convergence studies for the system described and visualized in Section 6.4, where we replaced the gold crosses with the background permittivity $\varepsilon_{\mathrm{bg}} = 1$. The wavelength for the calculation is 1070 nm. In all layers and all computations, we use the same ASR function to compress the coordinate lines. Its parameters are equal in x^1 and x^2 direction and read $\bar{x}_1 = P_{0,x^1}$, $\bar{x}_2 = 0.5 - a$, $\bar{x}_3 = 0.5 + a$, $\bar{x}_4 = S_{0,x^1}$, $\Delta x_1 = 0.2$, $\Delta x_2 = 0.2$, $\Delta x_3 = 0.2$, see Sections 6.3 and 5.3.7 for definitions.

We performed the computations for a varying number of layers. In the first layer (where the first cross would be), we used a Cartesian mesh. In the layer where the second, rotated cross would be, we used a mesh with rotation angle $\varphi = \varphi_0$. Figure 6.8 sketches how many intermediate layers were used in the computations and how the rotation angles of the mesh are defined. The layers where the crosses would be are shaded in yellow—this is only supposed to guide the eye, in the actual computations of this section we have $\bar{\varepsilon} = \varepsilon_{\mathrm{bg}}$ everywhere in the untransformed space.

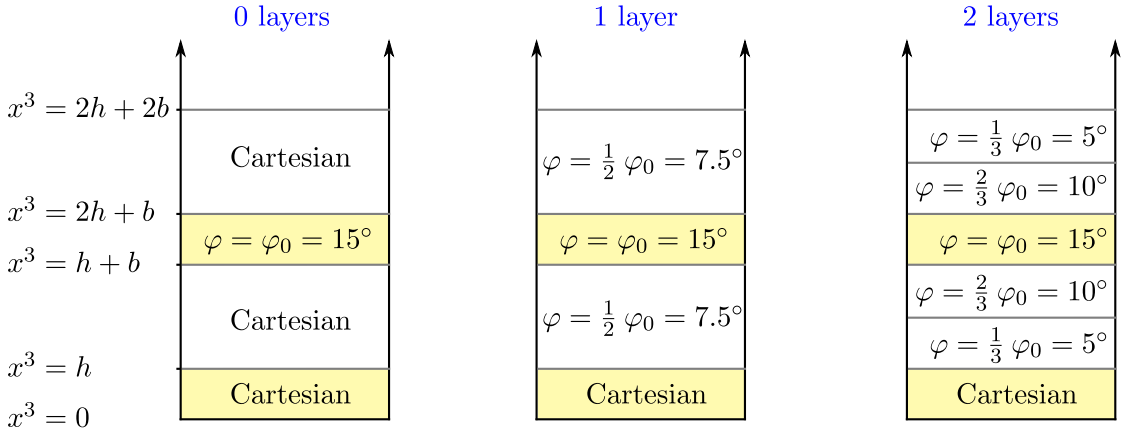

Figure 6.8: Number of intermediate layers for the calculation. In all layers the same ASR compression is used. This figure sketches how the AC (and, thereby, the permittivities and permeabilities) look like in each layer. In the case of 0 layers we transform the mesh only in the layer with $x^3 \in [h + b, 2h + b]$. The permittivity tensor used for the eigenproblem in this layer is depicted in Fig. 6.7(c). For 1 intermediate layer we solve 4 eigenproblems besides the incoming and outgoing layer—the effective permittivities that correspond to each eigenproblem are depicted in Fig. 6.7(a)-(d), only with the crosses replaced with $\varepsilon_{\mathrm{bg}}$. Even though the system consists of two-dimensional slices, the permittivity tensor in each slice contains the information of the three-dimensional rotation due to its full anisotropy, cf. Fig. 6.7.

The results of the empty lattice computations are depicted in Fig. 6.9. The first test of the three-dimensional coordinate transformations reveals certain weaknesses. In Fig. 6.9(a), we display a convergence study for the transmittance. We calculated the total transmittance for 50 to 1000 plane waves in steps of 25 and used a circular truncation scheme in k-space. In all cases, the transmittance does not reach one. With more than 600 plane waves the result only exhibits a relative variation by less than 10^{-4}. The computation with 0 layers (dashed) shows the same behavior like the computations with more layers but has a small offset to

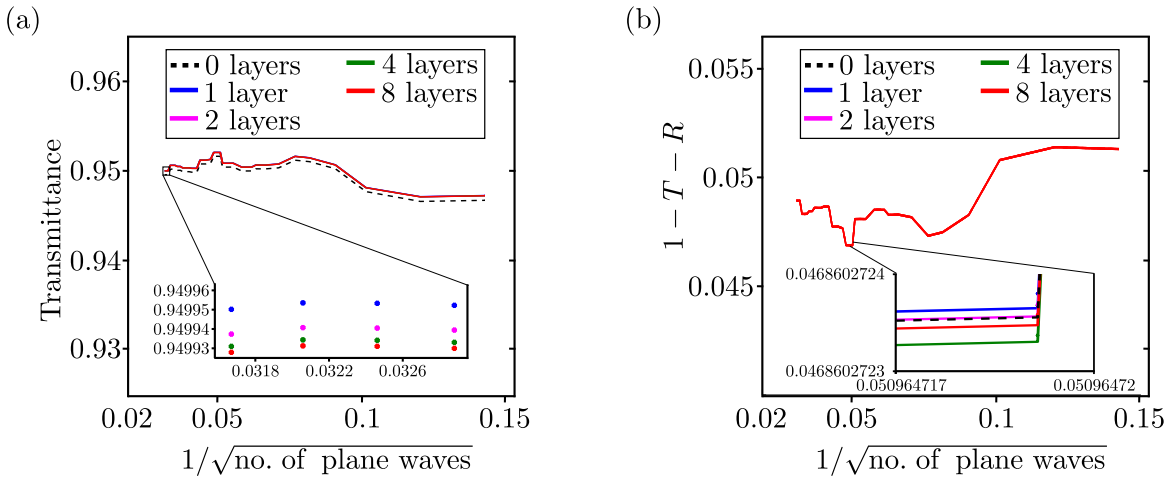

Figure 6.9: Convergence studies for the empty lattice calculated with the three-dimensional mesh at 1070 nm. Panel (a) displays the transmittance and panel (b) depicts the absorption of the system both in dependence of the square root of the reciprocal number of plane waves. Panel (a) shows that not all light is transmitted, whereas panel (b) depicts the absorption of the system.

them. The computations with 1, 2, 4 and 8 layers are rather close together, namely in an interval of $3 \cdot 10^{-5}$. In fact, this is an interesting result: positively speaking one could say that already one intermediate layer shows results close to 8 intermediate layers. Negatively speaking one could all call them equally wrong.

Fig. 6.9(b) depicts the absorption of the system, i.e., one minus transmittance T minus reflectance R. The reflectance of the system is rather small—however, we still miss about 5% of the systems energy.

Since our structure is C_4-symmetric, TE and TM polarization should yield the same results for normal incidence. We checked the difference between TE and TM for the values depicted in Fig. 6.9(a). In the case of 0 layers, the transmittance for TE and TM only differ by $1 \cdot 10^{-9}$. For all other numbers of layers, the transmittance for TE and TM polarization differs by a nearly constant value of $8 \cdot 10^{-4}$.

These results of the empty lattice calculation are not too promising. However, they give us a hint in which order of magnitude the error is. We discuss possible sources of error in Section 6.5.3.

6.5.2 Test structure calculation - two layers of crosses

In this section, the numerical results for the test structure depicted in Fig. 6.2 are discussed. The system parameters are as described in Section 6.4 and the ASR function used is the same as in the computations for the empty lattice. The wavelength for the convergence study in Fig. 6.10 is 1070 nm. Again, we calculated the total transmittance for 50 to 1000 plane waves in steps of 25 and used a circular truncation scheme in k-space. The periodic structure is illuminated under normal incidence with TE polarization. In this convergence plot, the transmittance is depicted as a function of the square root of the reciprocal number of plane waves. The transmittance was computed for a Cartesian mesh, with 0 intermediate layers between the AC layers with $\varphi = 0$ and $\varphi = \varphi_0$, and with 1, 2, 4 and 8 intermediate layers like described in Fig. 6.8.

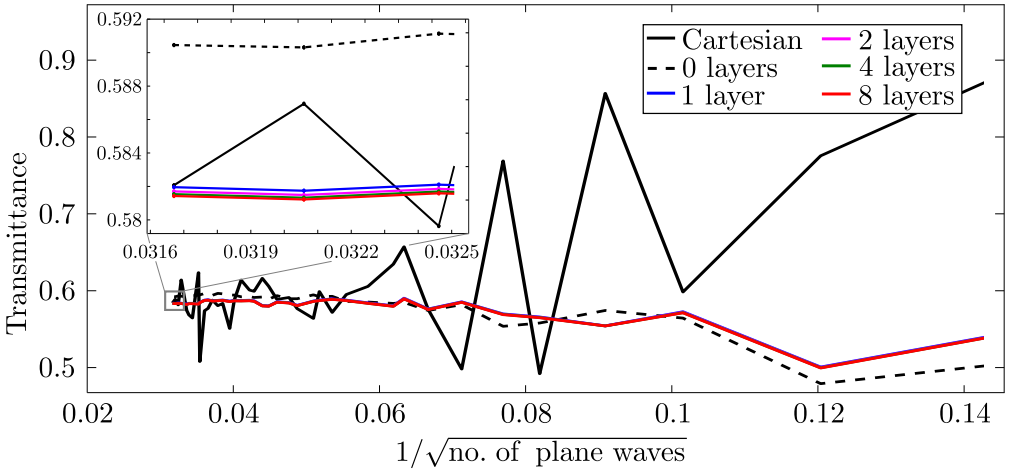

Figure 6.10: Convergence investigation for the transmittance of the double cross structure at 1070 nm in TE polarization for different numbers of intermediate layers. The cross rotation angle φ is 15°. The Cartesian mesh leads to an erratic convergence behavior while the three-dimensional mesh exhibits a smooth form.

The results are quite interesting: while the Cartesian mesh shows a very erratic convergence behavior, the transmittance calculations using the three-dimensional adaptive mesh converge very quickly. In particular, the transmittance using the Cartesian mesh shows variations for up to 50% for small numbers of plane waves. The three-dimensional AC and ASR mesh, on the other hand, varies only little even for few plane waves. Interestingly, like in Fig. 6.9, it does not make too much of a difference how many intermediate layers are chosen—the results for 1, 2, 4 and 8 show very little deviation from one another.

Unfortunately, a problem that we hinted at in the previous section is observable in the calculations for the test structure, too: the transmittance for TM polarization differs from the one for TE polarization, cf. Figs. 6.10 and 6.11(b). Again, due to the symmetry of the system, this should not be the case. For 0 layers TE and TM polarization yield the same results. In Fig. 6.11(a) we show the transmittance spectrum of the system for TE polarization obtained with 4 intermediate layers and 797 plane waves.

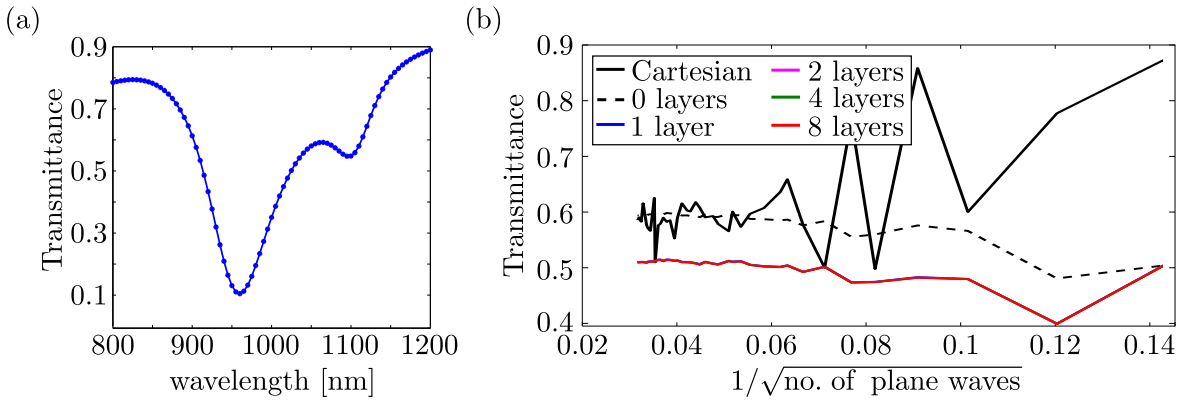

Figure 6.11: Transmittance spectrum for the double cross test structure with incident TE polarization, 4 intermediate layers and 797 plane waves shown in panel (a) and convergence study with TM polarization depicted in panel (b). While the data for the Cartesian mesh in panel (b) is consistent with Fig. 6.10, the results for the three-dimensional mesh show a deviation compared to the TE calculation. Due to the system's C_4 symmetry, this should not be the case.

6.5.3 Interpretation and specific problems

The results of the computations for the empty lattice and the two layers of mutually rotated crosses were ambiguous. The convergence behavior of the computations with the three-dimensional mesh are much smoother than the corresponding Cartesian computation. On the other hand, the strong difference between results for incoming TE and TM polarization points to remaining challenges.

In essence, developing a three-dimensional AC and ASR mesh is an important step towards new fields of application for the FMM. However, the method cannot be deemed reliable at this point. The issues occurring suggest that there is either an error in the FMM code itself or in the way we constructed the mesh and the effective permittivity. A hint towards an incorrect implementation is the strong absorption in the empty lattice calculation, cf. Fig. 6.9(b). A significant non-zero reflection would have hinted to problems with the matching of the layers. However, this is not the case. A possible source of error would be an incorrectly derived Poynting flux. Since TE and TM polarization yield the same results for two layers of crosses with 0 intermediate layers (cf. Figs. 6.10 and 6.11(b)) the (implementational or conceptual) error could be an effect of the rotation, i.e., $\varepsilon^{13} \neq 0 \neq \varepsilon^{23}$. Also, we might have made a conceptual mistake in either the construction and application of the three-dimensional adaptive mesh or in the interpretation of the numerical data. In conclusion, the open issues of this method have to be left for further studies.

There is a specific problem that we did not address up to this point: starting a plane wave in the AC and ASR approach is not always easy. As we discussed earlier, the expansion basis of the fields change due to the use of AC and ASR coordinate transformations. When we start a plane wave in the transformed space, this does not necessarily mean that it is also a plane wave in the untransformed (and, thereby, physical!) space. In fact, this is hardly ever the case. Therefore, a first approach is to start the eigenmode of the transformed system that is closest to a plane wave in the physical, Cartesian space. We applied this approach in the simulations presented in this chapter. A possible solution to this concern is examined in Section 6.6.

Although this is an important issue, it does not seem to be the cause for the problems observable in the previous sections. In the empty lattice, any mode should propagate regardless of whether it is a plane wave or not. Especially, this does not explain the energy loss discussed in Fig. 6.9(b).

6.6 Advanced concept

We stated above that it is difficult to start a plane wave in physical space, since this plane wave is also transformed when we change the basis functions due to the ASR transformation we perform in every layer. Here, we present an idea how this may be tackled. Note that this section solely addresses the problem of the properly started plane wave. The suggestions here are not expected to have a positive impact on the problems concerning the empty lattice calculations in Section 6.5.1.

In the above scheme, we gradually rotate the mesh when increasing the x^3 component. In analogy, we could also start to introduce the ASR function gradually with increasing x^3 before rotating the mesh. Thereby, the basis functions of the problem would be in the real, physical space. Therefore, we could easily start an ordinary plane wave in the incoming, Cartesian, physical half-space. Then, we could introduce several intermediate layers to start the ASR. The general procedure is sketched in Fig. 6.12(a). In this sketch, we start by a Cartesian layer at the bottom, cf. Fig. 6.12(b). In the next three layers, we gradually introduce the ASR as discussed in Section 5.3.7. "1/3 ASR" figuratively means that the ASR has reached a third of its desired strength, see Figs. 6.12(c) and (d).

Once the ASR is fully introduced at its desired strength (cf. Fig. 6.12(e)), the layer with the first cross can be computed (shaded in yellow). Then, like before, we rotate the mesh, only with an ASR applied before that, see Fig. 6.12(f). Once the mesh is rotated up to the cross rotation angle φ_0, we can compute the layer of the rotated cross, again shaded in yellow in Fig. 6.12(a). The mesh that is used to compute the effective permittivity in this layer is depicted in Fig. 6.12(g). Like above, we then gradually reverse the mesh changes—first, the mesh is rotated back, then the ASR is decreased until we reach the outgoing layer with a Cartesian mesh.

Mathematically, this looks the following: when we want the increase of the density to happen on the interval $x^3 \in [0, c]$, then the mapping has to obey

$$\bar{x}^1(x^1, 0) \stackrel{!}{=} x^1, \tag{6.13a}$$

$$\bar{x}^1(x^1, c) \stackrel{!}{=} ASR(x^1). \tag{6.13b}$$

Here, ASR denotes the compression function (cf. $\bar{x}(x)$ in Section 5.3.7). A linear introduction of the ASR seems most reasonable. Therefore, a suitable function fulfilling the requirements is

$$\bar{x}^1(x^1, x^3) = \frac{1}{c}\left(ASR(x^1) - x^1\right) x^3 + x^1 \tag{6.13c}$$

The $\bar{x}^2$ mapping is constructed similarly.

Conceptually, the whole coordinate transformation still has the form of Eqs. (6.1). For any given value of x^3 we first compress the coordinate lines and then apply the AC coordinate transformation. The result are meshes like in Fig. 6.12. The great advantage of such a procedure would be that it could be easily incorporated into any classical FMM code which

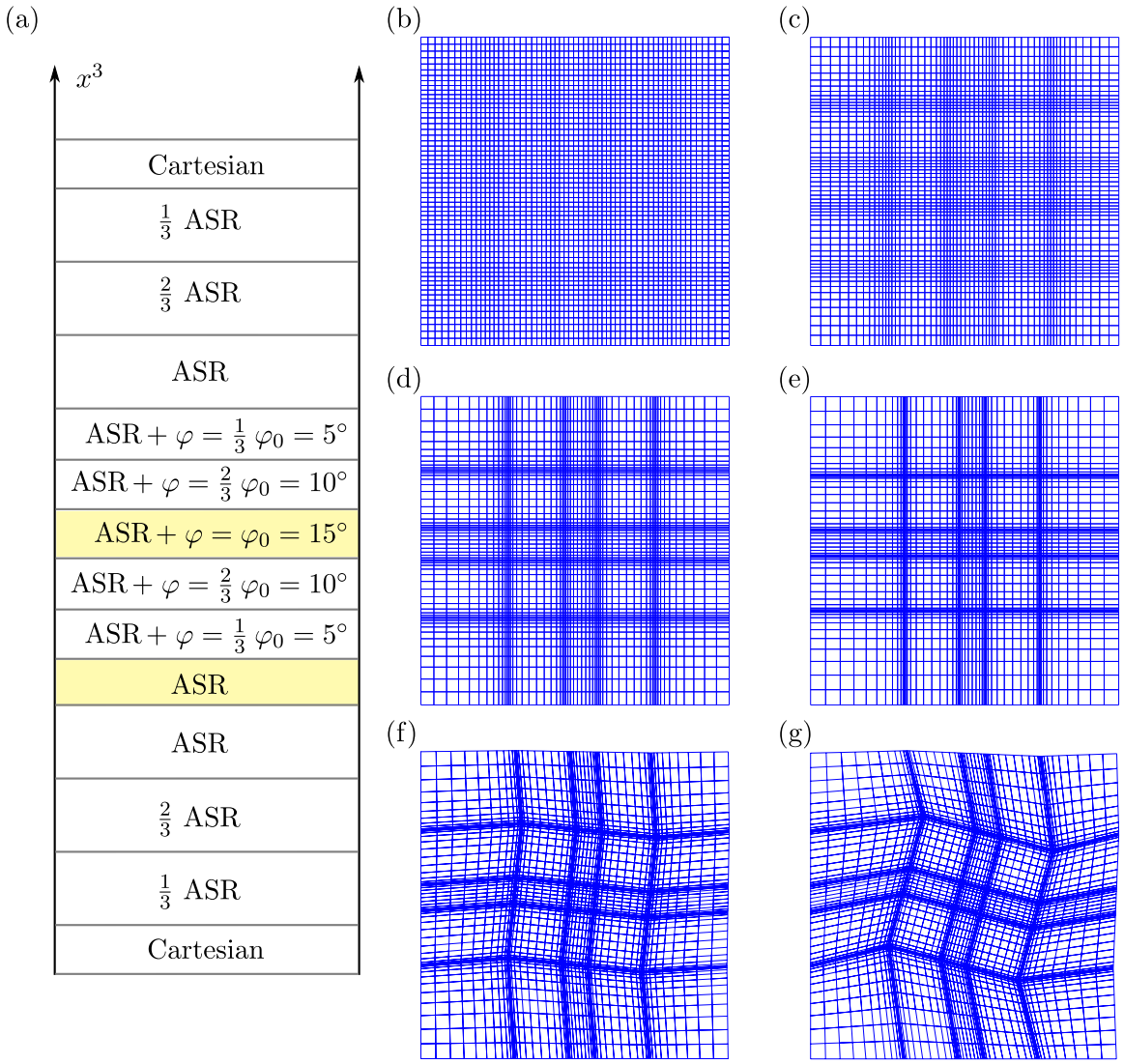

Figure 6.12: Three-dimensional meshing with a Cartesian layer as first and last layer. Starting from Cartesian, physical, untransformed space, we could gradually increase the density of coordinate lines using a x^3 dependent compression function. Then, after the layer with the grid-aligned cross, the mesh is rotated up to the angle φ_0 in the layer with the second cross. After this, the mesh is rotated back and the coordinate line density is reduced until the mesh is Cartesian again. The corresponding meshes are depicted in panels (b) to (g). From those meshes we can compute the transformed permittivity and permeability tensors.

can solve the large eigenproblem. Since the incoming and outgoing layer are Cartesian, this is perfectly compatible. So any classical FMM code that can solve the large eigenproblem could just be given the transformed permittivity and permeability and would, thereby, incorporate three-dimensional coordinate transformations. This could be particularly interesting when using ASR and AC in combination with open source codes of the classical FMM, see Refs. [38, 39].

Chapter 7

Coupled-Dipole Models for Slabs of Metallic Nanostructures

Up to this point we predicted the optical properties of slabs of periodic nanostructures by solving Maxwell's equations using a suitable dielectric function ε to describe the structure's optical response. To do so, we found ways to predict the optimal mesh parameter regions for numerical calculations with the Fourier Modal Method. However, often enough we are not interested in high accuracy calculations but rather in finding optimized designs. This calls for a different approach since finding such designs by solving Maxwell's equations for various geometries is time- and memory-consuming. Therefore, a simple and analytical model to predict optical properties would be of great help. The aim of this chapter is to find a model for periodic, metallic, multi-layer nanostructures that is able to identify interesting geometries or parameter regions with the desired properties. These geometries can then be investigated further using common Maxwell solvers. In my "Wissenschaftliche Arbeit zur Zulassung zum ersten Staatsexamen im Fach Physik" [62] (from now on referred to as *Staatsexamensarbeit*) I started to design such a model. This chapter presents several extensions to this work.

I carried on to develop this model since it became clear at the end of the Staatsexamensarbeit that the approach had to be extended.

Before we focus on the details of the model, we start by reviewing related methods and models in Section 7.1. The systems considered in this chapter are discussed in Section 7.2. This is followed by a review of the methods and the dipole model used in the Staatsexamensarbeit in Section 7.3. Here, we encounter strengths and shortcomings of the dipole model. A particular strength of this model is investigated in Section 7.4. Because the dipole model in Ref. [62] does not include effects of the lattice, we show how these effects can be incorporated in the method in Section 7.5.

The mentioned shortcomings of the dipole model lead us to an important new model—the twin dipole model. Here, we first face certain technical aspects of the model's development in Section 7.6. This is followed by the presentation of the model's predictions in Section 7.7. There, we show that the new twin dipole model is significantly better than the dipole model since it reproduces physical aspects of the investigated systems that are absent in the dipole model. In Section 7.8 we demonstrate how a near-field coupling can be incorporated in the method. Although the results are ambiguous, they lay the route for possible future work. This is also the case for the approach presented in Section 7.9 where a generalized model with a continuous charge distribution is outlined. The chapter is concluded in Section 7.10 with a summary and an outlook.

The development of the models presented in this chapter was conducted over a long period of time. Along this route, many people offered ideas how to proceed and improve the models.

In particular, this work has benefited from the regular input and discussions with Kurt Busch and Christian Wolff.

7.1 Related methods

In the past years, many models were developed to describe the optical properties of metallic nanostructures. Different models emerged for different structures. For example, a common model for split ring resonators is an inductor-capacitor circuit [63]. For the systems investigated in this chapter (see Section 7.2) there exist various models. They deal either with the description of the single meta-atom, i.e., the basic building blocks that metamaterials consist of (see Ref. [64]) or they try to describe the light propagation in these metamaterials by an effective medium approach [65, 66, 67]. Therein, it is assumed that the material's response can be described by means of an effective permittivity tensor. The aim of these models is to derive the effective material properties by considering different physical mechanisms.

A method similar to the model presented in this thesis is the discrete dipole approximation, see Ref. [68]. Here, each element of the constituent meta-atoms is modeled as a point dipole with electric (and possibly magnetic) polarizability. However, depending on the number of dipoles, this method is on the edge between numerical and analytical method.

Especially when the metamaterial consists of several layers, the interlayer coupling is a controversially debated topic. There are several models, some of which contain dipole-dipole coupling [69], inductive coupling [70] and higher order multipoles [65]. So far, the 'holy grail' has not yet been found—although many models show features similar to either experiment or ab initio numerics, they often lack the ability to fully describe and predict the transmission properties of light through the considered nanostructures.

7.2 Considered systems

In this section, we briefly discuss the investigated systems and their basic physical properties. The numerical data is presented together with the predictions of the models in the subsequent sections. Since the basic idea of these models is to describe metallic nanostructures as coupled dipoles, the structures we investigate have a suitable form: the simplest structure in this chapter is one layer of periodically arranged metallic rods. These rods may be rotated within the unit cell, see Fig. 7.1.

Throughout this chapter, the incident light is linearly polarized in x-direction. Naturally, the system strongly depends on the polarization of the incident light. The more the polarization coincides with the orientation of the rod, the more the charges are displaced from their equilibrium positions. This also means that the absorption is strongest, when the polarization is parallel to the rods. Hence, the system exhibits linear dichroism. In general, the transmission is strongly influenced by the polarization's orientation with respect to the rod. Therefore, we also find linear birefringence-like behavior. The problem is that the term birefringence refers to different permittivities for different field components. However, the system is not very thick and, thus, it is questionable how well an effective medium description of this system in terms of an effective permittivity tensor can be.

Another important question is whether circular effects occur. Due to the symmetry of the single meta-atom, it does not show circular effects. Yet, the periodic arrangement does, see

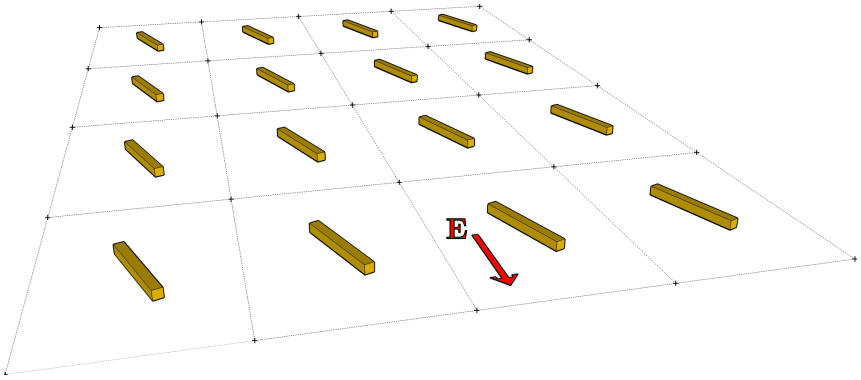

Figure 7.1: The basic system consists of one layer of periodically arranged rods. While the incident field is always assumed to be linearly polarized in x-direction, the rods may be rotated within the unit cell.

Ref. [62]. When a circularly polarized field is incident on the structure, the light transmitted through the periodic arrangement is a superposition of left- and right-circularly polarized fields (LCP, RCP). For the periodic arrangement of rotated rods, the conversion from incident RCP to transmitted LCP does not yield the same results as for LCP to RCP. A similar effect has been observed in 'fish-scale' metameterials, see Ref [71].

The second structure we investigate is a layer of rotated crosses. Effectively, this structure can be regarded as two superimposed, perpendicular rods. This structure does not show linear polarization effects which is due to its C_4 symmetry. Any incident linear polarization can be split into parts parallel to one of the crosses' arms. Then, each of these parts 'sees' only one rod and is transmitted like in the case of one layer of unrotated rods. Behind the cross, the two parts can be recombined again with the result of light that is identical to the light transmitted by an unrotated rod. This picture is valid for any cross rotation angle. Hence, no linear effects occur.

The more complex systems considered in this chapter are depicted in Fig. 7.2.

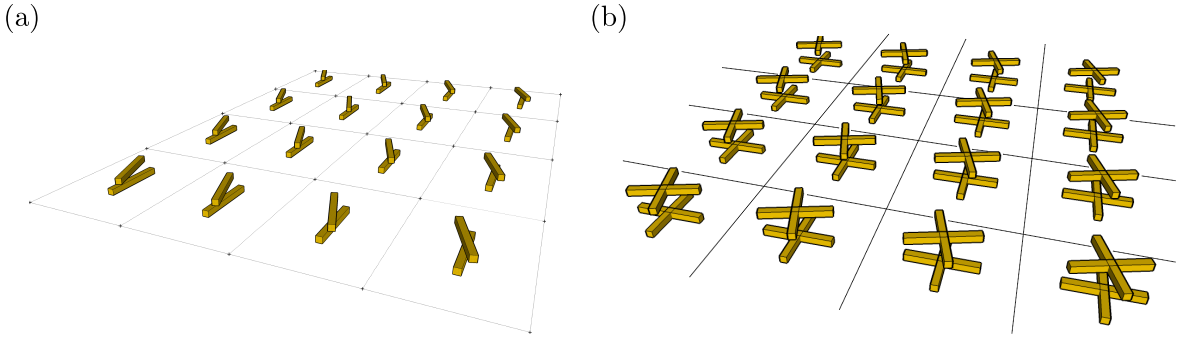

Figure 7.2: The most complex structures considered in this chapter are two layers of periodically arranged, mutually rotated, metallic rods and crosses.

An important property of such systems is the coupling between the layers. In this chapter, we present models based on the assumption that the coupling is dominated by the dipole-dipole interaction between the rods. For two layers of rods we investigate the transmitted light when the upper rod is rotated. Then, the polarization behind the slab is elliptically. Again, linear dichroism occurs.

The most complex and physically challenging structure is depicted in Fig. 7.2(b)—two layers of mutually rotated crosses. This structure has gathered a lot of attention, see Refs. [58, 72, 73]. Here, we touch the subject of *chirality*. A structure is called chiral when it has a handedness, a sense of rotation. For most angles this is the case for the structure shown in Fig. 7.2(b). The question arises whether circular effects occur, i.e., whether σ^+ and σ^- polarizations are treated differently since one has the same sense of rotation like the structure and the other does not. Since the structure is C_4 symmetric, the same line of argument as for one layer of crosses applies—thus, the structure does not show linear polarization effects. Hence, any polarization rotation can directly be attributed to the different transmission behavior of left- and right-circularly polarized light. More elaborate analyses of chiral nanostructures can be found in Refs. [8, 74, 75, 76].

The parameters of the investigated systems are discussed at the appropriate places where the numerical data and the model's predictions are discussed. The rods and crosses are assumed to be cuboids, i.e., invariant in z-direction since this makes the numerical investigations drastically easier. The numerical reference computations used throughout this chapter were obtained by Sabine Essig with the classical Fourier Modal Method [34]. For each calculation, 841 plane waves were used. The reason for applying the classical FMM in all cases is that no fully reliable three-dimensional ASR and AC calculations are available, yet. Naturally, we could use ASR and AC for single layer structures. However, we would then fit the free parameters of the models to numerical data obtained with one method and, thereafter, try to fit the coupling for multi-layer systems to numerical data obtained with another method. Therefore, it seems most reasonable to use the same method for all calculations to ensure consistency.

In Chapter 6, we argued that rotated, metallic structures are very challenging for the classical FMM. For example, resonances in the transmittance tend to shift even between calculations with high but different numbers of plane waves. However, the models applied contain free parameters such as the resonance frequency—a shift in the numerical data would just result in a slightly varied fit parameter. Thus, the underlying physics is not affected—after all, this is what we try to model in this chapter.

7.3 Review of own previous work

In this section, I review the most important content of my Staatsexamensarbeit [62]. Naturally, content, notation and formulation are closely related to Ref. [62]. This is an important section since we reuse many of the formulations and concepts presented here throughout the entire chapter.

I start by discussing the field emitted by an oscillating charge in Section 7.3.1. This is followed by the discussion of a scattering matrix formalism in Section 7.3.2. In the subsequent Section 7.3.3 I review how light is transmitted through a slab of identical, randomly distributed, non-interacting particles. The three following Sections 7.3.4, 7.3.5 and 7.3.6 present the predictions of the model for a layer of rods and crosses and two layers of rods and crosses. The section is concluded with a short summary in Section 7.3.7.

7.3.1 Theoretical background: field and dipole moment of an oscillating charge

Assume an illuminated, oscillating particle with charge $-e$. Since the particle is accelerated by the external field it emits radiation. The field at the point $\mathbf{Q}$ is given by [20]

$$\mathbf{E}_{rad}(\mathbf{Q},t) = -\frac{1}{4\pi\varepsilon_0}\,\frac{e}{r\,c^2}\,\left[\mathbf{n}\times(\mathbf{n}\times\ddot{\mathbf{r}}_{\text{oscill}}(t))\right]_{t-\frac{r}{c}}, \tag{7.1}$$

where r is the distance to the observer and $\mathbf{r}_{\text{oscill}}$ is the position vector of the oscillator, see Fig. 7.3.

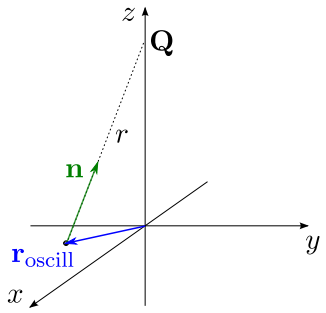

Figure 7.3: The unit vector $\mathbf{n}$ points from the position of the oscillator to the observer at $\mathbf{Q}$.

The vector $\mathbf{n}$ is the unit vector pointing from the position of the oscillator to the observer:

$$\mathbf{n} = \frac{\mathbf{Q}-\mathbf{r}_{\text{oscill}}}{|\mathbf{Q}-\mathbf{r}_{\text{oscill}}|}. \tag{7.2}$$

Since the observer is located at distance r, a retardation $(t-\frac{r}{c})$ enters into Eq. (7.1). Using Eq. (7.1) we can determine the field emitted by the charge at any point of the system.

By performing a multipole expansion like in [21], we obtain the dipole moment of a charge distribution ρ as

$$\mathbf{P} = \int d^3r'\mathbf{r}'\rho(\mathbf{r}'), \tag{7.3}$$

which reduces for a single electron (whose charge distribution is characterized by a delta function at the point of the charge) to

$$\mathbf{p} = -e\,\mathbf{r}(t). \tag{7.4}$$

7.3.2 Theoretical background: scattering matrix formalism

We already introduced scattering matrices in the framework of the Fourier Modal Method. They related the fields between different layers. Here, we introduce a scattering matrix that works similarly. This new scattering matrix relates the electric field incident on a scatterer (a plane, harmonic wave) with the light scattered by it. For this purpose, we define different coordinate systems which are depicted in Fig. 7.4.[1]

[1] The content of this and the subsequent section follows Ref. [18] and, thus, uses their notation. Furthermore, Figs. 7.4 and 7.5 are adapted from Refs. [18] and [62].

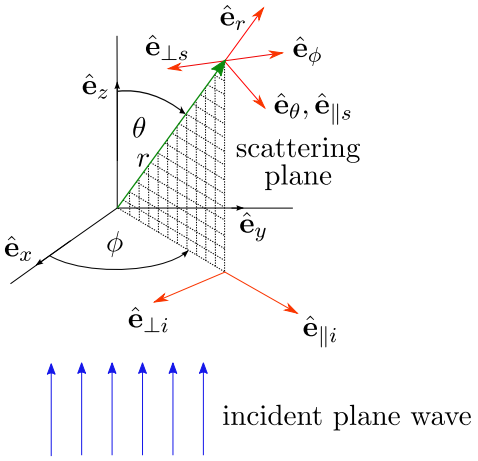

Figure 7.4: Coordinate systems used for the scattering matrix formalism. The scatterer defines the origin of the coordinate system $Oxyz$.

As depicted in Fig. 7.4, the propagation direction of the incident plane wave, also called the *forward direction*, defines the z-axis. Any point of the particle may be used as origin. The x and y axes form a Cartesian coordinate system with the z axis but underlie no further restrictions. The so-called *scattering plane* is defined by the scattering direction $\hat{\mathbf{e}}_r$ and the forward direction $\hat{\mathbf{e}}_z$. When $\hat{\mathbf{e}}_r$ is parallel to $\hat{\mathbf{e}}_z$, we choose $\phi = 0$ to determine the scattering plane.

We start by decomposing the incident electric field (which lies in the xy plane) into parts parallel and perpendicular to the scattering plane, i.e.,

$$\mathbf{E}_i = (E_{0x}\,\hat{\mathbf{e}}_x + E_{0y}\,\hat{\mathbf{e}}_y)\; e^{ikz-i\omega t} = E_{\parallel i}\,\hat{\mathbf{e}}_{\parallel i} + E_{\perp i}\,\hat{\mathbf{e}}_{\perp i}, \tag{7.5}$$

with

$$\hat{\mathbf{e}}_{\perp i} = -\hat{\mathbf{e}}_\phi, \qquad \hat{\mathbf{e}}_{\parallel i} = \sin\theta\,\hat{\mathbf{e}}_r + \cos\theta\,\hat{\mathbf{e}}_\theta, \tag{7.6}$$

which form a right-handed coordinate system with $\hat{\mathbf{e}}_z$:

$$\hat{\mathbf{e}}_{\perp i} \times\ \hat{\mathbf{e}}_{\parallel i} = \hat{\mathbf{e}}_z. \tag{7.7}$$

In Eq. (7.6) we use the orthonormal basis vectors $\hat{\mathbf{e}}_r$, $\hat{\mathbf{e}}_\theta$ and $\hat{\mathbf{e}}_\phi$ of the common spherical coordinate system (r, θ, ϕ).

In the far-field region (characterized by $kr \gg 1$), the scattered electric field $\mathbf{E}_s$ is approximately transverse and has the asymptotic form [20]

$$\mathbf{E}_s \quad \sim \quad \frac{e^{ikr}}{-ikr}\,\mathbf{A}, \qquad\qquad \hat{\mathbf{e}}_r \cdot \mathbf{A} = 0. \tag{7.8}$$

Thus, in the far-field region we can decompose it using the coordinate system

$$\hat{\mathbf{e}}_{\parallel s} = \hat{\mathbf{e}}_\theta, \qquad \hat{\mathbf{e}}_{\perp s} = -\hat{\mathbf{e}}_\phi, \qquad \hat{\mathbf{e}}_{\perp s} \times \hat{\mathbf{e}}_{\parallel s} = \hat{\mathbf{e}}_r. \tag{7.9}$$

Then the scattered electric field in the far-field region reads

$$\mathbf{E}_s = E_{\parallel s}\,\hat{\mathbf{e}}_{\parallel s} + E_{\perp s}\,\hat{\mathbf{e}}_{\perp s}. \tag{7.10}$$

Since the boundary conditions for Maxwell's equations at the surface between two media are linear, the amplitude of the scattered field is a linear function of the amplitude of the incident

field [18, 20]. This can be formulated in a matrix relation between the incident and scattered electric field

$$\begin{pmatrix} E_{\parallel s} \\ E_{\perp s} \end{pmatrix} = \frac{e^{ik(r-z)}}{-ikr} \begin{pmatrix} S_2 & S_3 \\ S_4 & S_1 \end{pmatrix} \begin{pmatrix} E_{\parallel i} \\ E_{\perp i} \end{pmatrix}, \tag{7.11}$$

where z denotes the z-component of the observer and r denotes the distance between the particle and the observer. It is noteworthy that $\mathbf{E}_i$ and $\mathbf{E}_s$ are expressed in different coordinate systems, see Eqs. (7.5) and (7.10). Also, we should keep in mind that the entries of this amplitude scattering matrix are angular dependent, i.e.,

$$S_j = S_j(\theta, \phi), \qquad j = 1, ..., 4. \tag{7.12}$$

Therefore, we obtain a different scattering matrix when the point of observation changes.

7.3.3 Theoretical background: reflection and transmission through a slab

The aim of the dipole model is to predict the transmission properties of light through periodic nanostructures. However, we assume that the response of a single scatterer is independent of the surrounding scatterers. Consequently, we assume that our slab of periodically arranged scatterers may as well be described by a slab of randomly distributed, non-interacting scatterers. Therefore, we discuss the transmission properties of such a slab. It is assumed to be infinitely extended in the xy-plane and finite in z-direction. The scatterer's distribution is assumed to be random but more or less uniform. A sketch is depicted in Fig. 7.5. In the following, we assume a sufficiently large number of particles such that the summation over the scattered field can be approximated by an integration. In a certain sense, we describe the slab of scatterers as an effective medium.

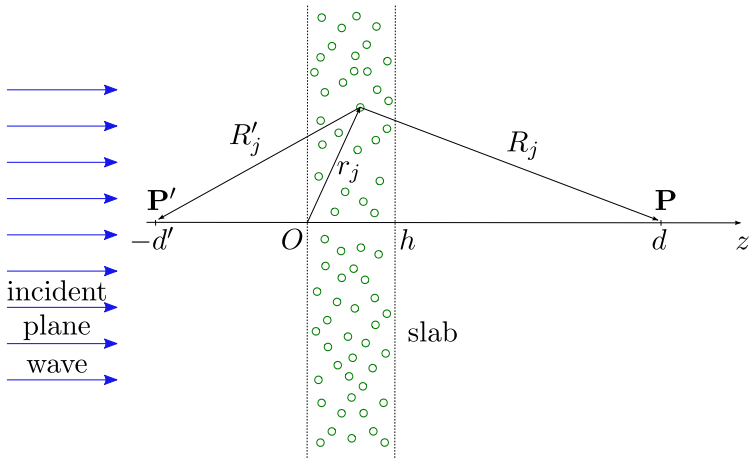

Figure 7.5: Sketch of a slab with randomly distributed scatterers. A plane wave is incident in z-direction. The observer is located at point $\mathbf{P}$. The field at $\mathbf{P}$ is given by the superposition of the incident field and the field scattered by each particle.

The incident field is assumed to be a plane wave which is polarized in x-direction, i.e.,

$$\mathbf{E}_i = E_0 \, e^{ikz - i\omega t} \, \hat{\mathbf{e}}_x. \tag{7.13}$$

The scattered field at a point $\mathbf{P}$ is given by the sum of the incident field and all scattered fields. With the field $\mathbf{E}_{sj}$ scattered by the jth particle this reads

$$\mathbf{E}_t = \mathbf{E}_i + \sum_j \mathbf{E}_{sj}. \tag{7.14}$$

Next, we introduce the so-called *vector scattering amplitude*, defined as

$$\mathbf{X} = (S_2 \cos\phi + S_3 \sin\phi)\ \hat{\mathbf{e}}_{\parallel s} + (S_4 \cos\phi + S_1 \sin\phi)\ \hat{\mathbf{e}}_{\perp s}. \tag{7.15}$$

The symbol $\mathbf{X}$ is used as a reminder that the incident plane wave is polarized in x-direction. This is the case throughout the entire chapter. The unit vectors in Eq. (7.15) are defined as in Section 7.3.2 and the S_i are the entries of the amplitude scattering matrix as defined in Eq. (7.11).

With the definitions in Eqs. (7.11) and (7.15) we can calculate the scattered field at the point $\mathbf{P}$ caused by the jth particle at position (x_j, y_j, z_j). It reads

$$\mathbf{E}_{sj} = \frac{e^{ikR_j}}{-ikR_j}\,\mathbf{X}_j(\hat{\mathbf{e}}_j)\,E_0 e^{ikz_j - i\omega t}, \qquad R_j = |\mathbf{R}_j|\,, \tag{7.16a}$$

$$\hat{\mathbf{e}}_j = \frac{\mathbf{R}_j}{R_j}, \qquad \mathbf{R}_j = -x_j\,\hat{\mathbf{e}}_x - y_j\,\hat{\mathbf{e}}_y + (d - z_j)\,\hat{\mathbf{e}}_z. \tag{7.16b}$$

Note that the vector scattering amplitude (and, thereby, the scattering matrix entries) depends on $\hat{\mathbf{e}}_j$, i.e., the position of the particle relative to the observer.

Next, we simplify the sum over all scattered fields in Eq. (7.14). Firstly, we realize that our material consists of identical particles and secondly, we assume that the number of particles per unit volume is sufficiently large such that the summation in Eq. (7.14) may be replaced by an integration over the continuous variables x, y and z. Therefore, the sum turns into

$$\sum_j \mathbf{E}_{sj} \simeq E_0 e^{-i\omega t} \int_0^h dz \int_{-\infty}^{\infty}\int_{-\infty}^{\infty} \frac{e^{ik(R+z)}}{-ikR}\,\mathbf{X}(\hat{\mathbf{e}})\,\mathcal{N}\,dx\,dy, \tag{7.17}$$

where $R = \sqrt{x^2 + y^2 + (d-z)^2}$, $\hat{\mathbf{e}} = \frac{\mathbf{R}}{R}$ and $\mathcal{N}$ denotes the number of particles per unit volume. Although the integrals' limits in Eq. (7.17) are infinite, the integrals have a finite value since it is independent of the lateral extent of the slab if the extent is large compared to $\sqrt{4\pi d/k}$ (see Ref. [18]). Evaluating the integrals yields

$$\mathbf{E}_t = E_0\, e^{-i\omega t + ikd}\,\left[\left(1 - \frac{2\pi\mathcal{N}}{k^2}(\mathbf{X}\cdot\hat{\mathbf{e}}_x)_{\theta=0} h\right)\,\hat{\mathbf{e}}_x - \frac{2\pi\mathcal{N}}{k^2}(\mathbf{X}\cdot\hat{\mathbf{e}}_{\mathbf{y}})_{\theta=0} h\,\hat{\mathbf{e}}_y\right] \tag{7.18}$$

for the transmitted field at point $\mathbf{P}$. We recognize two features in Eq. (7.18). Firstly, the polarization of the field will be rotated if $(\mathbf{X}\cdot\hat{\mathbf{e}}_y)_{\theta=0} \neq 0$. Secondly, we only need the scattering information in forward direction to determine the transmitted field ($\theta = 0$). As we have stated in Section 7.3.2, we choose $\phi = 0$ to determine the scattering plane in forward direction. In that case, i.e., $\theta = \phi = 0$, the vector scattering amplitude reduces to

$$\mathbf{X}(\theta = \phi = 0) = S_2(0,0)\,\hat{\mathbf{e}}_x + S_4(0,0)\,(-\hat{\mathbf{e}}_y). \tag{7.19}$$

This means that we only have to determine two scattering matrix entries for one particle and, thereby, obtain the field that is transmitted through the slab.

In a similar fashion we can calculate the field reflected by the slab. The reflected field $\mathbf{E}_r$ at the point $\mathbf{P}'$ is given by the sum of all scattered fields

$$\mathbf{E}_r = \sum_j \frac{e^{ikR'_j}}{-ikR'_j}\,\mathbf{X}_j(\hat{\mathbf{e}}_j)\,E_0 e^{ikz_j - i\omega t}, \tag{7.20}$$

where $\mathbf{R}'_j = -(x_j\,\hat{\mathbf{e}}_x + y_j\,\hat{\mathbf{e}}_y + (d' + z_j)\,\hat{\mathbf{e}}_z)$. By applying the same methods and assumptions as before, we obtain

$$\mathbf{E}_r = -E_0 e^{-i\omega t + ikd'} \left(1 - e^{i2kh}\right) \frac{i\pi\mathcal{N}}{k^3}\,\mathbf{X}_{\theta=180^\circ}. \tag{7.21}$$

As discussed in [18],

$$\mathbf{X}_{\theta=0} = \mathbf{X}_{\theta=180^\circ} \tag{7.22}$$

is valid for particles small compared to the wavelength, which holds true in our case.

A characteristic quantity we use in the subsequent sections is the *transmittance* which is defined by

$$T = \frac{|\mathbf{E}_t|^2}{|\mathbf{E}_i|^2}. \tag{7.23}$$

The *reflectance* is defined analogously. Since we do not neglect absorption, reflectance and transmittance do not add up to one.

7.3.4 One layer of rods and one layer of crosses

Basic course of action

In this section, we discuss the first, easy applications of the dipole model[2]. The systems under investigation are a layer of periodically arranged rods and a layer of periodically arranged crosses, see Fig. 7.6. This section also demonstrates how the general calculation of the transmitted field looks like. First, we replace the rod by a dipole centered in the middle of the rod. The cross is modeled by two dipoles orthogonal to each other. Then, we set up equations of motion for the charge that is oscillating due to the external field, similar to the equation of motion for a Lorentz oscillator (see Section 2.2.1). Then, we derive the dipole field that is emitted by the oscillator and, thereby, obtain the suitable scattering matrix, see Section 7.3.2. This scattering matrix is used to derive the field transmitted through a slab of particles according to Section 7.3.3. Finally, the free parameters of the model are fitted to numerical data.

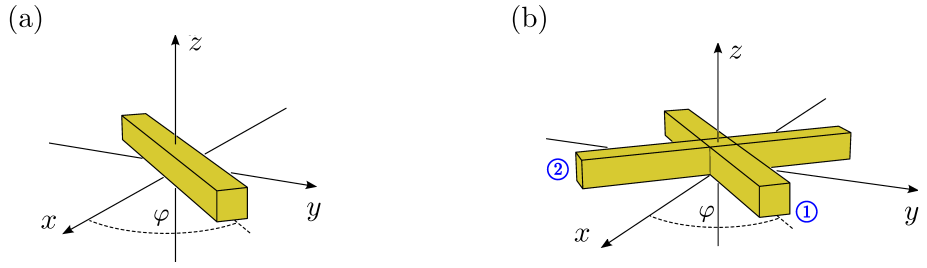

Figure 7.6: The two building blocks of the investigated structured layers. The layers discussed in this section consist of a periodic arrangement of rotated rods (panel (a)) and rotated crosses (panel (b)).

In the following, we choose the origin of the coordinate system to be in the middle of the bottom surface of the rod (or the cross). Therefore, the center of the rod, which is also the

[2]Throughout the chapter, the terms “dipole model” and “oscillator model” are used interchangeably.

position of the oscillator, is given by $(0, 0, h/2)$, with the rod height h. The incident field is a plane wave polarized in x-direction propagating in z-direction.

Equation of motion for a single rod

The oscillator is a point dipole that is excited in the direction of the longest extent of the rod. Using cylindrical coordinates, we find the oscillator at

$$\mathbf{r}(t) = \begin{pmatrix} \rho(t)\,\cos\varphi \\ \rho(t)\,\sin\varphi \\ \frac{1}{2}h \end{pmatrix}, \tag{7.24}$$

where the rod is rotated by the angle φ with respect to the x axis. The equation of motion we want to use includes a damping term γ and a resonance frequency ω_0. We always assume the incident field to be polarized in x-direction. Therefore, the rotated rod is only excited by the field component parallel to the largest extent of the rod. Thus, the equation of motion reads

$$\ddot{\rho} + \Gamma\,\dot{\rho} + \omega_0^2\,\rho = -\frac{N\,e}{N\,m}\,E_0\,e^{-i\omega t + ik\frac{h}{2}}\,\cos\varphi. \tag{7.25}$$

Here, N is the number of free electrons contributing to the dipole. With a time-harmonic ansatz $e^{-i\omega t}$ for ρ, the solution to Eq. (7.25) is given by

$$\rho(t) = -\frac{e}{m}\,\frac{1}{\omega_0^2 - \omega^2 - i\omega\Gamma}\,E_0\,e^{-i\omega t + ik\frac{h}{2}}\,\cos\varphi. \tag{7.26}$$

We note that the rod is not excited when it is oriented along the y-direction and that the influence of neighboring rods in adjacent unit cells is not explicitly included in the equation of motion.

Derivation of the scattering matrix entries

The far-field of the dipole is given by Eq. (7.1). In our case, on the z axis we observe the field

$$\mathbf{E}_{\mathrm{rad}}\,(0, 0, r + h/2, t) = -\frac{1}{4\pi\varepsilon_0}\,\frac{N\,e}{r\,c^2}\,\begin{pmatrix} -\ddot{\rho}(t)\,\cos\varphi \\ -\ddot{\rho}(t)\,\sin\varphi \\ 0 \end{pmatrix}_{t-\frac{r}{c}}. \tag{7.27}$$

Since the derivation of the scattering matrix included different coordinate systems, see Fig. 7.4, we first have to define the scattering plane. As stated in Section 7.3.2, we choose $\phi = 0$ in the case of normal incidence, i.e., $\theta = 0$. Equations (7.6) and(7.9) then yield

$$\hat{\mathbf{e}}_{\parallel i} = \hat{\mathbf{e}}_x, \qquad \hat{\mathbf{e}}_{\perp i} = -\hat{\mathbf{e}}_y, \qquad\qquad \hat{\mathbf{e}}_{\parallel s} = \hat{\mathbf{e}}_x, \qquad \hat{\mathbf{e}}_{\perp s} = -\hat{\mathbf{e}}_y, \tag{7.28}$$

for the coordinate systems used in the scattering matrix in Eq. (7.11). With those coordinate systems the scattering matrix equation (7.11) takes the form

$$-\frac{N\,e}{4\pi\varepsilon_0\,r\,c^2}\,\begin{pmatrix} -\ddot{\rho}(t)\,\cos\varphi \\ \ddot{\rho}(t)\,\sin\varphi \end{pmatrix}_{t-\frac{r}{c}} \stackrel{!}{=} \frac{1}{-ikr}\,\begin{pmatrix} S_2 & S_3 \\ S_4 & S_1 \end{pmatrix}\,\begin{pmatrix} E_0\,e^{-i\omega t + ik\left(\frac{h}{2}+r\right)} \\ 0 \end{pmatrix}. \tag{7.29}$$

Entering the expressions above, we obtain

$$S_2(0,0) = \frac{-i\,k^3\,N\,e^2}{4\pi\varepsilon_0\,m\,(\omega_0^2 - \omega^2 - i\omega\Gamma)}\,\cos^2\varphi, \tag{7.30a}$$

$$S_4(0,0) = \frac{i\,k^3\,N\,e^2}{4\pi\varepsilon_0\,m\,(\omega_0^2 - \omega^2 - i\omega\Gamma)}\,\sin\varphi\,\cos\varphi, \tag{7.30b}$$

for the scattering matrix entries. Here, the arguments of $S_2(0,0)$ shall stress that the scattering matrix entries are depended on the position of the observer, see Section 7.3.2. This will be suppressed in the following.

Transmittance and reflectance

The field that is transmitted through a slab was discussed in Eq. (7.18). At the point $(0,0,d)$, $d > h$, it reads

$$\begin{aligned}\mathbf{E}_t &= E_0 e^{-i\omega t+ikd}\left[\left(1-\frac{2\pi\,\mathcal{N}}{k^2}\,S_2\,h\right)\hat{\mathbf{e}}_x-\frac{2\pi\,\mathcal{N}}{k^2}\,S_4\,h\,\hat{\mathbf{e}}_y\right]\\ &= E_0 e^{-i\omega t+ikd}\left[\left(1-\frac{2\pi}{k^2\,A}\,S_2\right)\hat{\mathbf{e}}_x+\frac{2\pi}{k^2\,A}\,S_4\,\hat{\mathbf{e}}_y\right].\end{aligned} \tag{7.31}$$

The number of oscillators per unit volume, $\mathcal{N}$, is one per unit cell. The area of the unit cell is denoted by A and the height of the slab corresponds to the height of the rod. As we see in Eq. (7.31), the polarization of the transmitted field is rotated except when the rod rotation angle φ is zero (or ninety) degrees.

The reflected field is obtained from Eq. (7.21). At the point $(0,0,-d')$, $d' > 0$, it reads

$$\begin{aligned}\mathbf{E}_r &= -E_0\,e^{-i\omega t+ikd'}\left(1-e^{i2kh}\right)\frac{i\pi\,\mathcal{N}}{k^3}\,\mathbf{X}_{\theta=180^\circ}\\ &= -E_0\,e^{-i\omega t+ikd'}\left(1-e^{i2kh}\right)\frac{i\pi}{A\,h\,k^3}\,\left(S_2\,\hat{\mathbf{e}}_x+S_4\,(-\hat{\mathbf{e}}_y)\right).\end{aligned} \tag{7.32}$$

The transmittance is defined as

$$T=\frac{|\mathbf{E}_t|^2}{|\mathbf{E}_i|^2}=\left|1-\frac{2\pi}{k^2\,A}\,S_2\right|^2+\left|\frac{2\pi}{k^2\,A}\,S_4\right|^2. \tag{7.33}$$

Analogously, the reflectance reads

$$R=\frac{|\mathbf{E}_r|^2}{|\mathbf{E}_i|^2}=\left|\left(e^{i2kh}-1\right)\,\frac{i\pi}{A\,h\,k^3}\right|^2\cdot\left(|S_2|^2+|S_4|^2\right). \tag{7.34}$$

Emitted field of a rotated cross

In Section 7.2, we argued that a rotated cross should physically behave like an unrotated rod due to its symmetry. Here, we show that the dipole model yields this result. A cross that is rotated by an angle φ with respect to the lattice is modeled as two perpendicular oscillators. They are located at

$$\mathbf{r}_1(t)=\begin{pmatrix}\rho_1(t)\,\cos\varphi\\ \rho_1(t)\,\sin\varphi\\ \frac{1}{2}h\end{pmatrix},\qquad \mathbf{r}_2(t)=\begin{pmatrix}\rho_2(t)\,\sin\varphi\\ -\rho_2(t)\,\cos\varphi\\ \frac{1}{2}h\end{pmatrix}. \tag{7.35}$$

Each one is excited by the external, x-polarized field. The equations of motion read

$$\ddot{\rho}_1+\Gamma\,\dot{\rho}_1+\omega_0^2\,\rho_1 = -\frac{e}{m}\,E_0\,e^{-i\omega t+ik\frac{1}{2}h}\,\cos\varphi, \tag{7.36a}$$

$$\ddot{\rho}_2+\Gamma\,\dot{\rho}_2+\omega_0^2\,\rho_2 = -\frac{e}{m}\,E_0\,e^{-i\omega t+ik\frac{1}{2}h}\,\sin\varphi, \tag{7.36b}$$

where we neglect any possible interaction of the two oscillators. The solution is then of form

$$\rho_1(t) = -\frac{e}{m}\,\frac{1}{\omega_0^2-\omega^2-i\omega\Gamma}\,E_0\,e^{-i\omega t+ik\frac{1}{2}h}\,\cos\varphi, \tag{7.37a}$$

$$\rho_2(t) = -\frac{e}{m}\,\frac{1}{\omega_0^2-\omega^2-i\omega\Gamma}\,E_0\,e^{-i\omega t+ik\frac{1}{2}h}\,\sin\varphi. \tag{7.37b}$$

Next, we can investigate the radiated dipole field, similarly to the case of the single rod. It is a superposition of both radiated fields:

$$\begin{aligned}
\mathbf{E}_{rad}\left(0,0,r+\frac{h}{2}\right) &= -\frac{N\,e}{4\pi\varepsilon_0\,r\,c^2}\,\mathbf{n}\times(\mathbf{n}\times\ddot{\mathbf{r}}_1)_{t-\frac{r}{c}} - \frac{N\,e}{4\pi\varepsilon_0\,r\,c^2}\,\mathbf{n}\times(\mathbf{n}\times\ddot{\mathbf{r}}_2)_{t-\frac{r}{c}} \\
&= -\frac{N\,e}{4\pi\varepsilon_0\,r\,c^2}\begin{pmatrix}-\ddot{\rho}_1\,\cos\varphi\\-\ddot{\rho}_1\,\sin\varphi\\0\end{pmatrix}_{t-\frac{r}{c}} - \frac{N\,e}{4\pi\varepsilon_0\,r\,c^2}\begin{pmatrix}-\ddot{\rho}_2\,\sin\varphi\\\ddot{\rho}_2\,\cos\varphi\\0\end{pmatrix}_{t-\frac{r}{c}} \\
&= -\frac{N\,e}{4\pi\varepsilon_0\,r\,c^2}\begin{pmatrix}-\omega^2\,\frac{e}{m}\,\frac{1}{\omega_0^2-\omega^2-i\omega\Gamma}\,E_0\,e^{-i\omega t+ikr+ik\frac{1}{2}h}\,\cos\varphi\,\cos\varphi\\-\omega^2\,\frac{e}{m}\,\frac{1}{\omega_0^2-\omega^2-i\omega\Gamma}\,E_0\,e^{-i\omega t+ikr+ik\frac{1}{2}h}\,\cos\varphi\,\sin\varphi\\0\end{pmatrix} \\
&\quad -\frac{N\,e}{4\pi\varepsilon_0\,r\,c^2}\begin{pmatrix}-\omega^2\,\frac{e}{m}\,\frac{1}{\omega_0^2-\omega^2-i\omega\Gamma}\,E_0\,e^{-i\omega t+ikr+ik\frac{1}{2}h}\,\sin\varphi\,\sin\varphi\\+\omega^2\,\frac{e}{m}\,\frac{1}{\omega_0^2-\omega^2-i\omega\Gamma}\,E_0\,e^{-i\omega t+ikr+ik\frac{1}{2}h}\,\sin\varphi\,\cos\varphi\\0\end{pmatrix} \\
&= \frac{N\,e}{4\pi\varepsilon_0\,r\,c^2}\,\omega^2\,\frac{e}{m}\,\frac{1}{\omega_0^2-\omega^2-i\omega\Gamma}\,E_0\,e^{i\omega t+ikr+ik\frac{1}{2}h}\,\hat{\mathbf{e}}_x.
\end{aligned} \tag{7.38}$$

Thus, Eq. (7.38) describes the radiated field of not only an excited unrotated rod (cf. Eq. (7.26) entered in Eq. (7.27) with $\varphi = 0$) but also of the excited rotated cross as predicted in Section 7.2.

Parameter fit and first predictions

Having derived the general expressions for the transmittance and reflectance, we can fit the free parameters of the model to numerical data computed with the Fourier Modal Method. The system is a rod (length 500 nm, height 50 nm, width 50 nm) centered in a rectangular unit cell (length 1350 nm, width 900 nm). The fit is performed for $\varphi = 0°$, i.e., for grid-aligned rods. The fit parameters are the total mass of the oscillator, the resonance frequency and the damping. For a further discussion see Ref. [62]. All parameters are assumed to be independent of frequency in the considered spectral range. The fitted values read

$$m_{\text{tot}} = N{\cdot}m = N{\cdot}m_e{\cdot}3.35 = 2.16{\cdot}10^{-22}\text{ kg},\quad \omega_0 = 1.21{\cdot}10^{15}\text{ Hz},\quad \Gamma = 1.42{\cdot}10^{14}\text{ Hz}, \tag{7.39}$$

where N is the number of free electrons in the rod. It is given by the product of the rod's volume and the free electron density $\varrho_e = 5.707\cdot10^{28}\ {}^1/_{\text{m}^3}$. This number originates from the Drude model used for the numerical computations, see Ref. [25]. The Drude model's plasma frequency can be translated into the electron density[3] [62].

Figure 7.7(a) shows the transmittance and reflectance for one layer of unrotated rods, both for the FMM and the dipole model with the parameters from Eq. (7.39). At this point, all

[3]It should be mentioned that, in practice, the effective free electron density in gold can vary a great deal depending on the system under consideration, see Ref. [77].

parameters of the model are fixed. This means that there is no free parameter left to fit when the rod is rotated. Figure 7.7(b) shows the azimuthal and the ellipticity angle of the light transmitted by a layer of rods that are rotated by $\varphi = -25°$. Both angles, which together contain the polarization information of the transmitted light, are reproduced very well over the entire spectrum. This is even valid for larger rotation angles (not shown here).

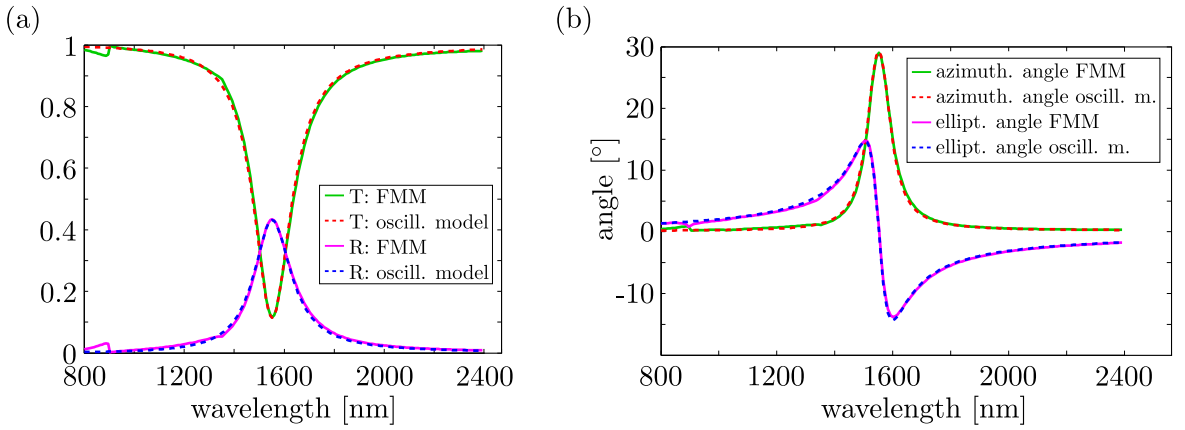

Figure 7.7: Panel (a) displays the transmittance of a layer of unrotated rods. The dipole model's parameters are fitted such that the numerical FMM data is reproduced. Panel (b) shows the polarization state (azimuthal and ellipticity angle) of the transmitted light for a layer of rods rotated by $\varphi = -25°$. The dipole model can reproduce this numerical data without any additional free parameter.

In both panels of Fig. 7.7 there is an important feature: there are spikes at 900 nm and 1350 nm. These are lattice resonances. Since the dipole model assumes non-interacting and randomly distributed scatterers, it cannot reproduce these features. They occur in all subsequent spectra and, thus, we will not always state their origin again. We show in Section 7.5 that they can be incorporated in the model.

Optimized designs

The motivation to search for a simple model was the prospect of a deeper physical insight on the one hand and the prospect of the ability to find optimized designs on the other. For one layer of rods, I searched for optimized structures with respect to the azimuthal angle and the largest field in y-direction. The incident field is assumed to be x-polarized. First, we have a look at Fig. 7.8(a). Here, the azimuthal angle, i.e., the angle by which the electric field behind the slab of rods is rotated, was calculated as a function of the wavelength of the incident plane wave and the rod rotation angle.

The interesting result is that the largest azimuthal angle is found for a rod rotation angle of $\varphi = -30°$. The maximum azimuthal angle is $\psi = 29.6°$. This is somewhat surprising since one may have expected the biggest polarization rotation at $\varphi = -45°$.

In Fig. 7.8(b) we plot the absolute value of the normalized y-component of the transmitted electric field over the rod rotation angle and the wavelength of the incident light. Here, we find that the largest field in y-direction can be obtained for a rod configuration with $\varphi = -45°$. This is understandable upon careful inspection of the angular dependence of the expressions in Eqs. (7.30b) and (7.31).

It is worth mentioning that the computational effort for both calculations in Fig. 7.8 is minimal and barely reaches a second.

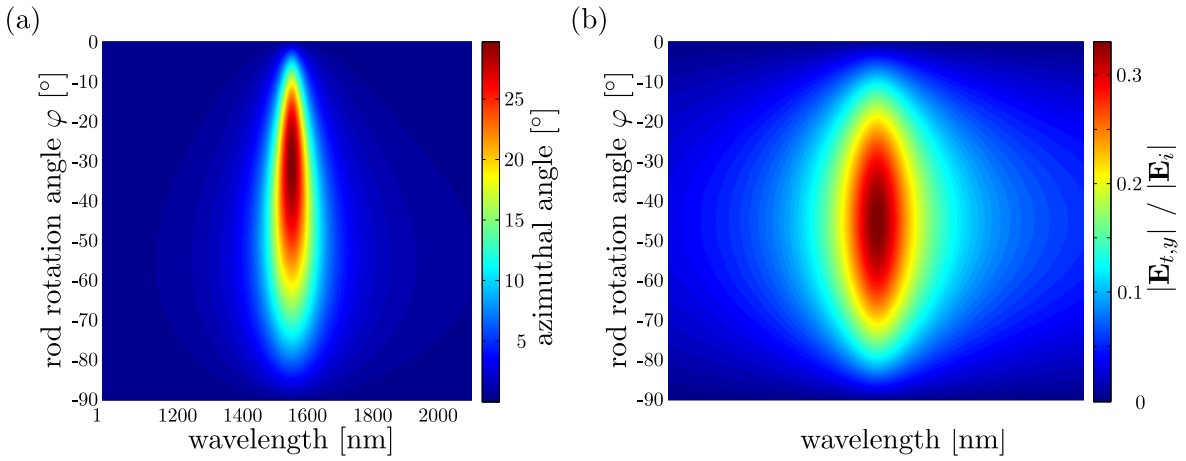

Figure 7.8: Azimuthal angle (panel (a)) and absolute value of $\mathbf{E}_{t,y}$ (panel (b)) over wavelength and rod rotation angle φ. The largest polarization rotation is obtained for $\varphi = -30°$ at the resonance. The largest field in y-direction is present for $\varphi = -45°$.

Transmission and reflection coefficients

In the subsequent section, we need coefficients for transmission and reflection for multiple scattering processes. They are a handy tool to obtain the transmitted field by just multiplying with the corresponding coefficient. The reflection coefficient $\tilde{r}_\varphi$ for a layer of rotated rods is given by

$$\begin{aligned} \tilde{r}_\varphi &= \frac{\mathbf{E}_r \cdot \mathbf{E}_i^*}{\mathbf{E}_i \cdot \mathbf{E}_i^*} = \frac{E_0 \left(e^{i2kh} - 1\right) \frac{i\pi}{A\,h\,k^3} \left(S_2\,\hat{\mathbf{e}}_x + S_4\,(-\hat{\mathbf{e}}_y)\right) \cdot E_0^*\,\hat{\mathbf{e}}_x}{|E_0|^2} \\ &= \left(e^{i2kh} - 1\right) \frac{i\pi}{A\,h\,k^3} \frac{-i\,k^3\,N\,e^2\,\cos^2\varphi}{4\pi\varepsilon_0\,m\,(\omega_0^2 - \omega^2 - i\omega\Gamma)}, \end{aligned} \tag{7.40}$$

where $\mathbf{E}^*$ denotes the complex conjugate of the electric field. An alternative way to obtain this coefficient is via

$$\tilde{r}_\varphi = \frac{\tilde{r}_0\,\mathbf{E}_\parallel}{\mathbf{E}_\perp + \mathbf{E}_\parallel}, \tag{7.41}$$

where $\mathbf{E}_\perp$ and $\mathbf{E}_\parallel$ denote the field components perpendicular and parallel to the rod, respectively. The corresponding transmission coefficient reads

$$\tilde{t}_\varphi = \frac{\mathbf{E}_t \cdot \mathbf{E}_i^*}{\mathbf{E}_i \cdot \mathbf{E}_i^*} = 1 - \frac{2\pi}{k^2\,A} \frac{-i\,k^3\,N\,e^2}{4\pi\varepsilon_0\,m\,(\omega_0^2 - \omega^2 - i\omega\Gamma)}\,\cos^2\varphi. \tag{7.42}$$

There are three important things to note about these coefficients. Firstly, the phases are defined such that the transmission coefficient multiplied with the field *behind* the rod gives us the transmitted field through the slab. Secondly, we note that this field is only the transmitted part parallel to the incident field. Thirdly, the reflection coefficient multiplied with the incident field in front of the rod yields the field at the same point after reflection in direction of the incident field.

7.3.5 Two layers of rods

In this section, we address the very delicate question of how to describe multi-layer structures. As we have discussed, the coupling of layers is a difficult topic. We assume a certain form based on dipole-dipole interaction in the equations of motion and use a fit parameter. The most basic test system we can investigate consists of two layers of rods, possibly mutually rotated, see Fig. 7.9. The lower rod is expected to be oriented in x-direction such that it is exposed to the whole x-polarized incident field. Once one of the rods is rotated, the transmitted and reflected field is going to be polarized elliptically.

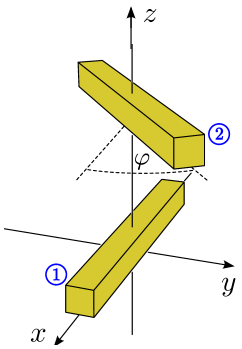

Figure 7.9: Sketch of one building block for the investigated system consisting of two layers of mutually rotated crosses.

In the following, we have to discuss multiple scattering between the layers and the form of the coupling. This has to be known before setting up the equations of motion. The general course of action is outlined in Fig. 7.10.

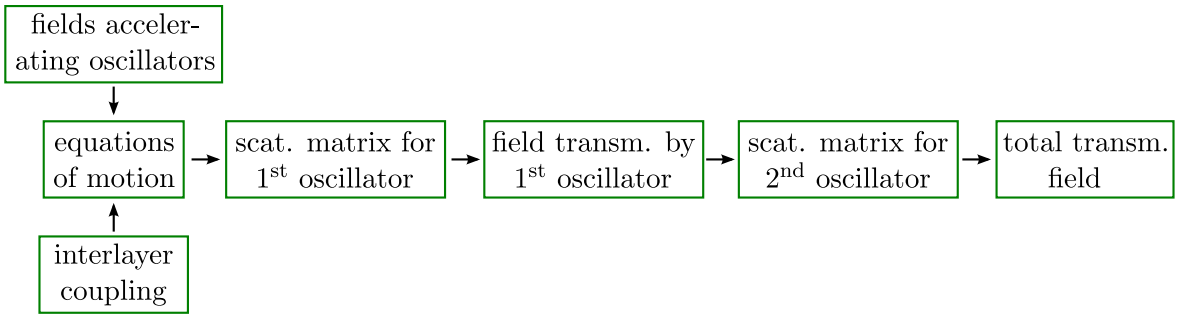

Figure 7.10: Course of action to obtain the transmittance of two layers via the dipole model.

The idea of Fig. 7.10 is to help keeping the calculation's course of action in mind. This is complicated since, on the one hand, we set up equations of motion for single oscillators but, on the other hand, use the field transmitted and reflected through a whole slab as input for the equations of motion.

The first problem is finding suitable positions for the oscillators. In the case of one layer this did not matter—here, we have to decide whether they are placed in the center of the rods or, e.g., at opposing sides. We choose the symmetric version and place the oscillators in the

center of the rods, resulting in

$$\mathbf{r}_1(t) = \begin{pmatrix} \rho_1(t) \\ 0 \\ \frac{1}{2}h \end{pmatrix}, \qquad \mathbf{r}_2(t) = \begin{pmatrix} \rho_2(t)\,\cos\varphi \\ \rho_2(t)\,\sin\varphi \\ b + \frac{3}{2}h \end{pmatrix}. \tag{7.43}$$

The reason is that the other possibilities have been checked and the best results were found for the choice in Eq. (7.43). Like in the previous section, the height of the rods is denoted by h. The spacing between the rods is denoted by b.

The next steps are the following: Firstly, we discuss the accelerating fields, taking multiple scattering into account. Secondly, we set up the equations of motion for the coupled oscillators. Thirdly, we construct the scattering matrices for the first and second layer and derive the transmittance of the system. Finally, we fit the coupling, which is used as a free parameter, to numerical data and investigate the behavior of the system upon the rotation of a rod.

Accelerating fields

When light is incident on two plane-parallel plates, multiple back-scattering from each plate is encountered, see Fig. 7.11. Technically, this is known as a Fabry-Pérot interferometer which can, e.g., be used for optical filters.

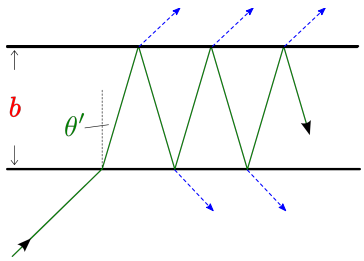

Figure 7.11: Multiple reflection and transmission for two plane-parallel plates.

This multiple scattering has to be taken into account since the reflectance is not negligibly small, see Fig. 7.7(a). Especially near the resonance it is very high. Consequently, we have to add up all fields that affect the two oscillators. Since we restrict ourselves to normal incidence, the angle θ' in Fig. 7.11 is assumed to be zero. Therefore, we collect a phase of

$$\delta = \frac{4\pi}{\lambda}\, b \tag{7.44}$$

in case of a double traversal of the space between the rods (surface to surface). First of all, we look at the fields acting on the first oscillator. Note that the reflection coefficient $\tilde{r}_\varphi$ in Eq. (7.40) gives us the field reflected back *in the direction of polarization of the incident field.* As the field incident on the second rod is x-polarized (because the first grid-aligned rod does not change the polarization) a multiplication with $\tilde{r}_\varphi$ and with the phase will give us the first reflected field acting on the first oscillator. The fields acting on the first oscillator are (with the abbreviation $E_i = E_0\, e^{-i\omega t}$):

$$E_i\, e^{ik\frac{h}{2}}, \quad E_i\, \tilde{t}_0\, \tilde{r}_\varphi\, e^{i\delta}\, e^{ik\frac{3}{2}h}, \quad E_i\, \tilde{t}_0\, \tilde{r}_\varphi^2\, \tilde{r}_0\, e^{i2\delta}\, e^{ik\frac{3}{2}h}, \quad \ldots$$
$$\ldots \quad , \quad E_i\, \tilde{t}_0\, \tilde{r}_\varphi^{(p-1)}\, \tilde{r}_0^{(p-2)}\, e^{i(p-1)\delta}\, e^{ik\frac{3}{2}h},$$

with p being the number of approaching waves. Just as a short explanation we discuss the first two terms, the others are derived the same way. The first term $E_i\, e^{ik\frac{h}{2}}$ is the original incident field. The second field is obtained the following way: the incident field gets transmitted and, therefore, the field on the backward surface[4] of the rod is $E_i e^{ikh}\tilde{t}_0$. Then the wave propagates to the second rod and gets reflected, with the field on the surface looking like $E_i e^{ikh}\tilde{t}_0 e^{i\delta/2}\tilde{r}_\varphi$. This is the field in x-direction, i.e. parallel to the first rod. Then the field propagates for $b+\frac{1}{2}h$ in $-z$ direction and there it acts on the first oscillator.

Now we sum up the first p fields acting on the first oscillator[5]:

$$\begin{aligned} E^{(1^{st})}(p) &= \left(e^{ik\frac{h}{2}} + \tilde{t}_0\,\tilde{r}_\varphi\, e^{i\delta+ik\frac{3}{2}h}\,\left(1+\tilde{r}_\varphi\tilde{r}_0\, e^{i\delta} + ... + (\tilde{r}_\varphi\tilde{r}_0)^{(p-2)}\, e^{i(p-2)\delta}\right)\right)\, E_i \\ &= \left(e^{ik\frac{h}{2}} + \tilde{t}_0\,\tilde{r}_\varphi\, e^{i\delta}\, e^{ik\frac{3}{2}h}\,\frac{1-(\tilde{r}_\varphi\,\tilde{r}_0\, e^{i\delta})^{p-1}}{1-\tilde{r}_\varphi\,\tilde{r}_0\, e^{i\delta}}\right)\, E_i. \end{aligned} \tag{7.45}$$

Since we consider the angle of the incident light to be zero, we have a large number of reflected waves. As $|\mathrm{Re}\left(\tilde{r}_\varphi\,\tilde{r}_0\, e^{i\delta}\right)| < 1$ and $|\mathrm{Im}\left(\tilde{r}_\varphi\,\tilde{r}_0\, e^{i\delta}\right)| < 1$ the series in Eq. (7.45) converges. For $p\to\infty$ we obtain

$$E^{(1^{st})} \equiv E^{(1^{st})}(\infty) = \underbrace{\left(e^{ik\frac{h}{2}} + \frac{\tilde{t}_0\,\tilde{r}_\varphi\, e^{i\delta}\, e^{ik\frac{3}{2}h}}{1-\tilde{r}_\varphi\,\tilde{r}_0\, e^{i\delta}}\right)}_{=:\,\alpha_1}\, E_0\, e^{-i\omega t}. \tag{7.46}$$

Analogously, we derive the total field acting on the second oscillator. The first p fields acting on the second oscillator are

$$\begin{aligned} &E_i\,\tilde{t}_0\, e^{i\frac{\delta}{2}}\, e^{ik\frac{3}{2}h}\,\cos\varphi, \qquad E_i\,\tilde{t}_0\, e^{i\frac{\delta}{2}}\, e^{ik\frac{3}{2}h}\,\tilde{r}_\varphi\,\tilde{r}_0\, e^{i\delta}\,\cos\varphi, \qquad ... \\ &\qquad\qquad ... \qquad , \qquad E_i\,\tilde{t}_0\, e^{i\frac{\delta}{2}}\, e^{ik\frac{3}{2}h}\,\tilde{r}_\varphi^{(p-1)}\,\tilde{r}_o^{(p-1)}\, e^{i(p-1)\delta}\,\cos\varphi. \end{aligned}$$

The first field approaching the second oscillator is the field that is transmitted by the first rod. The second rod is rotated by φ so the field *acting* on the oscillator will only be the part parallel to it, namely the field multiplied with the factor $\cos\varphi$.

Adding the first p fields results in

$$\begin{aligned} E^{(2^{nd})}(p) &= \tilde{t}_0\, e^{i\frac{\delta}{2}}\, e^{ik\frac{3}{2}h}\,\cos\varphi\,\left(1+\tilde{r}_\varphi\,\tilde{r}_0\, e^{i\delta} + ... + \left(\tilde{r}_\varphi\,\tilde{r}_0\, e^{i\delta}\right)^{p-1}\right)\, E_i \\ &= \tilde{t}_0\, e^{i\frac{\delta}{2}}\, e^{ik\frac{3}{2}h}\,\cos\varphi\,\frac{1-(\tilde{r}_\varphi\,\tilde{r}_0\, e^{i\delta})^{p}}{1-\tilde{r}_\varphi\,\tilde{r}_0\, e^{i\delta}}\, E_i. \end{aligned} \tag{7.47}$$

Just like before, we consider $p\to\infty$

$$E^{(2^{nd})} \equiv E^{(2^{nd})}(\infty) = \underbrace{\frac{\tilde{t}_0\, e^{i\frac{\delta}{2}}\, e^{ik\frac{3}{2}h}\,\cos\varphi}{1-\tilde{r}_\varphi\,\tilde{r}_0\, e^{i\delta}}}_{=:\,\alpha_2}\, E_0\, e^{-i\omega t}. \tag{7.48}$$

Thereby, we have obtained the total fields acting on the two oscillators due to multiple reflections.

[4] Note that we mean at $(0,0,z=h)$. Of course, the dipole model does not reproduce the correct continuity conditions at the surface of the metallic rod.

[5] With the help of the geometric sum: $1+x+x^2+x^3+...+x^p = \frac{1-x^{p+1}}{1-x}$.

Equations of motion

The next step in calculating the transmittance and reflectance for the system of two layers of rods is to set up the equations of motion. The coupling mechanism between the layers is assumed to be due to the dipole moment, see Ref. [62]. We set up the equations of motion to be

$$\ddot{\rho}_1 + \Gamma\,\dot{p}_1 + \omega_0^2\,\rho_1 + L\,\cos\varphi\,\rho_2 = -\frac{e}{m}\,\alpha_1\,E_0\,e^{-i\omega t}, \tag{7.49a}$$

$$\ddot{\rho}_2 + \Gamma\,\dot{p}_2 + \omega_0^2\,\rho_2 + L\,\cos\varphi\,\rho_1 = -\frac{e}{m}\,\alpha_2\,E_0\,e^{-i\omega t}, \tag{7.49b}$$

with the coupling L. This coupling is used as fit parameter for each distance b. The cosine term in the coupling enters because the upper rod is rotated and the dipole moments do not point in the same direction anymore. Using a time-harmonic ansatz we write Eqs. (7.49a) and (7.49b) in matrix form

$$\begin{pmatrix} \omega_0^2 - \omega^2 - i\omega\Gamma & L\,\cos\varphi \\ L\,\cos\varphi & \omega_0^2 - \omega^2 - i\omega\Gamma \end{pmatrix} \begin{pmatrix} \rho_1 \\ \rho_2 \end{pmatrix} = -\frac{e}{m}\,E_0\,e^{-i\omega t} \begin{pmatrix} \alpha_1 \\ \alpha_2 \end{pmatrix}. \tag{7.50}$$

By inverting the matrix[6] we get the solution to the equations of motion

$$\begin{pmatrix} \rho_1(t) \\ \rho_2(t) \end{pmatrix} = -\frac{1}{n}\,\frac{e}{m}\,E_0\,e^{-i\omega t} \begin{pmatrix} \omega_0^2 - \omega^2 - i\omega\Gamma & -L\,\cos\varphi \\ -L\,\cos\varphi & \omega_0^2 - \omega^2 - i\omega\Gamma \end{pmatrix} \begin{pmatrix} \alpha_1 \\ \alpha_2 \end{pmatrix}, \tag{7.51}$$

with the abbreviation $n = (\omega_0^2 - \omega^2 - i\omega\Gamma)^2 - L^2\,\cos^2\varphi$. The two oscillatory eigenmodes of the system, corresponding to parallel and anti-parallel movement of the oscillators, are discussed in detail in Ref. [62].

By knowing how the oscillators are moving, we can determine the scattering matrices of the layers. In this case we have two: the first one determines the field between the layers of rods and the second one describes the final field transmitted through both layers.

Scattering matrix of the first rod

The field radiated by the first oscillator reads ($\tilde{r}_1 > 0$)

$$\mathbf{E}_{rad,\mathbf{1}}(0,0,\tilde{r}_1 + h/2, t) = -\frac{1}{4\pi\varepsilon_0}\,\frac{N\,e}{\tilde{r}_1\,c^2} \begin{pmatrix} -\ddot{\rho}_1 \\ 0 \\ 0 \end{pmatrix}_{t-\frac{\tilde{r}_1}{c}}. \tag{7.52}$$

Here we again have to rewrite the fields into fields parallel and perpendicular to the scattering plane (see Section 7.3.2 and Eq. (7.28)). Then we relate incident and scattered field:

$$-\frac{N\,e}{4\pi\varepsilon_0\,\tilde{r}_1\,c^2} \begin{pmatrix} -\ddot{\rho}_1 \\ 0 \end{pmatrix}_{t-\frac{\tilde{r}_1}{c}} \stackrel{!}{=} \frac{1}{-ik\tilde{r}_1} \begin{pmatrix} S_{2\mathbf{1}} & S_{3\mathbf{1}} \\ S_{4\mathbf{1}} & S_{1\mathbf{1}} \end{pmatrix} \begin{pmatrix} E_0\,e^{-i\omega t + ik\left(\frac{h}{2}+\tilde{r}_1\right)} \\ 0 \end{pmatrix}, \tag{7.53}$$

where the bold **1** indicates that we deal with the first layer (and, therefore, the first oscillator). As scattering matrix entries we obtain

$$S_{2\mathbf{1}} = \frac{-i\,k^3\,N\,e^2}{4\pi\varepsilon_0\,m\,n\,e^{ik\frac{h}{2}}} \left[\left(\omega_0^2 - \omega^2 - i\omega\Gamma\right)\,\alpha_1 - L\,\cos\varphi\,\alpha_2\right], \tag{7.54a}$$

$$S_{4\mathbf{1}} = 0. \tag{7.54b}$$

[6] Inverting the matrix is possible since $L\,\cos\varphi \neq \omega_0^2 - \omega^2 - i\omega\Gamma$ is the case.

Since the rod is parallel to the incoming polarization we know from Section 7.3.4 that $S_{41} = 0$. Thereby, we obtain the field transmitted by the first layer, namely at $(0, 0, d + h)$, $d > 0$:

$$\mathbf{E}_{t1}(0, 0, d + h, t) = E_0\, e^{-i\omega t + ikh + ikd} \left(1 - S_{21}\, \frac{2\pi}{k^2\, A}\right) \hat{\mathbf{e}}_x. \tag{7.55}$$

Scattering matrix of the second rod

The field emitted by the second oscillator, observed from a distance $\tilde{r}_2$, is given by

$$\mathbf{E}_{rad,2}\left(0, 0, \tilde{r}_2 + b + \frac{3}{2}h, t\right) = -\frac{1}{4\pi\varepsilon_0}\, \frac{N\, e}{\tilde{r}_2\, c^2} \begin{pmatrix} -\ddot{\rho}_2(t)\, \cos\varphi \\ -\ddot{\rho}_2(t)\, \sin\varphi \\ 0 \end{pmatrix}_{t - \frac{\tilde{r}_2}{c}}. \tag{7.56}$$

After changing the coordinate system like above we obtain the scattering matrix equation

$$\frac{-Ne}{4\pi\varepsilon_0 \tilde{r}_2 c^2} \begin{pmatrix} -\ddot{\rho}_2(t)\, \cos\varphi \\ \ddot{\rho}_2(t)\, \sin\varphi \end{pmatrix}_{t - \frac{\tilde{r}_2}{c}} \stackrel{!}{=} \frac{1}{-ik\tilde{r}_2} \begin{pmatrix} S_{22} & S_{32} \\ S_{42} & S_{12} \end{pmatrix} \begin{pmatrix} E_{x,t1}\left(0, 0, b + \frac{3}{2}h + \tilde{r}_2, t\right) \\ 0 \end{pmatrix}. \tag{7.57}$$

Entering the solution of the equation of motion for the second rod (see Eq. (7.51)) in the latter equation yields the following scattering matrix entries for the second rod:

$$S_{22} = \frac{-i\, k^3\, N\, e^2}{4\pi\varepsilon_0\, m\, n}\, \cos\varphi\, \frac{-L\, \cos\varphi\, \alpha_1 + \left(\omega_0^2 - \omega^2 - i\omega\Gamma\right)\, \alpha_2}{e^{ikb + ik\frac{3}{2}h} \left(1 - S_{21}\, \frac{2\pi}{k^2\, A}\right)}, \tag{7.58a}$$

$$S_{42} = \frac{i\, k^3\, N\, e^2}{4\pi\varepsilon_0\, m\, n}\, \sin\varphi\, \frac{-L\, \cos\varphi\, \alpha_1 + \left(\omega_0^2 - \omega^2 - i\omega\Gamma\right)\, \alpha_2}{e^{ikb + ik\frac{3}{2}h} \left(1 - S_{21}\, \frac{2\pi}{k^2\, A}\right)}. \tag{7.58b}$$

The next step after having derived both scattering matrices is to calculate the transmittance.

Transmittance

As shown in Eq. (7.18), we obtain the transmitted field by multiplying the incoming field with a term connected to the scattering matrix. The incident field on the second oscillator is not $\mathbf{E}_i$ anymore but $\mathbf{E}_{t1}$. Therefore, the field transmitted through two layers of rods at the point $(0, 0, e)$, $e = h + b + h + e'$, $e' > 0$, is

$$\mathbf{E}_{t2} = E_0\, e^{-i\omega t + ike} \left(1 - \frac{2\pi\, S_{21}}{k^2\, A}\right) \left[\left(1 - \frac{2\pi\, S_{22}}{k^2\, A}\right) \hat{\mathbf{e}}_x + \frac{2\pi\, S_{42}}{k^2\, A}\, \hat{\mathbf{e}}_y\right]. \tag{7.59}$$

For $S_{42} \neq 0$ we find a field in y-direction. So, as expected, there is a change in the polarization state for all angles except for 0° and 90°.

With Eq. (7.23) we calculate the transmittance for the double layer of rotated rods

$$T = \left|1 - \frac{2\pi\, S_{21}}{k^2\, A}\right|^2 \cdot \left[\left|1 - \frac{2\pi\, S_{22}}{k^2\, A}\right|^2 + \left|\frac{2\pi\, S_{42}}{k^2\, A}\right|^2\right]. \tag{7.60}$$

Fit of the coupling to numerical data

In the previous section, we fixed the parameters m, ω_0 and Γ of the dipole model. Since the coupling L enters the model as a new parameter, cf. Eq. (7.49), we have to fit it to numerical data. In Fig. 7.12, the transmittance is displayed for two layers of unrotated rods with a distance of $b = 50$ nm. The coupling was fitted to be $L = 1.2 \cdot 10^{29}\ \frac{1}{s^2}$.

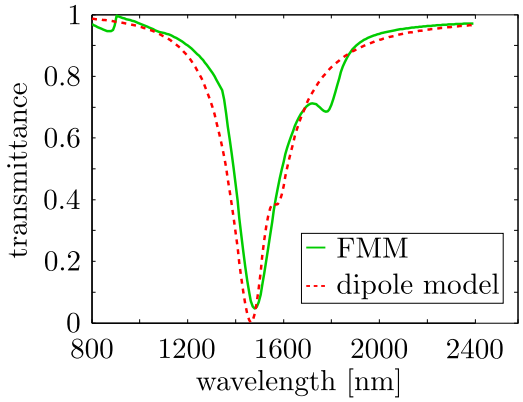

Figure 7.12: Transmittance for two layers of rods. The rods are unrotated, i.e., $\varphi = 0°$, the distance between the rods is $b = 50$ nm and the fitted coupling parameter is $L = 1.2 \cdot 10^{29}\ \frac{1}{s^2}$. Qualitatively, the numerical data is reproduced, although not on a quantitative level.

The physical behavior can be reproduced qualitatively—there are two resonances corresponding to two oscillatory eigenmodes of the system. However, the model does not reproduce the correct frequency and height of the second resonance. At this point it is important to point out that we can perform the fit either to the transmittance itself or to the transmitted field. Since the transmitted field carries the phase information (which is important for the polarization state), we performed the fit to the transmitted field (not shown) and calculated the transmittance in Fig. 7.12 afterwards.

The distance dependence of the coupling is another interesting topic. I performed investigations for distances between 25 nm and 150 nm which all display similar features as the transmittance in Fig. 7.12. The result is a rather slow decrease—the coupling declines with $b^{-0.4}$ which is slower than what one might expect for dipole coupling. The corresponding plots and the fit data can be found in the appendix of Ref. [62].

Predictions for rotated rods

Once the coupling is fixed for a certain distance between the rods, the model does not have any free parameters left. Thus, we enter the corresponding fitted coupling L and the rotation angle φ into the model and compare to numerical data. In Fig. 7.13, the polarization state for two layers of rods, mutually rotated by $\varphi = -20°$, is displayed.

Like in the case of the transmittance, the polarization state, namely the azimuthal and ellipticity angle, are qualitatively reproduced. Both angles show a large and a smaller resonance that can also be found in the dipole model. However, the model predicts larger angles than the ones obtained with the FMM.

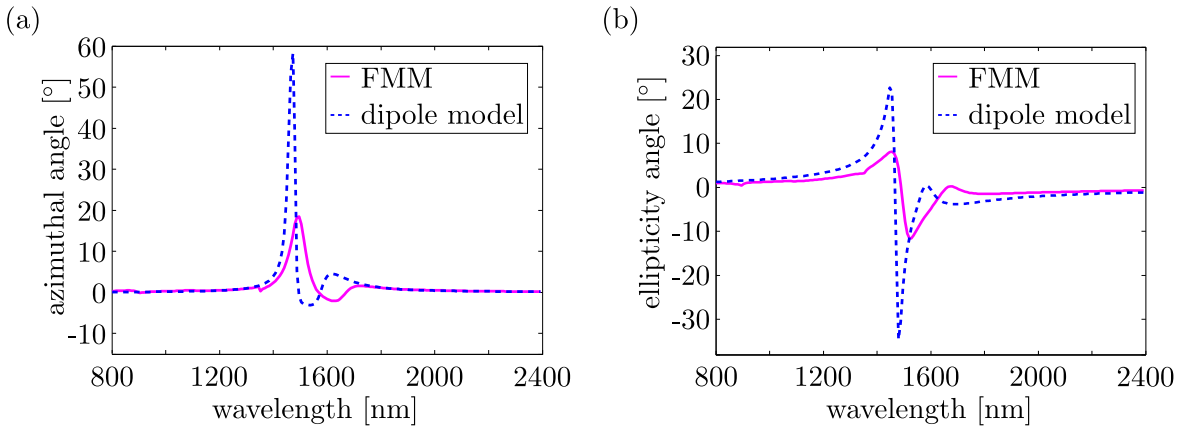

Figure 7.13: Polarization state of the transmitted light for two layers of mutually rotated rods with $\varphi = -20°$ and $b = 50$ nm. The dipole model reproduces the numerical results but overestimates the angles at the resonance.

Large spacings b

We have shown that the coupling of the dipole model does not yet sufficiently describe the numerically obtained spectra for small layer distances b. For large distances, this changes. Figure 7.14(a) shows the transmittance for a system of two layers of unrotated rods that are $b = 1000$ nm apart. At this large distance, the coupling should be practically zero. Therefore, we enter $L = 0$ into the dipole model and obtain the red, dashed curve in Fig. 7.14(a). As we see, the dipole model describes the system well for this distance. Also, we can rotate the upper rod. The resulting polarization state behind the second layer of rods is depicted in Fig. 7.14(b). Again, the coupling was set to $L = 0$. Although minor deviations occur, the dipole model describes the numerical data very well for large spacings.

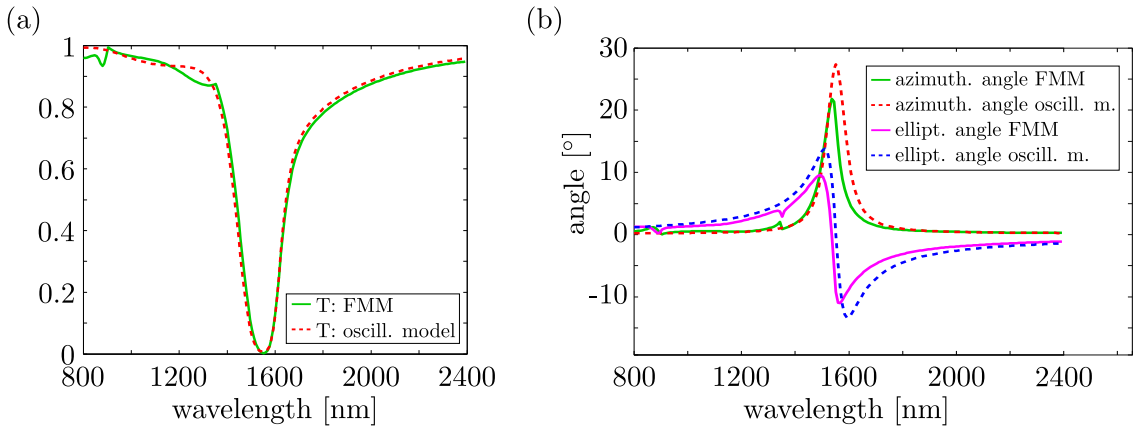

Figure 7.14: Panel (a) shows the transmittance of the FMM and the dipole model for two layers of unrotated rods with a large spacing of $b = 1000$ nm. The oscillator model uses $L = 0$ for the coupling since it is assumed to vanish. Panel (b) shows the polarization state for the light transmitted through two layers of rods, where the upper rod is rotated by $\varphi = -20°$ and $b = 1000$ nm. Again, the oscillator model with $L = 0$ reproduces the numerical data well.

7.3.6 Two layers of crosses

The most complex structure investigated with the dipole model is depicted in Fig. 7.15—two layers of mutually rotated crosses.

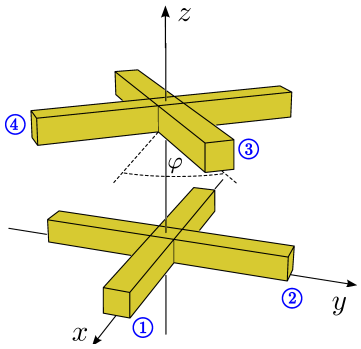

Figure 7.15: Sketch of the basic building block for the system investigated in this section—two layers of mutually rotated crosses. Due to the sense of rotation, both circular polarizations are expected to be transmitted differently.

As discussed above, this structure is very interesting since it exhibits a handedness, a sense of rotation. For most angles[7] φ this is the case for the structure shown in Fig. 7.15. As we see in the following, this structure changes the polarization state of the incident, linear x-polarized light. Furthermore, the structure has C_4 symmetry. Therefore, we can expect all linear polarizations to be transmitted equally.

In the following, we show that the oscillator model presented so far and the numerical calculations using the Fourier Modal Method show fundamentally different results.

We proceed analogously to the case of two layers of rods. It might be helpful to recapitulate the course of action depicted in Fig. 7.10. After calculating the acting fields, we can set up and solve the equations of motion which leads us to the scattering matrices and, thereby, the transmission through the whole structure.

Like above, the distance between the surfaces of the crosses is denoted by b, the height of the rods by h. We find the four oscillators at

$$\mathbf{r}_1 = \begin{pmatrix} \rho_1 \\ 0 \\ \frac{1}{2}h \end{pmatrix}, \quad \mathbf{r}_2 = \begin{pmatrix} 0 \\ \rho_2 \\ \frac{1}{2}h \end{pmatrix}, \quad \mathbf{r}_3 = \begin{pmatrix} \rho_3 \cos\varphi \\ \rho_3 \sin\varphi \\ b + \frac{3}{2}h \end{pmatrix}, \quad \mathbf{r}_4 = \begin{pmatrix} \rho_4 \sin\varphi \\ -\rho_4 \cos\varphi \\ b + \frac{3}{2}h \end{pmatrix}. \tag{7.61}$$

When ρ_4 gets positive, the fourth oscillator is located in the area with positive x and negative y values (this is sketched in Fig. 7.15 by the encircled four). This is of particular importance when we deal with the coupling.

As we consider only dipole coupling, let us take a look at the dipole moments to understand which terms enter the equations of motion. When ρ_1 and ρ_3 have positive values then the dipole moments of the two oscillators are parallel. The coupling has, therefore, a positive sign. Now imagine ρ_2 and ρ_4 having positive values. Due to the definitions in Eq. (7.61) their dipole moments are anti-parallel. Thus, their coupling has a negative sign.

[7] There is no handedness for $\varphi = 0° \pm m\ 90°$ and $\varphi = \pm m\ 45°$, $m \in \mathbb{N}$.

Note that this is all a matter of definition. For instance, we could have defined the fourth oscillator as $\tilde{\mathbf{r}}_4 = (-\tilde{\rho}_4 \ \sin\varphi, \ +\tilde{\rho}_4 \ \cos\varphi, \ b + 3/2 \ h)$. Then all couplings would have a positive sign. However, the negative sign enters when a field in positive x-direction drives the first oscillator to positive values of ρ_1 but the oscillator at $\tilde{\mathbf{r}}_4$ is driven to negative values of $\tilde{\rho}_4$. Therefore, the results of our analysis are not dependent on the algebraic signs in the definitions given in Eq. (7.61).

Accelerating fields

In Section 7.3.4, we discussed that a single rotated cross behaves like an unrotated rod in terms of the transmitted and reflected field. The first cross is grid-aligned, so it transmits like a rod lying in x-direction for an incoming x polarized wave. No matter how the second rod is rotated, it will reflect like a rod parallel to the incoming polarization, i.e. a rod in x-direction. Consequently, the accelerating fields for the two layers of rotated crosses are the same as the fields for the system of *two layers of unrotated rods*. Therefore, as we have seen in Eq. (7.46), the field impinging on the first cross is

$$E^{(1^{st})} \equiv E^{(1^{st})}(\infty) = \left(e^{ik\frac{h}{2}} + \frac{\tilde{t}_0 \, \tilde{r}_0 \, e^{i\delta} \, e^{ik\frac{3}{2}h}}{1 - \tilde{r}_0^2 \, e^{i\delta}} \right) E_0 \, e^{-i\omega t}, \tag{7.62}$$

and the field approaching the second cross is (see Eq. (7.48))

$$E^{(2^{nd})} \equiv E^{(2^{nd})}(\infty) = \frac{\tilde{t}_0 \, e^{i\frac{\delta}{2}} \, e^{ik\frac{3}{2}h}}{1 - \tilde{r}_0^2 \, e^{i\delta}} \, E_0 \, e^{-i\omega t}. \tag{7.63}$$

Remember that those are the fields impinging on the oscillators, i.e., the field values in x-direction. Since the rods are rotated, the fields exciting the various oscillators are only the parts parallel to them:

$$E_1 = \left(e^{ik\frac{h}{2}} + \frac{\tilde{t}_0 \, \tilde{r}_0 \, e^{i\delta} \, e^{ik\frac{3}{2}h}}{1 - \tilde{r}_0^2 \, e^{i\delta}} \right) E_0 \, e^{-i\omega t} \quad =: \quad \beta_1 \, E_0 \, e^{-i\omega t}, \tag{7.64a}$$

$$E_2 = 0, \tag{7.64b}$$

$$E_3 = \frac{\tilde{t}_0 \, e^{i\frac{\delta}{2}} \, e^{ik\frac{3}{2}h}}{1 - \tilde{r}_0^2 \, e^{i\delta}} \, \cos\varphi \, E_0 \, e^{-i\omega t} \quad =: \quad \beta_2 \, \cos\varphi \, E_0 \, e^{-i\omega t}, \tag{7.64c}$$

$$E_4 = \frac{\tilde{t}_0 \, e^{i\frac{\delta}{2}} \, e^{ik\frac{3}{2}h}}{1 - \tilde{r}_0^2 \, e^{i\delta}} \, \sin\varphi \, E_0 \, e^{-i\omega t}, \tag{7.64d}$$

with E_l denoting the field acting on the l-th oscillator.

Equations of motion

There are two oscillators in each layer, each of which couples to both oscillators in the other layer while the strength of the coupling is equal for all rods since all rods are identical (except for the angular term due to the rotation of the rods and the problem of the sign we have discussed before). With the fields obtained above, the equations of motion read

$$\ddot{\rho}_1 + \Gamma \, \dot{\rho}_1 + \omega_0^2 \, \rho_1 + L \, \cos\varphi \, \rho_3 + L \, \sin\varphi \, \rho_4 = -\frac{e}{m} \, E_1, \tag{7.65a}$$

$$\ddot{\rho}_2 + \Gamma \, \dot{\rho}_2 + \omega_0^2 \, \rho_2 + L \, \sin\varphi \, \rho_3 - L \, \cos\varphi \, \rho_4 = -\frac{e}{m} \, E_2, \tag{7.65b}$$

$$\ddot{\rho}_3 + \Gamma \, \dot{\rho}_3 + \omega_0^2 \, \rho_3 + L \, \cos\varphi \, \rho_1 + L \, \sin\varphi \, \rho_2 = -\frac{e}{m} \, E_3, \tag{7.65c}$$

$$\ddot{\rho}_4 + \Gamma \, \dot{\rho}_4 + \omega_0^2 \, \rho_4 + L \, \sin\varphi \, \rho_1 - L \, \cos\varphi \, \rho_2 = -\frac{e}{m} \, E_4. \tag{7.65d}$$

Just like in Section 7.3.5 we have not added a phase to the coupling L although it might seem reasonable. Yet this does not change the basic results we obtain. To prove this, one might assume $L = |L|\ e^{ikb}$ and follow the calculation process which will lead to the result that no qualitative differences arise between the calculation with and without phase. This is due to the fact that all couplings would have the same phase determined by the distance of the oscillators.

Using the time-harmonic ansatz and writing the equations in matrix form results in[8]

$$\begin{aligned}
\begin{pmatrix} \rho_1 \\ \rho_2 \\ \rho_3 \\ \rho_4 \end{pmatrix} &= \begin{pmatrix} \Sigma & 0 & L\cos\varphi & L\sin\varphi \\ 0 & \Sigma & L\sin\varphi & -L\cos\varphi \\ L\cos\varphi & L\sin\varphi & \Sigma & 0 \\ L\sin\varphi & -L\cos\varphi & 0 & \Sigma \end{pmatrix}^{-1} \left(-\frac{e}{m}\right) \begin{pmatrix} E_1 \\ E_2 \\ E_3 \\ E_4 \end{pmatrix} \\
&= \frac{-\ e\ E_0\ e^{-i\omega t}}{m\ (L^2-\Sigma^2)} \begin{pmatrix} -\Sigma & 0 & L\cos\varphi & L\sin\varphi \\ 0 & -\Sigma & L\sin\varphi & -L\cos\varphi \\ L\cos\varphi & L\sin\varphi & -\Sigma & 0 \\ L\sin\varphi & -L\cos\varphi & 0 & -\Sigma \end{pmatrix} \begin{pmatrix} \beta_1 \\ 0 \\ \beta_2\cos\varphi \\ \beta_2\sin\varphi \end{pmatrix} \\
&= -\frac{e\ E_0\ e^{-i\omega t}}{m\ (L^2-\Sigma^2)} \begin{pmatrix} L\beta_2 - \Sigma\beta_1 \\ 0 \\ (L\beta_1 - \Sigma\beta_2)\cos\varphi \\ (L\beta_1 - \Sigma\beta_2)\sin\varphi \end{pmatrix},
\end{aligned} \tag{7.66}$$

with the abbreviation $\Sigma = \omega_0^2 - \omega^2 - i\omega\Gamma$. This yields the first surprising result: the second oscillator is not excited and, therefore, does not scatter any light! One might have expected a movement as both the third and fourth oscillator couple to it. Surprisingly, both effects cancel each other. This can be understood the following way: the third oscillator (that 'feels' the cosine of the incoming x-polarized field) couples positive with a sine term to the second oscillator. The fourth oscillator (that 'feels' the sine of the incoming x-polarized field) couples negative with a cosine term to the second oscillator. As a consequence, we have equal coupling terms that cancel each other.

Knowing how the oscillators are moving, we can determine the scattering matrices. Just like in the case of two layers of rods we have two: the first one determines the field transmitted by the first cross and the second one describes the field transmitted through the whole structure.

Scattering matrix of the first cross

Observed from distance $\tilde{r}_1$ on the z axis, the field radiated by the two oscillators in the first layer is

$$\mathbf{E}_{rad,\mathbf{1}} = -\frac{N\,e}{4\pi\varepsilon_0\,\tilde{r}_1\,c^2}\ \left(\mathbf{n}\times(\mathbf{n}\times\ddot{\mathbf{r}}_1) + \mathbf{n}\times(\mathbf{n}\times\ddot{\mathbf{r}}_2)\right)_{t-\frac{\tilde{r}_1}{c}}, \tag{7.67}$$

with $\mathbf{n} = (0,0,1)$. With Eqs. (7.61) and (7.66) we write the scattering matrix equation

$$-\frac{N\,e}{4\pi\varepsilon_0\,\tilde{r}_1\,c^2} \begin{pmatrix} -\ddot{\rho}_1(t) \\ 0 \end{pmatrix}_{t-\frac{\tilde{r}_1}{c}} \stackrel{!}{=} \frac{1}{-ik\tilde{r}_1} \begin{pmatrix} S_{\mathbf{21}} & S_{\mathbf{31}} \\ S_{\mathbf{41}} & S_{\mathbf{11}} \end{pmatrix} \begin{pmatrix} E_0\, e^{-i\omega t + ik\left(\frac{h}{2}+\tilde{r}_1\right)} \\ 0 \end{pmatrix}. \tag{7.68}$$

[8] We assume all oscillators to be identical in this argumentation. Therefore, damping, the number of electrons and the resonance frequency are equal for all rods.

The bold **1** is a reminder that we deal with the first layer. Using Eq. (7.66), the scattering matrix entries are

$$S_{21} = \frac{-i\,k^3\,N\,e^2}{4\pi\varepsilon_0\,m\,e^{ik\frac{h}{2}}}\,\frac{L\,\beta_2-\Sigma\,\beta_1}{L^2-\Sigma^2}, \tag{7.69a}$$

$$S_{41} = 0. \tag{7.69b}$$

Since the second oscillator is not excited there is no polarization rotation. The field transmitted by the first and second oscillator observed at the point $(0,0,d+h)$, $d>0$, is

$$\mathbf{E}_{t\mathbf{1}}(0,0,d+h,t) = E_0\,e^{-i\omega t+ikh+ikd}\left(1-S_{21}\,\frac{2\pi}{k^2\,A}\right)\hat{\mathbf{e}}_x, \tag{7.70}$$

and therefore x-polarized.

Scattering matrix of the second cross

Observed from a distance $\tilde{r}_2$ on the z axis, the field emitted by the second cross is given by

$$\begin{aligned}
\mathbf{E}_{rad,\mathbf{2}} &= -\frac{N\,e}{4\pi\varepsilon_0\,c^2\,\tilde{r}_2}\,\left((\mathbf{n}\times(\mathbf{n}\times\ddot{\mathbf{r}}_3)+(\mathbf{n}\times(\mathbf{n}\times\ddot{\mathbf{r}}_4)\right)_{t-\frac{\tilde{r}_2}{c}}\\
&= -\frac{N\,e}{4\pi\varepsilon_0\,c^2\,\tilde{r}_2}\begin{pmatrix}-\ddot{\rho}_3\,\cos\varphi-\ddot{\rho}_4\,\sin\varphi\\ -\ddot{\rho}_3\,\sin\varphi+\ddot{\rho}_4\,\cos\varphi\\ 0\end{pmatrix}_{t-\frac{\tilde{r}_2}{c}}\\
&= \frac{N\,e^2\,\omega^2\,E_0e^{-i\omega t}}{4\pi\varepsilon_0\,m\,c^2\,\tilde{r}_2}\,\frac{L\beta_1-\Sigma\beta_2}{L^2-\Sigma^2}\begin{pmatrix}\cos\varphi\cos\varphi+\sin\varphi\sin\varphi\\ \cos\varphi\sin\varphi-\sin\varphi\cos\varphi\\ 0\end{pmatrix}_{t-\frac{\tilde{r}_2}{c}}.
\end{aligned} \tag{7.71}$$

Here, we have the second surprise—not only does the second oscillator not contribute to the system, the rotation angle of the second cross does not play a role at all. This is understandable in a similar fashion as before. The third oscillator (which is exposed to the cosine of the incoming field) couples with a cosine to the first oscillator. The fourth oscillator (which is exposed to the sine of the incoming field) couples with a sine to the first oscillator—as a result both coupling terms add up as if there was only one rod with the orientation of the polarization of the incoming plane wave.

Based on

$$\frac{Ne^2k^2E_0e^{-i\omega t+ik\tilde{r}_2}}{4\pi\varepsilon_0\,m\,\tilde{r}_2}\,\frac{L\beta_1-\Sigma\beta_2}{L^2-\Sigma^2}\begin{pmatrix}1\\0\end{pmatrix}\stackrel{!}{=}\frac{1}{-ik\tilde{r}_2}\begin{pmatrix}S_{22}&S_{32}\\S_{42}&S_{12}\end{pmatrix}\begin{pmatrix}E_{x,t\mathbf{1}}(\mathbf{d},t)\\0\end{pmatrix}, \tag{7.72}$$

with $\mathbf{d}=(0,0,b+\frac{3}{2}h+\tilde{r}_2)$, we obtain as scattering matrix entries

$$S_{22} = \frac{-i\,k^3\,N\,e^2}{4\pi\varepsilon_0\,m}\,\frac{1}{e^{ikb+ik\frac{3}{2}h}\left(1-\frac{S_{21}\,2\pi}{k^2\,A}\right)}\,\frac{(L\,\beta_1-\Sigma\,\beta_2)}{L^2-\Sigma^2}, \tag{7.73a}$$

$$S_{42} = 0. \tag{7.73b}$$

Transmitted field

Since we know the scattering matrix of the second layer, we can now calculate the field transmitted through the whole structure—the two layers of periodically arranged, mutually rotated crosses. Observed on the z axis at the point $(0, 0, e)$, $e = h + b + h + e'$, $e' > 0$, the transmitted field is

$$\mathbf{E}_{t\mathbf{2}} = E_0\, e^{-i\omega t + ike} \left(1 - \frac{S_{\mathbf{21}}\, 2\pi}{k^2\, A}\right) \left(1 - \frac{S_{\mathbf{22}}\, 2\pi}{k^2\, A}\right) \hat{\mathbf{e}}_x. \tag{7.74}$$

Comparing these results with the transmitted field from the system of two layers of unrotated rods, we find that the crosses, no matter which value the angle φ has, behave like two layers of unrotated rods. Therefore, no polarization conversion effects are observable.

Parameter fit

In Sections 7.3.4 and 7.3.5, the system under consideration was a rod (or two rods) in a rectangular unit cell. Since two layers of crosses as sketched in Fig. 7.15 exhibit a building block that is C_4 symmetric, it makes sense to choose the unit cell accordingly. Otherwise, the unit cell would reduce the systems symmetry. Therefore, we consider a rod of size 250 nm $\times$ 50 nm $\times$ 25 nm (length, width, height) in a square unit cell of length 400 nm. Naturally, this means that we have to perform new parameter fits. The course of action is like before: first, the mass, resonance frequency and damping are fitted to numerical data obtained for one layer of unrotated rods with incident x-polarized light. The resulting transmittance is depicted in Fig. 7.16(a). The fit parameters read

$$m_{tot} = 3.46 \cdot 10^{-23}\ \text{kg}, \qquad \omega_0 = 1.82 \cdot 10^{15}\ \text{Hz}, \qquad \Gamma = 3.62 \cdot 10^{14}\ \text{Hz}. \tag{7.75}$$

Second, the coupling between two layers has to be fitted. The transmittance spectrum for two layers of grid-aligned rods is shown in Fig. 7.16(b), together with the dipole model's description. The coupling strength is $L = 2.63 \cdot 10^{29}\, \frac{1}{\text{s}^2}$ for a layer spacing of $b = 50$ nm.

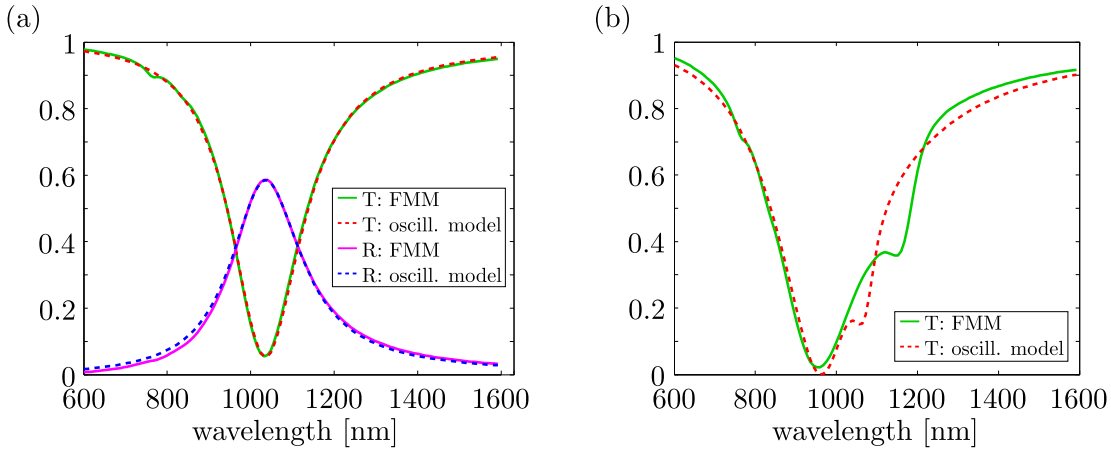

Figure 7.16: Transmittance for one layer of rods (panel (a)) and two layers of unrotated rods (panel (b)) for the setup with the square unit cell. It is square in order to preserve the systems symmetry. See text for further details.

Since the model's parameters are now fixed, we can investigate the predictions of the model for light impinging on two layers of mutually rotated crosses.

Predictions for two layers of mutually rotated crosses

Using Eq. (7.74) and the fitted values for the dipole model's parameters, we can plot the predictions of the dipole model for the light transmitted by two layers of mutually rotated crosses. The results are shown in Fig. 7.17. As we see, the model exhibits the same difficulties as before—the resonances in Fig. 7.17(a) are not reproduced well. The important aspect is that the model does not predict an electric field in y-direction, cf. Fig. 7.17(b), in contrast to the numerical simulation with the FMM. We found this result already while inspecting Eqs. (7.66) and (7.71).

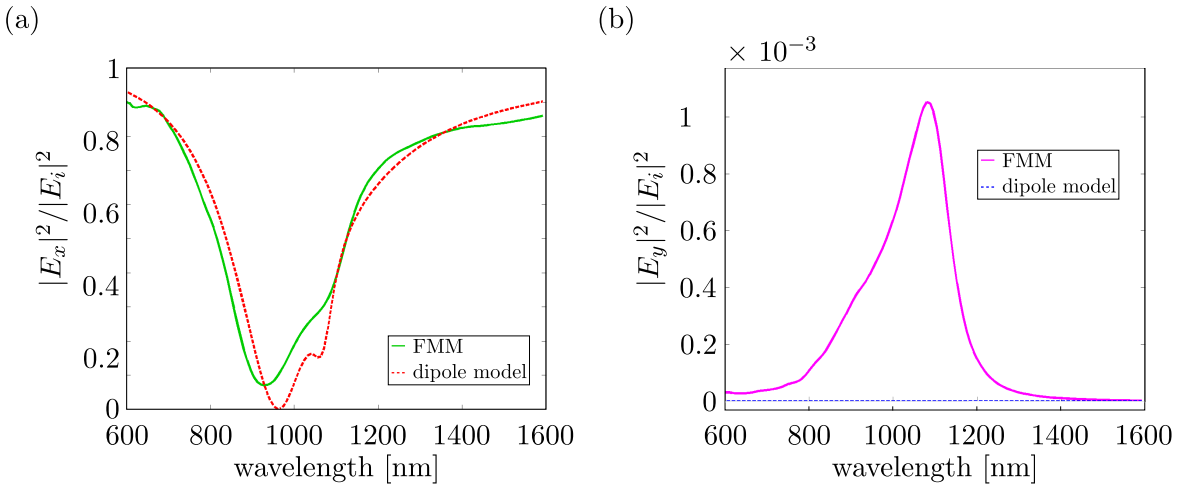

Figure 7.17: Transmitted light in x- and y-direction. The dipole model shows features in x-direction similar to the numerical data. They fundamentally differ in y-direction: while the dipole model does not predict any light, the FMM finds a nonzero y-component of the transmitted electric field.

7.3.7 Summary and conclusion

This section contains the information gathered for the dipole model in Ref. [62], which was supposed to describe the transmission properties of certain (multi-layered) nanostructures.

The model's basic assumptions were that we can represent a metallic rod by an oscillating dipole and that looking at the optical atom itself instead of doing an analysis of the whole array, would be sufficient.

We started with the simplest structure possible, one layer of metallic rods. We analyzed the motion of the oscillator due to the incident electric field and were, thereby, able to determine the scattered field. We fitted the free parameters of the model to numerical data and were able to reproduce one layer of rods very well. The success was evident, especially when the rods were rotated in the unit cell and the model could still reproduce numerical data perfectly without additional fitting.

Thereafter, we tried to model two layers of rods. This is a difficult task since there are multiple reflections and couplings between the layers to consider. We carried out the necessary analysis and found that the transmittance spectrum of the nanostructures cannot be fully explained by the dipole model in its current form.

Finally, we investigated two layers of mutually rotated crosses. This structure is special because it is C_4 symmetric and shows a handedness for most rotation angles. We found a fundamental difference between the predictions of the oscillator model and numerical calculations: the FMM results shows a polarization rotation and the oscillator model does not.

Due to the results obtained, we conclude that the model should be extended to describe the transmission properties of the considered nanostructures, although very good results were obtained for single layer structures. A first attempt to extend the model by describing one rod as two perpendicular oscillators did not show qualitatively new results, see App. A of Ref. [62]. In the following sections, we discuss further predictions and developments of new models based on the dipole model.

7.4 Two layers of rods - large spacing

In this section, we start with new insights gained beyond my previous work from my Staatsexamensarbeit. However, we do not yet develop the method further. Instead, we continue to study the model described in Section 7.3. The system of interest in this section consists of two layers of unrotated rods that are far apart, see Fig. 7.18.

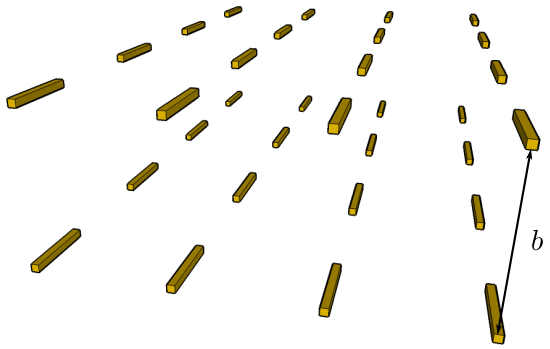

Figure 7.18: The system of interest: two layers of unrotated rods with a large spacing b. The geometrical parameters are like in Section 7.3.5: the rods are 500 nm long, have a height and width of 50 nm and are centered within a 1350 nm × 900 nm unit cell. Their distance is denoted by b.

We already discussed a system with two layers ($\varphi = 0°$ and $b = 1000$ nm) in Section 7.3.5. The transmittance could be reproduced by the dipole model (cf. Fig. 7.14(a)) with the reasonable assumption that the interlayer coupling is zero, i.e., $L = 0$. Since there is no coupling left, only one resonance appears in the spectrum. Also, the polarization state could be described well, cf. Fig. 7.14(b).

In this section, we examine how the transmittance changes upon an increase of the spacing b. For that, Figs. 7.19(a) to (e) display the transmittance of the system as predicted by the FMM and the dipole model. For the dipole model, Eqs. (7.54) to (7.60) were used with a vanishing coupling, i.e., $L = 0$. It is remarkable how well the dipole model reproduces the numerical data. Note that no fit parameters were adjusted. Only the distance b changes. The system's behavior for small wavelengths is particularly interesting. Here, strong oscillations occur which are also well described by the dipole model. In order to find their origin, we

display in Fig. 7.19(f) a curve (dashed blue) that is obtained by just multiplying two single layers of the dipole model. To be precise, we calculate the transmittance by

$$S_2 = \frac{-i\,k^3\,N\,e^2}{4\pi\varepsilon_0\,m\,(\omega_0^2-\omega^2-i\omega\Gamma)}, \tag{7.76a}$$

$$T = \frac{|\mathbf{E}_t|^2}{|\mathbf{E}_i|^2} = \left|1-\frac{2\pi}{k^2\,A}\,S_2\right|^4. \tag{7.76b}$$

Here, S_2 is the scattering matrix entry for a single layer of unrotated rods, cf. Eq. (7.30b) with $\varphi = 0°$. As we see, the herewith obtained curve in Fig. 7.19(f) does not at all resemble the numerical data. No oscillations for small wavelengths are found. What is the difference between the dipole model for two layers as presented in Section 7.3.5 and the transmittance in Eq. (7.76)? Contrary to Eq. (7.76), in the case of the proper dipole model multiple scattering is taken into account, cf. Fig. 7.11. This insight leads us to the conclusion that the oscillations in Fig. 7.19 stem from Fabry-Pérot oscillations, i.e., the multiple scattering processes between the layers. This shows the strengths of an analytical model—we can intentionally vary the model and study the impact of the variation on the model's predictions. Thereby, we gain an understanding of the occurring physical processes.

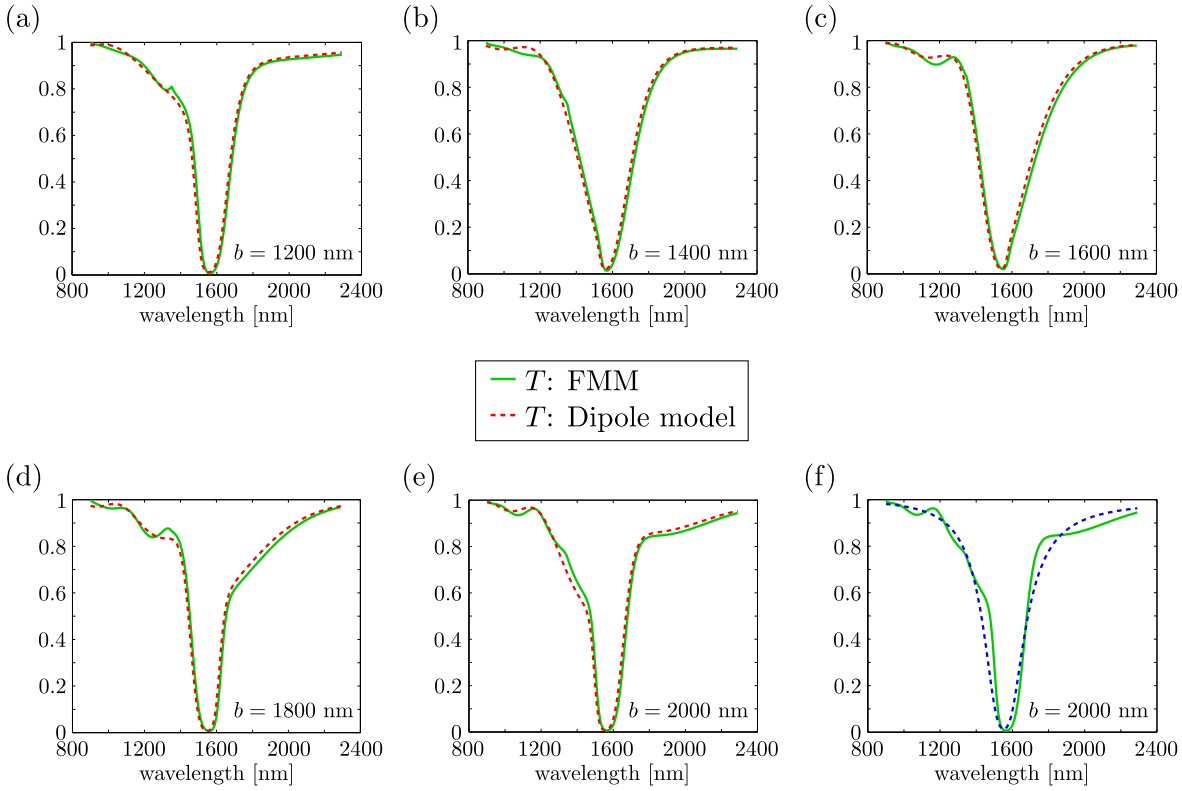

Figure 7.19: Panels (a) to (e) depict the transmittance computed with the FMM and the dipole model (with coupling $L = 0$) for varying layer distances b. Their agreement is excellent. Panel (f) shows a transmittance curve obtained by multiplying two single layer transmission coefficients in the dipole model. The result is poor. This means that the oscillations at small wavelengths can be attributed to the multiple back reflections between the layers, i.e., Fabry-Pérot oscillations, since they are incorporated in the proper dipole model discussed in Section 7.3.5.

After having understood the spectra in detail, we can use another strength of the analytical model: we can easily predict the transmittance spectra for a great number of different layer spacings b with very little computational effort. Figure 7.20 shows the transmittance color-coded over the wavelength of the incident light and the layer spacing b. Panels (a), (b), (c) and (d) show the transmittance for systems where the upper rod is rotated by $\varphi = 0°$, $-30°$, $-60°$ and $-90°$, respectively.

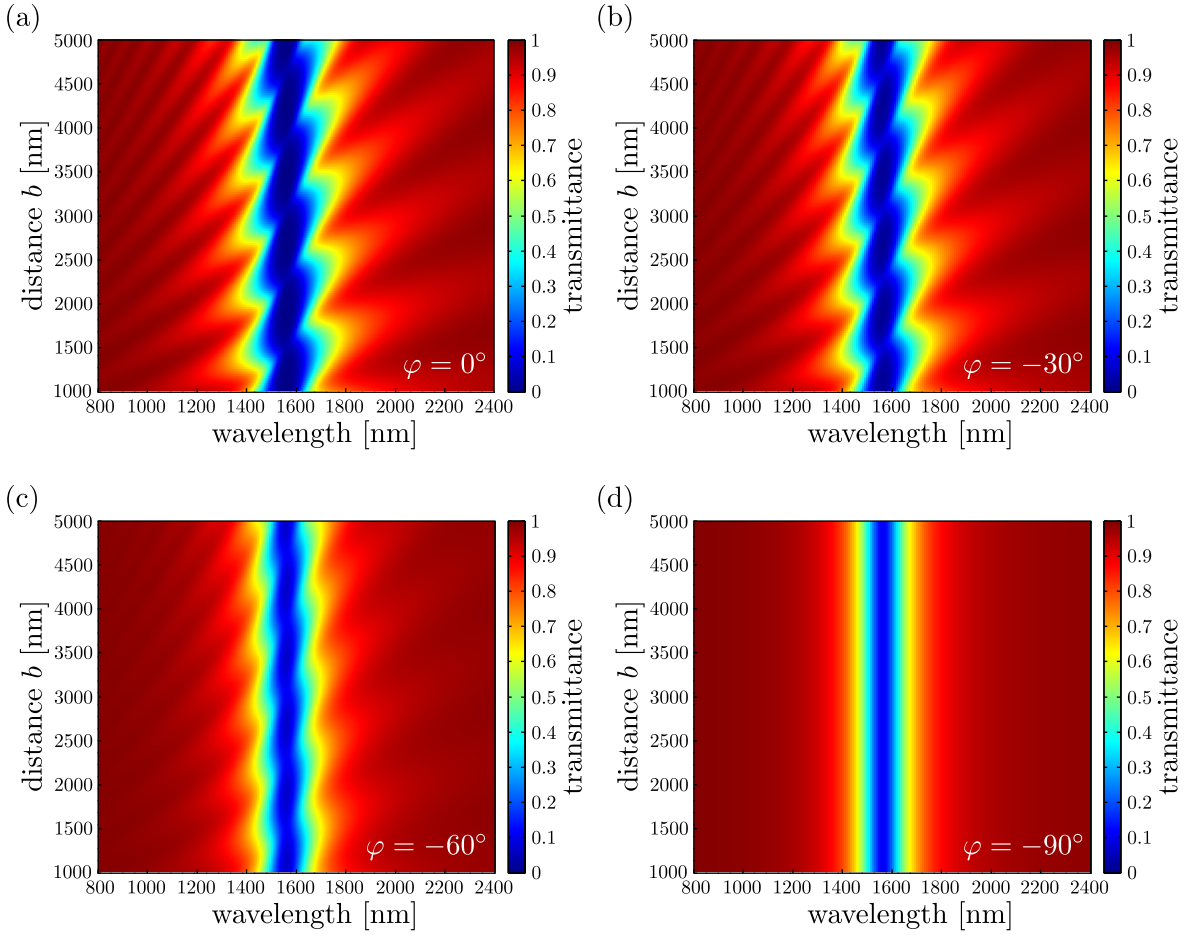

Figure 7.20: Dipole model predictions for the transmittance over layer distance b and wavelength for different rod rotation angles. The more the rods in the second layer are rotated with respect to the first layer, the less they influence the transmittance behavior. While they cause strong Fabry-Pérot oscillations for $\varphi = 0°$, the influence of the second layer is non-existent for $\varphi = -90°$. For angles close to $\varphi = 0°$ the transmittance reaches minimal values. The reason is that the second layer of rods absorbs and reflects most around these angles.

The strongest Fabry-Pérot oscillations occur for unrotated rods. The more the rods are rotated (cf. Fig. 7.20(b) and (c)) the weaker the oscillations get until they disappear, cf. Fig. 7.20(d). This is plausible, since the second layer reflects less, the more the rods are rotated. For $\varphi = -90°$, the second rod is perpendicular to the incident electric field and, thus, the dipole is not excited. Therefore, no reflections occur at the second layer of rods and, thus, no Fabry-Pérot oscillations are observable. Like in previous cases, the computational effort for these large parameter scans is of the order of seconds.

7.5 Lattice-periodic calculation

Up to this point we assumed that all particles within the slab are identical, non-interacting and randomly distributed, see Section 7.3.3. This allowed us to describe the transmission properties of light through the investigated periodic nanostructures. Apparently, the model does not include the lattice resonances that can be observed, e.g., in Fig. 7.7. In this section, I demonstrate that the dipole model can qualitatively reproduce the lattice resonances if it is changed accordingly. We start by reviewing the theory of light scattering by particle arrays [78]. Then, we reproduce the results for a test system discussed in Ref. [78]. Finally, we apply the lattice periodic calculation to the dipole model.

7.5.1 Light scattering by particle arrays

In the following, we consider periodically arranged particles on a square lattice with lattice constant a. The particles are located at the lattice sites $\mathbf{R}_n$ as depicted in Fig. 7.21.

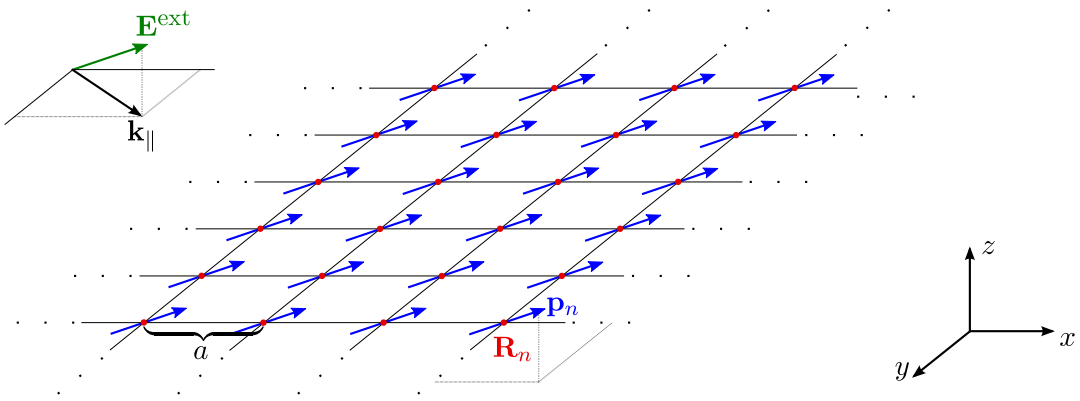

Figure 7.21: A two-dimensional array of particles illuminated by an electric field $\mathbf{E}^{\text{ext}}$. On each lattice site $\mathbf{R}_n$ a dipole moment $\mathbf{p}_n$ is induced.

Any electric field $\mathbf{E}$ induces a dipole moment $\mathbf{p}_n$ given by

$$\mathbf{p}_n = \alpha_E \, \mathbf{E}(\mathbf{R}_n), \tag{7.77}$$

where α_E is the polarizability of the particle. This dipole moment at lattice site $\mathbf{R}_n$ itself creates an electric field. At some point $\mathbf{r}$ this field reads[9]

$$\mathbf{E}(\mathbf{r}) = \mathcal{G}^0(\mathbf{r} - \mathbf{R_n}) \, \mathbf{p}_n, \tag{7.78}$$

where we used the dipole-dipole interaction tensor $\mathcal{G}^0$ defined as

$$\mathcal{G}^0(\mathbf{r}) = \left(k^2 \mathbb{1}_3 + \nabla\nabla\right) \frac{e^{ikr}}{r}. \tag{7.79}$$

Here, $\mathbb{1}_3$ denotes the three-dimensional unit matrix. The action of $\mathcal{G}^0$ on a dipole moment $\mathbf{p}$ is then given by

$$\mathcal{G}^0(\mathbf{r}) \cdot \mathbf{p} = \frac{e^{ikr}}{r^3} \left(((kr)^2 + ikr - 1) \, \mathbf{p} - \frac{(kr)^2 + 3ikr - 3}{r^2} (\mathbf{r} \cdot \mathbf{p}) \, \mathbf{r} \right) \tag{7.80}$$

[9] In this section, we use Gaussian units. We will skip to SI units when we apply the lattice calculation to the dipole model.

Explicitly, the tensor components read

$$\mathcal{G}^0_{xx} = k^2 \frac{e^{ikr}}{r} + e^{ikr} \left(\frac{ik}{r^2} - \frac{k^2x^2}{r^3} - \frac{1}{r^3} - \frac{3ikx^2}{r^4} + \frac{3x^2}{r^5} \right), \tag{7.81a}$$

$$\mathcal{G}^0_{xy} = \mathcal{G}^0_{yx} = e^{ikr} \left(-\frac{k^2xy}{r^3} - \frac{3ikxy}{r^4} + \frac{3xy}{r^5} \right), \tag{7.81b}$$

$$\mathcal{G}^0_{xz} = \mathcal{G}^0_{zx} = e^{ikr} \left(-\frac{k^2xz}{r^3} - \frac{3ikxz}{r^4} + \frac{3xz}{r^5} \right), \tag{7.81c}$$

$$\mathcal{G}^0_{yy} = k^2 \frac{e^{ikr}}{r} + e^{ikr} \left(\frac{ik}{r^2} - \frac{k^2y^2}{r^3} - \frac{1}{r^3} - \frac{3iky^2}{r^4} + \frac{3y^2}{r^5} \right), \tag{7.81d}$$

$$\mathcal{G}^0_{yz} = \mathcal{G}^0_{zy} = e^{ikr} \left(-\frac{k^2yz}{r^3} - \frac{3ikyz}{r^4} + \frac{3yz}{r^5} \right), \tag{7.81e}$$

$$\mathcal{G}^0_{zz} = k^2 \frac{e^{ikr}}{r} + e^{ikr} \left(\frac{ik}{r^2} - \frac{k^2z^2}{r^3} - \frac{1}{r^3} - \frac{3ikz^2}{r^4} + \frac{3z^2}{r^5} \right). \tag{7.81f}$$

After thoroughly defining the interaction tensor, we are interested in the self-consistent dipole moment at the lattice site $\mathbf{R}_n$. It is important to note that every dipole moment affects every other dipole moment since it causes a field interacting with all other dipoles. This is the reason why the dipole moment has to be deduced self-consistently. It reads

$$\mathbf{p}_n = \alpha_E \left(\mathbf{E}^{\text{ext}}(\mathbf{R}_n) + \sum_{n' \neq n} \mathcal{G}^0(\mathbf{R}_n - \mathbf{R}_{n'}) \, \mathbf{p}_{n'} \right), \tag{7.82}$$

where

$$\mathbf{E}^{\text{ext}}(\mathbf{R}_n) = \mathbf{E}^{\text{ext}} \, e^{i\mathbf{k}_\parallel \mathbf{R}_n} \tag{7.83}$$

is the external field into which the lattice site enters only with a phase factor. This phase factor is given by the in-plane component $\mathbf{k}_\parallel$ of the incident field's wave vector. The first part of Eq. (7.82) stems from Eq. (7.77) and describes the dipole moment induced by the external field. The second term sums up all contributions by the other dipole moments. Such statements are well-known from solid-state physics. Bloch's theorem, see Section 2.7.2, guarantees that the dipole moment $\mathbf{p}_n$ has the form

$$\mathbf{p}_n = \mathbf{p} \, e^{i\mathbf{k}_\parallel \mathbf{R}_n}. \tag{7.84}$$

We enter Eq. (7.84) in Eq. (7.82) and obtain

$$\mathbf{p} \, e^{i\mathbf{k}_\parallel \mathbf{R}_n} = \alpha_E \left(\mathbf{E}^{\text{ext}}(\mathbf{R}_n) + \sum_{n' \neq n} \mathcal{G}^0(\mathbf{R}_n - \mathbf{R}_{n'}) \, \mathbf{p} \, e^{i\mathbf{k}_\parallel \mathbf{R}_{n'}} \right) \tag{7.85a}$$

$$\Rightarrow \quad \mathbf{p} = \alpha_E \, \mathbf{E}^{\text{ext}} + \alpha_E \, \mathbf{p} \sum_{n' \neq n} \mathcal{G}^0(\mathbf{R}_n - \mathbf{R}_{n'}) \, e^{i\mathbf{k}_\parallel (\mathbf{R}_{n'} - \mathbf{R}_n)} \tag{7.85b}$$

using Eqs. (7.83) and (7.84). Without loss of generality we can use $n = 0$ and $\mathbf{R}_0 = 0$. Then, we can rewrite the last term in Eq. (7.85b)

$$\sum_{n' \neq 0} \mathcal{G}^0(0 - \mathbf{R}_{n'}) \, e^{i\mathbf{k}_\parallel (\mathbf{R}_{n'} - 0)} \quad \overset{\mathbf{R}_{n'} \to -\mathbf{R}_n}{=} \quad \sum_{n \neq 0} \mathcal{G}^0(\mathbf{R}_n) \, e^{-i\mathbf{k}_\parallel \mathbf{R}_n}. \tag{7.86}$$

In Eq. (7.86) we first changed the summation index from n' to n. Second, we used the fact that for every particle on lattice site $\mathbf{R}_n$ there is another particle at $-\mathbf{R}_n$. With this intermediate step we can write Eq. (7.85b) in a more convenient form:

$$\mathbf{p} = \alpha_E \, \mathbf{E}^{\text{ext}} + \alpha_E \, \mathbf{p} \sum_{n \neq 0} \mathcal{G}^0(\mathbf{R}_n) \, e^{-i\mathbf{k}_\parallel \mathbf{R}_n} \tag{7.87a}$$

$$\Rightarrow \quad \mathbf{p} \left(\frac{1}{\alpha_E} - \sum_{n \neq 0} \mathcal{G}^0(\mathbf{R}_n) \, e^{-i\mathbf{k}_\parallel \mathbf{R}_n} \right) = \mathbf{E}^{\text{ext}} \tag{7.87b}$$

$$\Rightarrow \quad \mathbf{p} = \frac{1}{\frac{1}{\alpha_E} - G(\mathbf{k}_\parallel)} \, \mathbf{E}^{\text{ext}} \tag{7.87c}$$

with the abbreviation

$$G(\mathbf{k}_\parallel) = \sum_{n \neq 0} \mathcal{G}^0(\mathbf{R}_n) \, e^{-i\mathbf{k}_\parallel \mathbf{R}_n}. \tag{7.88}$$

The expression we obtain for the dipole moment in Eq. (7.87c) is very elegant since it separates the contributions of the single particle (α_E) from the lattice contribution ($G(\mathbf{k}_\parallel)$).

As a first step, we derived the self-consistent dipole moment of the particles. However, what we are really interested in is the field that is transmitted through the arrangement of periodic scatterers. Obtaining the expression for the transmitted field of a single scatterer is the next objective, followed by the derivation of the total transmitted field.

Before we can handle the expression for the transmitted field we have to formulate some mathematical tools. First, we reformulate the right end of Eq. (7.79) by changing to the two-dimensional momentum space at $z = 0$, i.e., in the plane of the periodic arrangement of particles. This reads

$$\frac{e^{ikr}}{r} = \frac{i}{2\pi} \int \frac{d^2\mathbf{Q}}{\sqrt{k^2 - Q^2}} \, e^{i(\mathbf{QR} + \sqrt{k^2 - Q^2}|z|)}, \tag{7.89}$$

with the normal momentum $\sqrt{k^2 - Q^2}$ and the notation $\mathbf{R} = (x, y)$ and $\mathbf{r} = (\mathbf{R}, z)$. This way, Eq. (7.79) becomes

$$\mathcal{G}^0(\mathbf{r}) = \left(k^2 \mathbb{1}_3 + \nabla\nabla \right) \frac{e^{ikr}}{r} = \left(k^2 + \nabla\nabla \right) \frac{i}{2\pi} \int \frac{d^2\mathbf{Q}}{\sqrt{k^2 - Q^2}} \, e^{i(Q_x x + Q_y y + \sqrt{k^2 - Q^2}|z|)} \tag{7.90}$$

Next, we swap differentiation and integration and obtain expressions like

$$\mathcal{G}^0_{xx}(\mathbf{r}) = \frac{i}{2\pi} \int \frac{d^2\mathbf{Q}}{\sqrt{k^2 - Q^2}} \left(k^2 - Q_x^2 \right) \, e^{i(\mathbf{QR} + \sqrt{k^2 - Q^2}|z|)} \tag{7.91}$$

for the xx component of the interaction tensor.

In the following, we restrict ourselves to specular symmetry with respect to the xz-plane and normal incidence (i.e., $\mathbf{k}_\parallel = 0$). This is reasonable since we are interested in demonstrating that, in general, lattice resonances can be incorporated into a dipole model.

With the corresponding mathematical preparations at hand, we proceed to the field that is emitted by a single dipole. An observer at a point $\mathbf{r}$ finds the field to be

$$\mathbf{E}^{\text{trans}}_{\text{single}}(\mathbf{r}) = \left(\left(k^2 + \nabla\nabla \right) \frac{e^{ikr}}{r} \right) \mathbf{p}. \tag{7.92}$$

Next, we enter the self-consistent dipole moment from Eq. (7.87c) and the expression in Eq. (7.89) in Eq. (7.92) and obtain

$$\mathbf{E}^{\text{trans}}_{\text{single}}(\mathbf{r}) = \left((k^2 + \nabla\nabla) \frac{i}{2\pi} \int \frac{d^2\mathbf{Q}}{\sqrt{k^2 - Q^2}} \, e^{i(\mathbf{QR} + \sqrt{k^2 - Q^2}|z|)} \right) \frac{\mathbf{E}^{\text{ext}}}{\frac{1}{\alpha_E} - G(\mathbf{k}_\parallel)}. \tag{7.93}$$

Just like we did in the step from Eq. (7.90) to Eq. (7.91) we swap differentiation and integration in Eq. (7.93) and find

$$\mathbf{E}^{\text{trans}}_{\text{single}} = \left(\frac{i}{2\pi} \int \frac{d^2\mathbf{Q}}{\sqrt{k^2 - Q^2}} \left(k^2 - Q_x^2\right) \, e^{i(\mathbf{QR} + \sqrt{k^2 - Q^2}|z|)} \right) \frac{1}{\frac{1}{\alpha_E} - G_{xx}(0)} \, \mathbf{E}^{\text{ext}} \tag{7.94}$$

for the transmitted field caused by a single particle.

The final step is to derive an expression for the total transmitted field, i.e., the field that is found behind the periodic array of particles. Naturally, it consists of the external field and the sum of all fields caused by the induced dipole moments of the scatterers. The total transmitted field then reads

$$\mathbf{E}^{\text{trans}}_{\text{total}} = \mathbf{E}^{\text{ext}} + \sum_n \left(\frac{i}{2\pi} \int d^2\mathbf{Q} \, \frac{(k^2 - Q_x^2)}{\sqrt{k^2 - Q^2}} \, e^{i(\mathbf{QR}_n + \sqrt{k^2 - Q^2}|z|)} \right) \frac{\mathbf{E}^{\text{ext}}}{\frac{1}{\alpha_E} - G_{xx}(0)}. \tag{7.95}$$

Using the relation

$$\sum_n e^{i\mathbf{Q}\cdot\mathbf{R}_n} = \frac{(2\pi)^2}{A} \sum_{\mathbf{g}} \delta(\mathbf{Q} - \mathbf{g}) \tag{7.96}$$

with the sum over the two-dimensional reciprocal lattice vectors $\mathbf{g}$ and the unit cell area A we can reformulate Eq. (7.95) such that it reads

$$\begin{aligned} \mathbf{E}^{\text{trans}}_{\text{total}} &= \mathbf{E}^{\text{ext}} + \lim_{z\to 0} \left[\left(\frac{2\pi i}{A} \int d^2\mathbf{Q} \, \frac{(k^2 - Q_x^2)}{\sqrt{k^2 - Q^2}} \sum_{\mathbf{g}} \delta(\mathbf{Q} - \mathbf{g}) \, e^{i\sqrt{k^2 - Q^2}|z|} \right) \cdot \right. \\ &\qquad \left. \frac{1}{\frac{1}{\alpha_E} - G_{xx}(0)} \, \mathbf{E}^{\text{ext}} \right] \qquad (7.97) \\ &= \mathbf{E}^{\text{ext}} + \lim_{z\to 0} \left[\frac{2\pi i}{A} \sum_{\mathbf{g}} \frac{(k^2 - g_x^2)}{\sqrt{k^2 - g^2}} \, e^{i\sqrt{k^2 - g^2}|z|} \, \frac{\mathbf{E}^{\text{ext}}}{\frac{1}{\alpha_E} - G_{xx}(0)} \right]. \qquad (7.98) \end{aligned}$$

In the last step we integrated over the δ functions. Performing the limit value and restricting us to 0^{th} order yields

$$\mathbf{E}^{\text{trans}}_{\text{total}} = \underbrace{\left(1 + \frac{2\pi i k}{A} \, \frac{1}{\frac{1}{\alpha_E} - G_{xx}(0)} \right)}_{=:\tilde{t}} \mathbf{E}^{\text{ext}} \tag{7.99}$$

for the total transmitted field.

7.5.2 Investigation of a test system

In this section, we reproduce the results for a test system investigated in Ref. [78]. The expression for the reflected field (in terms of a reflection coefficient) is given by

$$\tilde{r} = -\frac{1}{1 + \frac{i\,A}{2\pi k}\mathrm{Re}\left(\frac{1}{\alpha_E} - G_{xx}(0)\right)}. \tag{7.100}$$

Since the derivation is lengthy, I do not present it here. However, since it is described only marginally in Ref. [78] I added the derivation to the appendix, see App. C.

The test system is a layer of perfectly conducting discs. They are arranged on a square lattice with lattice constant a. A sketch is depicted in Fig. 7.23(a). The polarizability of such a structure can be derived analytically by perceiving the disc as ellipsoid with vanishing height. The polarizability is given by

$$\alpha_E = \frac{1}{\frac{3\pi}{4b^3} - \frac{2ik^3}{3}}, \tag{7.101}$$

where b denotes the radius of the discs, see Ref. [18]. In the test system, the lattice constant a is chosen to be $a = 5b$. The distance from the origin to the lattice sites $\mathbf{R}_i$ is

$$|\mathbf{R}_i| = \sqrt{n^2a^2 + m^2a^2} = a\sqrt{n^2 + m^2}, \qquad n, m \in \mathbb{Z}. \tag{7.102}$$

With the unit cell area $A = a^2$, the reflection coefficient reads

$$\tilde{r} = -\left(1 + \frac{i\bar{\lambda}}{4\pi^2}\,\mathrm{Re}\left(\frac{3\pi 5^3}{4} - \frac{2i\,(2\pi)^3}{3\bar{\lambda}^3} - a^3\sum_{i\neq 0}\mathcal{G}^0_{xx}(\mathbf{R}_i)\right)\right)^{-1}. \tag{7.103}$$

In this formulation, $\bar{\lambda} = \lambda/a$ is the wavelength in units of the lattice constant. The lattice sum reads

$$\begin{aligned}\sum_{i\neq 0}\mathcal{G}^0_{xx}(\mathbf{R}_i) \;=\; & \frac{1}{a^3}\sum_{n,m=-\infty}^{\infty\,\prime} e^{i\frac{2\pi}{\bar{\lambda}}\sqrt{n^2+m^2}}\left(\frac{4\pi^2}{\bar{\lambda}^2\sqrt{n^2+m^2}} + \frac{i\,2\pi}{\bar{\lambda}\,(n^2+m^2)}\right.\\ & \left. - \frac{4\pi^2n^2}{\bar{\lambda}^2\sqrt{n^2+m^2}^3} - \frac{1}{\sqrt{n^2+m^2}^3} - \frac{3i\,2\pi\,n^2}{\bar{\lambda}\,(n^2+m^2)^2} + \frac{3n^2}{\sqrt{n^2+m^2}^5}\right),\end{aligned} \tag{7.104}$$

following Eq. (7.81a). The dash close to the sum symbol indicates that the summation does not include the element $n = m = 0$. The reflectance is calculated as the squared absolute value of the reflection coefficient.

Naturally, we cannot numerically compute the infinite sum in Eq. (7.104). Instead, we have to truncate the sum at a certain number of lattice sites. To determine how many sites are needed, a convergence study was performed. The results are depicted in Fig. 7.22.

The lattice sites for the study in Fig. 7.22 were chosen on a square array. Of course, other truncation schemes of the sum in Eq. (7.104) are possible. As we can see in Fig. 7.22, the lattice sum converges extremely slowly. Since this type of slowly converging lattice sums is known, techniques were developed to increase performance. For instance, a possible way is to reformulate Eq. (7.104) into a rapidly converging sum using Ewald's method, see Refs. [79, 80]. Since we are only interested in the basic proof that lattice resonances can be incorporated in the dipole model, we do not apply the method here.

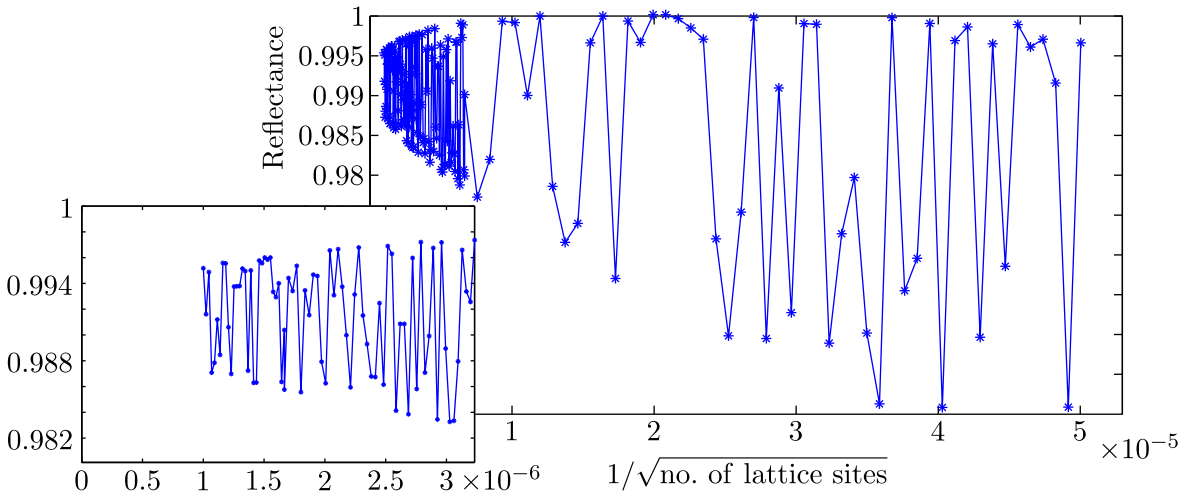

Figure 7.22: Convergence study for the lattice sum in Eq. (7.104). As shown in the inset, a large number of lattice sites is needed in order to reach an error below one percent. This study is performed at a normalized wavelength $\bar{\lambda} = 1.02$. This is the resonance wavelength as depicted in Fig. 7.23.

The highest number of lattice sites in one direction investigated in Fig. 7.22 is one million. According to the inset in Fig. 7.22, the lattice sum is converged up to less than one percent. We use this number of lattice sites to reproduce the reflectance presented in Ref. [78], see Fig. 7.23(a). Our results are depicted in Fig. 7.23(b).

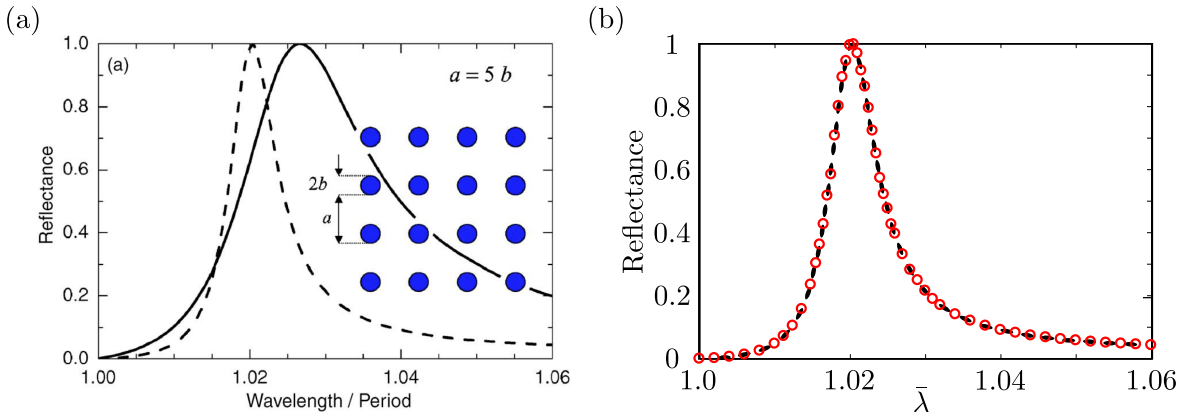

Figure 7.23: Sketch of the test system and reflectance over normalized wavelength. Panel (a) displays the results obtained in Ref. [78] (and is taken from there). Panel (b) displays our results obtained with one million lattice sites in each direction. The dashed black line is the line from panel (a), the red circles mark the points where we calculated the reflectance.

As we see, we can reproduce the reflectance for the test system very well. Thus, we proceed by applying the described formalism to the dipole model.

7.5.3 Application to the dipole model

In order to obtain the field that is transmitted through a layer of rods, we use the expression in Eq. (7.99) and include the polarizability we obtained for the dipole model. Again, we have to calculate the lattice sum which means that we deal with a term similar to Eq. (7.104). The difference is that we no longer have a quadratic unit cell since the unit cell in our investigations in Section 7.3.4 is a rectangle. This means that the lattice sites $\mathbf{R}_i$ are given by

$$|\mathbf{R}_i| = \sqrt{n^2(1350\text{nm})^2 + m^2(900\text{nm})^2} = \underbrace{900\text{nm}}_{=:a} \underbrace{\sqrt{n^2\left(\frac{1350}{900}\right)^2 + m^2}}_{=:\tau_{nm}}, \qquad n, m \in \mathbb{N}. \quad (7.105)$$

Like above we define the normalized wavelength

$$\bar{\lambda} := \frac{\lambda}{a}, \qquad\qquad k = \frac{2\pi}{\bar{\lambda}\, a}. \quad (7.106)$$

The lattice sum then reads

$$\begin{aligned} G_{xx}(0) \;=\; \sum_{i\neq 0} \mathcal{G}^0_{xx}(\mathbf{R}_i) = \frac{1}{a^3} \sum_{n,m=-\infty}^{\infty\,\prime} e^{i\frac{2\pi}{\bar{\lambda}}\tau_{nm}} \left(\frac{4\pi^2}{\bar{\lambda}^2\tau_{nm}} + \frac{i\,2\pi}{\bar{\lambda}\tau_{nm}^2} \right. \\ \left. - \frac{4\pi^2 n^2 \left(\frac{1350}{900}\right)^2}{\bar{\lambda}^2\tau_{nm}^3} - \frac{1}{\tau_{nm}^3} - \frac{3i\,2\pi\, n^2 \left(\frac{1350}{900}\right)^2}{\bar{\lambda}\tau_{nm}^4} + \frac{3n^2\left(\frac{1350}{900}\right)^2}{\tau_{nm}^5} \right). \end{aligned} \quad (7.107)$$

By entering this expression in Eq. (7.99) we obtain the transmitted field in Gaussian units

$$\mathbf{E}^{\text{trans}}_{\text{total}} = \left(1 + \frac{4\,\pi^2\, i}{\bar{\lambda}\,\frac{1350}{900}} \, \frac{1}{\frac{a^3}{\alpha_E} - G_{xx}(0)\, a^3} \right) \mathbf{E}_{\text{ext}}. \quad (7.108)$$

The next step is to enter the polarizability of the dipole model (see Section 7.3.4) and to obtain the transmittance in SI units. It reads

$$T = \left| 1 + \frac{4\pi^2 i}{\bar{\lambda}\,\frac{1350}{900}} \, \frac{1}{\frac{m}{e^2}\left(\omega_0^2 - \left(\frac{2\pi c}{a\,\bar{\lambda}}\right)^2 - i\frac{2\pi c}{a\,\bar{\lambda}}\Gamma\right) a^3\, \frac{4\pi\varepsilon_0}{N} - G_{xx}(0)\, a^3} \right|^2. \quad (7.109)$$

Note that m in Eq. (7.109) is not a summation index but the electron mass. At this point it is worth to once again point out the elegance of this expression: the contribution of the particle, namely the polarizability, and the contribution of the lattice, namely $G_{xx}(0)$, enter separately. This is particularly helpful since we only have to compute the lattice sum once and can then perform the fit to determine the dipole model's free parameters.

Like in Section 7.5.2, we first perform a convergence analysis, see Fig. 7.24. Here, the real part of the lattice sum from Eq. (7.107) without the prefactor $1/a^3$ is plotted over the square root of the inverse number of lattice sites.

The convergence behavior does not differ from the one displayed in Fig. 7.22. Again, high numbers of lattice sites are needed to ensure convergence up to one percent. Like in the previous section, we did not use enhanced truncation schemes. Instead, an equal amount of lattice sites in each direction was considered. Having obtained the lattice sum, we can

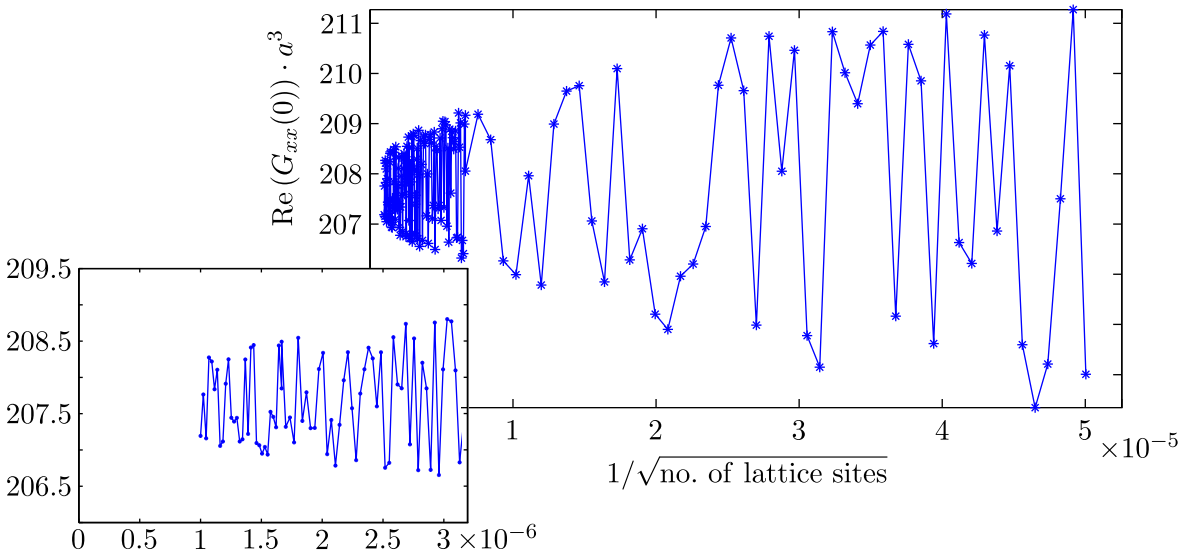

Figure 7.24: Convergence study for the real part of the lattice sum in Eq. (7.107). As shown in the inset, a large number of lattice sites is needed in order to reach an error below one percent. This study is performed at a normalized wavelength $\bar{\lambda} = 1.02$. The imaginary part of the lattice sum shows the same convergence behavior.

perform the fit of the dipole model's parameters to the FMM data. The results are depicted in Fig. 7.25.

The transmittance is reproduced well. The parameters for the dipole model read

$$m_{tot} = N \cdot m = N \cdot m_e \cdot 3.16, \qquad \omega_0 = 1.16 \cdot 10^{15} \text{ Hz}, \qquad \Gamma = 1.51 \cdot 10^{14} \text{ Hz}. \tag{7.110}$$

Since both the numerical transmittance in general and the lattice resonances in particular are reproduced qualitatively well, we successfully demonstrated that the contribution of the lattice can be incorporated in the dipole model.

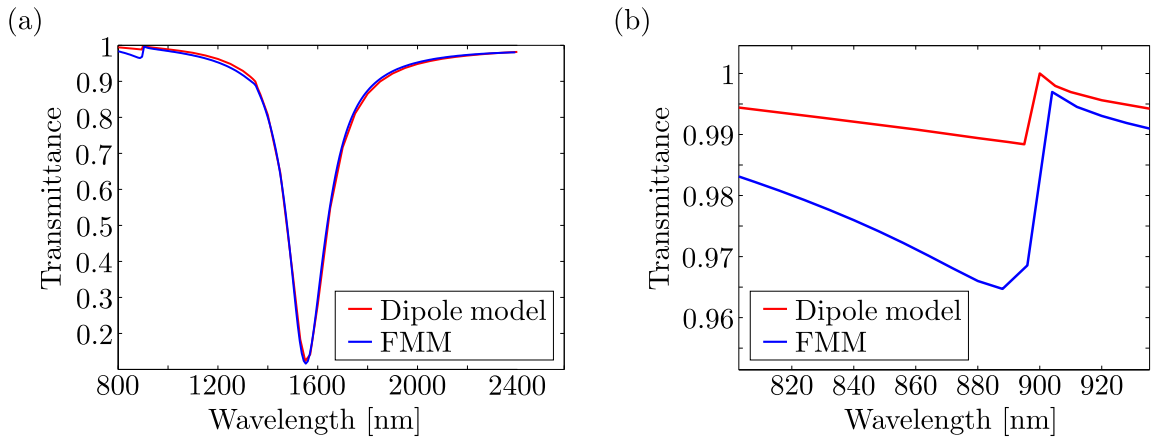

Figure 7.25: Transmittance spectrum for a single layer of unrotated rods. The lattice resonances can be reproduced both at 900 nm and 1350 nm, see panel (a). Panel (b) shows a close-up around the strong lattice resonance at 900 nm.

7.6 Twin dipole model - unprojected S_i

In the previous sections, the dipole model was introduced and both strengths and shortcomings were discussed. The strengths include the correct physical description of single layer structures and structures with a large interlayer spacing. On the other hand, the model faces problems to correctly determine the transmission properties of close-coupled layers. A particular shortcoming is that the model does not reproduce the polarization rotation occurring for two layers of mutually rotated crosses which should be found due to the structures' handedness. A first extension of the model, namely representing one rod by two perpendicular dipoles, was not successful to overcome this shortcoming, see Appendix A of Ref. [62].

In this section, we start to derive an extended model, called the *twin dipole model*, that successfully describes the physical properties of the two layers of rotated crosses. Before this extended model is presented in its final form in Section 7.7, we deal with an intermediate step in this section. Here, we encounter a particular technical problem that stems from the scattering matrix and the transmission through a slab, cf. Sections 7.3.2 and 7.3.3.

We first present the model using the example of one layer of rods in Section 7.6.1. The occurring problems and open questions are discussed. In Section 7.6.2, we find answers to these questions by investigating two layers of rods.

7.6.1 Single layer of rods

Like the name "twin dipole model" already implies, a rod is, from now on, described by two dipoles. These dipoles are arranged as sketched in Fig. 7.26.

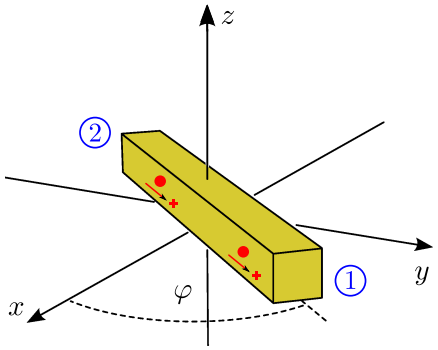

Figure 7.26: The twin dipole model describes one rod as two coupled dipoles, sketched here with red circles.

The two oscillators are located at the positions

$$\mathbf{r}_1 = \begin{pmatrix} \frac{l}{4}\cos\varphi + \rho_1\cos\varphi \\ \frac{l}{4}\sin\varphi + \rho_1\sin\varphi \\ \frac{h}{2} \end{pmatrix}, \qquad \mathbf{r}_2 = \begin{pmatrix} -\frac{l}{4}\cos\varphi + \rho_2\cos\varphi \\ -\frac{l}{4}\sin\varphi + \rho_2\sin\varphi \\ \frac{h}{2} \end{pmatrix}, \tag{7.111}$$

where l is the length of the rod, φ is the rod rotation angle and h denotes the height of the rod like in the previous sections. At the places $\mathbf{r}_i$ we find the dipoles with moment $\mathbf{p}_i$,

$i = 1, 2$. The dipole moments read

$$\mathbf{p}_1 = \begin{pmatrix} \rho_1 \cos\varphi \\ \rho_1 \sin\varphi \\ 0 \end{pmatrix} \frac{-N\,e}{2}, \qquad \mathbf{p}_2 = \begin{pmatrix} \rho_2 \cos\varphi \\ \rho_2 \sin\varphi \\ 0 \end{pmatrix} \frac{-N\,e}{2}, \qquad \hat{\mathbf{R}} = \begin{pmatrix} \cos\varphi \\ \sin\varphi \\ 0 \end{pmatrix}, \qquad R = \frac{l}{2}, \tag{7.112}$$

where N is the number of electrons in the whole rod and $\hat{\mathbf{R}}$ is the unit vector pointing from one dipole to the other. Due to the dipole-dipole potential, which has the form

$$U = \frac{1}{4\pi\varepsilon_0} \frac{\mathbf{p}_1 \cdot \mathbf{p}_2 - 3\,(\mathbf{p}_1 \cdot \hat{\mathbf{R}})\,(\mathbf{p}_2 \cdot \hat{\mathbf{R}})}{R^3}, \tag{7.113}$$

the equations of motion are

$$\ddot{\rho}_1 + \Gamma\,\dot{\rho}_1 + \omega_0^2\,\rho_1 - L\,\rho_2 = -\frac{e}{m}\,E_0\,e^{-i\omega t + ik\frac{h}{2}}\,\cos\varphi, \tag{7.114a}$$

$$\ddot{\rho}_2 + \Gamma\,\dot{\rho}_2 + \omega_0^2\,\rho_2 - L\,\rho_1 = -\frac{e}{m}\,E_0\,e^{-i\omega t + ik\frac{h}{2}}\,\cos\varphi. \tag{7.114b}$$

Here, the abbreviation $L := \frac{2}{N\,m}\,L'$ with $L' := \frac{2q^2}{4\pi\varepsilon_0\,(l/2)^3}$ was used. The charge q of a single oscillator is given by half the electrons of the rod, i.e., $q = -\frac{N}{2}e$. With the usual time-harmonic ansatz, the solution to the equations of motion is given by

$$\begin{pmatrix} \rho_1 \\ \rho_2 \end{pmatrix} = -\frac{e}{m}\,E_0\,e^{-i\omega t + ik\frac{h}{2}}\,\frac{\cos\varphi}{\omega_0^2 - \omega^2 - i\omega\Gamma - L}\begin{pmatrix} 1 \\ 1 \end{pmatrix}. \tag{7.115}$$

The emitted field of an oscillating charge has already been discussed in Section 7.3.1. We reuse the notation from Fig. 7.3. The observer is located on the z-axis at the point $\mathbf{Q}$, i.e.,

$$\mathbf{Q} = \begin{pmatrix} 0 \\ 0 \\ a + \frac{h}{2} \end{pmatrix}, \quad \mathbf{r}_{\text{oscill},1} = \begin{pmatrix} \frac{l}{4}\cos\varphi \\ \frac{l}{4}\sin\varphi \\ \frac{h}{2} \end{pmatrix}, \quad |\mathbf{Q} - \mathbf{r}_{\text{oscill},1}| = \left\| \begin{pmatrix} -\frac{l}{4}\cos\varphi \\ -\frac{l}{4}\sin\varphi \\ a \end{pmatrix} \right\| = \sqrt{\left(\frac{l}{4}\right)^2 + a^2} = r. \tag{7.116}$$

Figure 7.27 sketches the positions of the oscillators and the observer. Furthermore, the important quantity a which defines the position of the observer is depicted.

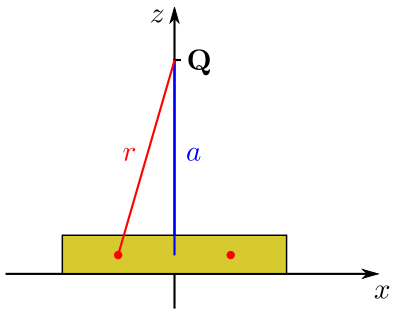

Figure 7.27: Sketch of the distance r between the oscillators and the observer $\mathbf{Q}$ and the distance a defining the observer's position.

The field emitted by the first dipole, $\mathbf{E}_1$, is given by

$$\mathbf{E}_1(\mathbf{Q}, t) = -\frac{1}{4\pi\varepsilon_0}\,\frac{N\,e}{2\,r^3\,c^2} \begin{pmatrix} -a^2\,\ddot{\rho}_1\cos\varphi \\ -a^2\,\ddot{\rho}_1\sin\varphi \\ -\frac{l}{4}\,a\,\ddot{\rho}_1 \end{pmatrix}_{t-\frac{r}{c}}, \tag{7.117}$$

where Eq. (7.1) was used. It is important to note that each dipole carries half the amount of electrons of the whole rod. The field $\mathbf{E}_2$ of the second oscillator differs from the field of the first only through a switched sign of the z-component. Thus, the total emitted field at $\mathbf{Q}$ reads

$$\mathbf{E}_{1+2}(\mathbf{Q},t) = \frac{1}{4\pi\varepsilon_0}\,\frac{N\,e^2\,a^2\,k^2}{r^3}\,\frac{e}{m}\,E_0\,e^{-i\omega t+ik\frac{h}{2}+ikr}\,\frac{\cos\varphi}{\omega_0^2-\omega^2-i\omega\Gamma-L}\begin{pmatrix}\cos\varphi\\ \sin\varphi\\ 0\end{pmatrix}. \tag{7.118}$$

In the previous sections, the general procedure after obtaining the emitted field of the scatterers was changing the coordinate system according to Eq. (7.28) and writing down the scattering matrix equation that links incident and emitted field, see Eq. (7.11). The right hand side of the scattering matrix equation is here given by

$$\ldots \stackrel{!}{=} \frac{1}{-ika}\begin{pmatrix}S_2 & S_3\\ S_4 & S_1\end{pmatrix}\begin{pmatrix}E_0\,e^{-i\omega t+ik\frac{h}{2}+ika}\\ 0\end{pmatrix}. \tag{7.119}$$

Note that the distance a enters, cf. Fig. 7.27. Combining Eqs. (7.118) and (7.119) yields the scattering matrix entries

$$S_2 = \frac{-i\,k^3\,N\,e^2}{4\pi\varepsilon_0\,m}\,\frac{\cos^2\varphi}{\omega_0^2-\omega^2-i\omega\Gamma-L}\,\frac{a^3}{\left(\sqrt{\left(\frac{l}{4}\right)^2+a^2}\right)^3}\,e^{ik\left(\sqrt{\left(\frac{l}{4}\right)^2+a^2}-a\right)}, \tag{7.120a}$$

$$S_4 = \frac{i\,k^3\,N\,e^2}{4\pi\varepsilon_0\,m}\,\frac{\cos\varphi\,\sin\varphi}{\omega_0^2-\omega^2-i\omega\Gamma-L}\,\underbrace{\frac{a^3}{\left(\sqrt{\left(\frac{l}{4}\right)^2+a^2}\right)^3}\,e^{ik\left(\sqrt{\left(\frac{l}{4}\right)^2+a^2}-a\right)}}_{=:f(a)}. \tag{7.120b}$$

At this point it may become clear why we emphasized the definition of a—unlike in previous cases (cf. Section 7.3), the scattering matrix entries still depend on the distance to the observer! The intuitive perception of the function f is, that it does not play a role for large distances. In fact, this is true, see Fig. 7.28. As we see, the real part converges rapidly towards 1. The imaginary part converges to zero, although slower than the real part.

Thus, the formulation in Eqs. (7.120) does not pose a problem for a single layer—we might directly take the limit value of f. However, for two layers that are close together, it is not a priori clear which formulation of the scattering matrix entries is correct—the unprojected formulation with $f(a)$ or the projected formulation with $f(\infty)=1$.

This problem of projecting the scattering matrix entries is the technical problem we mentioned earlier. In a first step, we proceed with the unprojected scattering matrix entries in this section and fit the numerical data to the model in order to obtain values for the free parameters. In a second step, we investigate two layers of rods with the twin dipole model. Therein, we encounter that only the projected scattering matrix entries can be used reasonably.

The transmittance is obtained from the scattering matrix like before (cf. Eq. (7.31)). We fit the model to the electric field rather than to the transmittance to include the information carried in the phase. Thus, we have to enter the distance at which we evaluate the field behind the structure. In our case, this distance was one unit cell length, i.e., 1350 nm. This

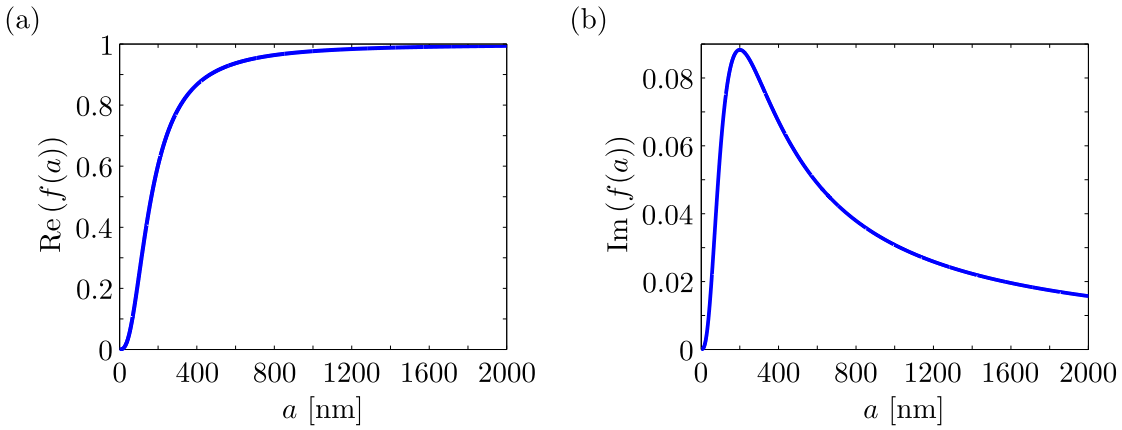

Figure 7.28: Real and imaginary part of the function f defined in Eq. (7.120) at the resonance wavelength of the rod. The real part converges rapidly to one while the imaginary part converges slowly to zero.

means that a is given by 1350 nm + $h/2$. The system's parameters are like in Section 7.3.4: the unit cell is 1350 nm long and 900 nm wide, the rod is 500 nm long and 50 nm wide and high. The rods are assumed to be unrotated, i.e., $\varphi = 0°$. The model's results obtained with the parameters

$$\omega_0 = 1.35 \cdot 10^{15} \text{ Hz}, \qquad \Gamma = 1.4 \cdot 10^{14} \text{ Hz}, \qquad m_{\text{tot}} = \frac{N}{2} \cdot \underbrace{m_e \cdot 3.35}_{=m} \tag{7.121}$$

are depicted in Fig. 7.29. Again, the model reproduces the numerical data well.

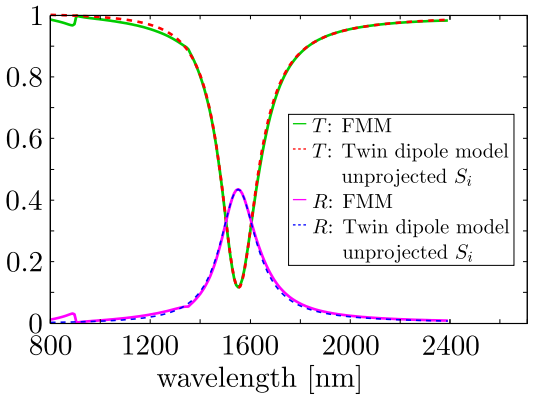

Figure 7.29: Transmittane and reflectance of a single layer of unrotated rods modeled with the twin dipole approach. Here, $a = 1375$ nm was used in the unprojected formulation of the model in Eq. (7.120).

The coupling between the oscillators forming the twin dipole is

$$L = \frac{1}{4\pi\varepsilon_0} \frac{N e^2}{m} \left(\frac{2}{l}\right)^3 = 3.486 \cdot 10^{29} \text{ Hz}^2, \tag{7.122}$$

where the fitted mass from Eq. (7.121) enters.

7.6.2 Double layer of rods

In this section, we model two layers of rods as two twin dipoles above each other, see Fig. 7.30.

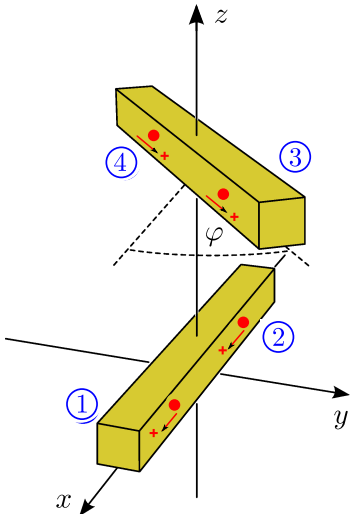

Figure 7.30: Two layers of rods are modeled as two twin dipoles above each other.

The positions of the twin dipoles are

$$\begin{aligned} \mathbf{r}_1 &= \begin{pmatrix} \tilde{L}+\rho_1 \\ 0 \\ \frac{h}{2} \end{pmatrix}, \quad \mathbf{r}_2 = \begin{pmatrix} -\tilde{L}+\rho_2 \\ 0 \\ \frac{h}{2} \end{pmatrix}, \\ \mathbf{r}_3 &= \begin{pmatrix} \tilde{L}\,\cos\varphi+\rho_3\,\cos\varphi \\ \tilde{L}\,\sin\varphi+\rho_3\,\sin\varphi \\ b+\frac{3}{2}\,h \end{pmatrix}, \quad \mathbf{r}_4 = \begin{pmatrix} -\tilde{L}\,\cos\varphi+\rho_4\,\cos\varphi \\ -\tilde{L}\,\sin\varphi+\rho_4\,\sin\varphi \\ b+\frac{3}{2}\,h \end{pmatrix}, \end{aligned} \tag{7.123}$$

where we introduced the abbreviation $\tilde{L} = l/4$. The dipole moments read

$$\frac{2\,\mathbf{p}_1}{q\,N} = \begin{pmatrix} \rho_1 \\ 0 \\ 0 \end{pmatrix}, \quad \frac{2\,\mathbf{p}_2}{q\,N} = \begin{pmatrix} \rho_2 \\ 0 \\ 0 \end{pmatrix}, \quad \frac{2\,\mathbf{p}_3}{q\,N} = \begin{pmatrix} \rho_3\cos\varphi \\ \rho_3\sin\varphi \\ 0 \end{pmatrix}, \quad \frac{2\,\mathbf{p}_4}{q\,N} = \begin{pmatrix} \rho_4\cos\varphi \\ \rho_4\sin\varphi \\ 0 \end{pmatrix}. \tag{7.124}$$

The unit vectors pointing from oscillator j to oscillator i are denoted $\hat{\mathbf{R}}_{ij}$ and are given by

$$\begin{aligned} \hat{\mathbf{R}}_{14} &= \begin{pmatrix} -\tilde{L}\,\cos\varphi-\tilde{L} \\ -\tilde{L}\,\sin\varphi \\ b+h \end{pmatrix}\frac{1}{c_2}, \quad \hat{\mathbf{R}}_{13} = \begin{pmatrix} \tilde{L}\,\cos\varphi-\tilde{L} \\ \tilde{L}\,\sin\varphi \\ b+h \end{pmatrix}\frac{1}{c_1}, \quad \hat{\mathbf{R}}_{12} = \begin{pmatrix} 1 \\ 0 \\ 0 \end{pmatrix}, \\ \hat{\mathbf{R}}_{23} &= \begin{pmatrix} \tilde{L}\,\cos\varphi+\tilde{L} \\ \tilde{L}\,\sin\varphi \\ b+h \end{pmatrix}\frac{1}{c_2}, \quad \hat{\mathbf{R}}_{24} = \begin{pmatrix} -\tilde{L}\,\cos\varphi+\tilde{L} \\ -\tilde{L}\,\sin\varphi \\ b+h \end{pmatrix}\frac{1}{c_1}, \quad \hat{\mathbf{R}}_{34} = \begin{pmatrix} \cos\varphi \\ \sin\varphi \\ 0 \end{pmatrix}. \end{aligned} \tag{7.125}$$

Here, c_1 and c_2 are defined for normalization and read

$$c_1 = \sqrt{(\tilde{L}\cos\varphi-\tilde{L})^2+(\tilde{L}\sin\varphi)^2+(b+h)^2} = \sqrt{2\tilde{L}^2-2\tilde{L}^2\cos\varphi+(b+h)^2}, \tag{7.126a}$$

$$c_2 = \sqrt{(\tilde{L}\cos\varphi+\tilde{L})^2+(\tilde{L}\sin\varphi)^2+(b+h)^2} = \sqrt{2\tilde{L}^2+2\tilde{L}^2\cos\varphi+(b+h)^2}. \tag{7.126b}$$

The distances between the oscillators are related by

$$R_{12} = R_{34} = \frac{l}{2}, \qquad R_{13} = R_{24} = c_1, \qquad R_{23} = R_{14} = c_2. \tag{7.127}$$

Since we model the system by two twin dipoles, we have a total of four interacting dipoles. Bearing in mind the potential in Eq. (7.113), the equations of motion have the form

$$\begin{pmatrix} \Sigma & -L & L_1 & L_2 \\ -L & \Sigma & L_2 & L_1 \\ L_1 & L_2 & \Sigma & -L \\ L_2 & L_1 & -L & \Sigma \end{pmatrix} \begin{pmatrix} \rho_1 \\ \rho_2 \\ \rho_3 \\ \rho_4 \end{pmatrix} = -\frac{e}{m} E_0 \, e^{-i\omega t} \begin{pmatrix} \alpha_1 \\ \alpha_1 \\ \alpha_2 \\ \alpha_2 \end{pmatrix}, \tag{7.128}$$

where we introduced the abbreviation $\Sigma = \omega_0^2 - \omega - i\omega\Gamma$. In the dipole model we discussed how the accelerating fields look like with multiple scattering between the layers. We reuse the formulations from Eqs. (7.46) and (7.48) for α_1 and α_2, namely

$$\alpha_1 = e^{ik\frac{h}{2}} + \frac{\tilde{t}_0 \, \tilde{r}_\varphi \, e^{i\delta} \, e^{ik\frac{3}{2}h}}{1 - \tilde{r}_\varphi \, \tilde{r}_0 \, e^{i\delta}}, \qquad \alpha_2 = \frac{\tilde{t}_0 \, e^{i\frac{\delta}{2}} \, e^{ik\frac{3}{2}h} \, \cos\varphi}{1 - \tilde{r}_\varphi \, \tilde{r}_0 \, e^{i\delta}}. \tag{7.129}$$

However, the transmission and reflection coefficients $\tilde{t}_0$ and $\tilde{r}_\varphi$ look differently than in Section 7.3.5. In the unprojected twin dipole model they are derived from Eqs. (7.120) and read

$$\tilde{r}_\varphi = \frac{\left(e^{i2kh} - 1\right) \, i\pi}{A \, h \, k^3} \, \frac{-i \, k^3 \, N \, e^2}{4\pi\varepsilon_0 \, m} \, \frac{\cos^2\varphi}{\omega_0^2 - \omega^2 - i\omega\Gamma - L} \, \frac{a^3 \, e^{ik\left(\sqrt{\left(\frac{l}{4}\right)^2 + a^2} - a\right)}}{\left(\sqrt{\left(\frac{l}{4}\right)^2 + a^2}\right)^3}, \tag{7.130a}$$

$$\tilde{t}_0 = 1 - \frac{2\,\pi}{k^2 \, A} \, \frac{-i \, k^3 \, N \, e^2}{4\pi\varepsilon_0 \, m \, (\omega_0^2 - \omega^2 - i\omega\Gamma - L)} \, \frac{a^3 \, e^{ik\left(\sqrt{\left(\frac{l}{4}\right)^2 + a^2} - a\right)}}{\left(\sqrt{\left(\frac{l}{4}\right)^2 + a^2}\right)^3}. \tag{7.130b}$$

The coupling terms in Eq. (7.128) have the form

$$L = \frac{N \, e^2}{4\pi\varepsilon_0 \, \left(\frac{l}{2}\right)^3 \, m}, \tag{7.131a}$$

$$L_1 = \tau \, \frac{\frac{N}{2} \, e^2}{4\pi\varepsilon_0} \, \frac{\cos\varphi + 3 \, \tilde{L}^2 \, (\cos\varphi - 1)^2 \, \frac{1}{c_1^2}}{c_1^3 \, m}, \tag{7.131b}$$

$$L_2 = \tau \, \frac{\frac{N}{2} \, e^2}{4\pi\varepsilon_0} \, \frac{\cos\varphi - 3 \, \tilde{L}^2 \, (\cos\varphi + 1)^2 \, \frac{1}{c_2^2}}{c_2^3 \, m}, \tag{7.131c}$$

where L is the coupling of the oscillators within one twin dipole like in Eq. (7.122). Also, we introduced a fit parameter τ. Applying the time-harmonic ansatz to the equations of motions yields the solution

$$\begin{pmatrix} \rho_1 \\ \rho_2 \\ \rho_3 \\ \rho_4 \end{pmatrix} = -\frac{\frac{e}{m} \, E_0 \, e^{-i\omega t}}{L_2^2 + 2 \, L_1 \, L_2 - \Sigma^2 - L^2 + L_1^2 + 2 \, \Sigma \, L} \begin{pmatrix} \alpha_2 \, L_2 - \alpha_1 \, \Sigma + \alpha_1 \, L + \alpha_2 \, L_1 \\ \alpha_2 \, L_2 - \alpha_1 \, \Sigma + \alpha_1 \, L + \alpha_2 \, L_1 \\ \alpha_1 \, L_2 + \alpha_1 \, L_1 - \alpha_2 \, \Sigma + \alpha_2 \, L \\ \alpha_1 \, L_2 + \alpha_1 \, L_1 - \alpha_2 \, \Sigma + \alpha_2 \, L \end{pmatrix}. \tag{7.132}$$

As a first step towards the transmitted field, we investigate the field emitted by the first oscillator, observed at $\mathbf{Q} = (0, 0, u + {}^{h}/_{2})$:

$$\mathbf{Q} = \begin{pmatrix} 0 \\ 0 \\ u + \frac{h}{2} \end{pmatrix}, \quad \mathbf{r}_{\text{oscill},1} = \begin{pmatrix} \tilde{L} \\ 0 \\ \frac{h}{2} \end{pmatrix}, \quad |\mathbf{Q} - \mathbf{r}_{\text{oscill},1}| = \left\| \begin{pmatrix} -\tilde{L} \\ 0 \\ u \end{pmatrix} \right\| = \sqrt{\tilde{L}^2 + u^2} =: r_1. \quad (7.133)$$

$$\mathbf{E}_1(\mathbf{Q}, t) = -\frac{1}{4\pi\varepsilon_0} \frac{\frac{N}{2}\, e}{r_1^3\, c^2} \left[\begin{pmatrix} -\tilde{L} \\ 0 \\ u \end{pmatrix} \times \left[\begin{pmatrix} -\tilde{L} \\ 0 \\ u \end{pmatrix} \times \begin{pmatrix} \ddot{\rho}_1 \\ 0 \\ 0 \end{pmatrix} \right] \right]_{t - \frac{r_1}{c}} = -\frac{1}{4\pi\varepsilon_0} \frac{N\, e}{2\, r_1^3\, c^2} \begin{pmatrix} -u^2\, \ddot{\rho}_1 \\ 0 \\ -\tilde{L}\, u\, \ddot{\rho}_1 \end{pmatrix}_{t - \frac{r_1}{c}} \quad (7.134)$$

The field $\mathbf{E}_2$ emitted by the second oscillator is nearly identical; only the z-component of the field changes its sign. Thus, the emitted field of the first twin dipole reads

$$\mathbf{E}_{1+2} = -\frac{N\, e\, k^2}{4\pi\varepsilon_0} \begin{pmatrix} \rho_1 \\ 0 \\ 0 \end{pmatrix}_{t - \frac{r_1}{c}} \frac{u^2}{r^3}. \quad (7.135)$$

Thus, the scattering matrix for the first layer of rods reads

$$S_{21} = \frac{i\, k^3\, N\, e}{4\pi\varepsilon_0} \frac{1}{E_0\, e^{-i\omega t + ik\frac{h}{2}}}\, \rho_1(t)\, \frac{u^3}{\left(\sqrt{\left(\frac{l}{4}\right)^2 + u^2}\right)^3}\, e^{ik\left(\sqrt{\left(\frac{l}{4}\right)^2 + u^2} - u\right)}, \quad (7.136a)$$

$$S_{41} = 0. \quad (7.136b)$$

Again, we find the same unprojected form of the scattering matrix. To find the scattering matrix of the second layer, we observe the field emitted by the third oscillator at the position $\mathbf{Q}' = (0, 0, d + b + {}^{3}/_{2}\, h)$:

$$\mathbf{r}_{\text{oscill},3} = \begin{pmatrix} \tilde{L}\, \cos\varphi \\ \tilde{L}\, \sin\varphi \\ b + \frac{3}{2}\, h \end{pmatrix}, \quad |\mathbf{Q}' - \mathbf{r}_{\text{oscill},3}| = \left\| \begin{pmatrix} -\tilde{L}\, \cos\varphi \\ -\tilde{L}\, \sin\varphi \\ d \end{pmatrix} \right\| = \sqrt{\tilde{L}^2 + d^2} =: r_2, \quad (7.137)$$

$$\begin{aligned} \mathbf{E}_3(\mathbf{Q}', t) &= \frac{-\frac{N}{2}\, e}{4\pi\varepsilon_0\, r_2^3\, c^2} \left[\begin{pmatrix} -\tilde{L}\cos\varphi \\ -\tilde{L}\sin\varphi \\ d \end{pmatrix} \times \left[\begin{pmatrix} -\tilde{L}\cos\varphi \\ -\tilde{L}\sin\varphi \\ d \end{pmatrix} \times \begin{pmatrix} \ddot{\rho}_3 \cos\varphi \\ \ddot{\rho}_3 \sin\varphi \\ 0 \end{pmatrix} \right] \right]_{t - \frac{r_2}{c}} \\ &= -\frac{1}{4\pi\varepsilon_0} \frac{N\, e}{2\, r_2^3\, c^2} \begin{pmatrix} -d^2\, \ddot{\rho}_3\, \cos\varphi \\ -d^2\, \ddot{\rho}_3\, \sin\varphi \\ -\tilde{L}\, d\, \ddot{\rho}_3 \end{pmatrix}_{t - \frac{r_2}{c}}. \end{aligned} \quad (7.138)$$

Analogously, the field for the fourth oscillator is obtained, which again just flips sign in the z-component. Therefore, the field radiated by the second twin dipole reads

$$\mathbf{E}_{3+4} = -\frac{1}{4\pi\varepsilon_0}\, N\, e\, k^2 \begin{pmatrix} \rho_3\, \cos\varphi \\ \rho_3\, \sin\varphi \\ 0 \end{pmatrix} \frac{d^2}{r_2^3} \quad (7.139)$$

The resulting scattering matrix entries are

$$S_{\mathbf{22}} = \frac{i\,k^3\,N\,e}{4\pi\varepsilon_0}\,\frac{\rho_3\,\cos\varphi}{\left(1-\frac{S_{2,\mathbf{1}}\,2\pi}{k^2\,A}\right)\,E_0\,e^{-i\omega t+\frac{3}{2}\,h+b}}\,\frac{d^3\,e^{ik\left(\sqrt{\left(\frac{l}{4}\right)^2+d^2}-d\right)}}{\left(\sqrt{\left(\frac{l}{4}\right)^2+d^2}\right)^3}, \tag{7.140a}$$

$$S_{\mathbf{42}} = \frac{-i\,k^3\,N\,e}{4\pi\varepsilon_0}\,\frac{\rho_3\,\sin\varphi}{\left(1-\frac{S_{2,\mathbf{1}}\,2\pi}{k^2\,A}\right)\,E_0\,e^{-i\omega t+\frac{3}{2}\,h+b}}\,\frac{d^3\,e^{ik\left(\sqrt{\left(\frac{l}{4}\right)^2+d^2}-d\right)}}{\left(\sqrt{\left(\frac{l}{4}\right)^2+d^2}\right)^3}. \tag{7.140b}$$

Like in the dipole model, the transmitted field is given by

$$\mathbf{E}_{t\mathbf{2}} = E_0\,e^{-i\omega t+ike}\,\left(1-\frac{2\pi\,S_{\mathbf{21}}}{k^2\,A}\right)\,\left[\left(1-\frac{2\pi\,S_{\mathbf{22}}}{k^2\,A}\right)\,\hat{\mathbf{e}}_x+\frac{2\pi\,S_{\mathbf{42}}}{k^2\,A}\,\hat{\mathbf{e}}_y\right]. \tag{7.141}$$

From Section 7.6.1 we know the values for ω_0, Γ and m. The other parameters read $a = b+h$, $u = b+h$ and $d = 1375$ nm. The latter is chosen like that since we fit the coupling to the numerical field obtained one unit cell behind the upper rod.

In Fig. 7.31(a), the transmittance for two layers of unrotated rods with a spacing of $b = 50$ nm is shown. The fit parameter is $\tau = 0.045$.

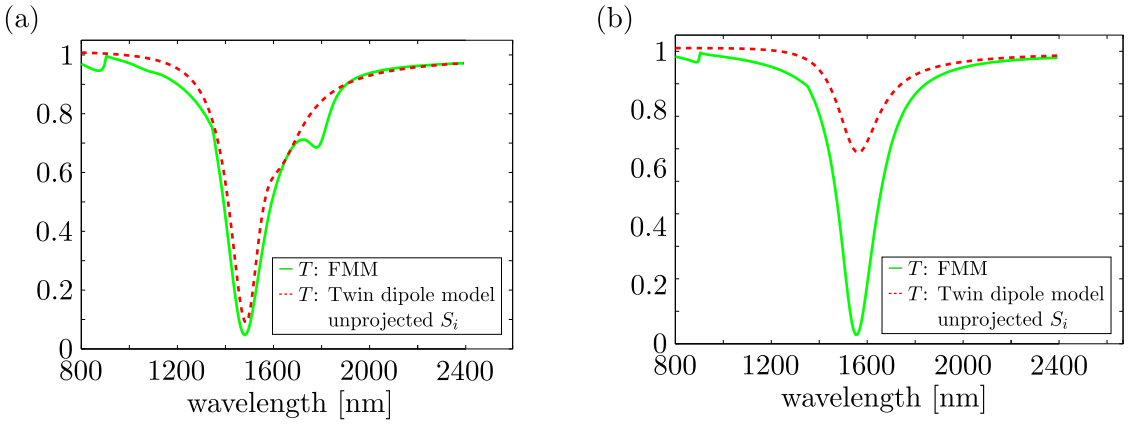

Figure 7.31: Transmittance obtained with the FMM and the unprojected twin dipole model for two layers of periodically arranged rods. Panels (a) and (b) display the results for unrotated rods and for $\varphi = -75°$, respectively. The unprojected formulation of the twin dipole model yields unphysical transmittance values above 1 and, furthermore, does not reduce to the transmittance of the single layer of rods for $\varphi = -90°$. This shows that a projected formulation needs to be used.

The model's description of the numerical data is not particularly better than previous results of the dipole model. In fact, it exhibits transmittance values above one for small wavelengths which is unphysical. In Fig. 7.31(b), the transmittance for $b = 50$ nm and a rotation of $\varphi = -75°$ is shown. As we see, there is a huge difference between the numerical data and the prediction of the unprojected twin dipole model. The reason can easily be understood on a formal level: the more the upper rod is rotated, the less it is excited by the external, x-polarized field. Thus, once the second rod is rotated by $\varphi = 90°$, the transmittance predicted

by the (twin) dipole model for two layers of rods should be identical to the model's predictions for one layer of rods. However, this is not the case in the unprojected formulation of the twin dipole model: Eq. (7.136a) with $\varphi = 90°$ does not equal Eq. (7.120a). The reason is that a in Eq. (7.120a) was set to 1375 nm (distance between oscillator and point where numerical data is obtained behind the layer) but u in Eq. (7.136a) was set to $b + h$ since that is the distance to the upper twin dipole. Yet, a would have to be equal to u for Eq. (7.136a) being identical to Eq. (7.120a). Of course, we could just set a to $b + h$ or u to 1375 nm. However, both versions lack geometrical sense.

Hence, the only sensible solution to the problem is to use the *projected* twin dipole model. This means that we use the limit values for $a \to \infty$ and $u \to \infty$, i.e., $f(\infty) = 1$. This means that $f(a)$ is set to 1 in Eqs. (7.120) and (7.130) as well as $f(u)$ in Eq. (7.136a). Consequently, we also have to set $f(d)$ to 1 in Eq. (7.140).

In the subsequent section, we discuss the effect of the projection and show the results for the projected twin dipole model, from now on referred to only as the *twin dipole model*.

7.7 Twin dipole model - projected S_i

In the previous section, we discussed the twin dipole approach and how it leads to the technical problem of the scattering matrix' distance dependence. We argued that an unprojected formulation does not lead to consistent results and, thus, we present the results of the projected twin dipole model in this section. We start by discussing a single layer of rods. This is followed by the results of the projected twin dipole model for two layers of rods. After applying the model to one layer of crosses, we finally arrive at the structure that was the reason for extending the dipole model—two layers of mutually rotated crosses. Here, the twin dipole model proves its ability to describe the system's physics correctly.

7.7.1 Single layer of rods

In Section 7.6.1, we presented the unprojected formulation of the twin dipole model. At the end of Section 7.6.2 we explained why this formulation cannot work and that we have to set $f(a)$, $f(u)$ and $f(d)$ to 1 in Eqs. (7.120) and (7.130), (7.136a) and (7.140), respectively. With this projected formulation, we find the new fit parameters

$$\omega_0 = 1.35 \cdot 10^{15}\ \text{Hz}, \qquad \Gamma = 1.4 \cdot 10^{14}\ \text{Hz}, \qquad m_{\text{tot}} = \frac{N}{2} \cdot m = \frac{N}{2} \cdot m_e \cdot 3.35, \tag{7.142}$$

for the 1350 nm × 900 nm unit cell with the 500 nm × 50 nm × 50 nm rods. The transmittance and reflectance are depicted in Fig. 7.32(a).

For the 400 nm × 400 nm unit cell with the 250 nm × 50 nm × 25 nm rods, the parameters read

$$\omega_0 = 2.1 \cdot 10^{15}\ \text{Hz}, \qquad \Gamma = 3.68 \cdot 10^{14}\ \text{Hz}, \qquad m_{\text{tot}} = \frac{N}{2} \cdot m = \frac{N}{2} \cdot m_e \cdot 2.1\ \text{kg}. \tag{7.143}$$

The results are shown in Fig. 7.32(b). For both unit cells, transmittance and reflectance are reproduced well.

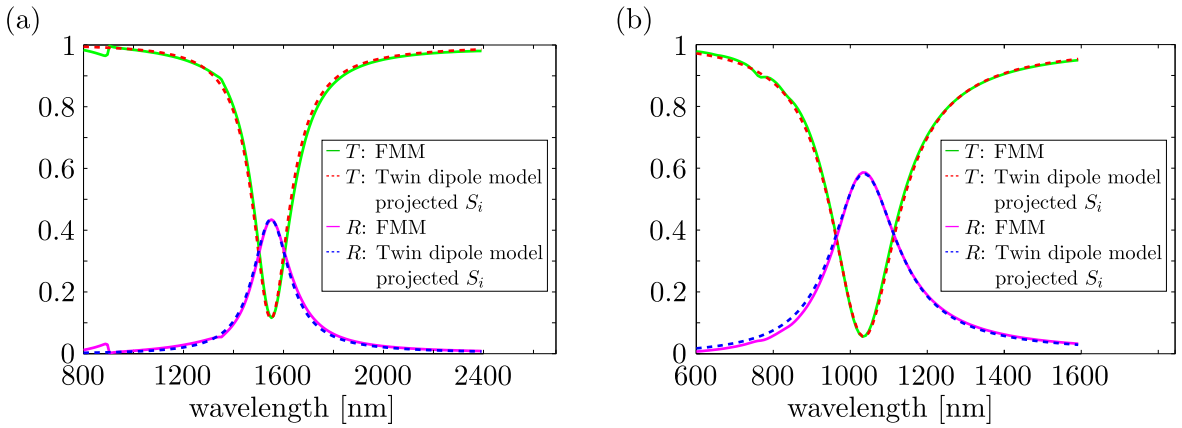

Figure 7.32: Transmittance and reflectance of FMM and projected twin dipole model for a single layer of unrotated rods. Panel (a) refers to the 1350 nm × 900 nm unit cell and panel (b) to the 400 nm × 400 nm unit cell.

7.7.2 Double layer of rods

Since we already derived the expressions for the twin dipole model for two layers of rods in the unprojected form in Section 7.6.2, we can directly present the results for the projected twin dipole model. Figure 7.33 shows the transmittance for two layers of unrotated rods for different values of the layer spacing b.

Qualitatively, the twin dipole model reproduces the numerical data. The physical behavior, namely the decrease in the transmittance at the second resonance, is described well by the model. The fit values for the coupling are:

b [nm]	τ
25	0.025
50	0.05
75	0.07
100	0.11
125	0.15
150	0.18

The values of τ suggest an increase in the coupling with increasing b. However, this is not true since the physical coupling is described by the parameters L_1 and L_2 in Eq. (7.131). They show the (physically) necessary decay with increasing layer spacing.

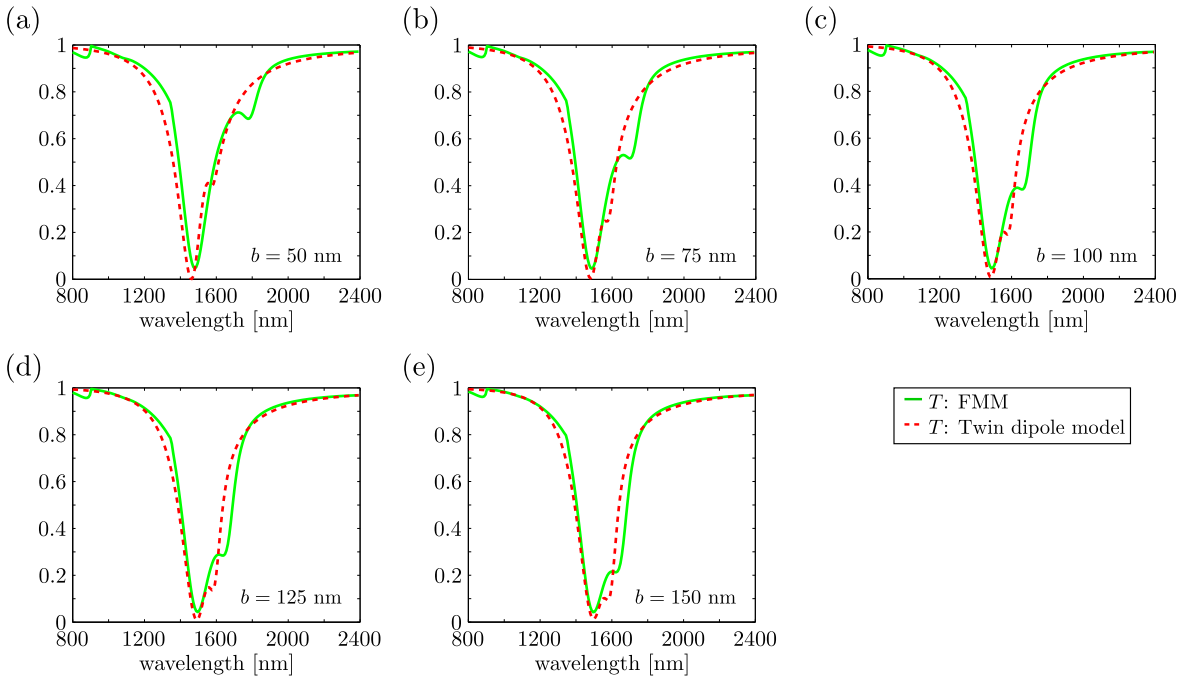

Figure 7.33: Transmittance of the FMM and the twin dipole model for two layers of unrotated rods with varying layer distance b. The data shown refers to the 1350 nm × 900 nm unit cell.

Having fixed the values for the interlayer coupling, we can rotate the upper twin dipole and investigate the transmittance and polarization state of the transmitted light. They are depicted in Fig. 7.34.

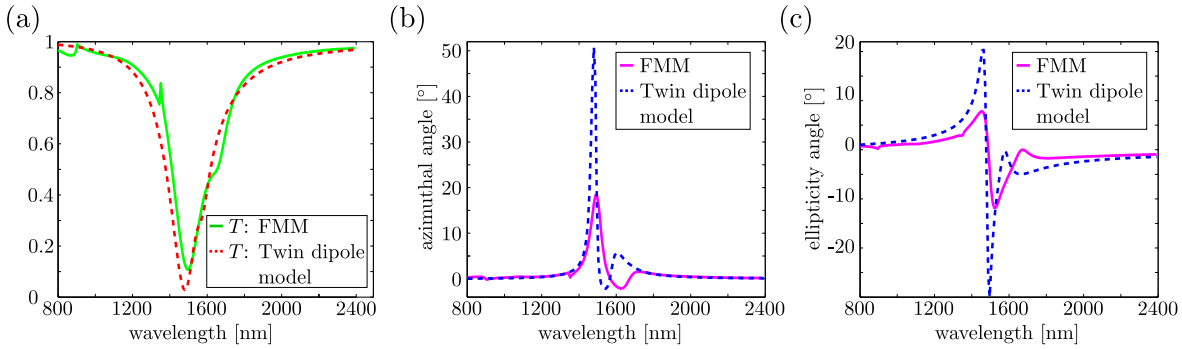

Figure 7.34: Transmittance and polarization state for the light transmitted through two layers of rotated rods with $b = 50$ nm, $\varphi = -20°$ and the 1350 nm × 900 nm unit cell. The twin model's predictions are better than the ones of the dipole model, cf. Fig. 7.34.

Although the twin dipole still overestimates the strength of the polarization rotation, it shows better results than the dipole model, compare Figs. 7.34 and 7.13.

Finally, we fit the coupling τ to the numerical data for the 400 nm × 400 nm unit cell that we need for the cross structures. The results with the fit parameter $\tau = 0.13$ for $b = 50$ nm are depicted in Fig. 7.35.

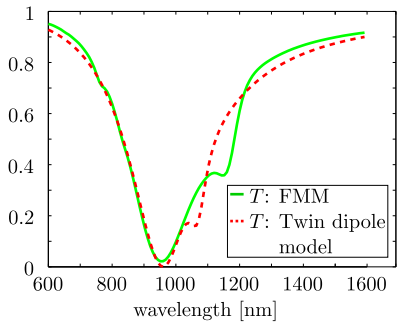

Figure 7.35: Transmittance of two layers of unrotated rods with the 400 nm × 400 nm unit cell and $b = 50$ nm. The twin dipole model's coupling is $\tau = 0.13$ for this system.

7.7.3 Single layer of crosses

So far, we modeled a layer of rods and two layers of rods as one twin dipole and two twin dipoles, respectively. The next system we investigate is one layer of crosses. They are modeled as two perpendicular twin dipoles as depicted in Fig. 7.36.

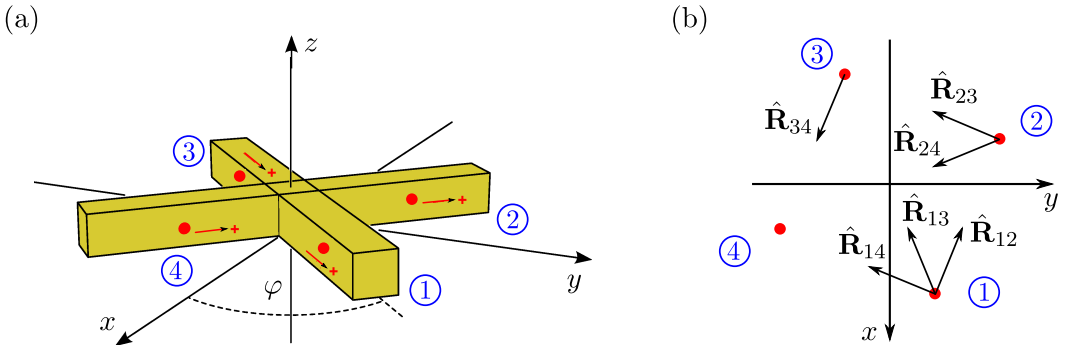

Figure 7.36: One layer of crosses is modeled as two superimposed twin dipoles (panel (a)). The unit vectors pointing from oscillator j to oscillator i are denoted $\hat{\mathbf{R}}_{ij}$ (panel (b)).

The oscillators are located at

$$\mathbf{r}_1 = \begin{pmatrix} \tilde{L}\,\cos\varphi + \rho_1\,\cos\varphi \\ \tilde{L}\,\sin\varphi + \rho_1\,\sin\varphi \\ h/2 \end{pmatrix}, \qquad \mathbf{r}_2 = \begin{pmatrix} -\tilde{L}\,\sin\varphi - \rho_2\,\sin\varphi \\ \tilde{L}\,\cos\varphi + \rho_2\,\cos\varphi \\ h/2 \end{pmatrix},$$
$$\mathbf{r}_3 = \begin{pmatrix} -\tilde{L}\,\cos\varphi + \rho_3\,\cos\varphi \\ -\tilde{L}\,\sin\varphi + \rho_3\,\sin\varphi \\ h/2 \end{pmatrix}, \qquad \mathbf{r}_4 = \begin{pmatrix} \tilde{L}\,\sin\varphi - \rho_4\,\sin\varphi \\ -\tilde{L}\,\cos\varphi + \rho_4\,\cos\varphi \\ h/2 \end{pmatrix}, \tag{7.144}$$

with the abbreviation $\tilde{L} = l/4$. Their moments are

$$\frac{2\,\mathbf{p}_i}{q\,N} = \begin{pmatrix} \rho_i\,\cos\varphi \\ \rho_i\,\sin\varphi \\ 0 \end{pmatrix}, \; i = 1, 3, \qquad \frac{2\,\mathbf{p}_j}{q\,N} = \begin{pmatrix} -\rho_j\,\sin\varphi \\ \rho_j\,\cos\varphi \\ 0 \end{pmatrix}, \; j = 2, 4. \tag{7.145}$$

The unit vectors pointing from one oscillator to the others are given by

$$\begin{aligned}
\hat{\mathbf{R}}_{12} &= \begin{pmatrix} -\tilde{L}\,\sin\varphi - \tilde{L}\,\cos\varphi \\ \tilde{L}\,\cos\varphi - \tilde{L}\,\sin\varphi \\ 0 \end{pmatrix} \frac{1}{c_1}, \qquad \hat{\mathbf{R}}_{13} = \begin{pmatrix} -\tilde{L}\,\cos\varphi - \tilde{L}\,\cos\varphi \\ -\tilde{L}\,\sin\varphi - \tilde{L}\,\sin\varphi \\ 0 \end{pmatrix} \frac{1}{c_2}, \\
\hat{\mathbf{R}}_{14} &= \begin{pmatrix} \tilde{L}\,\sin\varphi - \tilde{L}\,\cos\varphi \\ -\tilde{L}\,\cos\varphi - \tilde{L}\,\sin\varphi \\ 0 \end{pmatrix} \frac{1}{c_1}, \qquad \hat{\mathbf{R}}_{23} = \begin{pmatrix} -\tilde{L}\,\cos\varphi + \tilde{L}\,\sin\varphi \\ -\tilde{L}\,\sin\varphi - \tilde{L}\,\cos\varphi \\ 0 \end{pmatrix} \frac{1}{c_1}, \\
\hat{\mathbf{R}}_{24} &= \begin{pmatrix} \tilde{L}\,\sin\varphi + \tilde{L}\,\sin\varphi \\ -\tilde{L}\,\cos\varphi - \tilde{L}\,\cos\varphi \\ 0 \end{pmatrix} \frac{1}{c_2}, \qquad \hat{\mathbf{R}}_{34} = \begin{pmatrix} -\tilde{L}\,\sin\varphi - \tilde{L}\,\cos\varphi \\ \tilde{L}\,\cos\varphi - \tilde{L}\,\sin\varphi \\ 0 \end{pmatrix} \frac{1}{c_1}, \qquad (7.146)
\end{aligned}$$

which is also sketched in Fig. 7.36(b). The terms c_1 and c_2 are defined for normalization. The distances between the oscillators is given by

$$R_{12} \;=\; R_{14} \;=\; R_{23} \;=\; R_{34} \;=\; c_1, \qquad\qquad R_{13} \;=\; R_{24} \;=\; c_2. \qquad (7.147)$$

With the potential from Eq. (7.113) we can derive the equations of motion. They read

$$\begin{pmatrix} \Sigma & L_1 & L_2 & -L_1 \\ L_1 & \Sigma & -L_1 & L_2 \\ L_2 & -L_1 & \Sigma & L_1 \\ -L_1 & L_2 & L_1 & \Sigma \end{pmatrix} \cdot \begin{pmatrix} \rho_1 \\ \rho_2 \\ \rho_3 \\ \rho_4 \end{pmatrix} \;=\; \frac{q}{m}\, E_0\, e^{-i\omega t + ik\frac{h}{2}} \begin{pmatrix} \cos\varphi \\ -\sin\varphi \\ \cos\varphi \\ -\sin\varphi \end{pmatrix}. \qquad (7.148)$$

Here, we introduced the coupling terms L_1 and L_2 which are given by

$$\begin{aligned}
L_1 &= \frac{3\,\left(\frac{q}{c_1}\right)^2\,\tilde{L}^2}{4\pi\varepsilon_0\, c_1^3\, m\, \frac{N}{2}}, \\
L_2 &= \frac{q^2 - 3\,\left(\frac{q}{c_2}\right)^2\,\left(\frac{l}{2}\right)^2}{4\pi\varepsilon_0\, c_2^3\, m\, \frac{N}{2}} \;\overset{c_2 = l/2}{=}\; -\frac{2\,q^2}{4\pi\varepsilon_0\, c_2^3\, m\, \frac{N}{2}} \;=\; -L. \qquad (7.149)
\end{aligned}$$

The charge q of a single oscillator is given by half the electrons of the rod, i.e., $q = -\frac{N}{2}e$. The coupling L is known from the single twin dipole, cf. Eq. (7.114). The solution to the equations of motion is

$$\begin{pmatrix} \rho_1 \\ \rho_2 \\ \rho_3 \\ \rho_4 \end{pmatrix} = -\frac{e}{m}\, E_0\, e^{-i\omega t + ik\frac{h}{2}}\, \frac{1}{\Sigma - L} \begin{pmatrix} \cos\varphi \\ -\sin\varphi \\ \cos\varphi \\ -\sin\varphi \end{pmatrix}. \qquad (7.150)$$

Having obtained the motion of the four oscillators, we can deduce their radiated field. The field emitted by the first oscillator at the position of an observer at $\mathbf{Q} = (0, 0, a + h/2)$ on the z axis is given by

$$\mathbf{r}_{\text{oscill},1} = \begin{pmatrix} \tilde{L}\,\cos\varphi \\ \tilde{L}\,\sin\varphi \\ \frac{h}{2} \end{pmatrix}, \qquad |\mathbf{Q} - \mathbf{r}_{\text{oscill},1}| = \left\| \begin{pmatrix} -\tilde{L}\,\cos\varphi \\ -\tilde{L}\,\sin\varphi \\ a \end{pmatrix} \right\| = \sqrt{\tilde{L}^2 + a^2} =: r, \qquad (7.151)$$

$$\begin{aligned}\mathbf{E}_1(\mathbf{Q},t) &= \frac{-\frac{N}{2}\,e}{4\pi\varepsilon_0\,r^3\,c^2}\left[\begin{pmatrix}-\tilde{L}\cos\varphi\\-\tilde{L}\sin\varphi\\a\end{pmatrix}\times\left[\begin{pmatrix}-\tilde{L}\cos\varphi\\-\tilde{L}\sin\varphi\\a\end{pmatrix}\times\begin{pmatrix}\ddot{\rho}_1\cos\varphi\\\ddot{\rho}_1\sin\varphi\\0\end{pmatrix}\right]\right]_{t-\frac{r}{c}}\\ &= -\frac{1}{4\pi\varepsilon_0}\,\frac{N\,e}{2\,r^3\,c^2}\begin{pmatrix}-a^2\,\ddot{\rho}_1\,\cos\varphi\\-a^2\,\ddot{\rho}_1\,\sin\varphi\\-\tilde{L}\,a\,\ddot{\rho}_1\end{pmatrix}_{t-\frac{r}{c}}\end{aligned} \tag{7.152}$$

The fields caused by the other oscillators are obtained in a similar fashion. At the observer's position $\mathbf{Q}$ the sum of all fields ($i = 1, ..., 4$) reads

$$\begin{aligned}\mathbf{E}_{\sum_i}(\mathbf{Q},t) &= \frac{-N\,e}{8\pi\varepsilon_0\,r^3\,c^2}\begin{pmatrix}-a^2\ddot{\rho}_1\cos\varphi+a^2\ddot{\rho}_2\sin\varphi-a^2\ddot{\rho}_3\cos\varphi+a^2\ddot{\rho}_4\sin\varphi\\-a^2\ddot{\rho}_1\sin\varphi-a^2\ddot{\rho}_2\cos\varphi-a^2\ddot{\rho}_3\sin\varphi-a^2\ddot{\rho}_4\cos\varphi\\-\tilde{L}\,a\,\ddot{\rho}_1-\tilde{L}\,a\,\ddot{\rho}_2+\tilde{L}\,a\,\ddot{\rho}_3+\tilde{L}\,a\,\ddot{\rho}_4\end{pmatrix}_{t-\frac{r}{c}}\\ &= -\frac{1}{4\pi\varepsilon_0}\,\frac{N\,e^2\,k^2}{2\,r^3\,m}\,\frac{E_0\,e^{-i\omega t+ikr+ik\frac{h}{2}}}{\omega_0^2-\omega^2-i\omega\Gamma-L}\,(-2\,a^2).\end{aligned} \tag{7.153}$$

With Eq. (7.119) and $r = \sqrt{\tilde{L}^2 + a^2}$ we obtain the scattering matrix entries

$$S_2 = \frac{-i\,k^3\,N\,e^2}{4\pi\varepsilon_0\,m}\,\frac{1}{\omega_0^2-\omega^2-i\omega\Gamma-L}\,\underbrace{\frac{a^3}{r^3}\,e^{ik(r-a)}}_{=\,f(a)}, \tag{7.154a}$$

$$S_4 = 0. \tag{7.154b}$$

A first important property we can observe from Eq. (7.154) is that the polarization is not rotated, i.e., $S_4 = 0$. Since the structure is C_4 symmetric, all linear polarizations should be treated equally. This is the case. The second important property is that the scattering matrix entries in Eq. (7.154) are identical to the scattering matrix entries of one layer of unrotated rods derived with the twin dipole model, cf. Eq. (7.120). In the projected twin dipole model, we set $f(a) = 1$ and, thus, obtain the same results as for one layer of unrotated rods, see Fig. 7.32(b).

7.7.4 Double layer of crosses

In this final section of the twin dipole model, we examine the structure that has proven to be very challenging—two layers of mutually rotated rods. The dipole model was not able to reproduce the numerical data obtained with the FMM, see Section 7.3.6. Here, we show that the projected twin dipole model is able to describe the physical properties of the transmitted light reasonably well.

The system depicted in Fig. 7.37 is modeled as four twin dipoles. All eight oscillators interact with each other.

Since writing down the positions, couplings and unit vectors from one oscillator to the others is rather lengthy, I omitted them here and added them to the appendix, see App. D. We

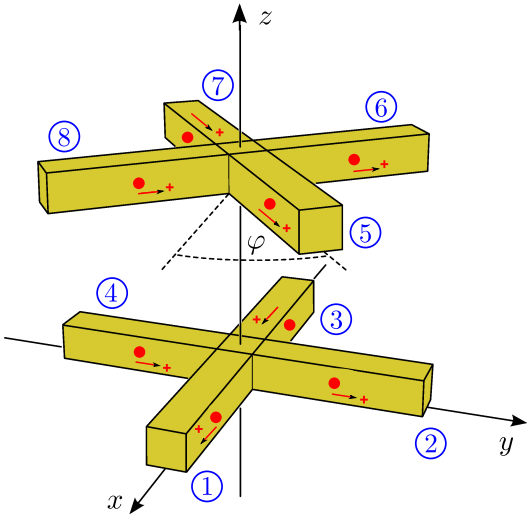

Figure 7.37: The structure under investigation in this section: two layers of periodically arranged, mutually rotated crosses. The crosses are modeled by two superimposed twin dipoles.

start right away with the equations of motion that read

$$\begin{pmatrix} \Sigma & L_1 & L_2 & -L_1 & L_3 & L_4 & L_5 & L_6 \\ L_1 & \Sigma & -L_1 & L_2 & -L_6 & L_3 & -L_4 & L_5 \\ L_2 & -L_1 & \Sigma & L_1 & L_5 & L_6 & L_3 & L_4 \\ -L_1 & L_2 & L_1 & \Sigma & -L_4 & L_5 & -L_6 & L_3 \\ L_3 & -L_6 & L_5 & -L_4 & \Sigma & L_1 & L_2 & -L_1 \\ L_4 & L_3 & L_6 & L_5 & L_1 & \Sigma & -L_1 & L_2 \\ L_5 & -L_4 & L_3 & -L_6 & L_2 & -L_1 & \Sigma & L_1 \\ L_6 & L_5 & L_4 & L_3 & -L_1 & L_2 & L_1 & \Sigma \end{pmatrix} \cdot \begin{pmatrix} \rho_1 \\ \rho_2 \\ \rho_3 \\ \rho_4 \\ \rho_5 \\ \rho_6 \\ \rho_7 \\ \rho_8 \end{pmatrix} = H \begin{pmatrix} E_1 \\ 0 \\ E_1 \\ 0 \\ E_2 \cos\varphi \\ -E_2 \sin\varphi \\ E_2 \cos\varphi \\ -E_2 \sin\varphi \end{pmatrix} \tag{7.155}$$

Here, we introduced the abbreviation $H = -\frac{e}{m} E_0 e^{-i\omega t}$ that we only use here and in Eq. (7.156). The coupling terms L_1 to L_6 can be looked up in App. D. Like before, we use the abbreviation $\Sigma = \omega_0^2 - \omega^2 - i\omega\Gamma$. The fields accelerating the oscillators are essentially the same as for the dipole model. The only difference is that the coupling term L enters which links the two oscillators forming a twin dipole. For further details, see App. D.

The solution to Eq. (7.155) is

$$\begin{pmatrix} \rho_1 \\ \rho_2 \\ \rho_3 \\ \rho_4 \\ \rho_5 \\ \rho_6 \\ \rho_7 \\ \rho_8 \end{pmatrix} = \frac{H}{g} \begin{pmatrix} E_1\Sigma - E_2\cos\varphi L_5 + E_1 L_2 + E_2 \sin\varphi L_6 + E_2 \sin\varphi L_4 - E_2 \cos\varphi L_3 \\ E_2\ (\cos\varphi\, L_6 + \sin\varphi\, L_3 + \cos\varphi\, L_4 + \sin\varphi\, L_5) \\ E_1\Sigma - E_2\cos\varphi L_5 + E_1 L_2 + E_2 \sin\varphi L_6 + E_2 \sin\varphi L_4 - E_2 \cos\varphi L_3 \\ E_2\ (\cos\varphi\, L_6 + \sin\varphi\, L_3 + \cos\varphi\, L_4 + \sin\varphi\, L_5) \\ E_2\ \cos\varphi\, \Sigma - E_1\, L_5 + E_2\ \cos\varphi\, L_2 - E_1\, L_3 \\ -(E_2\ \sin\varphi\, \Sigma + E_1\, L_4 + E_2\ \sin\varphi\, L_2 + E_1\, L_6) \\ E_2\ \cos\varphi\, \Sigma - E_1\, L_5 + E_2\ \cos\varphi\, L_2 - E_1\, L_3 \\ -(E_2\ \sin\varphi\, \Sigma + E_1\, L_4 + E_2\ \sin\varphi\, L_2 + E_1\, L_6) \end{pmatrix}, \tag{7.156}$$

with $g = \Sigma^2 + 2\,\Sigma\,L_2 - L_6^2 - L_4^2 - L_3^2 - L_5^2 + L_2^2 - 2\,L_6\,L_4 - 2\,L_3\,L_5$. At this point, it is worth interpreting the physical results contained in Eq. (7.156): the parameters ρ_2 and ρ_4 are non-zero. They describe the motion of the oscillators 2 and 4. Recall that the incident

electric field is x-polarized. Therefore, the external field itself does not excite the twin dipole formed by oscillators 2 and 4 since they are oriented perpendicular to the external field. That they still move is a consequence of the coupling between the layers. To show this, one can set the coupling terms between the layers (namely L_3, L_4, L_5 and L_6) to zero. Then, no field in y-direction is found.

The step after solving the equations of motion is to derive the field emitted by the oscillators in the first layer. It is given by

$$\mathbf{E}_{1+2+3+4}(\mathbf{Q},t) = -\frac{N\,e\,k^2}{4\pi\varepsilon_0} \begin{pmatrix}\rho_1\\ \rho_2\\ 0\end{pmatrix}_{t-\frac{r_1}{c}} \frac{u^2}{r_1^3}, \tag{7.157}$$

with the observer's position $\mathbf{Q} = (u, 0, {}^{h}\!/_{2})$ and the abbreviation $r_1 = \sqrt{\tilde{L}^2 + u^2}$. See App. D for further details. Note that $\rho_1 = \rho_3$ and $\rho_2 = \rho_4$ in Eq. (7.156). After the usual coordinate system change we can write the scattering matrix equation for the first layer:

$$-\frac{N\,e\,k^2}{4\pi\varepsilon_0}\,\frac{u^2}{r_1^3} \begin{pmatrix}\rho_1\\ -\rho_2\end{pmatrix}_{t-\frac{r_1}{c}} = \frac{1}{-i\,k\,u} \begin{pmatrix}S_{2,\mathbf{1}} & S_{3,\mathbf{1}}\\ S_{4,\mathbf{1}} & S_{1,\mathbf{1}}\end{pmatrix} \begin{pmatrix}E_0\,e^{-i\omega t + ik\left(\frac{h}{2}+u\right)}\\ 0\end{pmatrix}. \tag{7.158}$$

The resulting scattering matrix entries are

$$\begin{aligned} S_{2,\mathbf{1}} \;=\; & -\frac{i\,k^3\,N\,e^2}{4\pi\varepsilon_0\,m\,g}\,\frac{u^3}{\left(\sqrt{\tilde{L}^2+u^2}\right)^3}\,\frac{1}{e^{ik\frac{h}{2}}}\,e^{ik\left(\sqrt{\tilde{L}^2+u^2}-u\right)}\cdot \\ & \left(E_1\,\Sigma - E_2\,\cos\varphi\,L_5 + E_1\,L_2 + E_2\,\sin\varphi\,L_6 + E_2\,\sin\varphi\,L_4 - E_2\,\cos\varphi\,L_3\right), \end{aligned} \tag{7.159a}$$

$$\begin{aligned} S_{4,\mathbf{1}} \;=\; & \frac{i\,k^3\,N\,e^2}{4\pi\varepsilon_0\,m\,g}\,E_2\,\frac{u^3}{\left(\sqrt{\tilde{L}^2+u^2}\right)^3\,e^{ik\frac{h}{2}}}\,e^{ik\left(\sqrt{\tilde{L}^2+u^2}-u\right)}\cdot \\ & \left(\cos\varphi\,L_6 + \sin\varphi\,L_3 + \cos\varphi\,L_4 + \sin\varphi\,L_5\right). \end{aligned} \tag{7.159b}$$

Note that this is still the unprojected formulation. As we argued above, only the projected scattering matrix entries enter the final equations. Therefore, we project the terms in Eqs. (7.159) such that the proper scattering matrix entries of the twin dipole model for the first layer read

$$S_{2,\mathbf{1}} \;=\; -\frac{i\,k^3\,N\,e^2}{4\pi\varepsilon_0\,m\,g}\left(E_1\,\Sigma - E_2\,\cos\varphi\,L_5 + E_1\,L_2 + E_2\,\sin\varphi\,L_6 + E_2\,\sin\varphi\,L_4 - E_2\,\cos\varphi\,L_3\right) \tag{7.160a}$$

$$S_{4,\mathbf{1}} = \frac{i\,k^3\,N\,e^2}{4\pi\varepsilon_0\,m\,g}E_2\left(\cos\varphi\,L_6 + \sin\varphi\,L_3 + \cos\varphi\,L_4 + \sin\varphi\,L_5\right). \tag{7.160b}$$

The radiated fields of the second layer are obtained like before, see App. D. The superimposed fields of all four oscillators in the second layer at $\mathbf{Q}' = (d + b + {}^{3}\!/_{2}\;h)$ are

$$\mathbf{E}_{5+6+7+8}(\mathbf{Q}',t) = \frac{1}{4\pi\varepsilon_0}\,\frac{k^2 N e d^2}{r_2^3} \begin{pmatrix}-\rho_5\,\cos\varphi + \rho_6\,\sin\varphi\\ -\rho_5\,\sin\varphi - \rho_6\,\cos\varphi\\ 0\end{pmatrix}_{t-\frac{r_2}{c}} \tag{7.161}$$

with the abbreviation $r_2 = \sqrt{\tilde{L}^2 + d^2}$. Also, $\rho_5 = \rho_7$ and $\rho_6 = \rho_8$ is explicitly entered.

At this point, we derived the emitted fields of all oscillators. The upcoming, rather complicated step is the derivation of the scattering matrix entries for the second layer that we

need for predicting the transmittance through a slab of independent, randomly distributed particles.

We face the situation that the field between the layers is not linearly polarized anymore which is a consequence of the oscillators 2 and 4 being excited.

In all previous calculations, the incident field was x-polarized which allowed for an easy solution to the scattering matrix equation for the second layer. Furthermore, Eq. (7.18) then allowed for a simple calculation of the light transmitted through the slab. Since both x- and y-components are non-zero here, the scattering matrix equation and the transmitted field are much harder to predict. To do so, we have to explore how the suitable expressions change when y-polarized light is incident since this is not discussed in Ref. [18]. For a better understanding and visualization, Fig. 7.38 depicts the system's response to light incident in x- and y-direction, displayed in panels (a) and (b), respectively.

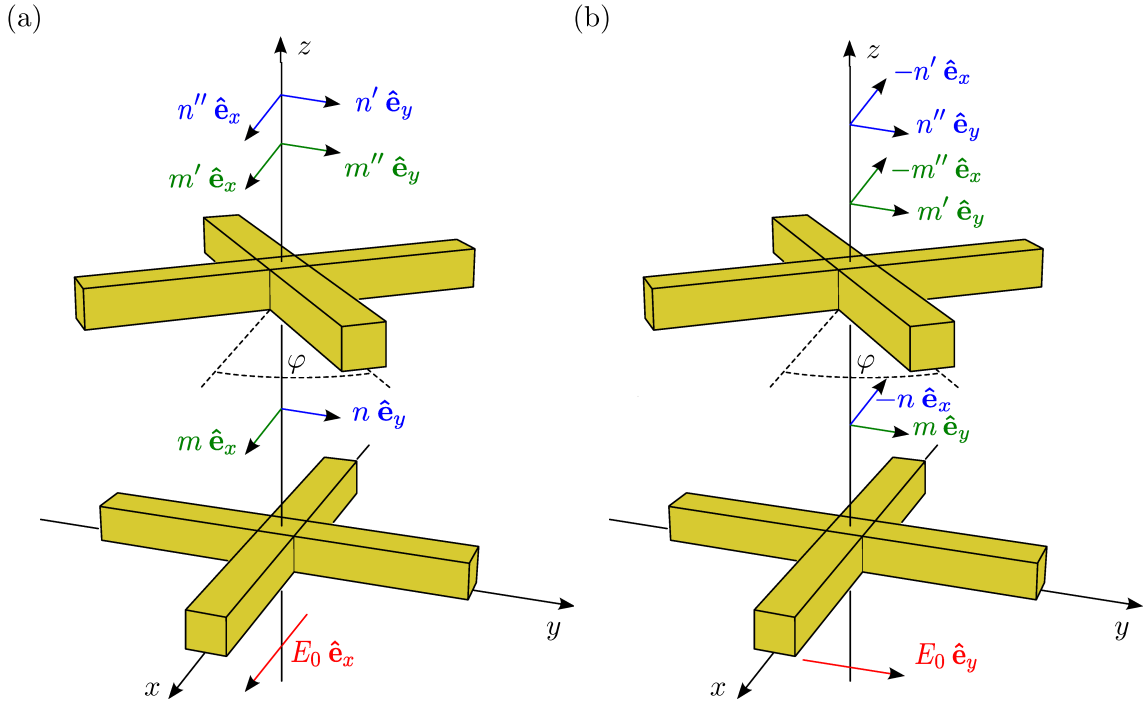

Figure 7.38: Visualization of the transmitted fields for incident x- and y-polarization, see panels (a) and (b), respectively.

To distinguish the two situations in Fig. 7.38, we denote the fields that are induced by an incident x-polarized field by E^x. Analogously, fields that are caused when the incident light is y-polarized, are called E^y.

The field transmitted by the first layer follows from Eqs. (7.160) and reads

$$\mathbf{E}^x_{t1,\mathrm{at2}} = E_0\, e^{-i\omega t+ikb+ik\frac{3}{2}h} \left(\left(1-\frac{S_{2,\mathbf{1}}\,2\pi}{k^2\,A}\right)\hat{\mathbf{e}}_x + \frac{S_{4,\mathbf{1}}\,2\pi}{k^2\,A}\,\hat{\mathbf{e}}_y\right) = m\,\hat{\mathbf{e}}_x + n\,\hat{\mathbf{e}}_y. \tag{7.162}$$

Here, we use the abbreviations m and n, see Fig. 7.38. The subscript "at2" indicates that the phase of the field is chosen such that the field is defined at the second layer of crosses.

Due to the systems's symmetry, an incident field polarized in y-direction causes the field

$$\mathbf{E}^y_{t1,\mathrm{at2}} = -n\,\hat{\mathbf{e}}_x + m\,\hat{\mathbf{e}}_y = E_0\, e^{-i\omega t+ikb+ik\frac{3}{2}h} \left(-\frac{S_{4,\mathbf{1}}\,2\pi}{k^2\,A}\,\hat{\mathbf{e}}_x + \left(1-\frac{S_{2,\mathbf{1}}\,2\pi}{k^2\,A}\right)\hat{\mathbf{e}}_y\right). \tag{7.163}$$

As we have seen in Eq. (7.161), the emitted fields of the second layer have the form

$$\mathbf{E}^x_{5+6+7+8} = \frac{1}{4\pi\varepsilon_0}\,\frac{k^2 N e d^2}{r_2^3}\,\begin{pmatrix} -\rho_5\,\cos\varphi + \rho_6\,\sin\varphi \\ -\rho_5\,\sin\varphi - \rho_6\,\cos\varphi \\ 0 \end{pmatrix}_{t-\frac{r_2}{c}} \tag{7.164}$$

for incident x-polarization. Consequently, the field emitted by the second layer with incident y-polarization reads

$$\mathbf{E}^y_{5+6+7+8} = \frac{1}{4\pi\varepsilon_0}\,\frac{k^2 N e d^2}{r_2^3}\,\begin{pmatrix} \rho_5\,\sin\varphi + \rho_6\,\cos\varphi \\ -\rho_5\,\cos\varphi + \rho_6\,\sin\varphi \\ 0 \end{pmatrix}_{t-\frac{r_2}{c}}. \tag{7.165}$$

To keep track it is helpful to follow the argument with one eye on Fig. 7.38. Before we write the scattering matrix equation, it is important to recall that the coordinate system is changed according to Section 7.3.2. With the scattering matrix equation

$$\mathbf{E}_s|_{t-\frac{r_2}{c}} \stackrel{!}{=} \frac{1}{-ikd}\begin{pmatrix} S_{2,\mathbf{2}} & S_{3,\mathbf{2}} \\ S_{4,\mathbf{2}} & S_{1,\mathbf{2}} \end{pmatrix} \cdot \mathbf{E}_{t1,\mathrm{at2}}|_{t-\frac{d}{c}} \tag{7.166}$$

we obtain a linear set of equations

$$\begin{aligned}
\gamma\cdot(-\rho_5\,\cos\varphi + \rho_6\,\sin\varphi) &= S_{2,\mathbf{2}}\cdot E^x_{t1,\mathrm{at2},x} + S_{3,\mathbf{2}}\cdot(-E^x_{t1,\mathrm{at2},y}) && \text{(7.167a)}\\
\gamma\cdot(\rho_5\,\sin\varphi + \rho_6\,\cos\varphi) &= S_{4,\mathbf{2}}\cdot E^x_{t1,\mathrm{at2},x} + S_{1,\mathbf{2}}\cdot(-E^x_{t1,\mathrm{at2},y}) && \text{(7.167b)}\\
\gamma\cdot(\rho_5\,\sin\varphi + \rho_6\,\cos\varphi) &= S_{2,\mathbf{2}}\cdot E^y_{t1,\mathrm{at2},x} + S_{3,\mathbf{2}}\cdot(-E^y_{t1,\mathrm{at2},y}) && \text{(7.167c)}\\
\gamma\cdot(\rho_5\,\cos\varphi - \rho_6\,\sin\varphi) &= S_{4,\mathbf{2}}\cdot E^y_{t1,\mathrm{at2},x} + S_{1,\mathbf{2}}\cdot(-E^y_{t1,\mathrm{at2},y}) && \text{(7.167d)}
\end{aligned}$$

with the abbreviation

$$\gamma = -\frac{i\,k^3\,N\,e\,d^3}{4\pi\varepsilon_0\,r_2^3}\,e^{ik(\sqrt{\tilde{L}^2+d^2}-d)}. \tag{7.168}$$

Here, we again identify the function $f(d)$ in Eq. (7.168). One last time we project the scattering matrix entries and, thus, continue our calculation with

$$\gamma = -\frac{i\,k^3\,N\,e}{4\pi\varepsilon_0}. \tag{7.169}$$

The scattering matrix entries we find as a solution to Eq. (7.167) are

$$S_{2,\mathbf{2}} = \frac{-\gamma(\rho_5\sin\varphi+\rho_6\cos\varphi)\frac{S_{4,\mathbf{1}}\,2\pi}{k^2\,A} + \gamma(\rho_6\sin\varphi-\rho_5\cos\varphi)\left(1-\frac{S_{2,\mathbf{1}}\,2\pi}{k^2\,A}\right)}{e^{-i\omega t+ikb+ik\frac{3}{2}h}\left[\left(\frac{S_{4,\mathbf{1}}\,2\pi}{k^2\,A}\right)^2+\left(1-\frac{S_{2,\mathbf{1}}\,2\pi}{k^2\,A}\right)^2\right]}, \tag{7.170}$$

$$S_{4,\mathbf{2}} = \frac{-\gamma(\rho_5\cos\varphi-\rho_6\sin\varphi)\frac{S_{4,\mathbf{1}}\,2\pi}{k^2\,A} + \gamma(\rho_5\sin\varphi+\rho_6\cos\varphi)\left(1-\frac{S_{2,\mathbf{1}}\,2\pi}{k^2\,A}\right)}{e^{-i\omega t+ikb+ik\frac{3}{2}h}\left[\left(\frac{S_{4,\mathbf{1}}\,2\pi}{k^2\,A}\right)^2+\left(1-\frac{S_{2,\mathbf{1}}\,2\pi}{k^2\,A}\right)^2\right]}. \tag{7.171}$$

Field behind the second layer of crosses

Between the layers, the electric field has non-zero x- and y-components. Each of these field components induces further fields in x- and y-direction. Since Ref. [18] only states the expressions for the transmission with incident x-polarized field, we deduce the field in our case by symmetry considerations.

The course of action is (cf. Fig. 7.38)

- ✧ Calculation of the fields caused by $m\ \hat{\mathbf{e}}_x$ (for incident x-polarization)
- ✧ Calculation of the fields caused by $-n\ \hat{\mathbf{e}}_x$ (for incident y-polarization)
- ✧ Convert $-n'\ \hat{\mathbf{e}}_x$ and $n''\ \hat{\mathbf{e}}_y$ into the fields that $n\ \hat{\mathbf{e}}_y$ would create for incident x-polarization

We already know

$$\mathbf{E}^x_{t1,\mathrm{at}2,x} = E_0\, e^{-i\omega t+ikb+ik\frac{3}{2}h} \left(1 - \frac{S_{2,\mathbf{1}}\, 2\pi}{k^2\, A}\right) \hat{\mathbf{e}}_x \;=\; m\, \hat{\mathbf{e}}_x. \tag{7.172}$$

Then, the transmitted field at the upper surface of the second cross (i.e., directly behind the crosses) is

$$\begin{aligned} \mathbf{E}^x_{t2,m-Teil} &= E_0\, e^{-i\omega t+ikb+ik2h} \left(1 - \frac{S_{2,\mathbf{1}}\, 2\pi}{k^2\, A}\right) \left[\left(1 - \frac{S_{2,\mathbf{2}}\, 2\pi}{k^2\, A}\right) \hat{\mathbf{e}}_x + \frac{S_{4,\mathbf{2}}\, 2\pi}{k^2\, A}\, \hat{\mathbf{e}}_y\right] \\ &= m'\, \hat{\mathbf{e}}_x + m''\, \hat{\mathbf{e}}_y. \end{aligned} \tag{7.173}$$

The next step is to calculate the field that is transmitted by the y-polarized part of the field between the crosses. To do so, we take the detour via the incident y-polarization and calculate the fields that are transmitted due to $-n\ \hat{\mathbf{e}}_x$. They read

$$\begin{aligned} \mathbf{E}^y_{t2,-n-part} &= E_0\, e^{-i\omega t+ikb+ik2h} \left(-\frac{S_{4,\mathbf{1}}\, 2\pi}{k^2\, A}\right) \left[\left(1 - \frac{S_{2,\mathbf{2}}\, 2\pi}{k^2\, A}\right) \hat{\mathbf{e}}_x + \frac{S_{4,\mathbf{2}}\, 2\pi}{k^2\, A}\, \hat{\mathbf{e}}_y\right] \\ &= -n'\, \hat{\mathbf{e}}_x + n''\, \hat{\mathbf{e}}_y. \end{aligned} \tag{7.174}$$

To gain the field caused by the y-component in between the crosses for incident x-polarization, we only make few recasts and arrive at

$$\mathbf{E}^x_{t2,n-part} = n''\, \hat{\mathbf{e}}_x + n'\, \hat{\mathbf{e}}_y \;=\; E_0\, e^{-i\omega t+ikb+ik2h}\, \frac{S_{4,\mathbf{1}}\, 2\pi}{k^2\, A} \left[-\frac{S_{4,\mathbf{2}}\, 2\pi}{k^2\, A}\, \hat{\mathbf{e}}_x + \left(1 - \frac{S_{2,\mathbf{2}}\, 2\pi}{k^2\, A}\right) \hat{\mathbf{e}}_y\right]. \tag{7.175}$$

Hereby, we obtained all expressions necessary to deduce the field that is transmitted through two layers of mutually rotated crosses when the light incident on the structure is x-polarized. It is the sum of $m'\ \hat{\mathbf{e}}_x$, $m''\ \hat{\mathbf{e}}_y$, $n''\ \hat{\mathbf{e}}_x$ and $n'\ \hat{\mathbf{e}}_y$.

$$\begin{aligned} \mathbf{E}^x_t = {} & E_0\, e^{-i\omega t+ikb+ik2h} \left[\left(1 - \frac{S_{2,\mathbf{1}}\, 2\pi}{k^2\, A}\right) \left(1 - \frac{S_{2,\mathbf{2}}\, 2\pi}{k^2\, A}\right) + \left(-\frac{S_{4,\mathbf{1}}\, 2\pi}{k^2\, A}\right) \left(\frac{S_{4,\mathbf{2}}\, 2\pi}{k^2\, A}\right)\right] \hat{\mathbf{e}}_x \\ & + E_0\, e^{-i\omega t+ikb+ik2h} \left[\left(\frac{S_{4,\mathbf{2}}\, 2\pi}{k^2\, A}\right) \left(1 - \frac{S_{2,\mathbf{1}}\, 2\pi}{k^2\, A}\right) + \left(\frac{S_{4,\mathbf{1}}\, 2\pi}{k^2\, A}\right) \left(1 - \frac{S_{2,\mathbf{2}}\, 2\pi}{k^2\, A}\right)\right] \hat{\mathbf{e}}_y \end{aligned} \tag{7.176}$$

Since no free parameters are left for fitting (the coupling τ was already adjusted in Section 7.7.2 for two layers of rods), the next step is to plot the predictions of the twin dipole model. For two layers of crosses, mutually rotated by $\varphi = -10°$, the numerical and modeled data is depicted in Fig. 7.39. Here, we see that the physical behavior of the system is qualitatively reproduced—two resonances occur with only minor displacement in frequency. This shows that the twin dipole approach is able to model the underlying physics in contrast to

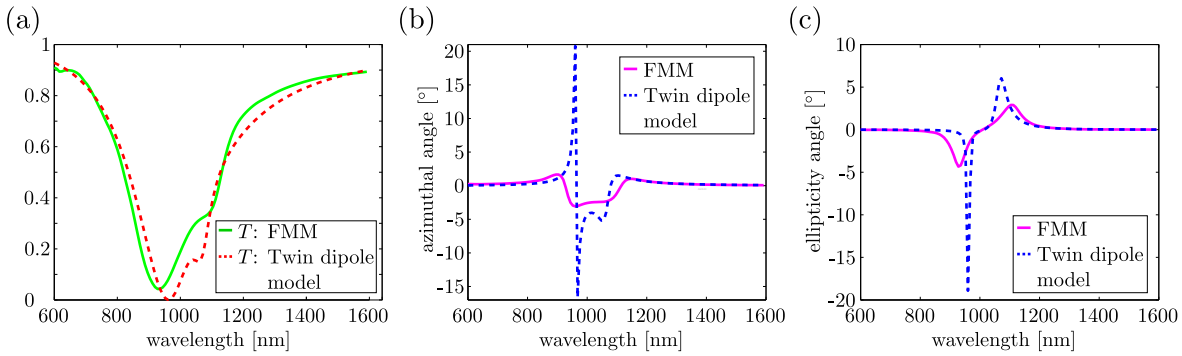

Figure 7.39: Transmittance (panel (a)) and polarization state (panels (b) and (c)) for two layers of rotated crosses with $\varphi = -10°$, $b = 50$ nm and the 400 nm $\times$ 400 nm unit cell. The coupling parameter τ was fixed in Section 7.7.2 with the value 0.13. Although the twin dipole model overestimates the strength of the polarization rotation, the two physical resonances are qualitatively reproduced. Here, the superiority of the twin dipole model over the dipole model is apparent.

the dipole model. Even though the angles in the polarization state are overestimated, the general characteristics of the model match the numerical data. Bearing this in mind, we can once more exploit the strengths of the model, namely a very rapid computation of all other cross rotation angles. As an example, Fig. 7.40 displays the azimuthal angle color-coded over the cross rotation angle and the wavelength. Naturally, the strongest polarization rotation is found near the main resonance.

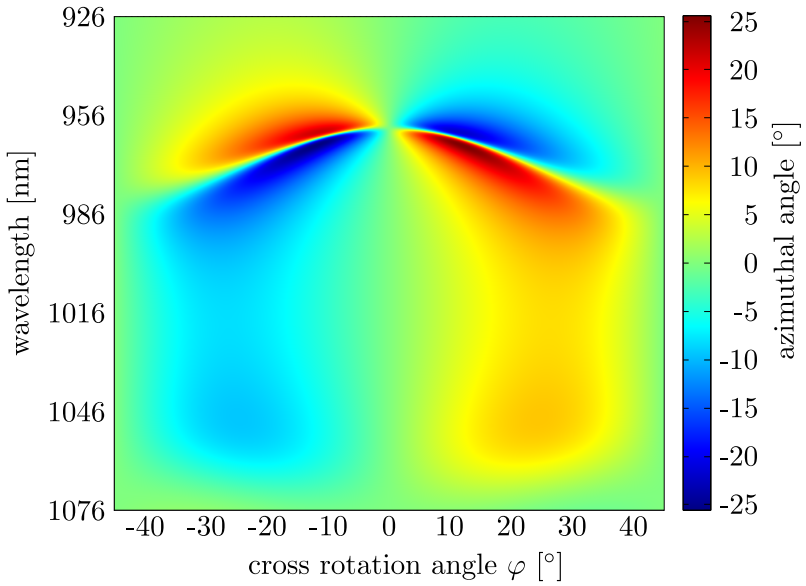

Figure 7.40: Azimuthal angle over cross rotation angle φ and wavelength. The layer distance is $b = 50$ nm and the coupling parameter is $\tau = 0.13$, cf. Fig. 7.39. When the cross is rotated in different directions (positive vs. negative angles) the sign of the azimuthal angle flips. The most pronounced rotations occur near the main resonance.

7.8 Twin dipole model with near-field coupling

The twin dipole model is a significant development of the dipole model. It describes the basic physical properties of the considered systems well, although not optimally. Especially the coupling between the layers is still not fully reproduced.

When analyzing the models so far, it becomes apparent that we always couple the (twin) dipoles in adjacent layers via their far-field. Then their emitted radiation is deduced and the transmission through a slab of such scatterers is determined with the help of a scattering matrix for each layer.

In this section, we couple the oscillators with their total dipole field, i.e., including near-field terms. Also, we realize that using scattering matrices for each layer may not be optimal. For two layers that are far apart, this seems reasonable. However, for two close layers, this is not necessarily the case, see Fig. 7.41.

Figure 7.41: For small layer spacings b, describing the problem with one scattering matrix rather than with two appears reasonable. Then, we describe the system as one layer of double-rods instead of two layers of rods.

The red circles sketch the procedure we used so far—we use two scattering matrices for *two layers of rods*. Since the rods are very close together and we couple them with their total dipole field, we change this procedure in this section. Instead of two layers of rods with two scattering matrices, we use one scattering matrix to calculate the transmission. Thus, we perceive the system as *one layer of double-rods*. This may seem like a technicality but is conceptually a big difference since only one scattering matrix is used and, thus, the slab approach assumes a slab consisting of randomly distributed double-rod scatterers.

To include the near-field coupling, we utilize the methodology introduced in Section 7.5. In particular, we use the dipole-dipole interaction tensor. This means that we first deduce the self-consistent dipole moments of all oscillators and then determine their radiated fields. The metallic rods are modeled by twin dipoles.

7.8.1 Tensorial polarizability, oscillator position and projection

In this introductory section, we deal with three technical topics: the polarizability of the oscillators, their position and a projection problem similar to the one we already know from the twin dipoles. First, we address the position issue.

In all previous calculations, we assumed that the oscillators are centered in the rods, i.e., they are placed on the main rotation axis of the rods[10]. When the rods are close together, this distance plays a crucial role. Figure 7.42 shows this dilemma—the oscillators could be located in the middle of the rods like before ($l_1 = l_2 = h/2$, they could be close together ($l_1 = h$, $l_2 = 0$) or they could be on opposing sides ($l_1 = 0$, $l_2 = h$).

[10] Although not shown, the other versions have been tested for all previous sections.

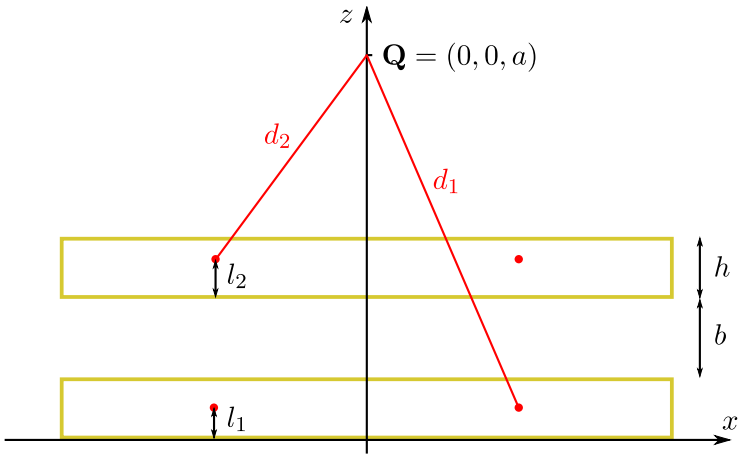

Figure 7.42: Sketch for the oscillator's positions defined by l_1 and l_2. Furthermore, we face a projection problem similar to the one in Sections 7.6 and 7.7 with the observer **Q** on the z axis.

In order to be as general as possible, we keep the quantities l_1 and l_2 as parameters.

The second topic of this section is the polarizability. So far, we never used it in the tensorial form. However, the derivation is essentially already contained in Section 7.3.4. Therefore, we only state the polarizability tensors here:

$$\underline{\underline{\alpha_E^1}} = \begin{pmatrix} 1 & 0 & 0 \\ 0 & 0 & 0 \\ 0 & 0 & 0 \end{pmatrix} \alpha_E, \qquad \underline{\underline{\alpha_E^2}} = \begin{pmatrix} \cos^2\varphi & \cos\varphi\,\sin\varphi & 0 \\ \cos\varphi\,\sin\varphi & \sin^2\varphi & 0 \\ 0 & 0 & 0 \end{pmatrix} \alpha_E \tag{7.177}$$

In Eq. (7.177), $\underline{\underline{\alpha_E^1}}$ is the polarizability of an unrotated oscillator. Since it is only excited in x-direction, all entries other than the xx-component are zero. The polarizability for the rotated oscillator is given by $\underline{\underline{\alpha_E^2}}$. In both expressions, the term α_E enters, which describes the scalar polarizability of the oscillators. For the twin dipole model it reads

$$\alpha_E = \frac{N}{2}\,\frac{e^2}{m}\,\frac{1}{\omega_0^2 - \omega^2 - i\omega\Gamma}, \tag{7.178}$$

where N is the total number of electrons in the rod, m is the effective electron mass, ω_0 the resonance frequency and Γ the damping term.

The third subject of this section is a projection similar to the one already encountered for the twin dipole model. As always, the scattering matrix uses the far-field with outgoing plane waves of the form $\exp(ikr)/r$ in z-direction. Since the emitters are not situated on the z-axis, small deviations occur. As we argued in Section 7.6 and 7.7, it makes sense to project the observer to infinity. The terms occurring in these sections were of the form

$$\frac{a^3}{\left(\sqrt{\left(\frac{l}{4}\right)^2 + a^2}\right)^3}\, e^{ik\left(\sqrt{\left(\frac{l}{4}\right)^2+a^2}-a\right)}. \tag{7.179}$$

Their limit value for $a \to \infty$ was found to be 1.

Since we apply a different methodology in this section, the terms we encounter take a different, but similar form. The notation follows Fig. 7.42. They read

$$\frac{a-l_1}{d_1}\,e^{ik(d_1-a)} = \underbrace{\frac{a\;e^{ik\left(\sqrt{\left(\frac{l}{4}\right)^2+(a-l_1)^2}-a\right)}}{\sqrt{\left(\frac{l}{4}\right)^2+(a-l_1)^2}}}_{\to\; e^{-ikl_1}\quad(a\to\infty)} - \underbrace{\frac{l_1\;e^{ik\left(\sqrt{\left(\frac{l}{4}\right)^2+(a-l_1)^2}-a\right)}}{\sqrt{\left(\frac{l}{4}\right)^2+(a-l_1)^2}}}_{\to\; 0\quad(a\to\infty)}. \tag{7.180}$$

Analogously, we find

$$\frac{a-l_1}{d_2}\,e^{ik(d_2-a)} \quad\to\quad e^{-ik(h+b+l_2)}+0 \qquad (a\to\infty). \tag{7.181}$$

7.8.2 Single layer of rods

Before we can predict the transmission properties of one layer of double-rods, we have to model one layer of rods according to the new procedure. We start by stating the positions of the oscillators forming the twin dipole:

$$\mathbf{r}_1 = \begin{pmatrix}\tilde{L}\cos\varphi\\ \tilde{L}\sin\varphi\\ l_1\end{pmatrix}, \qquad \mathbf{r}_2 = \begin{pmatrix}-\tilde{L}\cos\varphi\\ -\tilde{L}\sin\varphi\\ l_1\end{pmatrix}, \tag{7.182}$$

where we use the abbreviation $\tilde{L} = l/4$. They describe a rod that is rotated by φ. The z-coordinate is defined according to Fig. 7.42. The dipole moments of the oscillators have a general form of

$$\mathbf{p}_1 = \begin{pmatrix}p_1\cos\varphi\\ p_1\sin\varphi\\ 0\end{pmatrix}, \qquad \mathbf{p}_2 = \begin{pmatrix}p_2\cos\varphi\\ p_2\sin\varphi\\ 0\end{pmatrix}. \tag{7.183}$$

The next step is to formulate the self-consistent equations for the dipole moments. For that, we use the methodology described in Section 7.5.1. They read

$$\begin{aligned}
\mathbf{p}_1 &= \underline{\underline{\alpha}}^2\left(E_0e^{-i\omega t+ikl_1}\,\hat{\mathbf{e}}_x + \frac{f}{4\pi\epsilon_0}\,\mathcal{G}^0\left(\begin{pmatrix}\tilde{L}\cos\varphi\\ \tilde{L}\sin\varphi\\ l_1\end{pmatrix}-\begin{pmatrix}-\tilde{L}\cos\varphi\\ -\tilde{L}\sin\varphi\\ l_1\end{pmatrix}\right)\mathbf{p}_2\right)\\
&= \alpha_E E_0 e^{-i\omega t+ikl_1}\begin{pmatrix}\cos^2\varphi\\ \cos\varphi\sin\varphi\\ 0\end{pmatrix}+\\
&\quad \underline{\underline{\alpha}}^2\frac{f}{4\pi\epsilon_0}\frac{e^{ik2\tilde{L}}}{8\tilde{L}^3}\left((4k^2\tilde{L}^2+ik2\tilde{L}-1)\begin{pmatrix}p_2\cos\varphi\\ p_2\sin\varphi\\ 0\end{pmatrix}-\frac{4k^2\tilde{L}^2+6ik\tilde{L}-3}{4\tilde{L}^2}(2\tilde{L}p_2)\begin{pmatrix}2\tilde{L}\cos\varphi\\ 2\tilde{L}\sin\varphi\\ 0\end{pmatrix}\right)\\
&= \alpha_E E_0 e^{-i\omega t+ikl_1}\begin{pmatrix}\cos^2\varphi\\ \cos\varphi\sin\varphi\\ 0\end{pmatrix}+\alpha_E\frac{f}{4\pi\epsilon_0}\,\frac{e^{ik2\tilde{L}}}{8\tilde{L}^3}\,\left(2-4ik\tilde{L}\right)\,p_2\begin{pmatrix}\cos\varphi\\ \sin\varphi\\ 0\end{pmatrix}, \qquad (7.184)\\
\mathbf{p_2} &= \alpha_E E_0 e^{-i\omega t+ikl_1}\begin{pmatrix}\cos^2\varphi\\ \cos\varphi\sin\varphi\\ 0\end{pmatrix}+\alpha_E\frac{f}{4\pi\epsilon_0}\,\frac{e^{ik2\tilde{L}}}{8\tilde{L}^3}\,\left(2-4ik\tilde{L}\right)\,p_1\begin{pmatrix}\cos\varphi\\ \sin\varphi\\ 0\end{pmatrix}. \qquad (7.185)
\end{aligned}$$

Here, we explicitly used Eq. (7.79). Furthermore, we introduced a free parameter f so that the coupling between the oscillators of the twin dipole can be adjusted. As one might expect for the two oscillators forming the twin dipole, their movement is identical, i.e., $p_1 = p_2$. Inserting Eqs. (7.184) and (7.185) into each other yields

$$p_1 = \frac{\alpha_E \cos\varphi E_0 e^{-i\omega t+ikl_1} + \frac{f\,\alpha_E^2}{4\pi\epsilon_0}\cos\varphi E_0 e^{-i\omega t+ikl_1}\,\frac{e^{ik2\tilde{L}}}{8\tilde{L}^3}\left(2-4ik\tilde{L}\right)}{1-\left(\frac{f\,\alpha_E}{4\pi\epsilon_0}\right)^2\left(\frac{e^{ik2\tilde{L}}}{8\tilde{L}^3}\right)^2\left(2-4ik\tilde{L}\right)^2}. \tag{7.186}$$

The next step is to obtain the emitted field of the oscillators and link that to the scattering matrix. We assume an observer at $\mathbf{Q} = (0, 0, a)$, $a > 0$. The distance between observer and oscillators is denoted by $d = |\mathbf{Q} - \mathbf{r}_1|$. Using $p_1 = p_2$, the emitted field of the twin dipole reads

$$\mathbf{E}(\mathbf{Q}) = \frac{1}{4\pi\epsilon_0}\frac{e^{ikd}}{d}\left(2\left(k^2+\frac{ik}{d}-\frac{1}{d^2}\right)\begin{pmatrix}p_1\cos\varphi\\ p_1\sin\varphi\\ 0\end{pmatrix}-\left(\frac{k^2}{d^2}+\frac{3ik}{d^3}-\frac{3}{d^4}\right)\begin{pmatrix}2\tilde{L}^2\,p_1\cos\varphi\\ 2\tilde{L}^2\,p_1\sin\varphi\\ 0\end{pmatrix}\right). \tag{7.187}$$

Linking the far-field of Eq. (7.187) to the scattering matrix yields

$$\frac{2}{4\pi\epsilon_0}\frac{e^{ikd}}{d}\,k^2\,p_1\begin{pmatrix}\cos\varphi\\ -\sin\varphi\end{pmatrix} \stackrel{!}{=} \frac{1}{-ik(a-l_1)}\begin{pmatrix}S_2 & S_3\\ S_4 & S_1\end{pmatrix}\begin{pmatrix}E_0 e^{-i\omega t+ika}\\ 0\end{pmatrix}. \tag{7.188}$$

Thereby, we obtain the far-field scattering matrix entries for the oscillators coupled both with their near- and far-field. They read

$$S_2 = \frac{-ik^3}{4\pi\epsilon_0}\,2\,p_1\,\cos\varphi\,\frac{a-l_1}{d}e^{ik(d-a)}\,\frac{1}{E_0 e^{-i\omega t}} \stackrel{\text{proj.}}{=} \frac{-ik^3}{4\pi\epsilon_0}\,2\,p_1\,\cos\varphi\,\frac{e^{-ikl_1}}{E_0 e^{-i\omega t}}, \tag{7.189a}$$

$$S_4 = \frac{ik^3}{4\pi\epsilon_0}\,2\,p_1\,\sin\varphi\,\frac{a-l_1}{d}e^{ik(d-a)}\,\frac{1}{E_0 e^{-i\omega t}} \stackrel{\text{proj.}}{=} \frac{ik^3}{4\pi\epsilon_0}\,2\,p_1\,\sin\varphi\,\frac{e^{-ikl_1}}{E_0 e^{-i\omega t}}. \tag{7.189b}$$

For both scattering matrices, we entered the result of a projection of the type we discussed in Eq. (7.180).

Upon comparing Eqs. (7.189) and (7.186) we encounter that the choice of the oscillator's height within the rod (l_1, see Fig. 7.42) does not play a role for one layer of rods. This is due to the fact that Eq. (7.186) contains a phase $\exp(ikl_1)$ and Eq. (7.189) contains a phase $\exp(-ikl_1)$. This is consistent with all previous models where the oscillators' height did not enter for single layer structures.

In total, the transmitted field according to Eqs. (7.189) contains four fit parameters: the coupling strength f between the oscillators forming the twin dipole, the oscillator's mass m, its resonance frequency ω_0 and its damping Γ. Naturally, several different combinations yield good results. However, the twin dipole model with the near-field coupling does not reproduce the transmittance as well as the dipole or twin dipole model. There are minor deviations occurring that are due to the near-field coupling between the oscillators and especially this term's phase in Eq. (7.186). Neglecting this term and assuming an instantaneous coupling could be a possible route for further studies.

In Tab. 7.1 we collected some parameter sets that describe both the transmittance for the single layer of unrotated rods and the field behind the structure. The first three sets show slightly better results than the last three.

f	ω_0 [Hz]	Γ [Hz]	m
0.1	$1.235 \cdot 10^{15}$	$1.45 \cdot 10^{14}$	$m_e \cdot 2.97$
0.5	$1.31 \cdot 10^{15}$	$9.9 \cdot 10^{13}$	$m_e \cdot 3.22$
0.75	$1.36 \cdot 10^{15}$	$7.7 \cdot 10^{13}$	$m_e \cdot 3.22$
1	$1.41 \cdot 10^{15}$	$5.5 \cdot 10^{13}$	$m_e \cdot 3.17$
1.25	$1.465 \cdot 10^{15}$	$3.4 \cdot 10^{13}$	$m_e \cdot 2.97$
1.5	$1.51 \cdot 10^{15}$	$9 \cdot 10^{12}$	$m_e \cdot 2.97$

Table 7.1: Fit parameter sets for a layer of rods described by the twin dipole model with near-field coupling. The first three sets describe the system well, while the performance of the last three is slightly worse.

Figure 7.43 shows the results for the fourth parameter set in Tab. 7.1. Panel (a) displays the transmittance which shows minor deviations due to the near-field coupling's phase. Panels (b) and (c) depict the real and imaginary part of the transmitted field in x-direction, respectively. The numerical field is obtained one unit cell length behind the layer, i.e., at $z = 1350$ nm + 50 nm.

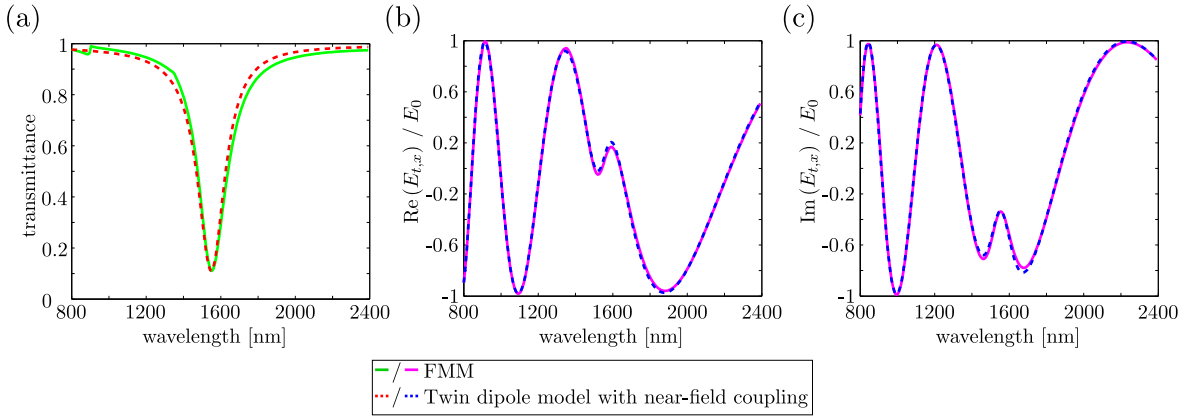

Figure 7.43: Transmittance (panel (a)) and transmitted field in x-direction (panels (b) and (c)) for a layer of unrotated rods described by the twin dipole model with near-field coupling with the fourth parameter set of Tab. 7.1. The numerical data is reproduced, although minor deviations occur.

7.8.3 Double layer of rods

After having applied the twin dipole model with the near-field terms to one layer of rods, we employ it to two layers of rods in this section. The positions of the four oscillators forming the two twin dipoles is

$$\mathbf{r}_1 = \begin{pmatrix} \tilde{L} \\ 0 \\ l_1 \end{pmatrix}, \qquad \mathbf{r}_2 = \begin{pmatrix} -\tilde{L} \\ 0 \\ l_1 \end{pmatrix}, \qquad \mathbf{r}_3 = \begin{pmatrix} \tilde{L}\cos\varphi \\ \tilde{L}\sin\varphi \\ h+b+l_2 \end{pmatrix}, \qquad \mathbf{r}_4 = \begin{pmatrix} -\tilde{L}\cos\varphi \\ -\tilde{L}\sin\varphi \\ h+b+l_2 \end{pmatrix}. \tag{7.190}$$

We already sketched the setup in Fig. 7.42. The dipole moments are

$$\mathbf{p}_{1/2} = p_{1/2}\,\hat{\mathbf{e}}_x, \qquad \mathbf{p}_{3/4} = \begin{pmatrix} p_{3/4}\cos\varphi \\ p_{3/4}\sin\varphi \\ 0 \end{pmatrix}. \tag{7.191}$$

Since the four oscillators have different distances to each other, there are three different couplings present. For each, we introduce a fit parameter, see Tab. 7.2. Pairs of oscillators are abbreviated like "(oscillator 1, oscillator 2)". The coupling parameter f is already known from Section 7.8.2—it links the oscillators within the twin dipoles, i.e., oscillator pairs (1,2) and (3,4).

quantity	meaning
f	coupling parameter of (1,2) and (3,4)
g	coupling parameter of (1,3) and (2,4)
w	coupling parameter of (1,4) and (2,3)
q	distance of (1,3) and (2,4)
s	distance of (1,4) and (2,3)

Table 7.2: Couplings and distances for the twin dipole model with near-field terms.

The distances defined in Tab. 7.2 are given by

$$q = |\mathbf{r}_1 - \mathbf{r}_3| = \sqrt{(\tilde{L} - \tilde{L}\cos\varphi)^2 + \tilde{L}^2 \sin\varphi^2 + (l_1 - h - b - l_2)^2}, \tag{7.192a}$$

$$s = |\mathbf{r}_1 - \mathbf{r}_4| = \sqrt{(\tilde{L} + \tilde{L}\cos\varphi)^2 + \tilde{L}^2 \sin\varphi^2 + (l_1 - h - b - l_2)^2}. \tag{7.192b}$$

The next step is to obtain the dipole moments that contain the interaction with all other dipoles of the two twin dipole system. Since that is rather lengthy, we show the result for oscillator one here. It is obtained by

$$\begin{aligned}
\mathbf{p}_1 &= \underline{\underline{\alpha}}^1 E_0 e^{-i\omega t + ikl_1} \hat{\mathbf{e}}_x + \underline{\underline{\alpha}}^1 \frac{1}{4\pi\epsilon_0} \left[f\, \mathcal{G}^0 \left(\begin{pmatrix} \tilde{L} \\ 0 \\ l_1 \end{pmatrix} - \begin{pmatrix} -\tilde{L} \\ 0 \\ l_1 \end{pmatrix} \right) \mathbf{p}_2 + \right. \\
&\quad \left. g\, \mathcal{G}^0 \left(\begin{pmatrix} \tilde{L} \\ 0 \\ l_1 \end{pmatrix} - \begin{pmatrix} \tilde{L}\cos\varphi \\ \tilde{L}\sin\varphi \\ h + b + l_2 \end{pmatrix} \right) \mathbf{p}_3 + w\, \mathcal{G}^0 \left(\begin{pmatrix} \tilde{L} \\ 0 \\ l_1 \end{pmatrix} - \begin{pmatrix} -\tilde{L}\cos\varphi \\ -\tilde{L}\sin\varphi \\ h + b + l_2 \end{pmatrix} \right) \mathbf{p}_4 \right] \\
&= \ldots \\
&= \alpha_E e^{-i\omega t + ikl_1} \hat{\mathbf{e}}_x + \frac{\alpha_E}{4\pi\epsilon_0} \hat{\mathbf{e}}_x \left[f\, \frac{e^{ik2\tilde{L}}}{8\tilde{L}^3} (2 - 4ik\tilde{L})\, p_2 + \right. \\
&\quad g\, \frac{e^{ikq}}{q^3} \left((k^2q^2 + ikq - 1)\cos\varphi + \frac{k^2q^2 + 3ikq - 3}{q^2} (\tilde{L}\cos\varphi - \tilde{L})^2 \right) p_3 + \\
&\quad \left. w\, \frac{e^{iks}}{s^3} \left((k^2s^2 + iks - 1)\cos\varphi - \frac{k^2s^2 + 3iks - 3}{s^2} (\tilde{L}\cos\varphi + \tilde{L})^2 \right) p_4 \right].
\end{aligned} \tag{7.193}$$

The third oscillator has a similar form. However, it is important to use the polarizability $\underline{\underline{\alpha}}^2$ of the rotated rod. Then, the dipole moment can be calculated via

$$\begin{aligned}
\mathbf{p}_3 &= \underline{\underline{\alpha}}^2 E_0 e^{-i\omega t + ik(h+b+l_2)} \hat{\mathbf{e}}_x + \\
&\quad \underline{\underline{\alpha}}^2 \frac{1}{4\pi\epsilon_0} \left[f\, \mathcal{G}^0 \left(\begin{pmatrix} \tilde{L}\cos\varphi \\ \tilde{L}\sin\varphi \\ h + b + l_2 \end{pmatrix} - \begin{pmatrix} -\tilde{L}\cos\varphi \\ -\tilde{L}\sin\varphi \\ h + b + l_2 \end{pmatrix} \right) \begin{pmatrix} p_4\cos\varphi \\ p_4\sin\varphi \\ 0 \end{pmatrix} + \right. \\
&\quad \left. g\, \mathcal{G}^0 \left(\begin{pmatrix} \tilde{L}\cos\varphi \\ \tilde{L}\sin\varphi \\ h + b + l_2 \end{pmatrix} - \begin{pmatrix} \tilde{L} \\ 0 \\ l_1 \end{pmatrix} \right) \mathbf{p}_1 + w\, \mathcal{G}^0 \left(\begin{pmatrix} \tilde{L}\cos\varphi \\ \tilde{L}\sin\varphi \\ h + b + l_2 \end{pmatrix} - \begin{pmatrix} -\tilde{L} \\ 0 \\ l_1 \end{pmatrix} \right) \mathbf{p}_2 \right].
\end{aligned} \tag{7.194}$$

The vectorial form reduces to a scalar equation when Eq. (7.191) is applied:

$$\begin{aligned} p_3 \;=\; & \alpha_E E_0 e^{-i\omega t+ik(h+b+l_2)}\cos\varphi + \underbrace{\frac{\alpha_E}{4\pi\epsilon_0}\, f\, \frac{e^{ik2\tilde{L}}}{8\tilde{L}^3}\,(2-4ik\tilde{L})}_{=:\bar{f}}\; p_4 + \\ & \underbrace{\frac{\alpha_E}{4\pi\epsilon_0}\, g\, \frac{e^{ikq}}{q^3}\,\left((k^2q^2+ikq-1)\cos\varphi + \frac{k^2q^2+3ikq-3}{q^2}(\tilde{L}\cos\varphi-\tilde{L})^2\right)}_{=:\bar{g}}\; p_1 + \\ & \underbrace{\frac{\alpha_E}{4\pi\epsilon_0}\, w\, \frac{e^{iks}}{s^3}\,\left((k^2s^2+iks-1)\cos\varphi - \frac{k^2s^2+3iks-3}{s^2}(\tilde{L}\cos\varphi+\tilde{L})^2\right)}_{=:\bar{w}}\; p_2. \end{aligned} \tag{7.195}$$

Here, we defined several terms that are also found in Eq. (7.193). The dipole moments of oscillators 2 and 4 are derived in a similar fashion. Together, the dipole moment equations for each oscillator form a linear set of equations. It reads

$$\begin{pmatrix} 1 & -\bar{f} & -\bar{g} & -\bar{w} \\ -\bar{f} & 1 & -\bar{w} & -\bar{g} \\ -\bar{g} & -\bar{w} & 1 & -\bar{f} \\ -\bar{w} & -\bar{g} & -\bar{f} & 1 \end{pmatrix} \cdot \begin{pmatrix} p_1 \\ p_2 \\ p_3 \\ p_4 \end{pmatrix} = \alpha_E\, E_0\, e^{-i\omega t} \begin{pmatrix} e^{ikl_1} \\ e^{ikl_1} \\ e^{ik(h+b+l_2)}\cos\varphi \\ e^{ik(h+b+l_2)}\cos\varphi \end{pmatrix}. \tag{7.196}$$

For solving it, we multiply by the inverse of the matrix on the left hand side and, thus, obtain the self-consistent dipole moments of the system with two twin dipoles above each other. They contain all parts of the dipole-dipole interaction, both near- and far-field, and read

$$\begin{pmatrix} p_1 \\ p_2 \\ p_3 \\ p_4 \end{pmatrix} = \frac{\alpha_E\, E_0\, e^{-i\omega t}}{n} \begin{pmatrix} -\bar{f}\, e^{ikl_1} + \bar{g}\, e^{ik(h+b+l_2)}\cos\varphi + \bar{w}\, e^{ik(h+b+l_2)}\cos\varphi + e^{ikl_1} \\ -\bar{f}\, e^{ikl_1} + \bar{g}\, e^{ik(h+b+l_2)}\cos\varphi + \bar{w}\, e^{ik(h+b+l_2)}\cos\varphi + e^{ikl_1} \\ -\bar{f}\, e^{ik(h+b+l_2)}\cos\varphi + \bar{g}\, e^{ikl_1} + \bar{w}\, e^{ikl_1} + e^{ik(h+b+l_2)}\cos\varphi \\ -\bar{f}\, e^{ik(h+b+l_2)}\cos\varphi + \bar{g}\, e^{ikl_1} + \bar{w}\, e^{ikl_1} + e^{ik(h+b+l_2)}\cos\varphi \end{pmatrix}, \tag{7.197}$$

where we used the abbreviation $n = \bar{f}^2 - 2\bar{f} + 1 - \bar{g}^2 - \bar{w}^2 - 2\bar{w}\bar{g}$. Physically, one would expect the oscillators forming the pairs (1,2) and (3,4) to move identically. This is the case, since $p_1 = p_2$ and $p_3 = p_4$.

After having obtained the self-consistent dipole moments, we can deduce their emitted electric fields. For the observer at $\mathbf{Q} = (0, 0, a)$, they are

$$\mathbf{E}(\mathbf{Q}) = \frac{1}{4\pi\varepsilon_0} \sum_{i=1}^{4} \mathcal{G}^0 (\mathbf{Q} - \mathbf{r}_i) \cdot \mathbf{p}_i \tag{7.198}$$

$$\begin{aligned}
&= \frac{1}{4\pi\epsilon_0} \frac{e^{ikd_1}}{d_1^3} \left((k^2 d_1^2 + ikd_1 - 1) \begin{pmatrix} p_1 \\ 0 \\ 0 \end{pmatrix} - \frac{k^2 d_1^2 + 3ikd_1 - 3}{d_1^2} (-\tilde{L} p_1) \begin{pmatrix} -\tilde{L} \\ 0 \\ a - l_1 \end{pmatrix} \right) \\
&+ \frac{1}{4\pi\epsilon_0} \frac{e^{ikd_1}}{d_1^3} \left((k^2 d_1^2 + ikd_1 - 1) \begin{pmatrix} p_2 \\ 0 \\ 0 \end{pmatrix} - \frac{k^2 d_1^2 + 3ikd_1 - 3}{d_1^2} \tilde{L} p_2 \begin{pmatrix} \tilde{L} \\ 0 \\ a - l_1 \end{pmatrix} \right) \\
&+ \frac{1}{4\pi\epsilon_0} \frac{e^{ikd_2}}{d_2^3} \left((k^2 d_2^2 + ikd_2 - 1) \begin{pmatrix} p_3 \cos\varphi \\ p_3 \sin\varphi \\ 0 \end{pmatrix} - \frac{k^2 d_2^2 + 3ikd_2 - 3}{d_2^2} (-\tilde{L} p_3) \begin{pmatrix} -\tilde{L} \cos\varphi \\ -\tilde{L} \sin\varphi \\ a - h - b - l_2 \end{pmatrix} \right) \\
&+ \frac{1}{4\pi\epsilon_0} \frac{e^{ikd_2}}{d_2^3} \left((k^2 d_2^2 + ikd_2 - 1) \begin{pmatrix} p_4 \cos\varphi \\ p_4 \sin\varphi \\ 0 \end{pmatrix} - \frac{k^2 d_2^2 + 3ikd_2 - 3}{d_2^2} \tilde{L} p_4 \begin{pmatrix} \tilde{L} \cos\varphi \\ \tilde{L} \sin\varphi \\ a - h - b - l_2 \end{pmatrix} \right).
\end{aligned}$$

For the scattering matrix we need only the far-field of this expression. Hence, we neglect the emitted near-field of the coupled dipoles. However, their coupling is still based on all parts of the dipole field. With the usual change in the coordinate system the scattering matrix equation reads

$$\frac{2\,k^2}{4\pi\epsilon_0} \left(\frac{e^{ikd_1}}{d_1} p_1 \begin{pmatrix} 1 \\ 0 \end{pmatrix} + \frac{e^{ikd_2}}{d_2} p_3 \begin{pmatrix} \cos\varphi \\ -\sin\varphi \end{pmatrix} \right) \stackrel{!}{=} \frac{1}{-ik(a - l_1)} \begin{pmatrix} S_2 & S_3 \\ S_4 & S_1 \end{pmatrix} \begin{pmatrix} E_0 e^{-i\omega t + ika} \\ 0 \end{pmatrix}. \tag{7.199}$$

This yields the scattering matrix entries

$$\begin{aligned}
S_2 &= \frac{-2ik^3}{4\pi\epsilon_0} \frac{1}{E_0 e^{-i\omega t}} \left(p_1 \frac{a - l_1}{d_1} e^{ik(d_1 - a)} + p_3 \cos\varphi \frac{a - l_1}{d_2} e^{ik(d_2 - a)} \right) \\
&\stackrel{\text{proj.}}{=} \frac{-2ik^3}{4\pi\epsilon_0} \frac{1}{E_0 e^{-i\omega t}} \left(p_1 e^{-ikl_1} + p_3 \cos\varphi\, e^{-ik(h+b+l_2)} \right), \qquad (7.200a) \\
S_4 &= \frac{2ik^3}{4\pi\epsilon_0} p_3 \sin\varphi \frac{a - l_1}{d_2} e^{ik(d_2 - a)} \frac{1}{E_0 e^{-i\omega t}} \\
&\stackrel{\text{proj.}}{=} \frac{2ik^3}{4\pi\epsilon_0} p_3 \sin\varphi\, e^{-ik(h+b+l_2)} \frac{1}{E_0 e^{-i\omega t}}. \qquad (7.200b)
\end{aligned}$$

Here, we remember that the twin dipole model's scattering matrix entries need to be projected. The terms for the projection were explained in Eqs. (7.180) and (7.181).

The final step is fitting the model to numerical data. For that, we assume that the coupling parameters w and g (see Tab. 7.2) are equal since there is no physical or geometrical reason why they should differ. Note that g and w are only factors in front of terms that contain the actual distance dependence of the coupling.

Since we left l_1 and l_2 (see Fig. 7.42) as free parameters so far, we have to discuss several possible realizations. In the following, we discuss the results of the efforts made to find suitable parameters for the model. In all discussed realizations of l_1 and l_2 we used each of

the parameter sets in Tab. 7.1 and searched for suitable coupling parameters g ($= w$). The distance of the layers used in these investigations is $b = 50$ nm.

For $l_1 = h$ and $l_2 = 0$, which corresponds to the situation that the oscillators are as close together as possible, no sensible fit can be performed for any of the parameter sets in Tab. 7.1. Any fit yields only one resonance in the transmittance spectrum.

For $l_1 = l_2 = 0$ the fits become better. For example, the parameter set with $f = 1.25$ and a coupling fit parameter $g = 0.16$ yields acceptable results similar to the ones of the dipole model. This means that the polarization state for a rotated upper rod is overestimated, but qualitatively correct. Unfortunately, the resonance in the unrotated case is shifted.

For $l_1 = l_2 = h/2$, the situation is similar. Some parameter sets ($f = 1.25$, $f = 1.5$) result in transmittances and polarization states for rotated rods that are comparable to the $l_1 = l_2 = 0$-case. Again, the resonances are shifted in frequency.

For $l_1 = 0$ and $l_2 = h$ the best results are obtained. The best fit uses the $f = 1$ parameter set—which is good since this means that we effectively get rid of one fit parameter. The fitted coupling parameter is $g = 0.4$. The result is displayed in Fig. 7.44. As we see, the polarization state (panels (a) and (b)) is reproduced rather well. Unfortunately, this is mainly the case because the whole spectrum is dominated by the main resonance. As we see in Fig. 7.44(c), the field near the second resonance is not described well. Therefore, the model still does not reproduce the physics correctly. Moreover, we performed the same fits for the distances $b = 25$ nm, 75 nm and 100 nm. In no case were the results satisfactory.

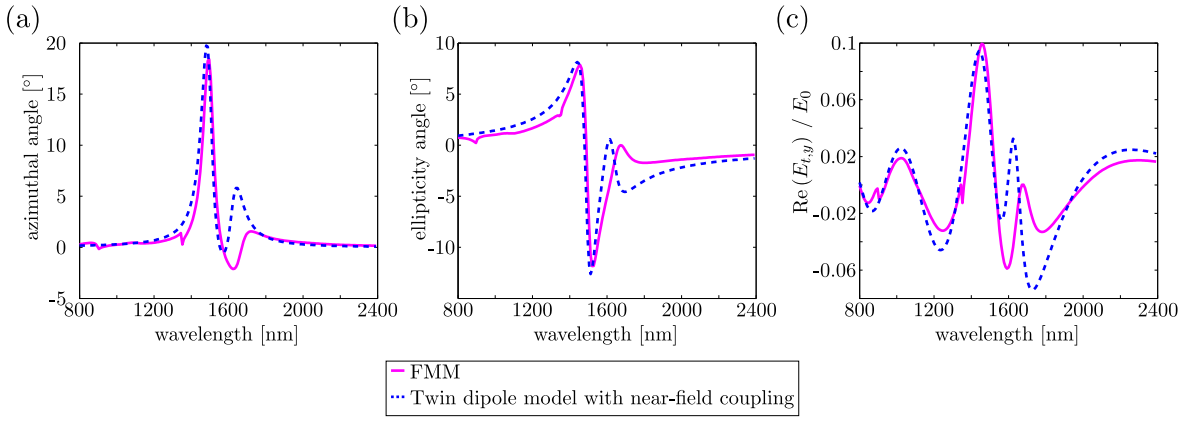

Figure 7.44: Polarization state (panels (a) and (b)) and real part of the transmitted field in y-direction for two layers of rotated rods with $\varphi = -20°$. The twin dipole model with one scattering matrix and near-field coupling reproduces the polarization state for this distance ($b = 50$ nm) well but the transmitted field still lacks a proper description. The field is evaluated one unit cell length behind the structure, i.e., at $z = 1450$ nm. We use the data for the 1350 nm × 900 nm unit cell. The model's parameters are $l_1 = 0$, $l_2 = h$, $g = w = 0.4$ and $f = 1$. ω_0, Γ and m are chosen according to Tab. 7.1.

Although the model as presented in this section is not yet an improvement over the other presented models, I still think of it as conceptually important. The reason is that two important concepts could be shown and discussed. Firstly, we showed a possible way to incorporate a near-field coupling into the (twin) dipole model. Secondly, we discussed that the question whether one or two scattering matrices should be used cannot be answered a

priori. Therefore, this section offers quite a few possible ways to continue research on the (twin) dipole model. Firstly, one scattering matrix could be used for the description of two layers of rods in the ordinary (twin) dipole model without near-field coupling. Secondly, we could use the near-field coupling but exclude the phase in the coupling between the oscillators in one layer. Thirdly, one might use two scattering matrices for two layers but still incorporate the near-field coupling in the equations of motion.

7.9 Further prospects - continuous charge distribution model

In the previous sections, we changed our description of metallic nanostructures from the dipole model to the twin dipole model. This enabled us to physically describe the transmission properties of light impinging on two layers of periodically arranged and mutually rotated crosses. The essential step was to describe one metallic rod as a twin dipole, i.e., two dipoles, instead of one. The next steps suggest themselves—either we could use three, four or more oscillators or we could assume a whole charge and current density along the rod. The latter seems to be the most general procedure. In this section, we briefly outline the basis of such a continuous charge distribution model (CCDM).

7.9.1 Fields of time-harmonic sources

The basic physics of charges that oscillate harmonic in time can be found in Ref. [20]. In this section, we review the elements needed for the proposed CCDM. We start by assuming a general time-harmonic dependence of charge and current density

$$\rho(\mathbf{r},t) = \rho(\mathbf{r})\, e^{-i\omega t}, \qquad \mathbf{J}(\mathbf{r},t) = \mathbf{J}(\mathbf{r})\, e^{-i\omega t}. \tag{7.201}$$

The fields and potentials have, therefore, the same time dependence. We assume all sources to be in free space. The resulting vector potential reads

$$\mathbf{A}(\mathbf{r},t) = \frac{\mu_0}{4\pi} \int d^3r' \int dt' \, \frac{\mathbf{J}(\mathbf{r}',t')}{|\mathbf{r}-\mathbf{r}'|}\, \delta\left(t' + \frac{|\mathbf{r}-\mathbf{r}'|}{c} - t\right), \tag{7.202}$$

where the delta function ensures causality. With the form of the time dependence in Eq. (7.201) we can integrate parts of Eq. (7.202) and obtain

$$\mathbf{A}(\mathbf{r}) = \frac{\mu_0}{4\pi} \int \frac{\mathbf{J}(\mathbf{r}')}{|\mathbf{r}-\mathbf{r}'|}\, e^{ik|\mathbf{r}-\mathbf{r}'|}\, d^3r'. \tag{7.203}$$

In the far-field, where the distance r between the observer and the emitter is much larger than the wavelength and the wavelength itself is much larger than the emitter's dimensions, we can approximate

$$|\mathbf{r}-\mathbf{r}'| \approx r - \mathbf{n}\cdot\mathbf{r}', \tag{7.204}$$

where $\mathbf{n}$ is the unit vector in the direction of $\mathbf{r}$ and $r = |\mathbf{r}|$. With this approximation the vector potential in the far-field reads

$$\lim_{kr\to\infty} \mathbf{A}(\mathbf{r}) = \frac{\mu_0}{4\pi}\, \frac{e^{ikr}}{r} \int \mathbf{J}(\mathbf{r}') e^{-ik\mathbf{n}\cdot\mathbf{r}'} d^3r' \tag{7.205}$$

7.9.2 Application to one layer of rods

As a first layout of the model, we assume a general form of

$$\rho(\mathbf{r},t) = a(\omega)\ \sin\left(\frac{\pi}{l}x\right)\ e^{-i\omega t}\ \delta(y)\ \delta(z)\ \Theta\left(\frac{l}{2}-|x|\right) \tag{7.206}$$

for the charge distribution. Here, l denotes the length of the rod which is located at the origin and oriented in x-direction. ρ describes a sinusoidal line charge density in x-direction with length l. The corresponding current density is the derivative of Eq. (7.206). The function $a(\omega)$ comprises the damping and the resonance of the system. Its concrete form would have to be developed.

Next, the current density corresponding to Eq. (7.206) can be entered in Eq. (7.203). The vector potential then reads

$$\begin{aligned}
\lim_{kr\to\infty}\mathbf{A}(\mathbf{r}) &= \frac{-i\omega\mu_0}{4\pi}\,\frac{l}{\pi}\,a(\omega)\,\frac{e^{ikr}}{r}\,\hat{\mathbf{e}}_x\int_{-l/2}^{l/2}\cos\left(\frac{\pi}{l}x'\right)e^{-ik\frac{xx'}{\sqrt{x^2+y^2+z^2}}}\,dx' \\
&= \frac{-i\omega\mu_0}{4\pi}\,\frac{l}{\pi}\,a(\omega)\,\frac{e^{ikr}}{r}\,\hat{\mathbf{e}}_x \\
&\qquad\left[\frac{e^{-ik\frac{xx'}{\sqrt{x^2+y^2+z^2}}}\left(-\frac{\pi}{l}\sin\left(\frac{\pi}{l}x'\right)+i\frac{kx}{\sqrt{x^2+y^2+z^2}}\cos\left(\frac{\pi}{l}x'\right)\right)}{\frac{k^2x^2}{\sqrt{x^2+y^2+z^2}}-\frac{\pi^2}{l^2}}\right]_{-l/2}^{l/2} \\
&= \ldots = \frac{i\omega\mu_0}{4\pi}\,a(\omega)\,\frac{e^{ikr}}{r}\,\frac{\cos\left(\frac{kxl}{2\sqrt{x^2+y^2+z^2}}\right)}{\frac{k^2x^2}{\sqrt{x^2+y^2+z^2}}-\frac{\pi^2}{l^2}}\hat{\mathbf{e}}_x.
\end{aligned} \tag{7.207}$$

The electric field caused by this vector potential is

$$\begin{aligned}
\mathbf{E}(\mathbf{r}) &= ik\sqrt{\frac{1}{\epsilon_0\mu_0}}\,[\mathbf{n}\times\mathbf{A}(\mathbf{r})]\times\mathbf{n} \\
&= ik\sqrt{\frac{1}{\epsilon_0\mu_0}}\left[\frac{1}{r}\begin{pmatrix}x\\y\\z\end{pmatrix}\times\begin{pmatrix}A_x\\0\\0\end{pmatrix}\right]\frac{1}{r}\begin{pmatrix}x\\y\\z\end{pmatrix} = ik\sqrt{\frac{1}{\epsilon_0\mu_0}}\,\frac{1}{r^2}\begin{pmatrix}0\\zA_x\\-yA_x\end{pmatrix}\times\begin{pmatrix}x\\y\\z\end{pmatrix} \\
&= ik\sqrt{\frac{1}{\epsilon_0\mu_0}}\,\frac{1}{r^2}\begin{pmatrix}z^2A_x+y^2A_x\\-xyA_x\\-xzA_x\end{pmatrix}.
\end{aligned} \tag{7.208}$$

We combine Eqs. (7.207) and (7.208), assume an observer at distance r_0 on the z-axis and find

$$\begin{aligned}
\mathbf{E}\,(r_0\hat{\mathbf{e}}_z) &= ik\sqrt{\frac{1}{\epsilon_0\mu_0}}\,\frac{1}{r_0^2}\,r_0^2\,A_x\,\hat{\mathbf{e}}_x \\
&= ik\sqrt{\frac{1}{\epsilon_0\mu_0}}\,\frac{i\omega\mu_0}{4\pi}\,a(\omega)\,\frac{e^{ikr_0}}{r_0}\,\frac{1}{-\frac{\pi^2}{l^2}}\,\hat{\mathbf{e}}_x \\
&= \frac{1}{4\pi\epsilon_0}\,k^2\,\frac{l^2}{\pi^2}\,a(\omega)\,\frac{e^{ikr_0}}{r_0}\,\hat{\mathbf{e}}_x.
\end{aligned} \tag{7.209}$$

Once the field radiated by the charge distribution is acquired in forward direction, we can translate this into a scattering matrix by

$$\begin{pmatrix} \frac{k^2}{4\pi\epsilon_0}\left(\frac{l}{\pi}\right)^2 a(\omega)\,\frac{e^{ikr_0}}{r_0} \\ 0 \end{pmatrix} = \frac{1}{-ikr_0}\begin{pmatrix} S_2 & S_3 \\ S_4 & S_1 \end{pmatrix}\cdot\begin{pmatrix} E_0\, e^{ikr_0-i\omega t} \\ 0 \end{pmatrix}. \tag{7.210}$$

Thus, the scattering matrix' non-zero entry reads

$$S_2 = \frac{-ik^3}{4\pi\epsilon_0}\left(\frac{l}{\pi}\right)^2 a(\omega)\,\frac{1}{E_0 e^{-i\omega t}}. \tag{7.211}$$

The similarity to the previously obtained statements using the dipole and the twin dipole model is evident.

The application of this CCDM is methodically rather similar to the previous approaches. In a certain sense, it is the generalization of the dipole and twin dipole model. Therefore, this approach would be a logical next step to continue the modeling of the metallic systems described in this thesis.

7.10 Summary and outlook

The overall aim of this chapter was to develop a model that can reproduce the physical properties of light transmitted through one or more slabs of periodically arranged, metallic nanostructures. In essence, we accomplished this task for the test structures under investigation.

The modeling started with the review of my Staatsexamensarbeit in Section 7.3. Here, we discussed one of the basic elements of the models: the approach which describes the slab as a large number of randomly distributed, non-interacting particles. Thus, the light transmitted through this slab can be obtained by deducing the scattering matrix of a single scatterer in forward direction. The model applied in Section 7.3 describes one metallic rod as one oscillating dipole centered in the rod. We encountered problems for small layer spacings and found the absence of polarization rotation for two layers of rotated crosses. On the other hand, we showed in Section 7.4 that the model yields very good results and insights for large layer spacings where the layers effectively decouple. In Section 7.5 we could show that the effects of the lattice's periodicity, namely spikes in the transmittance spectrum, can be incorporated in the model.

The absence of a polarization rotation for the double layer of crosses, however, made it necessary to develop a new approach which we called the twin dipole model. In this model, we describe one rod as two oscillators forming a twin dipole. We encountered the projection problem in Section 7.6 which originated from the scattering matrix and the slab formulation. We deduced how this dilemma has to be solved on physical grounds and, thereafter, demonstrated that the twin dipole yields a better performance than the dipole model, see Section 7.7. Especially, the twin dipole model was able to qualitatively reproduce the transmittance spectrum of two layers of mutually rotated crosses and, most important, the polarization state of the transmitted light.

Since the physical description of the coupling between the layers still remains a challenge, we examined a way to incorporate an interlayer coupling based on near-fields of the dipoles in Section 7.8. Also, we used only one scattering matrix instead of two like before. This meant

that we perceived the system of two layers of rods as one layer of double-rods. Although the results cannot yet be considered a breakthrough, they still outline the way to further research by demonstrating the methodology. In fact, we stated several possible ways to continue: we could either use the near-field coupling with two scattering matrices, we could use the double-rod perception without near-fields and, finally, we could omit the phase of the oscillators forming a twin dipole.

Another possible route to an even further improved description of the nanostructures was outlined in Section 7.9. Here, we generalized the dipole approach such that the rod is described by a continuous, sinusoidal line charge distribution. The next step on this route would be to model a suitable polarizability.

Another possible change in the physical description of the system could be that we enter different physical coupling mechanisms. A potential extension of the method would be to include magnetic dipole coupling and electric quadrupole coupling between the oscillators.

Naturally, developing the discussed models further is a complex endeavor. This is true particularly with regard to the different combinations—for example, we could use the continuous charge distribution model either with the effective slab approach or the lattice-periodic formulation. For two-layer systems, we can either incorporate near-fields or not. In the case of the slab formulation we can apply one scattering matrix or two. This large variety of the model's possible realizations is what makes it an interesting challenge, even beyond the successful improvements presented in this thesis.

Chapter 8

Conclusion

In this thesis, we dealt with the description of nano-photonic systems by means of numerical simulations and analytical models. The two major topics were the improvement of coordinate transformations for the Fourier Modal Method (FMM) and the design of dipole models for the description of periodic, metallic metamaterials. In the following, we summarize the results of these efforts and give an outlook on possible future work.

8.1 Summary

After introducing the fundamentals of electrodynamics, the Fourier Modal Method in curvilinear coordinates was discussed. Here, the effective permittivity and permeability, which comprise all effects of the applied coordinate transformations from Cartesian to curvilinear space, were introduced.

In Chapter 4, we examined opal photonic crystals by means of the classical FMM. We compared the numerical data for the bar and cross transmittance with experimental results and found a very good agreement. Deviations between simulation and experiment in the cross transmittance were attributed to stacking faults of the opal. By simulating samples with various numbers of opal layers we exploited the strengths of the FMM's scattering matrix algorithm and gained new physical insight: The change from bar to cross transmittance is a thickness-dependent effect that shows a sinusoidal behavior in dependence of the number of opal layers. Moreover, we showed that the minima in angle-resolved spectra can be predicted by a Bragg model.

The subsequent Chapter 5 dealt with several important aspects of two-dimensional coordinate transformations. First, we diagnosed that the nondifferentiable AC mesh for cylinders which is discussed in literature leads to a diverging effective permittivity. This laid the ground for the creation of smoothed and differentiable transformations that do not feature a grid-aligned effective permittivity but in return show a finite effective permittivity. For all of those types of meshes, i.e., nondifferentiable, smoothed and differentiable, we presented a general construction procedure based on the concept of characteristic points and coordinate lines. Beyond the technical aspects of enforcing periodicity and the treatment of nonrectangular unit cells, we explained the ASR function we use to increase the density along the specific coordinate lines. A very important aspect was the investigation of two test systems, namely a fiber with analytically known eigenmodes and an array of metallic cylinders. While the nondifferentiable mesh showed the overall best results for specific parameter sets, the differentiable mesh showed good results for a wide range of parameters. Using large parameter scans, we could identify sweet spots and a general principle to deduce suitable mesh parameters. According to this principle, the parameters have to be chosen such that numerical and

physical surface of the considered structures coincide. Finally, we formulated a modularity concept which allows for an arrangement of several sub-structures within a structure. Both the general mesh construction principle and the discovery of the sweet spots in the parameter space were previously unknown and close an essential gap in the use of two-dimensional coordinates in the context of the FMM.

With the knowledge of the two-dimensional coordinate transformations at hand, we generalized the approach to three dimensions. We constructed a three-dimensional mesh for two layers of mutually rotated crosses and introduced the concept of three-dimensional characteristic points. Due to the full anisotropic permittivity and permeability tensor we used the large FMM eigenproblem to solve Maxwell's equations. For the first test system, namely empty space, we observed that parts of the system's energy is absorbed. For two layers of mutually rotated, metallic crosses we found a very good convergence behavior but on the other hand faced the fact that TE and TM polarization did not yield the same results as they should due to symmetry. However, we demonstrated for the first time how three-dimensional coordinate transformations can be constructed and used in the FMM. To the best of my knowledge, there are no published efforts that use ASR and AC in three dimensions for the Fourier Modal Method.

Finally, we developed several analytical models to predict the transmission of light through slabs of metallic nanostructures in Chapter 7. First, we reviewed the dipole model, which was able to accurately describe single layer structures and double layer structures with large spacings. Also, we demonstrated the incorporation of lattice resonances into the model. However, the interlayer coupling for small spacings was not fully reproduced. Also, a qualitative difference occurred in the description of two layers of mutually rotated crosses. Here, the numerical data obtained with the FMM showed a polarization rotation while the dipole model did not. Therefore, we introduced the twin dipole model that showed a highly improved performance compared to the dipole model. After discussing the technical detail of the projection, we examined the model's predictions for two layers of mutually rotated crosses and qualitatively found the polarization rotation occurring in the FMM simulation. By discussing the twin dipole model with near-field coupling we aimed at improving the description of strongly coupled layers even further. Although the results were ambiguous, we demonstrated the methodology and discussed the important question of how many scattering matrices are needed. The chapter was concluded by the outline of the twin dipole model's extension to a continuous charge distribution model. In general, we were able to describe the physical properties of the transmitted light qualitatively well. The strengths of the twin dipole model could be exploited by predicting the general behavior upon the rotation of the rods and crosses.

8.2 Outlook

Beyond the work that has been described in this thesis, there are lots of possible projects worth pursuing in the future.

Regarding the generation of coordinate transformations for the Fourier Modal Method, further work on the three-dimensional transformations is necessary. Here, the most important first step is to find a solution to the challenges discovered in Chapter 6, namely the absorption of the system even for an empty lattice. It has to be checked whether this is an intrinsic and systematic error or a mistake in the implementation of either the effective permittivity or the

FMM itself. Once this challenge is coped with, the investigation of the gold helix structures discussed in Chapter 6 is an interesting project, especially with regard to optimization of the setup to gain an optimal polarization rotation. Also, the idea that the adaptive spatial resolution could be gradually introduced (see Section 6.6) should be tested for its influence on the performance. Finally, the generalization towards coordinate transformation of the form of Eq. (2.41) could be performed. A suitable test system is a metallic sphere which would be transformed into a cube. Since analytical solutions for the scattered field are available in Mie theory, this system is ideally suited to test whether the guidelines we formulated for two-dimensional transformations also hold in three dimensions.

In the case of the dipole models I already started to formulate possible future work at the end of Section 7.8.3. Essentially, a first important step is to test combinations of the presented approaches. This means that the predictions for several models could be checked: For example, one scattering matrix for twin dipoles without near-field coupling or two scattering matrices for twin dipoles with near-field coupling could be used. Finally, the continuous charge distribution model could help to further improve the description of two layers of mutually rotated rods. Beyond the presented approaches, different mechanisms of coupling could be incorporated in the models, i.e., magnetic dipole and electric quadrupole moments. A different but promising road is the application of the presented models to more complex single layer structures. Since the description of these structures is very good, an extension to, for example, structures showing electromagnetically induced transparency [81] is a propitious endeavor.

Appendix A

Fourier Transformation

In this part of the thesis, I briefly show the important aspects of Fourier transformations and convolutions which we need to correctly Fourier transform Maxwell's equations. For that, I first review the basics of Fourier transformations needed in this thesis and discuss the issue of how to properly transform products of step functions. Finally, I demonstrate the Fourier transformation of the anisotropic constitutive relations which we utilize in the FMM to formulate Maxwell's equations as an eigenvalue problem.

A.1 Basics of Fourier transformations

Fourier transformations in general are a broad topic, especially in the context of signal processing. Here, we restrict ourselves to the essentials needed to understand the FMM. Since we deal with periodic structures and expand Maxwell's equations into periodic function, we first deal with the one-dimensional Fourier transformation of a periodic function f with spatial period a. It reads

$$f(x) \;=\; \sum_{n=-\infty}^{\infty} \tilde{f}_n e^{i\frac{2\pi}{a}nx} \;\approx\; \sum_{n=-N}^{N} \tilde{f}_n e^{in\frac{2\pi}{a}x}, \tag{A.1}$$

where we already included the fact that a numerical simulation can only contain a finite number of coefficients $\tilde{f}_n$. These coefficients are obtained by

$$\tilde{f}_n = \frac{1}{a} \int_0^a f(x)\; e^{-in\frac{2\pi}{a}x}\; dx. \tag{A.2}$$

Since many quantities in Maxwell's equations are discontinuous somewhere in the unit cell, we have to be aware of the so-called *Gibbs phenomenon*. It refers to the effects occurring when Fourier transforming a step function. An example is depicted in Fig. A.1. Here, a step function (red) is reconstructed using 10 Fourier coefficients in panel (a) and 85 coefficients in panel (b). As we see, strong oscillations near the position of the step occur which cannot be removed by simply increasing the number of harmonics. More harmonics result in oscillations closer to the step, but even for high numbers of harmonics the overshoot of the Fourier series does not drop below 8.9% of the step's height.

While transforming Maxwell's equations one finds that products of functions need to be Fourier transformed which results in so-called *convolutions* in Fourier space. Such convolutions are performed as follows: assume a function $h(x) = f(x) \cdot g(x)$. Then, the coefficients for the Fourier expansion of h can be obtained from the coefficients of f and g by

$$h_n \;=\; \sum_{m=-\infty}^{\infty} f_{n-m}\; g_m \;\approx\; \sum_{m=-N}^{N} f_{n-m}\; g_m. \tag{A.3}$$

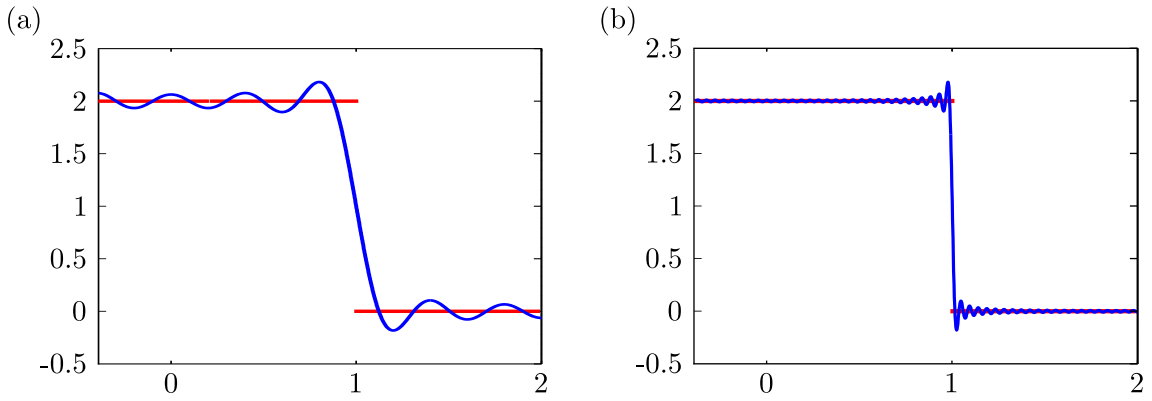

Figure A.1: Visualization of the Gibbs phenomenon. In panel (a) the step function (red) is reconstructed with 10 harmonics, in panel (b) with 85 harmonics. When the number of harmonics is increased, the frequency of the oscillation increases and the points of the maximal error between step function and reconstruction are located closer to the position of the jump. However, even for very high numbers of harmonics, the absolute value of this error does not drop below 8.9 % of the jump height. Only parts of the [-2,2] interval are shown.

Again, the numerical treatment can only contain a finite number of coefficients. Since we use it in the subsequent section, we realize that Eq. (A.3) can be written in terms of a matrix vector product. When we arrange all coefficients h_n and g_m in a row vector $\tilde{\mathbf{h}}$ and $\tilde{\mathbf{g}}$, respectively, we can relate them by

$$\underbrace{\begin{pmatrix} h_{-N} \\ h_{-N+1} \\ h_{-N+2} \\ \vdots \\ h_N \end{pmatrix}}_{=:\,\tilde{\mathbf{h}}} = \underbrace{\begin{pmatrix} f_0 & f_{-1} & f_{-2} & \cdots & f_{-2N} \\ f_1 & f_0 & f_{-1} & \cdots & f_{-2N+1} \\ f_2 & f_1 & f_0 & \cdots & \vdots \\ \vdots & \vdots & \vdots & \ddots & \vdots \\ f_{2N} & f_{2N-1} & f_{2N-2} & \cdots & f_0 \end{pmatrix}}_{=:\,[f]} \cdot \underbrace{\begin{pmatrix} g_{-N} \\ g_{-N+1} \\ g_{-N+2} \\ \vdots \\ g_N \end{pmatrix}}_{=:\,\tilde{\mathbf{g}}}, \tag{A.4}$$

where we arranged the coefficients of f in a so-called *Toeplitz matrix* $[f]$. Unfortunately, convolutions of functions with jumps are difficult to handle with the coefficients defined in Eq. (A.3). Although the finite Fourier sum of h converges to the correct values for large numbers of coefficients, the function is not represented well for small N. An example is depicted in Fig. A.2(a).

Here, we show the reconstruction of the convolution of f and g which exhibit concurrent jump discontinuities. This means that the jumps are pairwise complementary and, thus, the product of f and g is continuous. As we see, the finite representation is of poor quality.

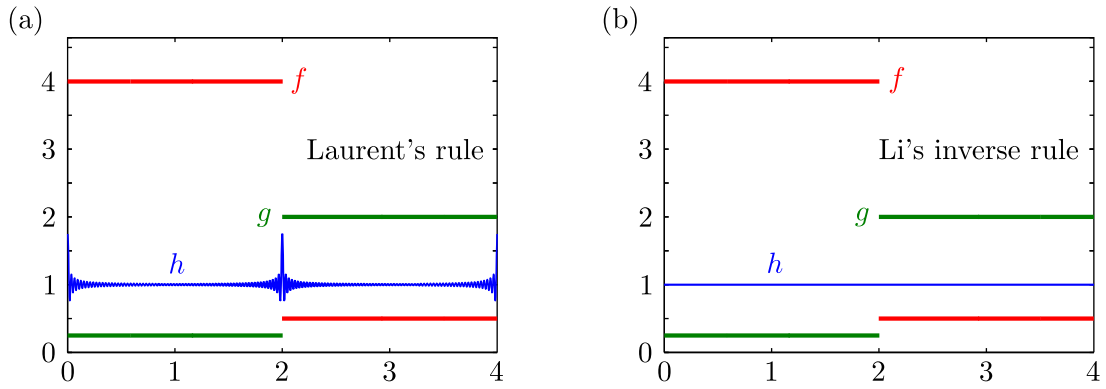

Figure A.2: Visualization of the numerical errors occurring when transforming a product of two functions with concurrent jump discontinuities. Panel (a) displays the results using the coefficients defined in Eq. (A.3). Panel (b) shows the reconstruction using Li's inverse rule, cf. Eq. (A.5) which yields much better results.

A suitable alternative was published by Li in Ref. [82]. He divided the problems into three classes:

- ✧ Type 1: Two piecewise-smooth, bounded, periodic functions *without* concurrent jump discontinuities shall be transformed. Then, the coefficients in Eq. (A.3) apply. We refer to type 1 as *Laurent's rule*.
- ✧ Type 2: Two piecewise smooth, bounded, periodic functions *with* concurrent jump discontinuities shall be transformed. The appropriate coefficients are obtained by

$$\tilde{\mathbf{h}} = \left[\!\left[\frac{1}{f}\right]\!\right]^{-1} \cdot \tilde{\mathbf{g}}. \tag{A.5}$$

  We refer to this way of determining the coefficients of h as *Li's inverse rule*.
- ✧ Type 3: Two piecewise-smooth, bounded, periodic functions that exhibit concurrent jumps which are not complementary. In this case, Li judged both rules as insufficient. Fortunately, the products in Maxwell's equations are of type 1 and 2.

The inverse rule is demonstrated in Fig. A.2(b). Here, the applied coefficients from Eq. (A.5) show a very good representation of h. The strong oscillations that occur for Laurent's rule are not present with Li's rule. Thus, we use this formulation to obtain the coefficients in the case of a convolution of type 2.

In general, a two-dimensional Fourier transformation of a periodic function f with period a_i in direction x^i, $i = 1, 2$, reads

$$f\left(x^1, x^2\right) = \sum_{n,m=-\infty}^{\infty} \tilde{f}_{nm}\, e^{i\left(n\frac{2\pi}{a_1}x^1 + m\frac{2\pi}{a_2}x^2\right)}, \tag{A.6}$$

where the coefficients are in general determined by

$$\tilde{f}_{nm} = \frac{1}{a_1\, a_2} \int_0^{a_1}\int_0^{a_2} f\left(x^1, x^2\right)\, e^{-i\left(n\frac{2\pi}{a_1}x^1 + m\frac{2\pi}{a_2}x^2\right)}\, dx^2\, dx^1. \tag{A.7}$$

However, we cannot use this formulation since the jumps in the permittivity and in the fields demand that type 1 and type 2 transformations are applied, sometimes even in different directions. Thus, we perform the transformation separately first into one and afterwards into the other direction. This is demonstrated in the subsequent section. Naturally, this results in a complicated composition of the matrices containing the coefficients, which then only have block Toeplitz structure. For the explicit form of these matrices we refer to Ref. [33].

Before applying the described transformation rules to the constitutive relations of Maxwell's equations, a few practical details should be mentioned. In our implementation of the FMM, we use the Fast Fourier Transform, a very efficient algorithm to determine the Fourier coefficients. Since it is most effective for a power of two, we normally use $1024 = 2^{10}$ coefficients in each direction for the transformation. This high number of coefficients also ensures that the aliasing effect is kept at a minimal level. To ensure a sufficient representation, we normally apply at least a fivefold oversampling. The numerical tools for the Fourier transformation used in the code are the FFTW library [83] (Fastest Fourier Transform in the West) and the MKL library [42] on Intel machines.

A.2 Fourier transformation of the anisotropic constitutive relations

In the FMM, Maxwell's equations are transformed into Fourier space and solved there. Due to the jumps in the permittivity and in the fields at material boundaries, this transformation is a delicate procedure as we have shown in the preceding section. This is particularly true for the constitutive relations. In this section, we demonstrate how the constitutive relation

$$D^\rho = \varepsilon^{\rho\sigma} E_\sigma \tag{A.8}$$

is transformed. The relation for the permeability is transformed analogously. We follow Refs. [12, 34, 33] for the presentation and do not discuss the procedure for every component of the fields. Instead, we demonstrate it for one component and state the result for the others.

We first perform the Fourier transformation along x^1. According to the continuity conditions of Maxwell's equations, the fields D^1, E_2 and E_3 are continuous functions of x^1, except for sharp material corners where D^1 and E_2 become singular. Since the number of those points is assumed to be small, we ignore them throughout the transformation. Before we perform the Fourier transformation, we reorganize Eq. (A.8) such that it reads

$$D^1 = \varepsilon^{11}\left(E_1 + \frac{\varepsilon^{12}}{\varepsilon^{11}}E_2 + \frac{\varepsilon^{13}}{\varepsilon^{11}}E_3\right), \tag{A.9}$$

$$D^2 = \frac{\varepsilon^{21}}{\varepsilon^{11}}D^1 + \left(\varepsilon^{22} - \frac{\varepsilon^{21}\varepsilon^{12}}{\varepsilon^{11}}\right)E_2 + \left(\varepsilon^{23} - \frac{\varepsilon^{21}\varepsilon^{13}}{\varepsilon^{11}}\right)E_3, \tag{A.10}$$

$$D^3 = \frac{\varepsilon^{31}}{\varepsilon^{11}}D^1 + \left(\varepsilon^{32} - \frac{\varepsilon^{31}\varepsilon^{12}}{\varepsilon^{11}}\right)E_2 + \left(\varepsilon^{33} - \frac{\varepsilon^{31}\varepsilon^{13}}{\varepsilon^{11}}\right)E_3. \tag{A.11}$$

All products occurring here are of type 1 or type 2, see Section A.1. Therefore, we can

perform the transformation in x^1 direction and obtain

$$\left[D^1\right]_1 = \left[\frac{1}{\varepsilon^{11}}\right]_1^{-1}\left([E_1]_1 + \left[\frac{\varepsilon^{12}}{\varepsilon^{11}}\right]_1 [E_2]_1 + \left[\frac{\varepsilon^{13}}{\varepsilon^{11}}\right]_1 [E_3]_1\right), \tag{A.12}$$

$$\left[D^2\right]_1 = \left[\frac{\varepsilon^{21}}{\varepsilon^{11}}\right]_1 \left[D^1\right]_1 + \left[\varepsilon^{22} - \frac{\varepsilon^{21}\varepsilon^{12}}{\varepsilon^{11}}\right]_1 [E_2]_1 + \left[\varepsilon^{23} - \frac{\varepsilon^{21}\varepsilon^{13}}{\varepsilon^{11}}\right]_1 [E_3]_1, \tag{A.13}$$

$$\left[D^3\right]_1 = \left[\frac{\varepsilon^{31}}{\varepsilon^{11}}\right]_1 \left[D^1\right]_1 + \left[\varepsilon^{32} - \frac{\varepsilon^{31}\varepsilon^{12}}{\varepsilon^{11}}\right]_1 [E_2]_1 + \left[\varepsilon^{33} - \frac{\varepsilon^{31}\varepsilon^{13}}{\varepsilon^{11}}\right]_1 [E_3]_1. \tag{A.14}$$

The lower case '1' is a reminder of the direction of transformation. In order to simplify the nomenclature, we define the quantities

$$Q_1^{11} = \left[\frac{1}{\varepsilon^{11}}\right]_1^{-1}, \tag{A.15a}$$

$$Q_1^{12} = \left[\frac{1}{\varepsilon^{11}}\right]_1^{-1}\left[\frac{\varepsilon^{12}}{\varepsilon^{11}}\right]_1, \tag{A.15b}$$

$$Q_1^{13} = \left[\frac{1}{\varepsilon^{11}}\right]_1^{-1}\left[\frac{\varepsilon^{13}}{\varepsilon^{11}}\right]_1, \tag{A.15c}$$

$$Q_1^{21} = \left[\frac{\varepsilon^{21}}{\varepsilon^{11}}\right]_1\left[\frac{1}{\varepsilon^{11}}\right]_1^{-1}, \tag{A.15d}$$

$$Q_1^{22} = \left[\frac{\varepsilon^{21}}{\varepsilon^{11}}\right]_1\left[\frac{1}{\varepsilon^{11}}\right]_1^{-1}\left[\frac{\varepsilon^{12}}{\varepsilon^{11}}\right]_1 + \left[\frac{\varepsilon^{11}\varepsilon^{22} - \varepsilon^{21}\varepsilon^{12}}{\varepsilon^{11}}\right]_1, \tag{A.15e}$$

$$Q_1^{23} = \left[\frac{\varepsilon^{21}}{\varepsilon^{11}}\right]_1\left[\frac{1}{\varepsilon^{11}}\right]_1^{-1}\left[\frac{\varepsilon^{13}}{\varepsilon^{11}}\right]_1 + \left[\frac{\varepsilon^{11}\varepsilon^{23} - \varepsilon^{21}\varepsilon^{13}}{\varepsilon^{11}}\right]_1, \tag{A.15f}$$

$$Q_1^{31} = \left[\frac{\varepsilon^{31}}{\varepsilon^{11}}\right]_1\left[\frac{1}{\varepsilon^{11}}\right]_1^{-1}, \tag{A.15g}$$

$$Q_1^{32} = \left[\frac{\varepsilon^{31}}{\varepsilon^{11}}\right]_1\left[\frac{1}{\varepsilon^{11}}\right]_1^{-1}\left[\frac{\varepsilon^{12}}{\varepsilon^{11}}\right]_1 + \left[\frac{\varepsilon^{11}\varepsilon^{32} - \varepsilon^{31}\varepsilon^{12}}{\varepsilon^{11}}\right]_1, \tag{A.15h}$$

$$Q_1^{33} = \left[\frac{\varepsilon^{31}}{\varepsilon^{11}}\right]_1\left[\frac{1}{\varepsilon^{11}}\right]_1^{-1}\left[\frac{\varepsilon^{13}}{\varepsilon^{11}}\right]_1 + \left[\frac{\varepsilon^{11}\varepsilon^{33} - \varepsilon^{31}\varepsilon^{13}}{\varepsilon^{11}}\right]_1, \tag{A.15i}$$

which enable use to write the partially transformed constitutive relation as

$$\left[D^i\right]_1 = Q_1^{ij}\,[E_j]_1\,. \tag{A.16}$$

As an example how to proceed, we investigate

$$\left[D^2\right]_1 = Q_1^{21}\,[E_1]_1 + Q_1^{22}\,[E_2]_1 + Q_1^{23}\,[E_3]_1\,. \tag{A.17}$$

The boundary conditions demand that D^2 and E_1 as functions of x^1 and x^2 are continuous almost everywhere with respect to x^2 and that E_3 is continuous everywhere. The question is whether this is still the case after partially transforming the functions in one direction. As shown in the appendix of Ref. [12], this is true. Therefore, we can Fourier transform

Eq. (A.17) in x^2-direction with the rules of type 1 and 2. The transformation reads

$$\begin{aligned}
[E_2]_1 &= \left(Q_1^{22}\right)^{-1}\left[D^2\right]_1 - \left(Q_1^{22}\right)^{-1} Q_1^{21}\,[E_1]_1 - \left(Q_1^{22}\right)^{-1} Q_1^{23}\,[E_3]_1 \qquad \text{(A.18)}\\
\Rightarrow [E_2]_{12} &= \left[\left(Q_1^{22}\right)^{-1}\right]_2 \left[D^2\right]_{12} - \left[\left(Q_1^{22}\right)^{-1} Q_1^{21}\right]_2 [E_1]_{12} - \left[\left(Q_1^{22}\right)^{-1} Q_1^{23}\right]_2 [E_3]_{12}\\
\Rightarrow \left[D^2\right]_{12} &= \left[\left(Q_1^{22}\right)^{-1}\right]_2^{-1} \left(\left[\left(Q_1^{22}\right)^{-1} Q_1^{21}\right]_2 [E_1]_{12} + [E_2]_{12} + \left[\left(Q_1^{22}\right)^{-1} Q_1^{23}\right]_2 [E_3]_{12}\right).
\end{aligned}$$

The lower case '2' indicates the transformation in x^2 direction. The procedure for the other components is analogously: the terms are rearranged such that D^2, E_1 and E_3 are on one side and then the equation is transformed. With the coefficient vectors of the fields, we can then relate the coefficients by

$$\tilde{\mathbf{D}}^i = \left[\!\left[\varepsilon^{ij}\right]\!\right]_{12} \tilde{\mathbf{E}}_i, \qquad \text{(A.19)}$$

where we introduce the abbreviations

$$\begin{aligned}
\left[\!\left[\varepsilon^{11}\right]\!\right]_{12} &= \left[Q_1^{11} - Q_1^{12}\left(Q_1^{22}\right)^{-1} Q_1^{21}\right]_2 + \left[Q_1^{12}\left(Q_1^{22}\right)^{-1}\right]_2 \left[\left(Q_1^{22}\right)^{-1}\right]_2^{-1} \left[\left(Q_1^{22}\right)^{-1} Q_1^{21}\right]_2,\\
\left[\!\left[\varepsilon^{12}\right]\!\right]_{12} &= \left[Q_1^{12}\left(Q_1^{22}\right)^{-1}\right]_2 \left[\left(Q_1^{22}\right)^{-1}\right]_2^{-1},\\
\left[\!\left[\varepsilon^{13}\right]\!\right]_{12} &= \left[Q_1^{13} - Q_1^{12}\left(Q_1^{22}\right)^{-1} Q_1^{23}\right]_2 + \left[Q_1^{12}\left(Q_1^{22}\right)^{-1}\right]_2 \left[\left(Q_1^{22}\right)^{-1}\right]_2^{-1} \left[\left(Q_1^{22}\right)^{-1} Q_1^{23}\right]_2,\\
\left[\!\left[\varepsilon^{21}\right]\!\right]_{12} &= \left[\left(Q_1^{22}\right)^{-1}\right]_2^{-1} \left[\left(Q_1^{22}\right)^{-1} Q_1^{21}\right]_2,\\
\left[\!\left[\varepsilon^{22}\right]\!\right]_{12} &= \left[\left(Q_1^{22}\right)^{-1}\right]_2^{-1},\\
\left[\!\left[\varepsilon^{23}\right]\!\right]_{12} &= \left[\left(Q_1^{22}\right)^{-1}\right]_2^{-1} \left[\left(Q_1^{22}\right)^{-1} Q_1^{23}\right]_2,\\
\left[\!\left[\varepsilon^{31}\right]\!\right]_{12} &= \left[Q_1^{31} - Q_1^{32}\left(Q_1^{22}\right)^{-1} Q_1^{21}\right]_2 + \left[Q_1^{32}\left(Q_1^{22}\right)^{-1}\right]_2 \left[\left(Q_1^{22}\right)^{-1}\right]_2^{-1} \left[\left(Q_1^{22}\right)^{-1} Q_1^{21}\right]_2,\\
\left[\!\left[\varepsilon^{32}\right]\!\right]_{12} &= \left[Q_1^{32}\left(Q_1^{22}\right)^{-1}\right]_2 \left[\left(Q_1^{22}\right)^{-1}\right]_2^{-1},\\
\left[\!\left[\varepsilon^{33}\right]\!\right]_{12} &= \left[Q_1^{33} - Q_1^{32}\left(Q_1^{22}\right)^{-1} Q_1^{23}\right]_2 + \left[Q_1^{32}\left(Q_1^{22}\right)^{-1}\right]_2 \left[\left(Q_1^{22}\right)^{-1}\right]_2^{-1} \left[\left(Q_1^{22}\right)^{-1} Q_1^{23}\right]_2.
\end{aligned}$$

In Ref. [12], Li introduced certain operators to reduce the complexity of the notation. First, the operators $l_i^{\pm}$ are introduced. They act on 3×3 matrices like

$$l_k^{\pm}\left(A^{ij}\right) = \begin{cases} \left(A^{kk}\right)^{-1}, & k = i = j \\ \left(A^{kk}\right)^{-1} A^{kj}, & i = k,\ k \neq j \\ A^{ik}\left(A^{kk}\right)^{-1}, & k = j,\ k \neq i \\ A^{ij} \pm A^{ik}\left(A^{kk}\right)^{-1} A^{kj}, & i \neq k \neq j \end{cases} \qquad \text{(A.20)}$$

which implies that $l_i^- l_i^+(A) = A = l_i^+ l_i^-(A)$. Next, F_i is defined for a matrix $B(x^1, x^2, x^3)$ such that $F_i(B)$ is a block matrix whose elements are Toeplitz matrices generated by the coefficients of B with respect to variable x^i. In total, these operators allow to write the matrices Q_1^{ij} in Eq. (A.15) as

$$Q_1 = l_1^+ F_1 l_1^-(\varepsilon) =: L_1(\varepsilon). \qquad \text{(A.21)}$$

The corresponding operator in x^2 direction can then be used to obtain a representation of the matrices $[\![\varepsilon^{ij}]\!]_{12}$ which reads

$$[\varepsilon]_{12} = L_2 L_1(\varepsilon). \tag{A.22}$$

So far, we did not address the issue why we first Fourier transformed in x^1 direction. Naturally, a first transformation in x^2 direction is equally well applicable. This would yield the result

$$[\varepsilon]_{21} = L_1 L_2(\varepsilon). \tag{A.23}$$

Unfortunately, the expressions in Eqs. (A.22) and (A.23) are not equal for a finite number of coefficients. Therefore, the example of a structure which is symmetric in x^1 and x^2 reveals that simply choosing one of them is not an option. Thus, we use a symmetrized form which reads

$$[\![\varepsilon]\!] = \frac{1}{2}\left([\varepsilon]_{12} + [\varepsilon]_{21}\right). \tag{A.24}$$

The downside of this choice is that energy conservation problems appear [12]. However, they vanish for a sufficiently large number of plane waves.

Appendix B

Numerical transmittance data of opal photonic crystals

In this appendix, transmittance spectra for opal photonic crystals are presented, some of which were already discussed in Chapter 4. Here, the plots are shown with a linear pseudo-color scale. For further details on the geometry see Section 4.3.

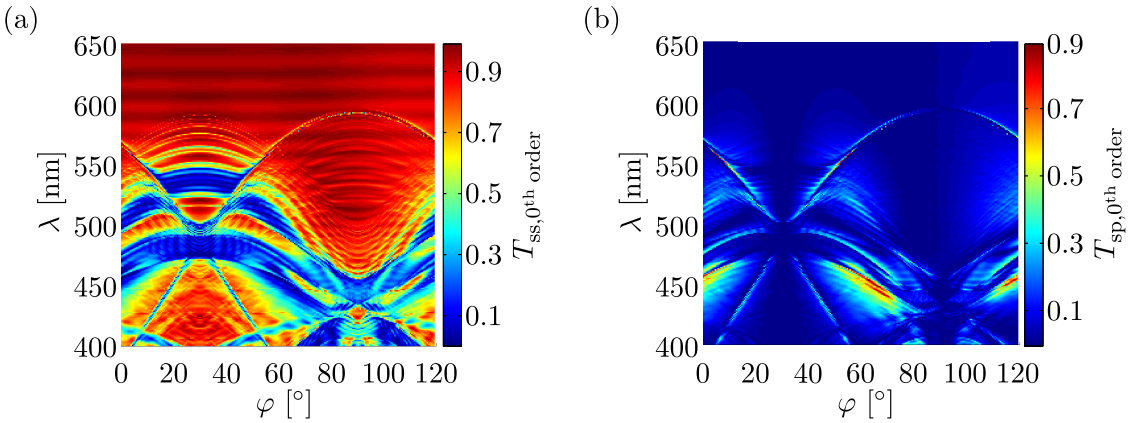

Figure B.1: Transmittance into zeroth order for $\theta = 30°$ and incoming s-polarization. Panel (a) displays the s-polarized part of the zeroth order and panel (b) the p-polarized part.

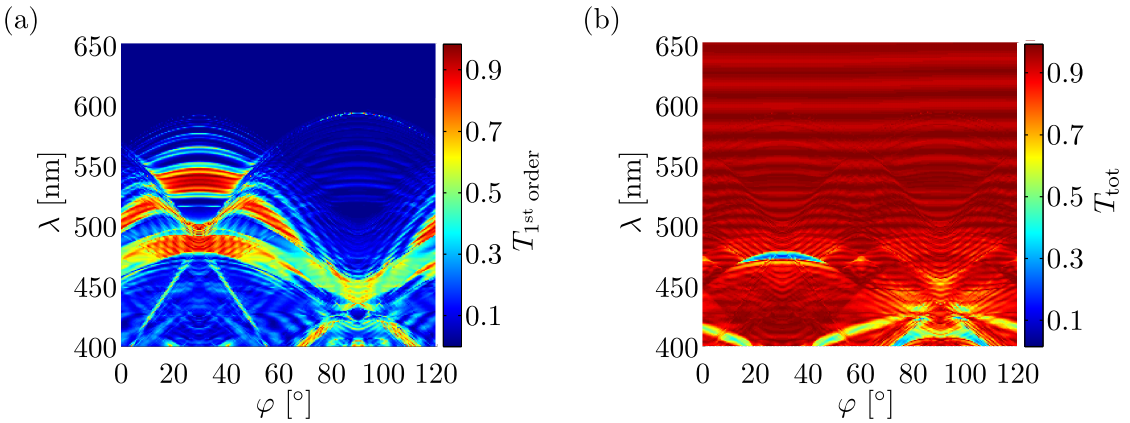

Figure B.2: Transmittance into first order and the total transmittance for $\theta = 30°$ and incoming s-polarization. Panel (a) displays the first order transmittance into all polarizations and panel (b) depicts the total transmittance.

The first order transmittance shows maxima at certain points where the zeroth order exhibits minima, cf. Figs. B.1(a) and B.2(a) at $\lambda = 480$ nm and $\lambda = 540$ nm at $\varphi = 40°$. When they are added to form the total transmittance, they nearly cancel each other such that the total transmittance shows 6-fold symmetry above 500 nm.

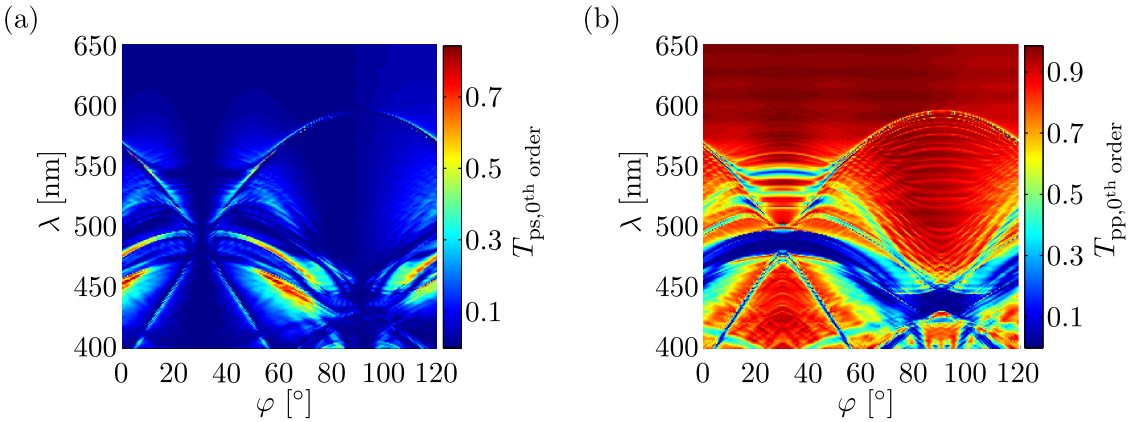

Figure B.3: Transmittance into zeroth order for $\theta = 30°$ and incoming p-polarization. Panel (a) displays the s-polarized part of the zeroth order and panel (b) the p-polarized part.

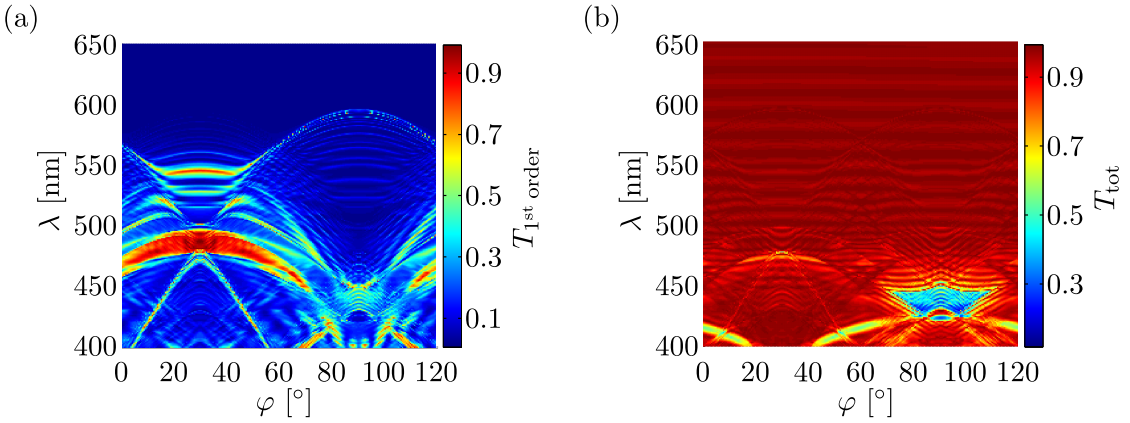

Figure B.4: Transmittance into first order and the total transmittance for $\theta = 30°$ and incoming p-polarization. Panel (a) displays the first order transmittance into all polarizations and panel (b) depicts the total transmittance.

A similar behavior is observed for incident p-polarized light. Again, a minimum in the zeroth order (see Fig. B.3(b)) is at the same place as a maximum in the first order (see Fig. B.4(a)). This again leads to an effective six-fold symmetry above 500 nm in the total transmittance depicted in Fig. B.4(b).

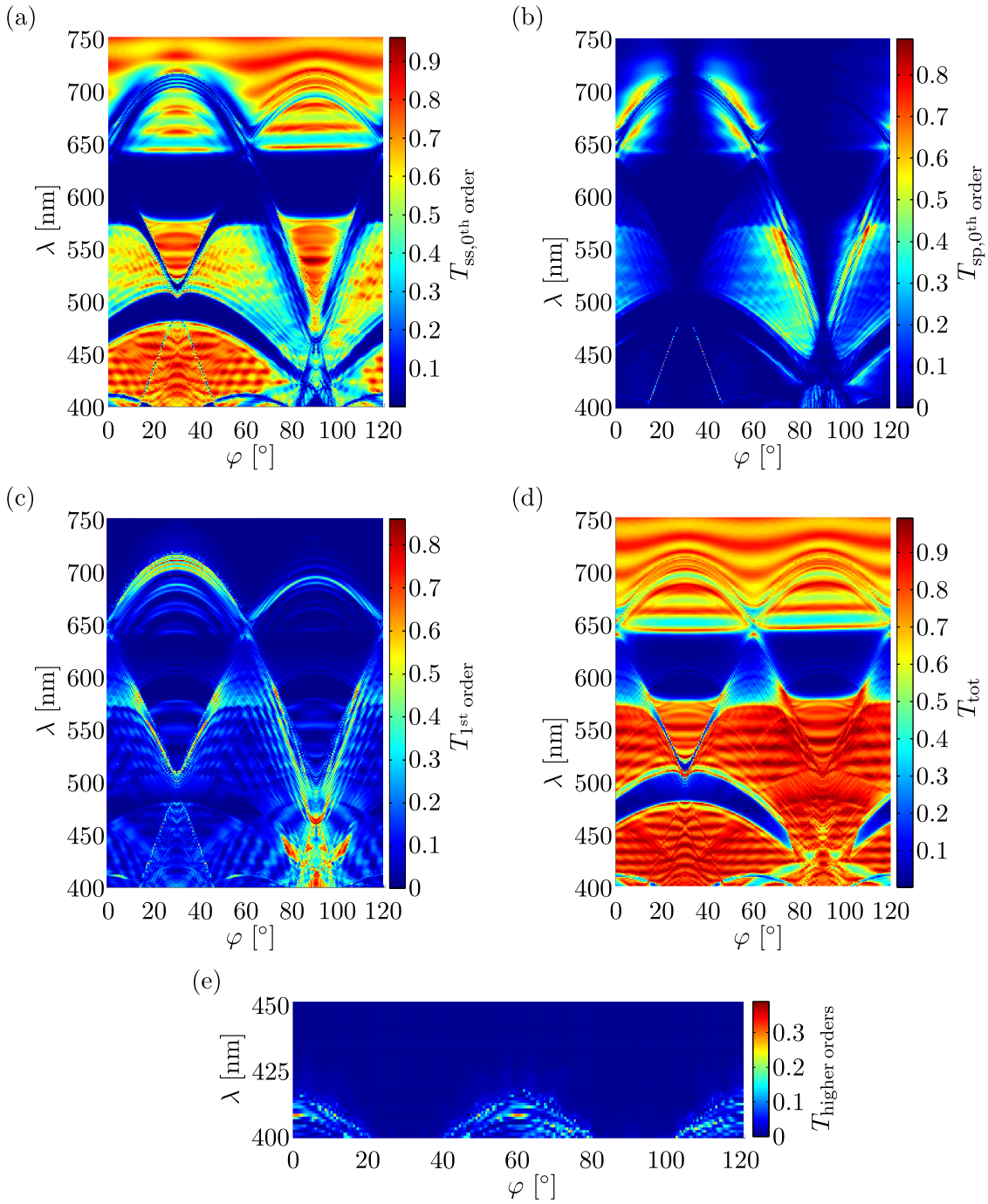

Figure B.5: Transmittance for $\theta = 65°$ and incoming s-polarization. Panel (a) displays the s-polarized part of the zeroth order and panel (b) the p-polarized part. Furthermore, the transmittance in first (panel (c)) and second order (panel (e)) are shown. They all add up to the total transmittance depicted in panel (d).

For light incident with an angle of $\theta = 65°$ (see Figs. B.5 and B.6), light is diffracted into not only the zeroth and first but also in the second order. However, this is only so for high frequencies, see Figs. B.5(e) and B.6(e). For higher wavelengths, there is only diffraction into zeroth and first order. Again, zeroth and first order add up such that an effective six-fold symmetry is observed above 600 nm in the total transmittance for incident s-polarized light.

With incident light in p-polarization, the effective six-fold symmetry is found for wavelengths higher than 650 nm.

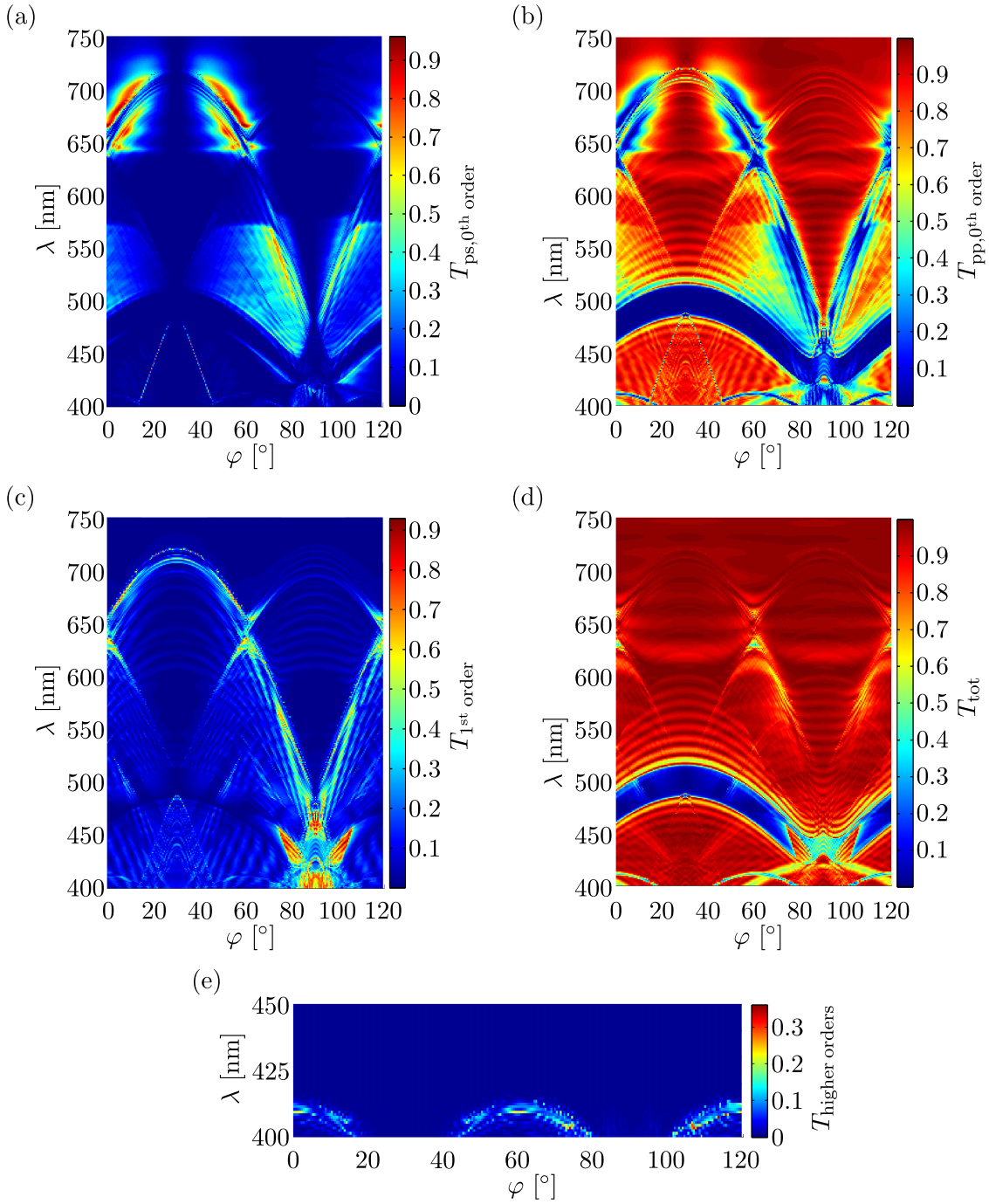

Figure B.6: Transmittance for $\theta = 65°$ and incoming p-polarization. Panel (a) displays the s-polarized part of the zeroth order and panel (b) the p-polarized part. Also, the transmittance in first order (panel (c)) and in the second order (panel (e)) are shown. They all add up to the total transmittance depicted in panel (d).

Appendix C

Derivation of the reflection coefficient for an array of periodic particles

In Section 7.5 we discussed the scattering of light by periodic arrays of particles. Specifically, we deduced a transmission coefficient for such an array in Section 7.5.1. It is denoted by $\tilde{t}$ in Eq. (7.99). For our test system, however, we used the reflection coefficient given by Eq. (7.100). The derivation of this equation is the topic of this part of the appendix[1]. I present the whole derivation here because only few information is given in Ref. [78].

We recall Eq. (7.99)

$$\mathbf{E}_{\text{total}}^{\text{trans}} = \underbrace{\left(1 + \frac{2\pi i k}{A} \frac{1}{\frac{1}{\alpha_E} - G_{xx}(0)}\right)}_{=:\tilde{t}} \mathbf{E}^{\text{ext}}. \tag{C.1}$$

This result was achieved with the assumptions that we use normal incidence (i.e., $\mathbf{k}_{\parallel} = 0$), a specular symmetry with respect to the xz-plane and that we only investigate the 0^{th} order transmitted field. We obtain the reflection coefficient $\tilde{r}$ by

$$\tilde{r} = \tilde{t} - 1 = \frac{2\pi i k}{A} \frac{1}{\frac{1}{\alpha_E} - G_{xx}(0)}. \tag{C.2}$$

Then, the absorbance of the array is found to be $1 - |1 + r|^2 - |r|^2$.

The aim is to derive Eq. (7.100) which we use in Section 7.5.2 from Eq. (C.2). We start by

[1] The definitions made in Section 7.5.1 remain valid.

reformulating the term $G_{xx}(0)$ that was defined in Eq. (7.88):

$$
\begin{aligned}
G_{xx}(0) &= \sum_{n\neq 0} \mathcal{G}^0_{xx}(\mathbf{R}_n)\; e^{-i\,0\mathbf{R}_n} && \text{(C.3)}\\
&= \sum_{n\neq 0} \frac{i}{2\pi} \int \frac{d^2\mathbf{Q}}{\sqrt{k^2-Q^2}} \left(k^2-Q_x^2\right)\; e^{i(\mathbf{Q}\mathbf{R}_n+\sqrt{k^2-Q^2}|z|)} && \text{(C.4)}\\
&\overset{(7.96)}{=} \lim_{z\to 0} \frac{2\pi i}{A} \int \frac{d^2\mathbf{Q}}{\sqrt{k^2-Q^2}} \left(k^2-Q_x^2\right) \sum_{\mathbf{g}} \delta(\mathbf{Q}-\mathbf{g})\; e^{i\sqrt{k^2-Q^2}|z|}\\
&\qquad - \lim_{z\to 0} \left(\frac{i}{2\pi} \int \frac{d^2\mathbf{Q}}{\sqrt{k^2-Q^2}} \left(k^2-Q_x^2\right)\; e^{i(\mathbf{Q}\mathbf{R}_n+\sqrt{k^2-Q^2}|z|)} \right)_{n=0} && \text{(C.5)}\\
&\overset{\mathbf{R}_0=0}{=} \lim_{z\to 0} \frac{2\pi i}{A} \int \frac{dQ_x\, dQ_y}{\sqrt{k^2-Q_x^2-Q_y^2}} \left(k^2-Q_x^2\right) \sum_{\mathbf{g}} \delta(Q_x-g_x)\delta(Q_y-g_y)\cdot\\
&\qquad e^{i\sqrt{k^2-Q_x^2-Q_y^2}|z|} - \lim_{z\to 0} \frac{i}{2\pi} \int \frac{d^2\mathbf{Q}}{\sqrt{k^2-Q^2}} \left(k^2-Q_x^2\right)\; e^{i\sqrt{k^2-Q^2}|z|)} && \text{(C.6)}\\
&= \lim_{z\to 0} \left(\frac{2\pi i}{A} \sum_{\mathbf{g}} \frac{1}{\sqrt{k^2-g^2}} \left(k^2-g_x^2\right)\; e^{i\sqrt{k^2-g^2}|z|} \right.\\
&\qquad \left. - \frac{i}{2\pi} \int \frac{d^2\mathbf{Q}}{\sqrt{k^2-Q^2}} \left(k^2-Q_x^2\right)\; e^{i\sqrt{k^2-Q^2}|z|)} \right). && \text{(C.7)}
\end{aligned}
$$

To get from Eq. (C.4) to Eq. (C.5) we first enter Eq. (7.96). Secondly, we realize that the summation in Eq. (C.4) does not include $n = 0$. So in order to be able to utilize Eq. (7.96) which sums over all elements including $n = 0$, we have to subtract the term for $n = 0$ after applying Eq. (7.96). This is the second term in Eq. (C.5).

Our aim is to obtain an analytic expression for the imaginary part of Eq. (C.7). For that, we first investigate the integral expression in Eq. (C.7) by introducing cylinder coordinates $Q_x = r\cos\phi$ and $Q_y = r\sin\phi$. It reads

$$
\begin{aligned}
&\int\int \frac{k^2-Q_x^2}{\sqrt{k^2-Q_x^2-Q_y^2}}\; e^{i\sqrt{k^2-Q_x^2-Q_y^2}|z|}\; dQ_x\; dQ_y\\
&= \int_0^\infty \int_0^{2\pi} \frac{k^2-r^2\cos^2\varphi}{\sqrt{k^2-r^2}}\; e^{i\sqrt{k^2-r^2}|z|}\; r\; d\varphi\; dr\\
&= \int_0^\infty \int_0^{2\pi} \frac{k^2\, e^{i\sqrt{k^2-r^2}|z|}}{\sqrt{k^2-r^2}}\; r\; d\varphi\; dr \;-\; \int_0^\infty \int_0^{2\pi} \frac{r^3\, e^{i\sqrt{k^2-r^2}|z|}}{\sqrt{k^2-r^2}}\; \cos^2\varphi\; d\varphi\; dr\\
&= 2\pi\, k^2 \int_0^\infty \frac{r\, e^{i\sqrt{k^2-r^2}|z|}}{\sqrt{k^2-r^2}}\; dr - \int_0^\infty \frac{r^3\, e^{i\sqrt{k^2-r^2}|z|}}{\sqrt{k^2-r^2}} \left[\frac{1}{2}\varphi + \frac{1}{4}\sin(2\varphi)\right]_0^{2\pi} dr\\
&= 2\pi\, k^2 \left[-\frac{1}{i|z|}\; e^{i\sqrt{k^2-r^2}|z|}\right]_0^\infty - \pi \left[\frac{2|z|\sqrt{k^2-r^2}+i\, r^2|z|^2+2i}{|z|^3}\; e^{i\sqrt{k^2-r^2}|z|}\right]_0^\infty\\
&= \frac{e^{ik|z|}}{|z|} \left(-2\pi\, k^2 i + \frac{2\pi\, k}{|z|} + \frac{2\pi i}{|z|^2}\right). && \text{(C.8)}
\end{aligned}
$$

The expression in Eq. (C.8) can be split in real and imaginary part:

$$
\begin{aligned}
&-\frac{i}{2\pi}\int\frac{d^2\mathbf{Q}}{\sqrt{k^2-Q^2}}\left(k^2-Q_x^2\right)\,e^{i\sqrt{k^2-Q^2}|z|)} \quad \overset{(C.8)}{=} \quad \frac{e^{ik|z|}}{|z|}\left(-k^2-\frac{i\,k}{|z|}+\frac{1}{|z|^2}\right)\\
&=\left(-\frac{\cos(k|z|)}{|z|^3}\,k^2|z|^2+\frac{\cos(k|z|)}{|z|^3}+\frac{\sin(k|z|)}{|z|^3}\,k|z|\right)\\
&\qquad\qquad +i\,\left(-\frac{\sin(k|z|)}{|z|^3}\,k^2|z|^2+\frac{\sin(k|z|)}{|z|^3}-\frac{\cos(k|z|)}{|z|^3}\,k|z|\right). \qquad \text{(C.9)}
\end{aligned}
$$

Applying l'Hôspital's rule several times, the limit value for $z\to 0$ of the imaginary part becomes

$$
\begin{aligned}
&\lim_{z\to 0}\left(-\frac{\sin(k|z|)}{|z|^3}\,k^2|z|^2+\frac{\sin(k|z|)}{|z|^3}-\frac{\cos(k|z|)}{|z|^3}\,k|z|\right)\\
=\;&\lim_{z\to 0}\frac{\sin(k|z|)\,k^2|z|^2-\sin(k|z|)+\cos(k|z|)\,k|z|}{|z|^3} \quad \overset{\text{l'H}}{=}\ldots \quad \overset{\text{l'H}}{=}\ldots\\
\overset{\text{l'H}}{=}\;&\lim_{z\to 0}\frac{1}{6}\,\Big(\cos(kz)k^5z^2+\sin(kz)k^4 2z+4\sin(kz)k^4z\\
&\qquad -4\cos(kz)k^3-\cos(kz)k^3-\sin(kz)k^4z+\cos(kz)k^3\Big) \;=\; -\frac{2}{3}\,k^3. \qquad \text{(C.10)}
\end{aligned}
$$

Up to this point, we arrived at an expression for the imaginary part of the second term in Eq. (C.7). Next, we achieve the same for the first term. For that, we recall that the wavelength of the incident light in our test system in Section 7.5.2 is larger than the lattice constant. This means that $|\mathbf{g}|>k$ and that all diffraction orders other than the 0^{th} order are evanescent. Then we deduce

$$
\begin{aligned}
&\frac{2\pi i}{A}\sum_{\mathbf{g}}\frac{1}{\sqrt{k^2-g^2}}\,(k^2-g_x^2)\,e^{i\sqrt{k^2-g^2}|z|}\\
&\qquad = \frac{2\pi i}{A}\,k\,e^{ik|z|}+\underbrace{\frac{2\pi i}{A}\sum_{\mathbf{g}\neq 0}\underbrace{\underbrace{\frac{1}{\sqrt{k^2-g^2}}}_{\in i\cdot\mathbb{R}}\,(k^2-g_x^2)\,\underbrace{e^{i\overbrace{\sqrt{k^2-g^2}}^{\in i\cdot\mathbb{R}}|z|}}_{\in\mathbb{R}}}_{\in i\cdot\mathbb{R}}}_{\in\mathbb{R}}. \qquad \text{(C.11)}
\end{aligned}
$$

This means that only the first part of the expression is complex while the rest of the sum is purely real. The limit value of the imaginary part is then given by

$$
\lim_{z\to 0}\frac{2\pi k}{A}\,\cos(k|z|)=\frac{2\pi k}{A}. \qquad \text{(C.12)}
$$

To sum up our findings we reformulate Eq. (C.7):

$$\begin{aligned} G_{xx}(0) &= \lim_{z\to 0}\left(\frac{2\pi i}{A}\sum_{\mathbf{g}}\frac{1}{\sqrt{k^2-g^2}}\,(k^2-g_x^2)\,e^{i\sqrt{k^2-g^2}|z|}\right. \\ &\qquad \left. -\frac{i}{2\pi}\int\frac{d^2\mathbf{Q}}{\sqrt{k^2-Q^2}}\,\left(k^2-Q_x^2\right)\,e^{i\sqrt{k^2-Q^2}|z|)}\right) \\ &= \lim_{z\to 0}\left[i\,\frac{2\pi}{A}\,k\,\cos(k|z|)-\frac{2\pi}{A}\,k\sin(k|z|)\,\frac{2\pi i}{A}\sum_{\mathbf{g}\neq 0}\frac{(k^2-g_x^2)}{\sqrt{k^2-g^2}}\,e^{i\sqrt{k^2-g^2}|z|}\right. \\ &\qquad +\left(-\frac{\cos(k|z|)}{|z|^3}\,k^2|z|^2+\frac{\cos(k|z|)}{|z|^3}+\frac{\sin(k|z|)}{|z|^3}\,k|z|\right) \\ &\qquad \left.+\,i\,\left(-\frac{\sin(k|z|)}{|z|^3}\,k^2|z|^2+\frac{\sin(k|z|)}{|z|^3}-\frac{\cos(k|z|)}{|z|^3}\,k|z|\right)\right]. \end{aligned} \tag{C.13}$$

The imaginary part of $G_{xx}(0)$ is given by the limit value of two terms. Since we know that both terms converge and that the limit value of each of the two terms exists we can deduce that the limit value of their sum also exists. Then, the total limit value of the imaginary part is given by the sum of the limit values of the two terms. This reads

$$\begin{aligned} \mathrm{Im}\,(G_{xx}(0)) &\overset{(C.13)}{=} \lim_{z\to 0}\left[\frac{2\pi}{A}\,k\,\cos(k|z|)\right. \\ &\qquad \left.+\left(-\frac{\sin(k|z|)}{|z|^3}\,k^2|z|^2+\frac{\sin(k|z|)}{|z|^3}-\frac{\cos(k|z|)}{|z|^3}\,k|z|\right)\right] \\ &\overset{(C.12),(C.10)}{=} \lim_{z\to 0}\left[\frac{2\pi}{A}\,k\,\cos(k|z|)\right] \\ &\qquad +\lim_{z\to 0}\left[\left(-\frac{\sin(k|z|)}{|z|^3}\,k^2|z|^2+\frac{\sin(k|z|)}{|z|^3}-\frac{\cos(k|z|)}{|z|^3}\,k|z|\right)\right] \\ &\overset{(C.12),(C.10)}{=} \frac{2\pi}{A}\,k-\frac{2}{3}\,k^3. \end{aligned} \tag{C.14}$$

So far, we only discussed the part of Eq. (C.2) that describes the lattice. For the polarizability there also exists a condition. It is given by the optical theorem and reads

$$\mathrm{Im}\left(\frac{1}{\alpha_E}\right)=-\frac{2k^3}{3}. \tag{C.15}$$

Finally, we combine Eqs. (C.2), (C.14) and (C.15) and obtain

$$\tilde{r} = \frac{2\pi i k}{A}\,\frac{1}{\mathrm{Re}\left(\frac{1}{\alpha_E}\right)+i\left(-\frac{2k^3}{3}\right)-\mathrm{Re}\,(G_{xx}(0))-i\left(\frac{2\pi k}{A}-\frac{2k^3}{3}\right)} \tag{C.16}$$

$$= \frac{2\pi i k}{A}\,\frac{1}{-i\frac{2\pi k}{A}+\mathrm{Re}\left(\frac{1}{\alpha_E}-G_{xx}(0)\right)} \tag{C.17}$$

$$= -\frac{1}{1+\frac{i\,A}{2\pi k}\mathrm{Re}\left(\frac{1}{\alpha_E}-G_{xx}(0)\right)}. \tag{C.18}$$

Thereby, we achieved to derive the form of the reflection coefficient in Eq. (7.100).

Appendix D

Details of the twin dipole model applied to two layers of crosses

In this appendix, we present information on the twin dipole model's application to two layers of mutually rotated crosses. The following notation is in line with Section 7.7. Especially Fig. 7.37 should be borne in mind.

With the abbreviation $\tilde{L} = {}^{l}/_{4}$ we write the positions of the oscillators forming the twin dipoles.

$$\mathbf{r}_1 = \begin{pmatrix} \tilde{L} + \rho_1 \\ 0 \\ \frac{h}{2} \end{pmatrix}, \qquad \mathbf{r}_2 = \begin{pmatrix} 0 \\ \tilde{L} + \rho_2 \\ \frac{h}{2} \end{pmatrix}, \qquad \mathbf{r}_5 = \begin{pmatrix} \tilde{L}\cos\varphi + \rho_5\cos\varphi \\ \tilde{L}\sin\varphi + \rho_5\sin\varphi \\ b + \frac{3}{2}\,h \end{pmatrix},$$

$$\mathbf{r}_4 = \begin{pmatrix} 0 \\ -\tilde{L} + \rho_4 \\ \frac{h}{2} \end{pmatrix}, \qquad \mathbf{r}_3 = \begin{pmatrix} -\tilde{L} + \rho_3 \\ 0 \\ \frac{h}{2} \end{pmatrix}, \qquad \mathbf{r}_6 = \begin{pmatrix} -\tilde{L}\sin\varphi - \rho_6\sin\varphi \\ \tilde{L}\cos\varphi + \rho_6\cos\varphi \\ b + \frac{3}{2}\,h \end{pmatrix},$$

$$\mathbf{r}_7 = \begin{pmatrix} -\tilde{L}\,\cos\varphi + \rho_7\,\cos\varphi \\ -\tilde{L}\,\sin\varphi + \rho_7\,\sin\varphi \\ b + \frac{3}{2}\,h \end{pmatrix}, \qquad \mathbf{r}_8 = \begin{pmatrix} \tilde{L}\,\sin\varphi - \rho_8\,\sin\varphi \\ -\tilde{L}\,\cos\varphi + \rho_8\,\cos\varphi \\ b + \frac{3}{2}\,h \end{pmatrix}. \tag{D.1}$$

The occuring dipole moments are

$$\mathbf{p}_1 = \begin{pmatrix} \rho_1 \\ 0 \\ 0 \end{pmatrix}, \quad \mathbf{p}_2 = \begin{pmatrix} 0 \\ \rho_2 \\ 0 \end{pmatrix}, \quad \mathbf{p}_5 = \begin{pmatrix} \rho_5\,\cos\varphi \\ \rho_5\,\sin\varphi \\ 0 \end{pmatrix}, \quad \mathbf{p}_6 = \begin{pmatrix} -\rho_6\,\sin\varphi \\ \rho_6\,\cos\varphi \\ 0 \end{pmatrix},$$

$$\mathbf{p}_3 = \begin{pmatrix} \rho_3 \\ 0 \\ 0 \end{pmatrix}, \quad \mathbf{p}_4 = \begin{pmatrix} 0 \\ \rho_4 \\ 0 \end{pmatrix}, \quad \mathbf{p}_7 = \begin{pmatrix} \rho_7\,\cos\varphi \\ \rho_7\,\sin\varphi \\ 0 \end{pmatrix}, \quad \mathbf{p}_8 = \begin{pmatrix} -\rho_8\,\sin\varphi \\ \rho_8\,\cos\varphi \\ 0 \end{pmatrix}. \tag{D.2}$$

We state the unit vectors from each oscillator to the others for completeness. They read:

$$\hat{\mathbf{R}}_{12} = \begin{pmatrix} -\tilde{L} \\ \tilde{L} \\ 0 \end{pmatrix} \frac{1}{c_1}, \qquad \hat{\mathbf{R}}_{15} = \begin{pmatrix} \tilde{L}\cos\varphi - \tilde{L} \\ \tilde{L}\sin\varphi \\ b + h \end{pmatrix} \frac{1}{c_3}, \qquad \hat{\mathbf{R}}_{56} = \begin{pmatrix} -\tilde{L}\sin\varphi - \tilde{L}\cos\varphi \\ \tilde{L}\cos\varphi - \tilde{L}\sin\varphi \\ 0 \end{pmatrix} \frac{1}{c_1},$$

$$\hat{\mathbf{R}}_{13} = \begin{pmatrix} -\frac{l}{2} \\ 0 \\ 0 \end{pmatrix} \frac{1}{c_2}, \qquad \hat{\mathbf{R}}_{16} = \begin{pmatrix} -\tilde{L}\sin\varphi - \tilde{L} \\ \tilde{L}\cos\varphi \\ b + h \end{pmatrix} \frac{1}{c_4}, \qquad \hat{\mathbf{R}}_{57} = \begin{pmatrix} -\tilde{L}\cos\varphi - \tilde{L}\cos\varphi \\ -\tilde{L}\sin\varphi - \tilde{L}\sin\varphi \\ 0 \end{pmatrix} \frac{1}{c_2},$$

$$\hat{\mathbf{R}}_{14} = \begin{pmatrix} -\tilde{L} \\ -\tilde{L} \\ 0 \end{pmatrix} \frac{1}{c_1}, \qquad \hat{\mathbf{R}}_{17} = \begin{pmatrix} -\tilde{L}\cos\varphi - \tilde{L} \\ -\tilde{L}\sin\varphi \\ b + h \end{pmatrix} \frac{1}{c_5}, \qquad \hat{\mathbf{R}}_{58} = \begin{pmatrix} \tilde{L}\sin\varphi - \tilde{L}\cos\varphi \\ -\tilde{L}\cos\varphi - \tilde{L}\sin\varphi \\ 0 \end{pmatrix} \frac{1}{c_1},$$

$$\hat{\mathbf{R}}_{23} = \begin{pmatrix} -\tilde{L} \\ -\tilde{L} \\ 0 \end{pmatrix} \frac{1}{c_1}, \quad \hat{\mathbf{R}}_{18} = \begin{pmatrix} \tilde{L}\sin\varphi - \tilde{L} \\ -\tilde{L}\cos\varphi \\ b+h \end{pmatrix} \frac{1}{c_6}, \quad \hat{\mathbf{R}}_{67} = \begin{pmatrix} -\tilde{L}\cos\varphi + \tilde{L}\sin\varphi \\ -\tilde{L}\sin\varphi - \tilde{L}\cos\varphi \\ 0 \end{pmatrix} \frac{1}{c_1},$$

$$\hat{\mathbf{R}}_{24} = \begin{pmatrix} 0 \\ -\frac{l}{2} \\ 0 \end{pmatrix} \frac{1}{c_2}, \quad \hat{\mathbf{R}}_{28} = \begin{pmatrix} \tilde{L}\sin\varphi \\ -\tilde{L}\cos\varphi - \tilde{L} \\ b+h \end{pmatrix} \frac{1}{c_5}, \quad \hat{\mathbf{R}}_{68} = \begin{pmatrix} \tilde{L}\sin\varphi + \tilde{L}\sin\varphi \\ -\tilde{L}\cos\varphi - \tilde{L}\cos\varphi \\ 0 \end{pmatrix} \frac{1}{c_2},$$

$$\hat{\mathbf{R}}_{34} = \begin{pmatrix} \tilde{L} \\ -\tilde{L} \\ 0 \end{pmatrix} \frac{1}{c_1}, \quad \hat{\mathbf{R}}_{35} = \begin{pmatrix} \tilde{L}\cos\varphi + \tilde{L} \\ \tilde{L}\sin\varphi \\ b+h \end{pmatrix} \frac{1}{c_5}, \quad \hat{\mathbf{R}}_{78} = \begin{pmatrix} \tilde{L}\sin\varphi + \tilde{L}\cos\varphi \\ -\tilde{L}\cos\varphi + \tilde{L}\sin\varphi \\ 0 \end{pmatrix} \frac{1}{c_1},$$

$$\hat{\mathbf{R}}_{45} = \begin{pmatrix} \tilde{L}\cos\varphi \\ \tilde{L}\sin\varphi + \tilde{L} \\ b+h \end{pmatrix} \frac{1}{c_4}, \quad \hat{\mathbf{R}}_{46} = \begin{pmatrix} -\tilde{L}\sin\varphi \\ \tilde{L}\cos\varphi + \tilde{L} \\ b+h \end{pmatrix} \frac{1}{c_5}, \quad \hat{\mathbf{R}}_{25} = \begin{pmatrix} \tilde{L}\cos\varphi \\ \tilde{L}\sin\varphi - \tilde{L} \\ b+h \end{pmatrix} \frac{1}{c_6},$$

$$\hat{\mathbf{R}}_{48} = \begin{pmatrix} \tilde{L}\sin\varphi \\ \tilde{L} - \tilde{L}\cos\varphi \\ b+h \end{pmatrix} \frac{1}{c_3}, \quad \hat{\mathbf{R}}_{36} = \begin{pmatrix} \tilde{L} - \tilde{L}\sin\varphi \\ \tilde{L}\cos\varphi \\ b+h \end{pmatrix} \frac{1}{c_6}, \quad \hat{\mathbf{R}}_{37} = \begin{pmatrix} \tilde{L} - \tilde{L}\cos\varphi \\ -\tilde{L}\sin\varphi \\ b+h \end{pmatrix} \frac{1}{c_3},$$

$$\hat{\mathbf{R}}_{38} = \begin{pmatrix} \tilde{L}\sin\varphi + \tilde{L} \\ -\tilde{L}\cos\varphi \\ b+h \end{pmatrix} \frac{1}{c_4}, \quad \hat{\mathbf{R}}_{47} = \begin{pmatrix} -\tilde{L}\cos\varphi \\ -\tilde{L}\sin\varphi + \tilde{L} \\ b+h \end{pmatrix} \frac{1}{c_6},$$

$$\hat{\mathbf{R}}_{26} = \begin{pmatrix} -\tilde{L}\sin\varphi \\ \tilde{L}\cos\varphi - \tilde{L} \\ b+h \end{pmatrix} \frac{1}{c_3}, \quad \hat{\mathbf{R}}_{27} = \begin{pmatrix} -\tilde{L}\cos\varphi \\ -\tilde{L}\sin\varphi - \tilde{L} \\ b+h \end{pmatrix} \frac{1}{c_4}. \tag{D.3}$$

Here, the terms c_i, $i = 1, ..., 6$ are used for normalization. They are given by

$$c_1 = \tilde{L}\sqrt{2}, \quad c_3 = \sqrt{2\tilde{L}^2 - 2\tilde{L}^2\cos\varphi + (b+h)^2}, \quad c_4 = \sqrt{2\tilde{L}^2 + 2\tilde{L}^2\sin\varphi + (b+h)^2},$$

$$c_2 = \frac{l}{2}, \qquad c_5 = \sqrt{2\tilde{L}^2 + 2\tilde{L}^2\cos\varphi + (b+h)^2}, \quad c_6 = \sqrt{2\tilde{L}^2 - 2\tilde{L}^2\sin\varphi + (b+h)^2}. \tag{D.4}$$

With the dipole-dipole potential from Eq. (7.113) the equations of motion for the four twin dipoles are derived. They are stated in Eq. (7.155). The occurring coupling terms are:

$$L_5 = \tau\, \frac{Ne^2\left(\cos\varphi - 3\left(\frac{l}{4c_5}\right)^2(\cos\varphi+1)^2\right)}{8\pi\varepsilon_0\, c_5^3\, m}, \; L_3 = \tau\, \frac{Ne^2\left(\cos\varphi + 3\left(\frac{l}{4c_3}\right)^2(\cos\varphi-1)^2\right)}{8\pi\varepsilon_0\, c_3^3\, m},$$

$$L_1 = \frac{3\,N\,e^2\,\tilde{L}^2}{8\pi\varepsilon_0\, c_1^5\, m}, \qquad L_4 = \frac{N\,e^2\left(-\sin\varphi + 3\left(\frac{l}{4\,c_4}\right)^2(\sin\varphi+1)^2\right)}{8\pi\varepsilon_0\, c_4^3\, m},$$

$$L_2 = \tau\, \frac{N\,e^2\left(1 - 3\,\frac{l^2}{4\,c_2^2}\right)}{8\pi\varepsilon_0\, c_2^3\, m}, \quad L_6 = \tau\, \frac{Ne^2\left(-\sin\varphi - 3\left(\frac{l}{4c_6}\right)^2(\sin\varphi-1)^2\right)}{8\pi\varepsilon_0\, c_6^3\, m}. \tag{D.5}$$

Interestingly, the term L_1 does not enter the resulting expressions for the transmittance—it does not play a role due to symmetry reasons. Furthermore, $L_2 = -L$ with L being the coupling of the two oscillators forming the twin dipoles, see Eq. (7.114). The negative sign is explained by the different definition of the ρ_i in the equations of motion. The parameter τ is the fit parameter of the interlayer coupling, cf. Eq. (7.131).

The field terms in the equations of motion (7.155) are given by

$$E_1 = e^{ik\frac{h}{2}} + \frac{\tilde{t}_0\,\tilde{r}_0\,e^{i\delta}\,e^{ik\frac{3}{2}h}}{1-\tilde{r}_0^2\,e^{i\delta}}, \qquad E_2 = \frac{\tilde{t}_0\,e^{i\frac{\delta}{2}}\,e^{ik\frac{3}{2}h}}{1-\tilde{r}_0^2\,e^{i\delta}}. \tag{D.6}$$

They are derived just like in the case of two layers of rods and/or crosses modeled with the dipole model and read

$$\tilde{r}_\varphi = \frac{\left(e^{i2kh}-1\right)i\pi}{A\,h\,k^3}\,\frac{-i\,k^3\,N\,e^2}{4\pi\varepsilon_0\,m}\,\frac{\cos^2\varphi}{\omega_0^2-\omega^2-i\omega\Gamma-L}, \tag{D.7a}$$

$$\tilde{t}_0 = 1-\frac{2\,\pi}{k^2\,A}\,\frac{-i\,k^3\,N\,e^2}{4\pi\varepsilon_0\,m\,(\omega_0^2-\omega^2-i\omega\Gamma-L)}. \tag{D.7b}$$

Here, we already used the projected formulation. The only difference to the dipole model is that the coupling L, which describes the coupling between two oscillators forming a twin dipole, enters.

With the help of the terms above, the equations of motion for the system can be solved. The solution is given in Eq. (7.156). The next step is deducing the field emitted by the first layer of oscillators. The field emitted by the first oscillator at the observer's position $\mathbf{Q}$ is obtained by

$$\mathbf{Q} = \begin{pmatrix}0\\0\\u+\frac{h}{2}\end{pmatrix}, \quad \mathbf{r}_{\text{oscill},1} = \begin{pmatrix}\tilde{L}\\0\\\frac{h}{2}\end{pmatrix}, \quad |\mathbf{Q}-\mathbf{r}_{\text{oscill},1}| = \left\|\begin{pmatrix}-\tilde{L}\\0\\u\end{pmatrix}\right\| = \sqrt{\tilde{L}^2+u^2} =: r_1 \tag{D.8}$$

$$\mathbf{E}_1(\mathbf{Q},t) = -\frac{1}{4\pi\varepsilon_0}\frac{\frac{N}{2}\,e}{r_1^3\,c^2}\left[\begin{pmatrix}-\tilde{L}\\0\\u\end{pmatrix}\times\left[\begin{pmatrix}-\tilde{L}\\0\\u\end{pmatrix}\times\begin{pmatrix}\ddot{p}_1\\0\\0\end{pmatrix}\right]\right]_{t-\frac{r_1}{c}} = -\frac{1}{4\pi\varepsilon_0}\frac{N\,e}{2\,r_1^3\,c^2}\begin{pmatrix}-u^2\,\ddot{p}_1\\0\\-\tilde{L}\,u\,\ddot{p}_1\end{pmatrix}_{t-\frac{r_1}{c}}. \tag{D.9}$$

The other oscillators follow in analogy. The sum of the emitted fields of the first layer is then found in Eq. (7.157).

Similarly, we derive the fields for the second layer. Exemplarily, the field of the fifth oscillator at $\mathbf{Q}' = (0,0,d+b+3/2\;h)$ reads

$$\mathbf{r}_{\text{oscill},5} = \begin{pmatrix}\tilde{L}\,\cos\varphi\\\tilde{L}\,\sin\varphi\\b+\frac{3}{2}\,h\end{pmatrix}, \quad |\mathbf{Q}'-\mathbf{r}_{\text{oscill},5}| = \left\|\begin{pmatrix}-\tilde{L}\,\cos\varphi\\-\tilde{L}\,\sin\varphi\\d\end{pmatrix}\right\| = \sqrt{\tilde{L}^2+d^2} =: r_2 \tag{D.10}$$

$$\begin{aligned}\mathbf{E}_5(\mathbf{Q}',t) &= \frac{-\frac{N}{2}\,e}{4\pi\varepsilon_0\,r_2^3\,c^2}\left[\begin{pmatrix}-\tilde{L}\cos\varphi\\-\tilde{L}\sin\varphi\\d\end{pmatrix}\times\left[\begin{pmatrix}-\tilde{L}\cos\varphi\\-\tilde{L}\sin\varphi\\d\end{pmatrix}\times\begin{pmatrix}\ddot{p}_3\cos\varphi\\\ddot{\rho}_3\sin\varphi\\0\end{pmatrix}\right]\right]_{t-\frac{r_2}{c}}\\ &= -\frac{1}{4\pi\varepsilon_0}\,\frac{N\,e}{2\,r_2^3\,c^2}\begin{pmatrix}-d^2\,\ddot{p}_3\,\cos\varphi\\-d^2\,\ddot{\rho}_3\,\sin\varphi\\-\tilde{L}\,d\,\ddot{\rho}_3\end{pmatrix}_{t-\frac{r_2}{c}}.\end{aligned} \tag{D.11}$$

The sum of all emitted fields, the resulting scattering matrix entries and the field transmitted through the whole structure are found in Section 7.7.4.

Bibliography

[1] K. Busch, G. von Freymann, S. Linden, S. F. Mingaleev, L. Tkeshelashvili, and M. Wegener, "Periodic nanostructures for photonics," *Physics Reports*, vol. 444, pp. 101–202, 2007.

[2] V. G. Vaselago, "The electrodynamics of substances with simultaneously negative values of ε and μ," *Sov. Phys. Usp.*, vol. 10, pp. 509–514, 1968.

[3] R. A. Shelby, D. R. Smith, and S. Schultz, "Experimental Verification of a Negative Index of Refraction," *Science*, vol. 292, pp. 77–79, 2001.

[4] J. B. Pendry, "Negative Refraction Makes a Perfect Lens," *Phys. Rev. Lett.*, vol. 85, pp. 3966–3969, 2000.

[5] E. Yablonovitch, "Inhibiting Spontaneous Emission in Solid-State Physics and Electronics," *Phys. Rev. Lett.*, vol. 58, pp. 2059–2062, 1987.

[6] S. John, "Strong Localization of Photons in Certain Disordered Dielectric Superlattices," *Phys. Rev. Lett.*, vol. 58, pp. 2486–2489, 1987.

[7] A. Fröhlich, J. Fischer, T. Zebrowski, K. Busch, and M. Wegener, "Complete three-dimensional photonic band gap in the visible," *Nature Materials*, (submitted).

[8] C. M. Soukoulis and M. Wegener, "Past achievements and future challenges in the development of three-dimensional photonic metamaterials," *Nature Photonics*, vol. 5, pp. 523–530, 2011.

[9] A. Taflove and S. Hagness, *Computational Electrodynamics: The Finite-Difference Time-Domain Method*. Artech House, 3rd ed., 2005.

[10] J. S. Hesthaven and T. Warburton, *Nodal Discontinuous Galerkin Methods: Algorithms, Analysis, and Applications*. Springer, 2008.

[11] P. Monk, *Finite Element Methods for Maxwell's Equations*. Oxford Univ. Pr., 2003.

[12] L. Li, "Fourier modal method for crossed anisotropic gratings with arbitrary permittivity and permeability tensors," *J. Opt. A*, vol. 5, pp. 345–355, 2003.

[13] L. Li, "Formulation and comparison of two recursive matrix algorithms for modeling layered diffraction gratings," *J. Opt. Soc. Am. A*, vol. 13, pp. 1024–1034, 1996.

[14] P. Lalanne and G. M. Morris, "Highly improved convergence of the coupled-wave method for TM polarization," *J. Opt. Soc. Am. A*, vol. 13, pp. 779–784, 1996.

[15] T. Weiss, G. Granet, N. A. Gippius, S. G. Tikhodeev, and H. Giessen, "Matched coordinates and adaptive spatial resolution in the Fourier modal method," *Opt. Express*, vol. 17, pp. 8051–8061, 2009.

[16] S. Essig and K. Busch, "Generation of adaptive coordinates and their use in the Fourier Modal Method," *Opt. Express*, vol. 18, pp. 23258–23274, 2010.

[17] G. Granet, "Reformulation of the lamellar grating problem through the concept of adaptive spatial resolution," *J. Opt. Soc. Am. A*, vol. 16, pp. 2510–2516, 1999.

[18] C. F. Bohren and D. R. Huffman, *Absorption and Scattering of Light by Small Particles.* Wiley-VCH, 2004.

[19] H. A. Lorentz, *The theory of electrons.* Dover Pub., 2nd ed., 1952. This book is a reprint of an earlier publication, based on Lorentz' lecture notes of 1906.

[20] J. D. Jackson, *Classical Electrodynamics.* de Gruyter, 3rd ed., 1999.

[21] T. Fließbach, *Elektrodynamik.* Spektrum, 4th ed., 2005.

[22] K. Kopitzki and P. Herzog, *Einführung in die Festkörperphysik.* Teubner, 4th ed., 2002.

[23] V. M. Agranovich and V. L. Ginzburg, *Crystal optics with spatial dispersion, and excitons.* Springer, 2nd ed., 1984.

[24] P. B. Johnson and R. W. Christy, "Optical Constants of the Noble Metals," *Phys. Rev. B*, vol. 6, pp. 4370–4379, 1972.

[25] A. Vial, A.-S. Grimault, D. Macías, D. Barchiesi, and M. L. de la Chapelle, "Improved analytical fit of gold dispersion: Application to the modeling of extinction spectra with a finite-difference time-domain method," *Phys. Rev. B*, vol. 71, 085416, 2005.

[26] W. Demtröder, *Experimentalphysik 2.* Springer, 4th ed., 2006.

[27] M. Born and E. Wolf, *Principles of Optics.* Cambridge Univ. Press, 7th ed., 2002.

[28] H. Schade and K. Neemann, *Tensoranalysis.* de Gruyter, 3rd ed., 2009.

[29] F. Bloch, "Über die Quantenmechanik der Elektronen in Kristallgittern," *Zeitschrift für Physik A*, vol. 52, pp. 555–600, 1928.

[30] K. Sakoda, *Optical Properties of Photonic Crystals.* Springer, 2001.

[31] J. W. Strutt, 3rd Baron Rayleigh, "On the Dynamical Theory of Gratings," *Proc. R. Soc. Lond. A*, vol. 79, pp. 399–416, 1907.

[32] R. W. Wood, "Anomalous Diffraction Gratings," *Phys. Rev.*, vol. 48, pp. 928–936, 1935.

[33] T. Zebrowski, *The full anisotropic adaptive Fourier Modal Method and its application to periodic and aperiodic photonic nanostructures.* PhD thesis, Karlsruhe Institute of Technology (KIT), 2012.

[34] S. Essig, *Advanced numerical methods in diffractive optics and applications to periodic photonic nanostructures.* PhD thesis, Karlsruhe Institute of Technology (KIT), 2011.

[35] A. J. Ward and J. B. Pendry, "Refraction and geometry in Maxwell's equations," *Journal of Mod. Opt.*, vol. 43, pp. 773–793, 1996.

[36] D. M. Shyroki, "Note on transformation to general curvilinear coordinates for Maxwell's curl equations," *arXiv:physics/0307029*, 2003.

[37] D. Schurig, J. B. Pendry, and D. R. Smith, "Calculation of material properties and ray tracing in transformation media," *Opt. Express*, vol. 14, pp. 9794–9804, 2006.

[38] V. Liu and S. Fan, "S^4: A free electromagnetic solver for layered periodic structures," *Comp. Phys. Comm.*, vol. 183, pp. 2233–2244, 2012.

[39] H. Kim, J. Park, and B. Lee, *Fourier Modal Method and its Applications in Computational Nanophotonics*. CRC Press, 2012.

[40] D. M. Whittaker and I. S. Culshaw, "Scattering-matrix treatment of patterned multilayer photonic structures," *Phys. Rev. B*, vol. 60, pp. 2610–2618, 1999.

[41] E. Anderson, Z. Bai, C. Bischof, S. Blackford, J. Demmel, J. Dongarra, J. D. Croz, A. Greenbaum, S. Hammarling, A. McKenney, and D. Sorensen, *LAPACK Users' Guide*. Society for Industrial and Applied Mathematics, 3rd ed., 1999.

[42] I. M. K. Library. `http://software.intel.com/en-us/intel-mkl`, Oct. 2012.

[43] C. Wolff, S. Romanov, J. Küchenmeister, U. Peschel, and K. Busch, "Polarization Dynamics in Cubic Photonic Crystals," (submitted).

[44] S. Romanov, J. Küchenmeister, C. Wolff, U. Peschel, and K. Busch, "Axial anisotropy of light transmission in opal photonic crystals," (in preparation).

[45] S. G. Johnson and J. D. Joannopoulos, "Block-iterative frequency-domain methods for Maxwell's equations in a planewave basis," *Opt. Express*, vol. 8, pp. 173–190, 2001.

[46] K. Busch, S. Lölkes, R. Wehrspohn, and H. Föll, *Photonic Crystals: Advances in Design, Fabrication, and Characterization*. Wiley-VCH, 2004.

[47] S. G. Romanov, U. Peschel, M. Bardosova, S. Essig, and K. Busch, "Suppression of the critical angle of diffraction in thin-film colloidal photonic crystals," *Phys. Rev. B*, vol. 82, 115403, 2010.

[48] J. F. Galisteo-López, E. Palacios-Lidón, E. Castillo-Martínez, and C. López, "Optical study of the pseudogap in thickness and orientation controlled artificial opals," *Phys. Rev. B*, vol. 68, 115109, 2003.

[49] J. F. Galisteo-López, M. Galli, M. Patrini, A. Balestreri, L. C. Andreani, and C. López, "Effective refractive index and group velocity determination of three-dimensional photonic crystals by means of white light interferometry," *Phys. Rev. B*, vol. 73, 125103, 2006.

[50] C. Wolff, *Band Structure Based Analysis of Certain Photonic Crystal Structures*. PhD thesis, Karlsruhe Institute of Technology (KIT), 2011.

[51] T. Vallius and M. Honkanen, "Reformulation of the Fourier modal method with adaptive spatial resolution: application to multilevel profiles," *Opt. Express*, vol. 10, pp. 24–34, 2002.

[52] G. Granet and J.-P. Plumey, "Parametric formulation of the Fourier modal method for crossed surface-relief gratings," *J. Opt. A*, vol. 4, pp. S145–S149, 2002.

[53] J. Küchenmeister, T. Zebrowski, and K. Busch, "A construction guide to analytically generated meshes for the Fourier Modal Method," *Opt. Express*, vol. 20, pp. 17319–17347, 2012.

[54] L. Li, "New formulation of the Fourier modal method for crossed surface-relief gratings," *J. Opt. Soc. Am. A*, vol. 14, pp. 2758–2767, 1997.

[55] A. W. Snyder and J. D. Love, *Optical Waveguide Theory*. Chapman and Hall, 1983.

[56] P. Russell, "Photonic Crystal Fibers," *Science*, vol. 299, pp. 358–362, 2003.

[57] T. R. Woliński, S. Ertman, P. Lesiak, A. W. Domański, A. Czapla, R. Dąbrowski, E. Nowinowski-Kruszelnicki, and J. Wojcik, "Photonic liquid crystal fibers - a new challenge for fiber optics and liquid crystals photonics," *Opto-Electron. Rev.*, vol. 14, pp. 329–334, 2006.

[58] M. Decker, M. Ruther, C. E. Kriegler, J. Zhou, C. M. Soukoulis, S. Linden, and M. Wegener, "Strong optical activity from twisted-cross photonic metamaterials," *Opt. Lett.*, vol. 34, pp. 2501–2503, 2009.

[59] J. K. Gansel, M. Thiel, M. S. Rill, M. Decker, K. Bade, V. Saile, G. Freymann, S. Linden, and M. Wegener, "Gold Helix Photonic Metamaterial as Broadband Circular Polarizer," *Science*, vol. 325, pp. 1513–1515, 2009.

[60] J. Chandezon, D. Maystre, and G. Raoult, "A new theoretical method for diffraction gratings and its numerical application," *J. Opt.*, vol. 11, pp. 235–241, 1980.

[61] I. Gushchin and A. V. Tishchenko, "Fourier modal method for relief gratings with oblique boundary conditions," *J. Opt. Soc. Am. A*, vol. 27, pp. 1575–1583, 2010.

[62] J. Küchenmeister, *Modelling of metallic nanostructures using a coupled dipole approach.* Wissenschaftliche Arbeit zur Zulassung zum ersten Staatsexamen im Fach Physik, 2008.

[63] S. Linden, C. Enkrich, M. Wegener, J. Zhou, T. Koschny, and C. M. Soukoulis, "Magnetic Response of Metamaterials at 100 Terahertz," *Science*, vol. 306, pp. 1351–1353, 2004.

[64] J. Petschulat, J. Yang, C. Menzel, C. Rockstuhl, A. Chipouline, P. Lalanne, A. Tünnermann, F. Lederer, and T. Pertsch, "Understanding the electric and magnetic response of isolated metaatoms by means of a multipolar field decomposition," *Opt. Express*, vol. 18, pp. 14454–14466, 2010.

[65] J. Petschulat, C. Menzel, A. Chipouline, C. Rockstuhl, A. Tünnermann, F. Lederer, and T. Pertsch, "Multipole approach to metamaterials," *Phys. Rev. A*, vol. 78, 043811, 2008.

[66] J. Petschulat, A. Chipouline, A. Tünnermann, T. Pertsch, C. Menzel, C. Rockstuhl, T. Paul, and F. Lederer, "Simple and versatile analytical approach for planar metamaterials," *Phys. Rev. B*, vol. 82, 075102, 2010.

[67] N. Liu, H. Liu, S. Zhu, and H. Giessen, "Stereometamaterials," *Nature Photonics*, vol. 3, pp. 157–162, 2009.

[68] P. T. Bowen, T. Driscoll, N. B. Kundtz, and D. R. Smith, "Using a discrete dipole approximation to predict complete scattering of complicated metamaterials," *New Journal of Physics*, vol. 14, 033038, 2012.

[69] N. Liu and H. Giessen, "Coupling effects in optical metamaterials," *Angew. Chem. Int. Ed.*, vol. 49, pp. 9838–9852, 2010.

[70] Y. Svirko, N. Zheludev, and M. Osipov, "Layered chiral metallic microstructures with inductive coupling," *Appl. Phys. Lett.*, vol. 78, pp. 498–500, 2001.

[71] A. S. Schwanecke, V. A. Fedotov, V. V. Khardikov, S. L. Prosvirnin, Y. Chen, and N. I. Zheludev, "Nanostructured Metal Film with Asymmetric Optical Transmission," *Nano Letters*, vol. 8, pp. 2940–2943, 2008.

[72] J. Dong, J. Zhou, T. Koschny, and C. Soukoulis, "Bi-layer cross chiral structure with strong optical activity and negative refractive index," *Opt. Express*, vol. 17, pp. 14172–14179, 2009.

[73] J. Zhou, J. Dong, B. Wang, T. Koschny, M. Kafesaki, and C. Soukoulis, "Negative refractive index due to chirality," *Phys. Rev. B*, vol. 79, 121104, 2009.

[74] B. Wang, J. Zhou, T. Koschny, M. Kafesaki, and C. M. Soukoulis, "Chiral metamaterials: simulations and experiments," *J. Opt. A: Pure Appl. Opt.*, vol. 11, 114003, 2009.

[75] E. Plum, J. Zhou, J. Dong, V. A. Fedotov, T. Koschny, C. M. Soukoulis, and N. I. Zheludev, "Metamaterial with negative index due to chirality," *Phys. Rev. B*, vol. 79, 035407, 2009.

[76] J. Budde, "Chiral Metamaterials," Master's thesis, Universität Karlsruhe (TH), 2007.

[77] J. N. Hodgson, "The optical properties of gold," *J. Phys. Chem. Solids*, vol. 29, pp. 2175–2181, 1968.

[78] F. J. G. de Abajo, "Light scattering by particle and hole arrays," *Reviews of Modern Physics*, vol. 79, 2007.

[79] M. L. Glasser and I. J. Zucker, *Theoretical Chemistry: Advances and Perspectives*, vol. 5. pp. 67–139: edited by H. Eyring and D. Henderson, Academic, New York, 1980.

[80] K. Kambe, "Theory of low-energy electron diffraction II. Cellular method for complex monolayers and multilayers," *Z. Naturforsch. A*, vol. 23, pp. 1280–1294, 1968.

[81] S. Zhang, D. A. Genov, Y. Wang, M. Liu, and X. Zhang, "Plasmon-Induced Transparency in Metamaterials," *Phys. Rev. Lett.*, vol. 101, 047401, 2008.

[82] L. Li, "Use of Fourier series in the analysis of discontinuous periodic structures," *J. Opt. Soc. Am. A*, vol. 13, pp. 1870–1876, 1996.

[83] M. Frigo and S. G. Johnson, "The design and implementation of FFTW3," *Proceedings of the IEEE*, vol. 93, pp. 216–231, 2005.

List of Publications

Articles in Peer-Reviewed Journals and in Preparation

- ✧ *A construction guide to analytically generated meshes for the Fourier Modal Method*; J. Küchenmeister, T. Zebrowski, and K. Busch, Opt. Express, vol. 20, pp. 17319–17347, 2012.
- ✧ *Direct Observation of Non-Markovian Radiation Dynamics in 3D Bulk Photonic Crystals*; U. Hoeppe, C. Wolff J. Küchenmeister, J. Niegemann, M. Drescher, H. Benner and K. Busch, Phys. Rev. Lett., vol. 108, 043603, 2012.
- ✧ *Polarization Dynamics in Cubic Photonic Crystals*; C. Wolff, S. G. Romanov, J. Küchenmeister, U. Peschel and K. Busch, Phys. Rev. Lett., (submitted).
- ✧ *B-Spline modal method: A polynomial approach compared to the Fourier modal method*; M. Walz, T. Zebrowski, J. Küchenmeister and K. Busch, (in preparation).
- ✧ *Axial anisotropy of light transmission in opal photonic crystals*; S. G. Romanov, J. Küchenmeister, C. Wolff, U. Peschel and K. Busch, (in preparation).

Conference Proceedings

- ✧ *A B-spline modal method in comparison to the Fourier modal method*; M. Walz, T. Zebrowski, J. Küchenmeister and K. Busch, AIP Conference Proceedings, vol. 1398, pp. 177-179, 2011.
- ✧ *Polarization Change in Face–Centered Cubic Opal Films*; C. Wolff, S. G. Romanov, J. Küchenmeister, U. Peschel and K. Busch, AIP Conference Proceedings, vol. 1398, pp. 112–114, 2011.
- ✧ *Cross–polarization breakdown in 3–dimensional opal photonic crystals*; C. Wolff, J. Küchenmeister, K. Busch, S. G. Romanov and U. Peschel, CLEO/Europe and EQEC 2011 Conference Digest CK9_6, 2011.

Oral Presentations

- ✧ *Analytically generated adaptive meshes for the Fourier Modal Method*; J. Küchenmeister, T. Zebrowski, S. Essig and K. Busch, DPG-Tagung Berlin, 2012.
- ✧ *Ein quantenphysikalischer Zufallszahlgenerator im Schülerlabor*; J. Küchenmeister, L. Führinger, A. Bergmann and J. Schmalian, DPG-Tagung Mainz, 2012.
- ✧ *Generation of adaptive coordinates for the Fourier Modal Method*; J. Küchenmeister, T. Zebrowski, S. Essig and K. Busch, 7th Workshop on Numerical Methods for Optical Nano Structures, Zurich, 2011.
- ✧ *Schulexperimente und Materialien zur Nanophysik*; J. Küchenmeister, Lehrerfortbildung Nanophysik – Nutzen und Visionen, Karlsruhe, 2010.

Acknowledgments

This thesis is the product of three years of hard work, long days, sometimes even long nights and lots of sugar. At this point, I thank all the people who helped me to make it to the finish line. I am going to take the unusual step to express my thanks in mother tongue.

Während ich diese Zeilen am Ende meiner Dissertation schreibe, bin ich erfüllt von großer Freude über das Erreichte - und darüber hinaus von Dankbarkeit und tiefer Demut gegenüber der erhaltenen Chance. Den folgenden Personen möchte ich herzlich danken:

- Prof. Dr. Kurt Busch. Du hast mich seit dem Beginn meiner Staatsexamensarbeit unterstützt und mir die Möglichkeit zur Promotion in Deiner Gruppe gegeben. Insbesondere hatte ich die Freiheit, die Entwicklung der Mesh-Generierung und der Dipolmodelle selbstständig voranzutreiben. Ich danke Dir sehr für die Unterstützung in den letzten Jahren.
- Prof. Dr. Martin Wegener. Sie haben sich die Zeit genommen, mein Korreferent zu sein, wofür ich Ihnen herzlich danke.
- Dr. Thomas Zebrowski. Du hast meine Arbeit betreut und warst ein Grund dafür, dass ich mich für die FMM entschieden habe. Deine tägliche Unterstützung (und insbesondere Deine Geduld bei Code-Fragen) war beispielhaft für jeden Betreuer. Darüber hinaus warst Du ein grandioser Bürokollege, dessen Kampfgeist (auch in schweren Zeiten) und Weitsichtigkeit mich inspiriert haben.
- Dr. Sabine Essig. Wir haben insbesondere im Rahmen des Dipolmodells gut zusammengearbeitet und Du hast ASR und AC in unserem FMM-Code verankert. Das gab mir die Möglichkeit an einem spannenden Thema zu arbeiten, das gleichzeitig mathematisch und physikalisch fordernd ist.
- Prof. Dr. Sergei Romanov. Durch die Kollaboration mit Ihnen war es mir möglich, die Stärken der FMM bei der Berechnung der Opal-Spektren zu benutzen. Für die gute Zusammenarbeit bedanke ich mich herzlich bei Ihnen.
- Dr. Christian Wolff. Du bist ein Quell der physikalischen Einsicht - die Arbeit mit Dir war immer interessant und lehrreich.
- Dr. Antje Bergmann. Du hast mir im Rahmen des Schülerlabors und der Lehramtsabteilung die Möglichkeit gegeben, meine akademische Herkunft nicht aus den Augen zu verlieren. Als Quelle der guten Laune bist Du unersetzlich.
- All jenen, die Teile dieser Arbeit Korrektur gelesen haben. Dafür danke ich insbesondere Thomas Zebrowski, Michael Walz, Paolo Longo, Julia Werra, Antje Bergmann, Christian Wolff, Michael König, Matthias Moeferdt, Eva Wollrab und Sabine Essig.
- All den vielen anderen aktuellen und früheren Mitgliedern der Photonics Group, insbesondere den Mitgliedern der Funky Photons, die hier noch unerwähnt geblieben sind. Die Atmosphäre in dieser Arbeitsgruppe war einzigartig.

Auch im privaten Bereich möchte ich viele Menschen nicht unerwähnt lassen.

- ✧ Mein Marathonengel Nadin. Der Dank könnte Seiten füllen, deshalb an dieser Stelle nur: Vielen Dank!
- ✧ Petra und Rainer. Ihr habt Nadin und mich auch in schwierigen Situationen immer unterstützt - wir werden Eurem Beispiel folgen.
- ✧ Laura und Andrew. Danke dafür, dass Ihr angehalten habt, als niemand sonst es tat.
- ✧ Julian, Tob, Sanne, Rolf, Eva und Vic. Ihr seid allesamt "Leidensgenossen" - danke dafür, dass Ihr für eine gute "Normierung" gesorgt habt.